Tampere University

PAULI LOSOI

Characterization of Large-Scale Bioreactors

Modeling Biological and Multi-Point Feed Approaches to Reactor Homogenization

Tampere University Dissertations 932

Tampere University Dissertations 932

PAULI LOSOI

Characterization of Large-Scale Bioreactors

Modeling Biological and Multi-Point Feed Approaches to Reactor Homogenization

ACADEMIC DISSERTATION
To be presented, with the permission of
the Faculty of Engineering and Natural Sciences
of Tampere University,
for public discussion in the Small Auditorium 1 (FA032)
of the Festia building, Korkeakoulunkatu 8, Tampere,
on 5 January 2024, at 12 o'clock.

ACADEMIC DISSERTATION
Tampere University, Faculty of Engineering and Natural Sciences
Finland

Responsible supervisor and Custos	Associate Professor Ville Santala Tampere University Finland	
Supervisor	Professor Jukka Konttinen Tampere University Finland	
Pre-examiners	Professor Ville Alopaeus Aalto University Finland	Professor Jérôme Morchain Université de Toulouse France
Opponent	Professor Peter Neubauer Technische Universität Berlin Germany	

The originality of this thesis has been checked using the Turnitin OriginalityCheck service.

Cover design: Roihu Inc.

ISBN 978-952-03-3225-9 (print)
ISBN 978-952-03-3226-6 (pdf)
ISSN 2489-9860 (print)
ISSN 2490-0028 (pdf)
http://urn.fi/URN:ISBN:978-952-03-3226-6

Carbon dioxide emissions from printing Tampere University dissertations have been compensated.

PunaMusta Oy – Yliopistopaino
Joensuu 2023

ACKNOWLEDGEMENTS

This work was carried out at the Faculty of Engineering and Natural Sciences, Tampere University. Financial support of TUT Graduate School, Academy of Finland, and Business Finland is acknowledged.

The biggest thanks belong to my supervisors, Associate Professor Ville Santala and Professor Jukka Konttinen, for the supervision, guidance, and insight, and for the possibility to conduct rather independent research. You have been most supportive throughout, even when I suggested to shift the main focus from co-culture scale-up to more general bioreactor modeling in spring 2021. I want to thank my co-author, Dr. Suvi Santala, for all the support and guidance, and for the first introduction to bacterial co-cultures.

I am also most grateful for the thorough and perceptive pre-examinations conducted by Professor Ville Alopeus and Professor Jérôme Morchain, and for Professor Peter Neubauer for agreeing to act as the opponent at the public examination of my thesis. Your publications on bioreactor modeling and bioprocesses have influenced my studies, and I am humbled by having you as reviewers of my thesis.

I have enjoyed my time in the Synbio group, not only for the sake of bioengineering, but also for the warm and friendly atmoshpere. Thanks to both current and former members: Ville, Suvi, Carlotta, Changshuo, Davide, Elena, Ella, Emmi, Heidi, Jenni, Jin, Johanna K., Johanna R-K., Kesi, Matti, Milla, Pietro, Rahul, Sara, Tapio, and Tongyu. I also thank Dr. Tommi Aho for the summer work that first introduced me to the group at TUT back in 2016.

Paljosta saa ihminen olla kiitollinen, ja ehkäpä etenkin toisista ihmisistä. Kiitos, isä, äiti ja sisarukset; kiitos, vaimoseni ja lapsukaiseni. Soli Deo gloria.

Tampere, December 2023
Pauli Losoi

ABSTRACT

Industrial microbial bioprocesses are an important subset of the world-wide chemical industry, contributing to the production of pharmaceuticals, chemicals, biocatalysts, and fuels alike. The conditions met by the microorganisms in industrial-scale reactors differ from those encountered at laboratory scale, decreasing titer, yield, and productivity achieved in the process.

Modeling has been used to characterize large-scale reactors, as experiments are challenging and costly. Thus far, the reactor models that admit physicochemical heterogeneity have been numerical. Analytical, simple, and generalized models would be preferable for preliminary investigations. The first aim of this study was to develop a comprehensive but analytically solvable bioreactor model encompassing mixing times, concentrations of substrate and dissolved oxygen, and profiles of pH, temperature, and carbon dioxide. The second objective was to study means to improve the mixing and to homogenize the relevant quantities in large-scale bioreactors operated in the fed-batch mode.

To achieve the goals, analytical solutions to axial diffusion equations were developed and validated against a large set of literature data, bioreactors were characterized using analytical and numerical models, optimal feed point placements were derived, and a stable bacterial co-culture capable of homogenizing the substrate profiles experienced by the constituent strains was constructed. The derived feed point placements and co-cultures were also modeled and simulated in large-scale bioreactors.

As a conclusion to the conducted modeling, great improvements in mixing should be achievable if the optimal feed arrangements could be implemented. The shared carbon flow in a co-culture also homogenized the substrate profiles experienced by the microorganisms. The study demonstrated a simple yet spatially accurate model of heterogeneous bioreactors and also two potential approaches to recover the reactor performance by efficient homogenization.

TIIVISTELMÄ

Mikrobiologisilla prosesseilla tuotetaan lääkkeitä, kemikaaleja, biokatalyyttejä sekä polttoaineita. Prosessin kasvattaminen tutkimuslaitteistosta tuotantomittakaavaan vaikuttaa tuottomikrobien elin- ja kasvuympäristöön ja pienentää saavutettua tuotteen pitoisuutta ja saantoa sekä reaktorin tuottavuutta.

Käytännön rajoitteet ja suuret kustannukset estävät tuotantomittakaavan reaktorien tutkimuskäytön, minkä vuoksi mallit ja simulaatiot ovat korvaamattomia reaktorien tutkimisessa. Fysikaalisesti tarkat avaruudelliset mallit ovat numeerisesti ratkaistavia, mutta yksinkertaiset analyyttiset mallit olisivat ihanteellisia nopeisiin yleiskatsauksiin. Tämän tutkimuksen yhtenä tavoitteena oli tuottaa kattava ja avaruudellisen vaihtelun salliva, mutta silti analyyttisesti ratkaistu bioreaktorimalli sekoittumisajoista, syötetyn substraatin ja liuenneen hapen paikallisista pitoisuuksista sekä pH:n, lämpötilan ja hiilidioksidin jakaumista. Toisena tavoitteena oli kehittää tapoja vähentää isoissa reaktoreissa tavanomaista pitoisuuksien avaruudellista hajontaa.

Päätavoitteet saavutettiin kehittämällä aksiaalisista diffuusioyhtälöistä analyyttinen malli, joka validoitiin laajalla julkaistuista artikkeleista kootulla sekoittumisaika- ja substraattipitoisuusaineistolla. Sekoittumisen kannalta parhaat syöttöasettelut kehiteltiin mallin pohjalta, ja kahdesta bakteerikannasta muodostettiin vakaa yhteisviljelmä, jonka kasvu perustuu varsinaisesta pääsubstraatista johdettuihin sivutuotteisiin. Sekä syöttöasettelujen että yhteisviljelmän toiminta tuottomittakaavan reaktoreissa mallinnettiin ja simuloitiin.

Mallintamisen perusteella monipistesyötöt pystyvät homogenoimaan suuretkin bioreaktorit tehokkaasti. Epäsuoraan hiilenkäyttöön perustuvan yhteisviljelmän käyttämien substraattien jakaumat olivat myös varsinaisen syötetyn substraatin jakaumaa homogeenisemmat. Tehty tutkimus tuotti yksinkertaisen, mutta avaruudellisesti tarkan mallin heterogeenisistä bioreaktoreista ja osoitti kaksi mahdollista reaktorin toimintaa parantavaa homogenointimenetelmää.

CONTENTS

ABBREVIATIONS

1D	one-dimensional
2D	two-dimensional
3D	three-dimensional
BDF	backward-differentiation formula
CDF	cumulative distribution function
CFD	computational fluid dynamics
CM	compartment model
COV	coefficient of variation
CRIM	conditional-replication, integration, and modular
DOT	dissolved oxygen tension
FBA	flux balance analysis
GFP	green fluorescent protein
OD	optical density
ODE	ordinary differential equation
ODR	oxygen demand rate
OTR	oxygen transfer rate
PDF	probability density function
RFP	red fluorescent protein
STD	standard deviation

SYMBOLS

A	area, cross-section (m^2)
C	concentration ($g\,L^{-1}$ or $mol\,m^{-3}$)
C_p	specific heat capacity ($J\,mol^{-1}\,K^{-1}$)
D	diameter (m), carbon dioxide concentration ($mol\,m^{-3}$)
d	axial dispersion coefficient ($m^2\,s^{-1}$)
F	cumulative distribution function (-)
f	probability density function (-), model prediction
g	generation time (h)
h	Henry's constant ($mol_L\,mol_G^{-1}$)
H	height (m)
ΔH_r	enthalpy of reaction ($J\,mol^{-1}$)
K	Monod or affinity constant ($g\,L^{-1}$)
k	first-order rate constant (s^{-1} or h^{-1})
k_La	gas-liquid mass transfer rate constant (s^{-1} or h^{-1})
L	length-scale (m)
M	substrate modulus (-)
N	amount, number (-)
n	stirrer rate (rpm), molar flow rate ($mol\,s^{-1}$)
O	oxygen concentration ($g\,L^{-1}$ or $mol\,m^{-3}$)
P	power (W)
p	pressure (Pa)

pH	negative ten-based logarithm of H^+ activity (-)
q	biomass-specific maximum reaction rate ($\mathrm{g\,g^{-1}\,h^{-1}}$)
Q	volumetric feed or production rate ($\mathrm{g\,L^{-1}\,h^{-1}}$ or $\mathrm{mol\,m^{-3}\,h^{-1}}$)
Q^2	logarithmic coefficient of determination (-)
r	volumetric reaction rate ($\mathrm{g\,L^{-1}\,h^{-1}}$ or $\mathrm{mol\,m^{-3}\,h^{-1}}$)
R	transfer resistance ($\mathrm{s\,m^{-3}}$)
Re	Reynolds number (-)
R^2	coefficient of determination (-)
S	substrate concentration ($\mathrm{g\,L^{-1}}$)
T	temperature (K or °C)
t	time (s)
t_{95}	95 % mixing time (s)
U	velocity ($\mathrm{m\,s^{-1}}$)
u	dimensionless concentration (-)
V	volume ($\mathrm{m^3}$)
v	volume flow rate ($\mathrm{m^3\,s^{-1}}$)
X	biomass concentration ($\mathrm{g\,L^{-1}}$)
x	dimensionless axial coordinate (-), coordinate (m), parameter
Y_{ij}	yield of i on j ($\mathrm{g_i\,g_j^{-1}}$)
z	axial coordinate (m)
Greek letters	
α	volume fraction (-)
β	production load (-)
δ	Dirac delta distribution
ϵ	specific power ($\mathrm{W\,kg^{-1}}$)
γ	dimensionless correlation constant (−)

μ	specific growth rate (h^{-1})
ν	kinematic viscosity ($m^2\,s^{-1}$)
ρ	density ($kg\,m^{-3}$)
σ	standard deviation
θ	dimensionless temperature (-)

Subscripts

0	feed point, initial, mechanical
B	buffer
C	circulation
G	gaseous, gassed, gas-phase, pneumatic
i	impeller
I	interstage
L	liquid, liquid-phase
T	tank, reactor

ORIGINAL PUBLICATIONS

Publication I Losoi, P., Konttinen, J., & Santala, V. (2023a). Modeling large-scale bioreactors with diffusion equations. Part I: Predicting axial dispersion coefficient and mixing times. *Biotecnology and Bionengineering*. Manuscript accepted for publication. https://doi.org/10.22541/au.168994090.09200674/v1

Publication II Losoi, P., Konttinen, J., & Santala, V. (2023b). Modeling large-scale bioreactors with diffusion equations. Part II: Characterizing substrate, oxygen, temperature, carbon dioxide, and pH profiles. *Biotecnology and Bionengineering*. Manuscript accepted for publication. https://doi.org/10.22541/au.168993582.23442290/v1

Publication III Losoi, P., Konttinen, J., & Santala, V. (2022). Substantial gradient mitigation in simulated large-scale bioreactors by optimally placed multiple feed points. *Biotechnology and Bioengineering*, *119*(12), 3549–3566. https://doi.org/10.1002/bit.28232

Publication IV Losoi, P. S., Santala, V. P., & Santala, S. M. (2019). Enhanced population control in a synthetic bacterial consortium by interconnected carbon cross-feeding. *ACS Synthetic Biology*, *8*(12), 2642–2650. https://doi.org/10.1021/acssynbio.9b00316

AUTHOR CONTRIBUTIONS

Publication I	PL designed the study and performed all mathematical and numerical work. PL drafted the manuscript and is the corresponding author. JK and VL supervised the work and revised the manuscript.
Publication II	PL designed the study and performed all mathematical and numerical work. PL drafted the manuscript and is the corresponding author. JK and VL supervised the work and revised the manuscript.
Publication III	PL designed the study and performed all mathematical and numerical work. PL drafted the manuscript and is the corresponding author. JK and VL supervised the work and revised the manuscript.
Publication IV	PL performed the experimental work with contributions by SS. PL performed all mathematical and numerical work. PL is the corresponding author and drafted the manuscript with SS. All authors designed the study. VS and SS supervised the work and revised the manuscript.

1 INTRODUCTION

Bioprocesses form a subset of catalytic chemical processes, in which reactants are converted to products under the presence of a catalyst in a reactor maintained at specific conditions. Some products of bioprocesses can be produced by non-biological catalysts by the chemical industry as well, but many products intrinsic to biochemical industry are impossible to produce without the biochemical catalysts, the cells and enzymes. Such products are *e.g.* recombinant proteins used in pharmaceutical applications. In contrast to laboratory-scale studies, heterogeneous distributions of substrate, dissolved oxygen, pH, carbon dioxide, and possibly temperature are found in industrial-scale reactors (Nadal-Rey et al., 2021), whose working volumes may be up to several hundred cubic meters (Neubauer & Junne, 2016). The heterogeneity has been associated with decreased biomass and product yields (Bylund et al., 1998, 2000; Larsson et al., 1996; Xu, Jahic, Blomsten, & Enfors, 1999).

Modeling has been widely employed to understand the interactions among mixing, transport phenomena, and reaction, and to estimate the consequences of these interactions during bioreactor scale-up. The conventional homogeneous ideal reactor models have the merits of simplicity, ease of use, and possibility to analytical solutions, but they are incapable of describing the spatial heterogeneity that distinguishes large reactors from the small. Compartment models (CMs) and computational fluid dynamics (CFD) simulations, on the other hand, do describe the spatial variation in various levels of detail, but they require numerical solution. For quick evaluation purposes, a simple analytical model would be preferred.

Thus, the first aim of this work was to study whether one-dimensional (1D) diffusion equations could fill the modeling gap and provide a generalized analytical model that represents also large-scale bioreactors. In addition to developing an analytical 1D model capable of describing the heterogeneous

profiles found in industrial-scale fed-batch processes, the aim of this work was to study and evaluate potential methods of homogenizing the reactors efficiently. The first method was based on using multiple feed points as has been suggested in literature (Cronin et al., 1994; Enfors et al., 2001; Larsson et al., 1996). The 1D diffusion equations were studied to determine generalized optimal multipoint feed placements, and mixing and reaction were simulated with the derived feed arrangements to confirm their utility.

Another potential method for reactor homogenization was identified in co-cultures, that have raised interest as potential production hosts enabling efficient utilization of substrate mixtures (Xia et al., 2012) and challenging biotransformations (Zhou et al., 2015). In the context of a production-scale reactor, the co-cultures could implement a carbon flow where the actually fed, heterogeneously distributed substrate is before assimilation converted to another compound with a more homogeneous distribution. The concept was modeled, a co-culture based on such an interconnected carbon flow was constructed, and the stability of the co-culture was demonstrated by cultivation experiments.

Chapter 2 covers the background for research objectives and hypotheses formulated in detail in Chapter 3. Chapter 4 reviews the materials and methods used to obtain the results presented and discussed in Chapter 5. In addition to summarizing the original publications I–IV, Chapters 4 and 5 also include previously unpublished material. Finally, conclusions are drawn in Chapter 6.

2 BACKGROUND

To set this study in a broader context, an overall view of fermentation processes is given in Section 2.1, and features and challenges particular to large-scale bioreactors and the commonly used fed-batch production mode are reviewed in Section 2.2. Production hosts are then described in Section 2.3 with a special emphasis on co-cultures and their potential benefits. Finally, modeling and simulation approaches are presented in Sections 2.4 and 2.5.

2.1 Microbial bioprocesses

Bioprocesses, a subset of chemical processes, are by definition catalytic as they employ enzymes or cells for the main conversion, and they share the overall goal of converting a feedstock to a product with the chemical industry. In addition to the biotransformation step, up- and downstream processes are involved to obtain the product in separate and pure form and to prepare the feedstock. At the advent of the biochemical industry, batch processes dominated (Neubauer & Junne, 2016), which is understandable since they require the least equipment and control technology and since most everyday fermentations occur naturally in batches. Subsequently, fed-batch became the standard as it allows greater productivity, titer, and yield by limiting substrate concentration and oxygen consumption (Neubauer & Junne, 2016). Continuous processing would be theoretically the most productive mode, but owing to challenges intrinsic to bioprocessing based on living cells (Kittler et al., 2021; Nguyen et al., 2021; Ramos et al., 2023; Rathore et al., 2023), it is not yet widely adopted. A shift towards the continuous processes may occur in the future.

The products of microbial bioprocesses range from bulk chemicals produced in the scale of even megatonnes per year (Straathof, 2014) to high-value recombinant proteins or secondary metabolites produced at a much smaller volume.

From a biochemical perspective, the produced bulk chemicals are generally primary metabolites or just few reaction steps from the glycolysis pathway or the citric acid cycle (Nurwono et al., 2023). Some notable examples are alcohols such as ethanol and 1-butanol and carboxylic acids such as citric, acetic, and lactic acid (Straathof, 2014). The fine chemicals include *e.g.* amino acids, fat derivatives, steroids, peptides, and nucleotides used by the pharmaceutical, cosmetic, and food industries (Straathof et al., 2002). Sometimes, the cells themselves are the main product, such as baker's yeast or probiotics.

As far as commodity chemicals are concerned, the target process metrics may be considered to be an 80 % yield in relation to the theoretical maximum, $15\,\mathrm{g\,L^{-1}\,h^{-1}}$ volumetric productivity, and a $100\,\mathrm{g\,L^{-1}}$ titer (Straathof et al., 2002). The cited figures applied to the chemical industry, and as such they cannot be used to judge each fermentation process. They nevertheless set the bar for the production of such compounds that could also be produced via conventional petrochemical routes.

2.2 Large-scale bioreactors and fed-batch processes

The vessels used in industrial-scale microbial bioprocesses, the bioreactors, are in general either mechanically agitated stirred tanks or pneumatically agitated bubble column or airlift reactors. Depending on the nature of the product, the vessel size can be at the smallest in the range of a cubic meter and at the largest up to several hundred cubic meters (George et al., 1998; Neubauer & Junne, 2016). This results in reactor diameters of a meter up to a few meters, depending on the aspect ratio. A standard geometry for a stirred vessel is considered to have an aspect ratio of 1, where the working height H (m) without possible expansion due to gassing equals the tank diameter D_T (m), and both the impeller diameter and its bottom clearance are a third of the tank diameter (Alopaeus et al., 2009; Morchain et al., 2014). However, bioprocesses are often aerobic, and higher aspect ratios and multiple impellers are used to enhance gas distribution and contact time. For multi-impeller vessels, the standard geometry is built by stacking the single-impeller standard geometries vertically, but with a symmetrical impeller placement, where the bottom clearance is half the tank diameter (Jahoda & Machoň, 1994). Figure 2.1 illustrates the

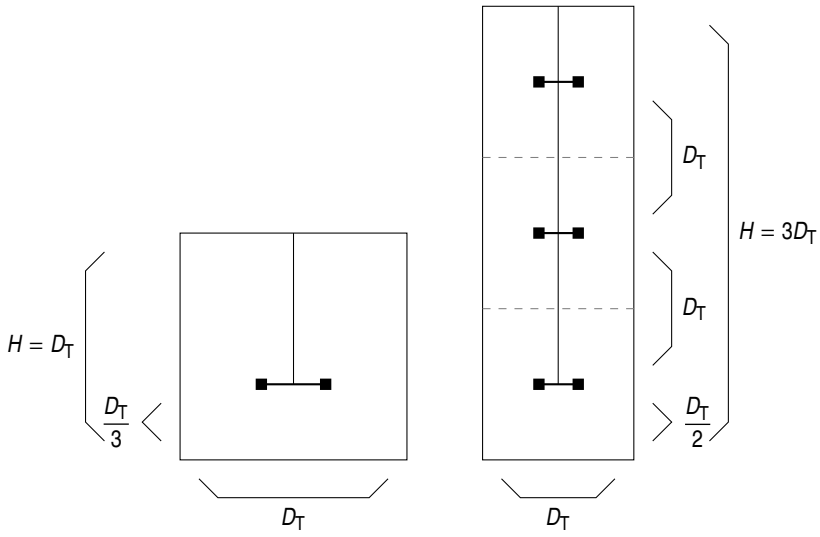

Figure 2.1 Standard geometry bioreactors with a single impeller (left) or multiple impellers (right). Illustration includes only the ungassed working volume. Symbols: H, working height (m); D_T, tank diameter (m).

standard geometry configurations. Interestingly, though, a non-symmetrical impeller distribution can retain a higher power number under aeration (Fitschen et al., 2019). Often the bottom impeller has a radial flow pattern for better gas dispersion even if the upper impellers pump axially, as such configurations achieve a higher rate of bulk mixing per power input (Bernauer et al., 2022; Vrábel et al., 2000). Other biotechnologically relevant impeller combinations include having only axial flow impellers (Magelli et al., 2013; Shewale & Pandit, 2006; Xie et al., 2014) or having a contoured-blade turbine at the bottom and flat-blade turbines above. In practice, large-scale multi-impeller stirred reactors tend to be somewhat shorter than standard geometry with the impeller-wise aspect ratio usually close to 0.75 (Bernauer et al., 2022; Rosseburg et al., 2018; Vrábel et al., 1999; Vrábel et al., 2000; Xing et al., 2009).

Physically and chemically the conditions are quite mild if compared with the chemical industry: usually head-space pressure is only at most 1 atm above the atmospheric pressure (Zahradník et al., 2001), pH is close to neutral, and temperature is close to ambient (Allman, 1999), but the latter two depend on the production organism. In high aspect ratio vessels the hydrostatic pressure can be on the 1 atm -scale as well, which implies a large gas-phase expansion with the

usual head-space pressures (Bernauer et al., 2022). Depending on the organism, biomass concentration, and the substrate's availability, dissolved carbon dioxide may reach 100 mbar values without the extra solubility due to hydrostatic pressure (Baez et al., 2009). In batch operations the substrate concentration is homogeneous throughout and relatively high, whereas most fed-batch operations deliberately limit the substrate's concentration to 10–100 $\mathrm{mg\,L^{-1}}$ levels (Larsson et al., 1996; Xu, Jahic, Blomsten, & Enfors, 1999) to avoid overflow metabolism or oxygen consumption rates exceeding the reactor's transfer capacity. The concentration of dissolved oxygen in aerobic processes is limited by oxygen's low solubility in water, which is approximately only 8 $\mathrm{mg\,L^{-1}}$ in a water-air system at room temperature and atmospheric pressure (Sander, 2023). Cell densities depend largely on the organism: Bacterial cultures can have biomass concentrations of *e.g.* 50 $\mathrm{g\,L^{-1}}$ and even beyond, which corresponds to cell number densities of $5 \cdot 10^{10}\,\mathrm{mL^{-1}}$ assuming a small cell volume of 1 $\mu\mathrm{m}^3$. Animal cell cultures have lesser cell densities of $5 \cdot 10^5$–$5 \cdot 10^6\,\mathrm{mL^{-1}}$ (Langheinrich et al., 1998; Langheinrich & Nienow, 1999).

As in many chemical processes with mechanical or pneumatic agitation, the flow in the reactor is generally turbulent as quantified by the impeller Reynolds number

$$\mathrm{Re} = \frac{nD_\mathrm{i}^2}{\nu}, \tag{2.1}$$

where n is the stirrer rate ($\mathrm{s^{-1}}$), D_i the impeller diameter (m), and ν the kinematic viscosity of the fluid ($\mathrm{m^2\,s^{-1}}$). In general turbulent flow is found at Reynolds numbers exceeding 10 000, which usually holds true in large reactors even if the fermentation broth is viscous. However, with broths of high 1 Pa s viscosities even the lower transition regime defined by $\mathrm{Re} < 1000$ may be relevant for industrial-size reactors (Mayr et al., 1994), which can result in markedly slower mixing (Vasconcelos et al., 1996). In stirred tanks the mechanical power input is often 0.5–5 $\mathrm{W\,kg^{-1}}$, though lower values are used if the cells are mechanically sensitive (Langheinrich et al., 1998). A mechanical scale-up problem is suggested already by the correlation of stirrer power in turbulent regime:

$$P = N_P \rho n^3 D_\mathrm{i}^5, \tag{2.2}$$

where P is the power input (W), N_P the dimensionless power number, generally

regarded as a constant in turbulent regime, and ρ the fluid density ($\mathrm{kg\,m^{-3}}$). Equation 2.2 implies an almost square-relationship between power and volume ($D_\mathrm{i} \sim V^{1/3}$ and thus $P \sim V^{5/3}$). The power input is often expressed as a specific power per liquid mass as $\epsilon = P/(\rho V)$ ($\mathrm{W\,kg^{-1}}$ or $\mathrm{m^2\,s^{-3}}$). To supply for aerobic metabolism, aeration rates could reach values of 1 vvm (volume flow of gas per minute per volume of liquid) (Zahradník et al., 2001). Assuming a design rule of $3\,\mathrm{cm\,s^{-1}}$ superficial gas velocity for homogeneous gas flow (Nauha et al., 2015), an approximately $(9.81\,\mathrm{m\,s^{-2}}) \times (0.03\,\mathrm{m\,s^{-1}}) \approx 0.29\,\mathrm{W\,kg^{-1}}$ pneumatic power input would be obtained. Unlike at small scale, a heterogeneous gas flow regime is likely instead in industrial-scale vessels that can hardly satisfy the $3\,\mathrm{cm\,s^{-1}}$ constraint (Nauha et al., 2015).

Mixing in bioreactors is usually quantified by injecting a tracer and monitoring its spread by an appropriate probe or probes away from the feed point, and such mixing times have been correlated to operating conditions and geometry. Without aeration, the mixing time eventually obeys an inverse relation to the stirrer rate in the turbulent flow regime ($\mathrm{Re} \geq 10\,000$) both in single- and multi-impeller vessels. This relation is expressed in the widely accepted standard geometry single-impeller correlation (Grenville & Nienow, 2003)

$$t_{95} = \frac{5.20}{N_P^{1/3}} \left(\frac{D_\mathrm{T}}{D_\mathrm{i}}\right)^2 \frac{1}{n} \approx 5.64 \left(\frac{D_\mathrm{T}}{D_\mathrm{i}}\right)^{1/3} \left(\frac{D_\mathrm{T}^2}{\epsilon}\right)^{1/3} \tag{2.3}$$

for the 95 % mixing times t_{95} (s) and also in a correlation for multiple impellers (Magelli et al., 2013)

$$t_{95} = \frac{2.40}{N_\mathrm{C}} \left(\frac{D_\mathrm{T}}{D_\mathrm{i}}\right)^{4/3} \left(N_\mathrm{i} N_P \frac{H^2}{\epsilon}\right)^{1/3} \approx \frac{2.60}{N_\mathrm{C}} \frac{D_\mathrm{T}^2 H}{D_\mathrm{i}^3} \frac{1}{n}, \tag{2.4}$$

where N_C is the flow number of a single impeller. Depending on the exact configuration, the factors 2.40 and 2.60 and the flow number N_C in Equation 2.4 might be adjusted to account for the merged flow of multiple tightly spaced radial flow impellers as previously indicated (Magelli et al., 2013). Equation 2.3 for single impellers notably implies that as far as the mixing time is concerned, the specific power input related to the turbulent energy dissipation governs the mixing times such that all impellers of the same $D_\mathrm{i}/D_\mathrm{T}$ ratio are equally energy-

efficient (Nienow, 1997). Multiple impellers behave contrastingly: the choice of the impeller combination and setup has a major effect on the relation between mixing time and specific power input (Bernauer et al., 2022; Jahoda & Machoň, 1994; Vrábel et al., 2000). The correlation Equation 2.4 also implies that the flow rate induced by the impellers, or the pumping capacity nD_i^3 ($\mathrm{m^3\,s^{-1}}$), is the controlling factor when multiple impellers are employed. To complicate further, the influence of aeration on mixing time can be positive, negative, or neutral (Vasconcelos et al., 1998; Vrábel et al., 1999; Vrábel et al., 2000). The correlation by Vasconcelos et al. (1995) illustrates how the loss of mechanical power due to gassing ($P_\mathrm{G} < P$) tends to increase the mixing time, whereas the pneumatic agitation tends to decrease it:

$$t_{95\mathrm{G}} = \frac{P}{P_\mathrm{G}} \left(t_{95} - \gamma \frac{v_\mathrm{G}}{n^2 D_\mathrm{i}^3} \right). \tag{2.5}$$

In Equation 2.5, $t_{95\mathrm{G}}$ is the 95 % mixing time under aeration (s), t_{95} the corresponding unaerated mixing time (s), P_G the power input under aeration (W), P the corresponding power without aeration (W), γ a dimensionless positive configuration constant, and v_G the volume flow rate of gas ($\mathrm{m^3\,s^{-1}}$). Modest aeration rates usually have relatively little influence on mixing times, however.

By dimensional analysis it is quickly seen that bioreactors cannot be scaled to production size whilst keeping the relevant dimensionless numbers constant across the scales (Oldshue, 1966). Different hydrodynamics and differences in ratios of mixing, transfer, and reaction rates are thus expected. Usually in large-scale fed-batches the time-scale of reaction eventually decreases below the time-scale of mixing, which leads to heterogeneity (Bylund et al., 1998; Larsson et al., 1996; Xu, Jahic, Blomsten, & Enfors, 1999). As a result, local excesses are found at the vicinity of the feed point, even though the mean concentration of substrate in a fed-batch is usually low. This also localizes the microorganism's demand of its own metabolic oxidative capacity and external oxygen availability such that both aerobic overflow and anaerobic fermentative metabolism may occur (Szenk et al., 2017; Xu, Jahic, Blomsten, & Enfors, 1999). Insufficient mixing with respect to reaction thus partly negates the very purpose and aim of the fed-batch technique, the limitation of substrate and oxygen consumption rates. The addition of pH-controlling acids or alkali can also lead

to heterogeneity at large scale, where mixing is less efficient (Langheinrich & Nienow, 1999; Spann et al., 2019). Furthermore, power dissipation in a stirred vessel is highest near the impeller(s) (Moilanen et al., 2008), which localizes the oxygen transfer capacity of the reactor (Oosterhuis & Kossen, 1984). The spatial distribution of the gas bubbles and their size distribution tend to be quite heterogeneous as well, further accentuating the uneven oxygen transfer capacity (Nauha et al., 2018).

In addition to undesired metabolism, reduced yields, and activation of stress responses (Schweder et al., 1999), increased cell lysis occurs in heterogeneous conditions at least in conjunction with recombinant protein production (Bylund et al., 2000). However, heterogeneity is not exclusively a negative feature of large-scale reactors: sometimes the environmental fluctuations result in more viable microorganisms (Enfors et al., 2001) or in greater product quality, such as a higher gassing power in baker's yeast (George et al., 1998) or less degraded recombinant proteins (Bylund et al., 2000)

As might be expected, the placement of the substrate and pH corrective feeds has a profound effect on the bulk macro-, dispersive meso-, and purely diffusive microscale mixing: Feeding close to an impeller improves meso- and microscale mixing and disperses the concentrated solutions effectively (Baldyga et al., 1993), mitigating pH and substrate concentration excursions and improving biomass yields (Fowler & Dunlop, 1989; Langheinrich & Nienow, 1999). In addition, placing the feed axially at the center decreases overall macroscale mixing times in multi-impeller reactors (Alves et al., 1997; Cronin et al., 1994; Vrábel et al., 1999). Consequently, it has been suggested that an inlet should be placed at each impeller or to multiple well-mixed zones (Cronin et al., 1994; Enfors et al., 2001; Larsson et al., 1996). In a pioneering work, biomass yield improved in a continuous cultivation upon using multiple feed points (Hansford & Humphrey, 1966). More recently, a case-specific CM was used to simulate all possible position-pairs of two feed points to find an optimal one for mixing in pneumatically agitated reactors (Fu et al., 2005), but unfortunately, the placement could not be generalized across reactor types and the approach suffered from exponential combinatorics.

2.3 Microbial production hosts and co-cultures

A major choice in any bioprocess catalyzed by cells is the production organism. Some naturally produce the product of interest, whereas others require genetic engineering. Microorganisms also tend to have strong preferences and requirements regarding growth media and substrates. Furthermore, the organisms react to the substrate excesses expected at production conditions in different ways: Likely due to limitations in membrane area available to oxidative phosphorylation (Szenk et al., 2017), the often used *Escherichia coli* and *Saccharomyces cerevisiae* direct excess glucose to aerobic overflow metabolism resulting in acetic acid (Xu, Jahic, Blomsten, & Enfors, 1999) and ethanol (George et al., 1993, 1998), respectively, even if dissolved oxygen is not limiting. In the lack of dissolved oxygen, fermentative metabolism activates, resulting in a mixture of organic acids or ethanol, respectively (Xu, Jahic, Blomsten, & Enfors, 1999). As a result, both biomass and recombinant protein yields have been lowered (Bylund et al., 1998; Larsson et al., 1996; Xu, Jahic, Blomsten, & Enfors, 1999). Growth and metabolism of *Corynebacterium glutamicum*, on the other hand, are relatively little affected by oscillations in substrate and oxygen availability (Käß et al., 2014). Despite converting locally excessive glucose to lactic acid similarly to *E. coli* diverting glucose to acetic acid, the lactic acid is rapidly consumed with no adverse effects on overall biomass growth and yield. In contrast, *Bacillus subtilis* regulates its glucose uptake rate in response to glucose and oxygen oscillations (Junne et al., 2011). As a final example, the soil bacterium *Acinetobacter baylyi* ADP1 does not even utilize glucose directly, but oxidizes it to gluconic acid, which it then subsequently imports and catabolizes (Taylor & Juni, 1961a, 1961b, 1961c; Vaneechouette et al., 2006). No overflow metabolites have been observed with the wild-type strain of this bacterium (Kannisto et al., 2014). Thus, the tolerance and reaction to conditions expected to prevail in large-scale reactors varies among organisms and even strains, and it would be preferable to use robustly performing production hosts whenever possible.

Given that in nature microorganisms quite invariably exist in multi-species communities, defined co-cultures of two or possibly more species or strains are an interesting alternative or supplement to the industrialized single-strain cultures.

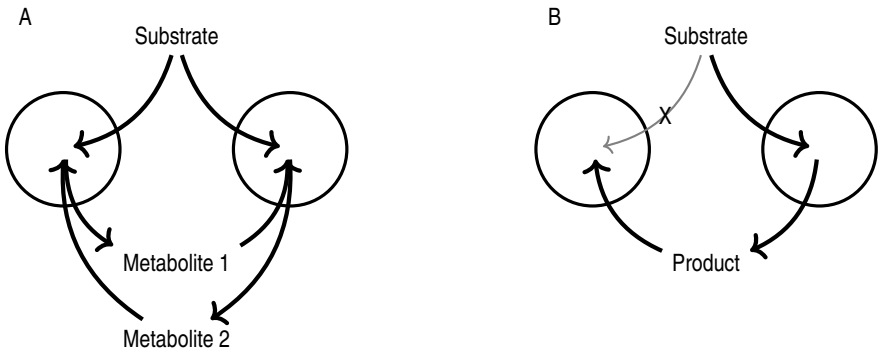

Figure 2.2 Stable co-culture dynamics. (A) A mutualistic co-culture, where both strains rely on the other strain for production of an essential metabolite. (B) A commensialistic co-culture, where one strain utilizes the substrate and supports the other through its product.

Co-cultures of appropriately chosen, complementary strains have enabled efficient utilization of substrate-mixtures (Atkinson et al., 2022; Eiteman et al., 2008; Xia et al., 2012), removal of inhibitory side-products such as acetate or ethanol (Bayer et al., 2009; Santala et al., 2014), and distributed implementation and optimization of challenging multistep reaction pathways (Zhang et al., 2015; Zhou et al., 2015).

A requisite for co-cultures is a population control mechanism that maintains a stable strain ratio. Stable co-cultures have been constructed using obligately mutualistic community dynamics, where both strains require the presence of the other for growth (Mee et al., 2014; Shou et al., 2007; Wintermute & Silver, 2010). However, many implementations have relied on the sharing of biosynthetically costly metabolites required also by the contributing strains themselves (Figure 2.2A), which risks the emergence of non-contributing subpopulations if a production-abolishing mutation should occur (Rugbjerg et al., 2018). Non-obligate mutualistic co-cultures have relied on one strain growing on the side-products of the other, such as a co-culture of *A. baylyi* ADP1 and *E. coli*, where the knock-out *A. baylyi* ADP1 could grow only on the acetate excreted by *E. coli* (Santala et al., 2014). Better production of both biomass and a recombinant protein were observed as *E. coli* was relieved of the acetate's detrimental effect. Figure 2.2B exemplifies such a co-culture, where one strain utilizes the substrate and supports the other through secreting end- or side-products suitable for assimilation.

A potential, not yet demonstrated, benefit of co-cultures could lie in a shared flow of the carbon source. The heterogeneous substrate (glucose) profile in a large reactor is the result of a rather point-like feed or source. The axial profiles of any side-products such as acetate, formate, or ethanol are, however, the result of not a point source but a volume-encompassing source defined by the glucose profile. Thus, a more homogeneous spatial profile should ensue. Indeed, Xu, Jahic, Blomsten, and Enfors (1999) found in a $20\,\mathrm{m}^3$ *E. coli* fed-batch experiment that the acetate concentration was less heterogeneous than the glucose concentration. Extrapolating to the aforementioned example of *A. baylyi* ADP1 and *E. coli* (Santala et al., 2014), this would translate to *A. baylyi* ADP1 experiencing a more homogeneous substrate (acetate) profile in a heterogeneous reactor than *E. coli* (glucose). Additionally, the knock-out *A. baylyi* ADP1 was capable of oxidizing glucose to gluconic acid, even though it was incapable of assimilating it. *E. coli* should thus experience a gluconic acid profile more uniform than the glucose profile in such a co-culture.

2.4 Bioreactor models

Experiments are rarely conducted with production-scale reactors, and thus modeling and simulations are necessary in understanding and predicting large-scale reactor performance. Mixing times, substrate and oxygen concentrations, and reaction rates are often modeled to estimate the key process metrics, the titer, yield, and productivity (Haringa et al., 2018; Pigou & Morchain, 2015; Vrábel et al., 2001). The modeling approaches are many, and so are the purposes of modeling. The objective may be to derive general conclusions about a particular process type, to pinpoint a specific problem in existing equipment, to tentatively investigate a new processing scheme, or to design and dimension equipment to implement a process. As different approaches suit different purposes, a meaningful comparison can be made only by keeping the potential objectives in mind.

A model can be physically grounded, or it can be simply a mathematical function with no underlying physical reasoning. The models invariably involve a free parameter or multiple such parameters, that are not directly specified by the operating conditions and reactor geometry, but need to be optimized

against a set of experimental data. In a best-case scenario, the model is capable of predicting the desired variables without being specifically optimized with these variables of interest. As an example: a mixing time model can be optimized using a set of mixing time data, or the predictor can be constructed mechanistically using *e.g.* volume flow rates, which have been correlated to operating conditions and reactor dimensions. The former model does represent the data set it was optimized against, but it cannot be considered predictive. The latter also represents the data, not because it was optimized to do so, but because its structure captured some essential features of the studied phenomenon. The latter model has thus been validated by the data. Though not in excess, fortunately some experimental data obtained at large scale are available in the open literature to aid in model construction and validation.

Apart from simple correlations of *e.g.* mixing time, oxygen transfer rate constant, gas holdup, or stirrer power, bioreactor modeling is based upon a general (incompressible) transport equation

$$\frac{\partial C}{\partial t} + U_i \frac{\partial C}{\partial x_i} = d \frac{\partial^2 C}{\partial x_i^2} + \sum r \tag{2.6}$$

where C is the considered quantity (*e.g.* concentration of substrate), t time (s), U the velocity vector ($\mathrm{m\,s^{-1}}$), d diffusivity ($\mathrm{m^2\,s^{-1}}$), x the spatial coordinate vector (m), and $\sum r$ the sum of source and sink terms such as reactions and volumetric feeds. The second term on the left-hand side is the advection term, which describes how the flow field transports the considered quantity. The first term on the right-hand side is the diffusion term, which smoothens local differences in concentration. The diffusivity may be only molecular diffusion, but usually it is used to also model the diffusion-like dispersive mixing due to turbulence. Various simplifications to Equation 2.6 are made to obtain different models.

Ideal flow models assume either perfectly mixed flow where Equation 2.6 is applied on the reactor's scale or the opposite of it, a plug or piston flow. Applying assumptions of a zero diffusivity or dispersivity and a steady state ($\partial C/\partial t \approx 0$) along with such kinetic simplifications that permit analytical solutions, these models are best suited to evaluating which generalized reactor type would be preferable for the considered kinetics. Furthermore, they are quite valuable in

dimensioning of equipment. As far as bioreactors are concerned, small-scale reactors can be assumed to be homogeneous. With some reservations, the gaseous phase in a bioreactor could be simplified to plug flow (Dahod, 1993; Royce & Thornhill, 1991), especially if coalescence of gas bubbles is suppressed by the medium's properties. Unfortunately, neither of the ideal flows is particularly suitable to model the liquid phase when the time-scale of reaction begins to compete with mixing.

Perhaps the simplest extension to the perfectly mixed model is to use a 1D stack or a two-dimensional (2D) network of homogeneous compartments connected by flow terms that represent the flows observed and measured inside bioreactors. Such CMs have successfully predicted mixing times (Vasconcelos et al., 1998) and provided a framework for modeling heterogeneous substrate concentrations (Vrábel et al., 2001). At simplest only a single compartment per impeller is applied in a 1D model (Jahoda & Machoň, 1994), though three has been found optimal (Alves et al., 1997), and at most complex over 10 000 compartments could be used in a three-dimensional (3D) model (Delafosse et al., 2014). In practice the CMs are always solved numerically, though in theory they are analytically solvable as long as the modeled phenomenona are entirely linear, such as when simulating the mixing of a tracer. The computation times are quite modest even with the 3D models if the model is appropriately vectorized and implemented with sparse matrices, and a suitable integration algorithm, usually implicit, or a suitable equation solver, is used. The flow matrices emanating from CMs have also found use in stochastic bioreactor modeling, where the trajectories of individual cells have been monitored numerically to discover the frequency distribution of the mean relative concentration experienced by microorganisms (Delvigne et al., 2005, 2006a, 2006b). Another approach that resembles CMs is the discretization of substrate distribution instead of the working volume. Previously observed biomass losses could be explained by a simple discretization into two substrate concentration values, a high and a low one (Maluta et al., 2020).

Interestingly, the 1D CMs can be interpreted as finite-volume discretizations of a general 1D diffusion equation (Figure 2.3)

$$\frac{\partial C}{\partial t} = d\frac{\partial^2 C}{\partial z^2} + r, \tag{2.7}$$

where z is the axial coordinate (m). Equation 2.7 is a closed-boundary 1D special case of the general transport Equation 2.6 where the up- and downflowing velocities cancel each other ($U = 0$), and in its context, the diffusivity d ($\mathrm{m^2\,s^{-1}}$) represents the mixing effects of both advective and dispersive flows and is often called the axial dispersion coefficient (Kasat & Pandit, 2004; Kawase & Moo-Young, 1989; Machon & Jahoda, 2000; Pinelli & Magelli, 2000). As exemplified in Figure 2.3, the flow rates between the compartments of a 1D CM are related to the dispersion coefficient of a finite-volume-discretized 1D diffusion equation (Versteeg & Malalasekera, 2007). The mathematics of diffusion has proved useful in the theory of heat conduction and mass transfer. Advantageously, many special cases of Equation 2.6 allow straightforward construction of analytical solutions through the Green's function method (Cole et al., 2010). Previously, the transient 1D diffusion equation without reaction has been fitted to tracer curves and mixing times (Machon & Jahoda, 2000; Pinelli & Magelli, 2000). However, the full potential of diffusion equations in modeling bioreactors has not been realized. This is probably due to the fact that the axial dispersion coefficient, the equation's parameter, has thus far required direct fitting to experiments, which decreases the model's predictive power.

Similarly to the CM approach, CFD simulations also discretize the domain into subvolumes. However, the number of compartments is generally much higher, and the flow field U_i is not predetermined but solved by applying Equation 2.6 to mass, energy, and momentum. CFD models require a higher number of compartments, usually in the range 100 000–1 000 000, for sufficient resolution of the flow field. Consequently, the computation costs are clearly higher than with the other approaches, which sets a limit on how complex kinetics can be implemented in a CFD framework. Perhaps more acute a challenge on other fields with faster reaction kinetics than in microbial processes, turbulence needs to be simplified and its effects need to be modeled using turbulence models. A practical technique to apply CFD together with complex metabolic, kinetic, or population balance models is to derive a CM from the CFD resolved flow field and to use the simplified flow model instead (Alopaeus et al., 1999; Delafosse et al., 2014; Laakkonen et al., 2006, 2007; Nauha & Alopaeus, 2015; Nauha et al., 2018). Microbial reactions do not in general influence the flow field itself, but gas fermentations are a notable exception (Ngu et al., 2022). In such cases,

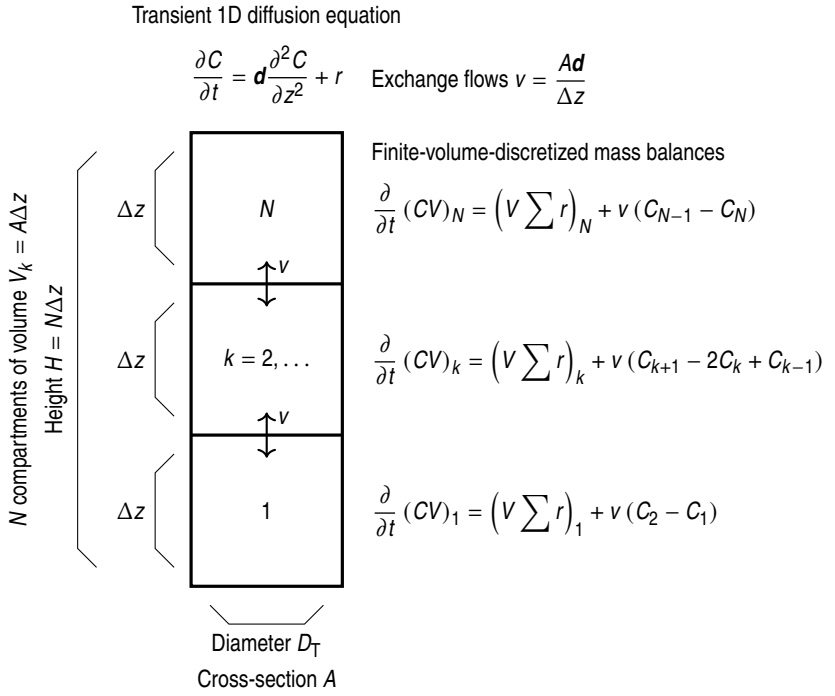

Figure 2.3 Correspondence between the transient 1D diffusion Equation 2.7 and 1D CMs. Finite-volume discretization of the 1D diffusion equation for the concentration C yields a 1D CM, where the exchange flows depend on the diffusion equation's axial dispersion coefficient d. A second-order central differencing of the diffusion term is shown in the discretized mass balances. By extension, a radially averaged 2D CM could be interpreted in terms of the diffusion equation and an axial dispersion coefficient. Volumetric source and sink terms such as reaction rates are represented by the term $\sum r$.

the microbial reaction affects the concentration of dissolved gases substantially, which in turn may influence the gas phase to such an extent that the whole flow field is affected.

2.5 Biological kinetics

In addition to hydrodynamics, the bioreactions themselves need to be modeled to study and describe phenomena characteristic to bioreactors. All kinetic modeling is based on fitting mathematical functions to experimental data. Some bioreaction models do have mechanistic elements based on metabolic reasoning, but in general, bioreaction models are little more than sets of correlations. However, it needs to be kept in mind that prediction of chemical reaction rate constants is not possible either. Especially with bioprocesses, the making of more comprehensive models by incorporating ever more reactions eventually becomes irrelevant. The number of reactions a single cell could catalyze enzymatically is vast. Even though many of them have been characterized for the most studied model organisms, some may still remain unknown even in the most familiar microbial species. The rates of reactions catalyzed by a cell depend on the intracellular enzyme and metabolite concentrations, enzyme concentrations on the cellular membrane, and metabolite concentrations in the periplasm. Gene expression plays a major role in regulating the entirety. The biochemical machinery is truly complex in all forms of life, and simplification is absolutely unavoidable.

Fortunately, the knowledge of all the details is not necessary for practical purposes, and good working models can be produced (Anane et al., 2017; Pigou & Morchain, 2015; Tang et al., 2017; Xu, Jahic, & Enfors, 1999). Normalized against the prevailing biomass concentration, it is possible to correlate the rate of biomass growth or substrate uptake against the substrate concentration and other measurable quantities. A Monod-type bilinear reaction rate expression is usually used as the basis. The characteristic features are an almost linear dependence on substrate concentrations lower than the so-called Monod or affinity constant and an eventual saturation towards a maximal rate after the concentration exceeds the affinity constant. However, Monod kinetics have been validated only for exponential growth in homogeneous environments, and

they are not necessarily applicable under dynamic conditions such as in a heterogeneous large-scale fed-batch reactor (Morchain et al., 2021). Populations adapted to a low substrate concentration can briefly consume the substrate at a rate higher than Monod kinetics would allow when suddenly exposed to a higher concentration (Xu, Jahic, Blomsten, & Enfors, 1999). Monod kinetics should be considered as an ideal that a population adapts to if given sufficient time (Morchain & Fonade, 2009; Morchain et al., 2013). Linearization of reaction rates is a potential simplification as it makes analytical solutions more accessible. In the context of chemical reaction engineering, many results have been obtained with linearized rate expressions.

A feature often ignored or even forgotten is the particular, corpuscular nature of all cells. They are often modeled as a dissolved species, even though they are a suspension in the liquid medium, much like chemical catalyst particles would be. Indeed, the cell population's response to external conditions is the average response of its members. Unlike chemical catalysts, cells constantly monitor their surroundings and adapt to them, and cultivation history shapes the population's response to perturbations in the environment (Brand et al., 2018). Population balances can account for both adaptation and phenotypical heterogeneity in a population of cells (Morchain et al., 2017; Pigou & Morchain, 2015) just as they can account for heterogeneity within any set of particles such as solid catalysts or gas bubbles.

3 RESEARCH HYPOTHESES AND OBJECTIVES

The literature review in Chapter 2 revealed a lack of analytically solvable models that reasonable depict and characterize large-scale bioreactors. Furthermore, the potential of feed configuration and production microorganism choice in reducing heterogeneity were recognized. The objectives of this study were thus set as:

(1) To apply 1D axial diffusion equations as a general analytical model of typical large-scale high aspect ratio bioreactors (I, II)

In literature, transient 1D diffusion equations have been fitted to both tracer curves and mixing times measured in high aspect ratio reactors. 1D steady-state diffusion equations with linear first-order or constant zeroth-order kinetics are analytically solvable. Linearization of kinetics has been a common simplification in chemical reaction engineering. Thus, 1D diffusion equations could be used to model the mixing of a tracer and the profiles of relevant variables in a fed-batch process.

(2) To derive an easy-to-use formula for predicting the overall axial dispersion coefficient from operating conditions and reactor geometry, allowing predictive use of the diffusion equations (I)

Previously published 1D and 2D CMs could be interpreted as discretized diffusion equations. The main flow parameters of these models are well correlated to operating conditions. Using a resistances-in-series analogy from basic heat transfer theory, a single overall dispersion coefficient could be computed from the flow structure and rates.

(3) To characterize mixing and the spatial profiles and distributions of the relevant physico-chemical quantities in large-scale bioreactors (I, II, III)

Using linearized kinetics in the 1D diffusion equations, analytical substrate

profiles could be obtained. Most fed-batches are operated with substrate limitation, and thus the consumption of oxygen and release of carbon dioxide are limited by the substrate feed rate. Oxygen consumption is responsible for majority of the heat release. Supplementing the analytical modeling, CM simulations could be used for numerical, case-specific characterization.

(4) To demonstrate that substrate heterogeneity could be decreased by appropriate feed configurations and co-culture systems (III, IV, unpublished)

Locating a feed point in the middle of the working height decreases mixing time. Both biomass yield and mixing times have been improved by injecting the feed near the bottom impeller instead of the stagnant top zone. The use of multiple feed points has decreased mixing time and increased biomass yield. Depending on the choice of substrate and microorganism, the provided substrate is not necessarily directly assimilated, but rather converted first to another compound. For instance, *A. baylyi* ADP1 oxidizes glucose to gluconate that is then subsequently used as the actual substrate. The produced gluconate should be more homogeneously distributed than the original substrate. Upon deleting *A. baylyi* ADP1's gluconate importer and using another strain incapable of using glucose but capable of assimilating gluconate and excreting *e.g.* acetic acid, a co-culture could be constructed where neither of the strains grow directly on the heterogeneously distributed glucose but on the derivative compounds that have more homogeneous axial distributions.

(5) To show that co-cultures with stable population dynamics can be constructed without the exchange of necessary metabolites (IV) Stable population dynamics within a co-culture are necessary for balanced and maintainable culture composition. Co-cultures based on obligate mutualism should be stable. Additional biosynthetic burden to co-cultivated strains should be avoided, as the exchange of important metabolites decreases the culture's growth rate and productivity and could lead to the appearance of non-contributing subpopulations.

4 SUMMARY OF MATERIALS AND METHODS

The literature data that were used to validate the modeling are described in Section 4.1. Experimental methods used in studying co-cultures are presented in Section 4.2. Modeling and simulations are summarized in Section 4.3. Green's function method (Cole et al., 2010) was used to solve 1D diffusion equations analytically (I, II). The numerical methods are reviewed in Section 4.4. The original publications (I–IV) and their supplementary materials provide further details. Section 4.3.2 contains previously unpublished methods, and the other Sections indicate if the respective methods were used also to obtain previously unpublished results.

4.1 Literature data (I, II)

The diffusion equation based models were validated against data from altogether 26 different previously published studies. The referenced data included experimentally determined mixing times and tracer curves, substrate concentrations measured simultaneously at different heights in large-scale reactors during fed-batch experiments, and also numerically simulated substrate concentrations in fed-batches. Table 4.1 reviews the 102 reactor configurations that were used in the cited mixing time experiments. Each combination of reactor geometry, impeller type and placement, and working medium was considered a distinct configuration, and glycerol solutions with differing viscosities were considered separate working media. Most of the reactors were equipped with two or more impellers, each usually having a working height equal to the tank diameter or slightly less. The data included altogether 31 unique impeller combinations with flat-blade Rushton turbines, contoured-blade radial flow turbines, and axial flow impellers such as pitched blade turbines, propellers, and hydrofoils (Supplementary Table S1 of publication I). Combinations of radial and axial

Table 4.1 Summary of the 102 reactors referenced from literature.

	V_L / m^3	H_L/D_T	D_i/D_T	N_i
Minimum	0.01	0.30	0.09	1
Lower decile	0.04	1.00	0.28	1
Lower quartile	0.06	1.79	0.33	2
Median	0.14	2.00	0.33	2
Upper quartile	1.30	3.00	0.43	3
Upper decile	8.25	4.00	0.50	4
Maximum	160.00	4.00	0.56	12

Symbols: V_L, liquid volume (m^3); H_L, liquid height (m); D_T, tank diameter (m); D_i, diameter of bottom impeller (m); N_i, amount of impellers.

flow impellers were also covered. The referenced fed-batch experiments and simulations were based on the same reactors as the mixing time experiments, and they are not taken into account in Table 4.1.

A set of 832 mixing times ranging from 3.2 s to 1840 s was obtained from 23 publications that comprised the aforementioned 102 unique reactor configurations (publication I). The amount of data obtained from each configuration varied from just 1 up to 35 mixing times. Notably, the data covered both transition and turbulent flow regimes ($187 \leq \mathrm{Re} \leq 5\,050\,000$), and 159 of the times were measured in working volumes exceeding 1 m^3. Approximately 36 % of the measured times were obtained with aeration rates of 0.0126−2 vvm (volume of gas per volume of liquid per minute), and these data covered dispersed, loading, as well as flooding regimes. The majority of mixing times were means of three to four measurements. The most common measurement method was to employ a single conductivity probe and a salt solution tracer, but the data covered multiple other techniques as well. Tables 1 and 2 of publication I give concise overviews of the data that are fully detailed study-wise in Supplementary Section S2.3 of publication I. Some gas holdups and impeller power losses due to aeration or tight impeller spacing were not provided in the original references, and were thus estimated as explained in Supplementary Section S2.2 of publication I.

Altogether 288 experimentally measured substrate concentrations were acquired (publication II) from fed-batch experiments reported in three studies (Bylund et al., 1998; Larsson et al., 1996; Xu, Jahic, Blomsten, & Enfors, 1999).

Concentrations were sampled simultaneously in a total of 96 time points at the top, middle, and bottom of the reactors. The liquid volumes of the reactors ranged from $8\,m^3$ up to $22\,m^3$, and the reactors were stirred with three to four Rushton turbines. The top feed data by Bylund et al. (1998) were not included in the 288 data values as they were subject to large fluctuations due to the vicinity of the feeding point. Liquid volumes, gas holdups, working heights, stirrer rates, and aeration rates of the reactors are given in Table 1 of publication II.

Two large-scale simulation studies in $20\,m^3$ liquid volumes stirred with four Rushton turbines were also used (publication II) in model validation (Larsson et al., 1996; Pigou & Morchain, 2015). Larsson et al. (1996) reported glucose contours from CFD simulations with standard Monod kinetics, and their data were considered as cumulative distribution functions (CDFs). Pigou and Morchain (2015) provided numerical values of glucose concentrations obtained with a 70-compartment model and a metabolic model coupled to a population balance. These values were used both as radially averaged 1D profiles and as CDFs.

4.2 Laboratory experiments (IV)

Altogether eight strains of *E. coli* and *A. baylyi* ADP1 were used (Table 4.2). Two strains, a wild-type and a glucose knock-out, of both species were obtained. Each of these four strains were used to construct a derivative strain that expressed a fluorescent protein under a constitutive promoter. The wild-types were *E. coli* K-12 BW25113 (CGSC 7636 from Yale University Coli Genetic Stock Center) and *A. baylyi* ADP1 (DSM 24193 from Deutsche Sammlung von Mikroorganismen und Zellkulturen). The knock-out *E. coli* $\Delta ptsI$ with PTS enzyme I gene deletion (Baba et al., 2006) was also obtained from Yale University Genetic Stock Center (CGSC 9918). The knock-out *A. baylyi* ADP1 $\Delta gntT$ with ACIAD0544 high-affinity gluconate permease gene deletion (de Berardinis et al., 2008) was a kind gift from Véronique de Berardinis (Genoscope, France). It is worth noting that the $\Delta gntT$ knock-out still oxidizes glucose to gluconate even though it is incapable of gluconate uptake. A kanamycin resistance gene replaced the deleted gene in both knock-outs.

Table 4.2 Strains of *E. coli* and *A. baylyi* ADP1 used in the co-culture experiments. Modified with permission from publication IV Table 1. Copyright 2019 American Chemical Society.

Description	Source
A. baylyi ADP1	DSM 24193
A. baylyi ADP1 Δ*gntT*::Kan(R)	(de Berardinis et al., 2008)
A. baylyi ADP1 Δ*poxB*::mScarlet	publication IV
A. baylyi ADP1 Δ*poxB*::mScarlet	publication IV
E. coli BW25113	CGSC 7636
E. coli Δ*ptsI*::Kan(R)	CGSC 9918 (Baba et al., 2006)
E. coli attϕ80::sfGFP	publication IV
E. coli attϕ80::sfGFP	publication IV

Abbreviations: DSM, Deutsche Sammlung von Mikroorganismen und Zellkulturen; CGSC, Yale University Coli Genetic Stock Center.

The fluorescent strains were constructed by genomic integration of a green fluorescent protein (GFP) expression cassette with a gentamicin resistance marker gene into *E. coli* and a red fluorescent protein (RFP) expression cassette with a chloramphenicol resistance marker gene into *A. baylyi* ADP1. The fluorescent proteins were superfolder GFP (Pédelacq et al., 2006) and mScarlet (Bindels et al., 2017). Conditional-replication, integration, and modular (CRIM) plasmids were used for the *E. coli* integrations as described by the original authors (Haldimann & Wanner, 2001). The two CRIM plasmids Burden monitor phi80 version (Addgene plasmid #66074) and pAH123 (Addgene plasmid #66077) were kind gifts from Tom Ellis (Ceroni et al., 2015). Integrations into *A. baylyi* ADP1 were done by solid-medium natural transformation (Luo et al., 2022) after first inserting the mScarlet expression cassette ordered from GenScript (New Jersey, USA) into another gene cassette that integrated into the neutral *poxB* locus (Santala et al., 2011). More details of the strain construction are provided in publication IV.

All cultivation experiments were carried out in 200 µL volumes on 96-well plates in a mineral salts medium (Hartmans et al., 1989) with glucose as the carbon source. Supplementary Section S5 of publication IV shows the medium composition. The same medium and temperature were used also for precultures, but Na-acetate and Na-gluconate were used as carbon sources instead of glucose for the knock-out strains. A Spark multimode microplate

reader (Tecan, Switzerland) was used to incubate the plates and to measure every 30 min optical density (OD) at 600 nm and fluorescence intensities with two excitation-emission-filter pairs appropriate to the expressed fluorescent proteins. The cultivation and measurement temperature was 30 °C, and the plates were shaked between measurements.

4.3 Modeling and simulations

4.3.1 Kinetics (II–IV)

The uptake rates of substrate and oxygen were modeled with standard Monod kinetics as well as first- and zeroth-order kinetics. The standard Monod kinetics

$$r_S = q_S \frac{S}{S + K_S} X \tag{4.1}$$

were used in CM simulations (publication III, unpublished) and also in analytical study of co-culture dynamics (publication IV). In Equation 4.1, r_S is the substrate uptake rate ($\mathrm{g\,L^{-1}\,h^{-1}}$), q_S the biomass-specific maximum of uptake rate ($\mathrm{g\,g^{-1}\,h^{-1}}$), S the concentration of substrate ($\mathrm{g\,L^{-1}}$), K_S the Monod or affinity constant ($\mathrm{g\,L^{-1}}$), and X the concentration of biomass ($\mathrm{g\,L^{-1}}$). For analytical fed-batch modeling (publication II), the uptake rate was linearized into

$$r_S = q_S \frac{S}{\langle S \rangle + K_S} X = k_S S, \tag{4.2}$$

where $\langle S \rangle$ is the volumetric average of the substrate concentration ($\mathrm{g\,L^{-1}}$) and k_S the first-order rate-pseudoconstant of substrate consumption ($\mathrm{h^{-1}}$). For comparison with experimental references from literature, the steady-state approximation between volumetric reaction and feed rates was employed ($r_S \approx Q_S$) and the mean concentration $\langle S \rangle$ was calculated or estimated directly from the reference data. With the numerical references both the kinetic parameters and mean concentration were accessible. Table 4.3 presents the values for kinetic parameters used in both analytical and numerical modeling in publications II and III. The respective publications indicate where the parameters were applied.

Similarly, the respiration of dissolved oxygen was modeled with Monod

Table 4.3 Kinetic parameters used in modeling and simulations of publications II and III.

Parameter	Unit	Value	Publication	Source
Q_S	$\mathrm{g\,L^{-1}\,h^{-1}}$	2.58–2.72	II	(Larsson et al., 1996)
		5.9	II	(Bylund et al., 1998)
		3.86	II	(Xu, Jahic, Blomsten, & Enfors, 1999)
		4	III	
$\langle S \rangle$	$\mathrm{g\,L^{-1}}$	0.01	II	(Larsson et al., 1996)
		0.01	II	(Bylund et al., 1998)
		0.03	II	(Xu, Jahic, Blomsten, & Enfors, 1999)
X	$\mathrm{g_X\,L^{-1}}$	20	II	
		10	III	10 (Morchain et al., 2014)
q_S	$\mathrm{g_S\,g_X^{-1}\,h^{-1}}$	1.70	II	(Larsson et al., 1996)
		1.35	II	(Xu, Jahic, & Enfors, 1999)
		1	III	0.6356 (Anane et al., 2017)
				1.25 (Xu, Jahic, & Enfors, 1999)
K_S	$\mathrm{g_S\,L^{-1}}$	0.18	II	(Larsson et al., 1996)
		0.05	II	(Xu, Jahic, & Enfors, 1999)
		0.025	III	0.0370 (Anane et al., 2017)
				0.05 (Xu, Jahic, & Enfors, 1999)
K_O	$\mathrm{mg_O\,L^{-1}}$	0.1	III	0.1 (Morchain et al., 2013)
Y_{XS}	$\mathrm{g_X\,g_S^{-1}}$	0.5	III	0.49–0.51 (Xu, Jahic, & Enfors, 1999)
Y_{OS}	$\mathrm{g_O\,g_S^{-1}}$	0.446	II	(Xu, Jahic, & Enfors, 1999)
		1.067	II, III	Complete oxidation stoichiometry
$k_\mathrm{L}a$	$\mathrm{h^{-1}}$	180	II, III	180 (Larsson et al., 1996)
				180 (Xu, Jahic, Blomsten, & Enfors, 1999)
$h_O O_\mathrm{G}$	$\mathrm{mg_O\,L^{-1}}$	12.69	III	Estimated

Symbols: Q_S, substrate feed rate; $\langle S \rangle$, mean substrate concentration; X, biomass concentration; q_S, specific substrate uptake rate; K_S, substrate affinity constant; K_O, oxygen affinity constant; Y_{XS}, maximum biomass yield on substrate; Y_{OS}, maximum oxygen consumption per substrate; $k_\mathrm{L}a$, oxygen transfer rate constant; $h_O O_\mathrm{G}$, equilibrium concentration of dissolved oxygen.

kinetics in compartment model simulations (publication III):

$$r_O = \frac{O_\mathrm{L}}{O_\mathrm{L} + K_O} Y_{OS} r_S, \tag{4.3}$$

where r_O is the volumetric consumption rate of dissolved oxygen ($\mathrm{g\,L^{-1}\,h^{-1}}$), O_L the concentration of dissolved oxygen ($\mathrm{mg\,L^{-1}}$), K_O the affinity or Monod constant ($\mathrm{mg\,L^{-1}}$), Y_{OS} the oxygen mass required for the aerobic consumption of a substrate (glucose) mass ($\mathrm{g\,g^{-1}}$), and r_S the volumetric rate of substrate uptake ($\mathrm{g\,L^{-1}\,h^{-1}}$, Equation 4.1). Axially dependent zeroth-order kinetics were used in analytical modeling of dissolved oxygen consumption (publication II), such that a mean oxygen demand rate (ODR) was calculated from the volumetric substrate feed rate using a constant yield coefficient. The mean ODR represented the rate of oxygen consumption that the microorganism would need for fully aerobic respiration. The local ODR was then obtained from the mean rate by weighting by the substrate concentration's axial profile. This resulted in

$$\mathrm{ODR} = Y_{OS} r_S, \tag{4.4}$$

where r_S is the linearized substrate uptake rate (Equation 4.2). Gas-liquid mass transfer for both oxygen and carbon dioxide was treated with a standard linear rate:

$$k_\mathrm{L}a(h_O O_\mathrm{G} - O_\mathrm{L}) \tag{4.5}$$

$$k_\mathrm{L}a(h_D D_\mathrm{G} - D_\mathrm{L}). \tag{4.6}$$

In the transfer rate expressions, $k_\mathrm{L}a$ is the transfer rate constant ($\mathrm{h^{-1}}$ or $\mathrm{s^{-1}}$), which can be considered to be the same for both (Dahod, 1993), h the Henry's constant ($\mathrm{mol_L\,mol_G^{-1}}$), O the concentration of $\mathrm{O_2}$ in the gas (G) and liquid (L) phases, and D similarly the concentration of $\mathrm{CO_2}$ in the gas and liquid phases.

4.3.2 Mutation model (unpublished)

The effect of mutations on the long-term stability of a mutualistic co-culture was estimated using a previously published mutation model (Rugbjerg et al., 2018), that contains two parameters: the escape rate of producing cells to a

non-productive geno- and phenotype and the production load associated with the engineered production pathway. The escape rate k (h^{-1}) represents the organism's intrinsic mutation rate and the propensity of the engineered pathway to be disrupted by mutations, and the production load β defined by $\mu = (1-\beta)\mu_0$ is the relative decrease in specific growth rate μ (h^{-1}) due to demand on cellular resources and possible toxicity of the pathway. Using the model, the half-life of the population's productive fraction (initially 100 %) under production load β and escape rate k is (Rugbjerg et al., 2018)

$$\frac{1}{2} = \frac{k + \beta\mu_0}{k\exp((k + \beta\mu_0)t_{1/2}) + \beta\mu_0}. \tag{4.7}$$

In the context of mutualistic co-cultures, Equation 4.7 is applied to either of the strains such that β represents the reduction in that strain's growth rate due to the mutualistic dynamics and k the rate at which the strain escapes the obligate mutualism and starts to grow independently of the other. By solving the half-life $t_{1/2}$ in Equation 4.7 and defining the subpopulation's generation time with the reduced co-culture growth rate $\mu = (1 - \beta)\mu_0$

$$g = \frac{\ln 2}{(1 - \beta)\mu_0}, \tag{4.8}$$

the strain's half-life number of generations complying with the mutualism could be solved:

$$N_{1/2} = \frac{(1 - \beta)\mu_0}{k + \beta\mu_0}\frac{\ln(2 + \beta\mu_0/k)}{\ln 2}. \tag{4.9}$$

4.3.3 Mass and energy balances (I–III)

The 1D diffusion equation was simplified to a mass balance of a tracer by keeping the time-dependency but removing the reaction term in Equation 2.7 (publications I and III):

$$\frac{\partial u}{\partial t} = \frac{d}{H^2}\frac{\partial^2 u}{\partial x^2}. \tag{4.10}$$

In Equation 4.10, u is the tracer's concentration normalized by its mean and x is a dimensionless axial coordinate $x = z/H$. Substrate profiles were determined in a pseudosteady-state, a common assumption in fed-batch contexts (Hristov et al., 2001; Morchain et al., 2014), and the reaction term was linearized (Equation

4.2), which simplified Equation 2.7 into (publication II)

$$\frac{\partial^2 u}{\partial x^2} + \frac{H^2 Q_S}{d \langle S \rangle} = M^2 u, \tag{4.11}$$

where the dimensionless number

$$M = H \sqrt{\frac{r_S}{d \langle S \rangle}} \tag{4.12}$$

is a substrate modulus analogous to the Thiele modulus in chemical reaction engineering. The substrate modulus is the square root of the ratio of the time-scales of mixing and reaction, H^2/d and $\langle S \rangle / r_S$, respectively, which relates the diffusion equation based model to time-scale analyses as well. Q_S is the substrate's volumetric feed rate ($\mathrm{g\,L^{-1}\,h^{-1}}$) in Equation 4.11. In practice, Q_S was localized to the feed coordinate x_0 by a Dirac delta distribution $\delta(x - x_0)$. The mass balance for gluconate produced by *A. baylyi* ADP1 was also modeled by Equation 4.11, but with the volumetric source term being weighted spatially according to the dimensionless glucose profile u.

Temperature T (K) was modeled by an energy balance based on a similar steady-state 1D diffusion equation with zeroth-order kinetics (publication II):

$$\rho C_p \frac{d}{H^2} \frac{\partial^2 T}{\partial x^2} = \Delta H_\mathrm{r} \mathrm{OUR} u - \Delta H_\mathrm{r} \mathrm{OUR}, \tag{4.13}$$

In Equation 4.13, $\rho = 1000\,\mathrm{kg\,m^{-3}}$ is the fluid's density, $C_p = 4180\,\mathrm{J\,kg^{-1}\,K^{-1}}$ the specific heat capacity of water (Rumble, 2022), $\Delta H_\mathrm{r} = 460\,\mathrm{kJ\,mol^{-1}} = 14\,375\,\mathrm{kJ\,kg^{-1}}$ the enthalpy of oxygen consumption (Doran, 2013), and OUR the overall oxygen uptake rate ($\mathrm{kg\,m^{-3}\,h^{-1}}$) that accounts for potential transfer limitation (publication II). The heat release rate was spatially weighted according to the substrate profile u (Equation 4.11), and cooling was kept spatially uniform.

All the preceding balances derived from the general 1D diffusion Equation 2.7 were solved with the Green's function method (Cole et al., 2010) with insulated boundaries (zero-gradient or symmetry condition). In contrast, the profile of CO_2(g) was modeled with a plug flow equation (publication II)

$$\frac{1}{V} \frac{\partial n_D}{\partial x} = Q_D u, \tag{4.14}$$

where n_D is the molar flow of CO_2(g) ($\mathrm{mol\,s^{-1}}$) and Q_D the release or production rate of CO_2(g) connected to the substrate consumption rate ($\mathrm{mol\,m^{-3}\,s^{-1}}$). Inlet flow was assumed to be zero, and the volumetric release rate was spatially weighted by the substrate's dimensionless profile, u. Dissolved O_2 and CO_2 were modeled analytically with simple balances by assuming that gas-liquid transfer exceeded the rate of mixing and by using zeroth-order kinetics weighted by the substrate profile (publication II):

$$k_{\mathrm{L}}a(h_O O_{\mathrm{G}} - O_{\mathrm{L}}) = \mathrm{ODR}u \tag{4.15}$$

$$k_{\mathrm{L}}a(D_{\mathrm{L}} - h_D D_{\mathrm{G}}) = Q_D u. \tag{4.16}$$

In numerical simulations (publication III, unpublished) a more general mass balance was applied for the concentration C ($\mathrm{g\,L^{-1}}$ or $\mathrm{mol\,L^{-1}}$) of the dissolved species (substrate, oxygen, pH-correcting agent, biomass classes):

$$\frac{\partial}{\partial t}(CV)_i = \left(V\sum r\right)_i + \sum_j v_{ij}C_j. \tag{4.17}$$

The index i refers to a subvolume V_i of the whole simulated domain, and j is an index that runs through all applicable compartments relative to i. The net reaction term $\sum r$ includes all volumetric sources and sinks, such as the feed, reactions, and gas-liquid mass transfer. The volume flow rates v_{ij} are zero with compartment pairs (i,j) that have no flow between them, and negative or positive in accordance with the flow pattern. The concentration at compartment i, C_i, is thus influenced by concentrations of other species in the same compartment through the reaction term, and by concentration of the same species in the other compartments j through the volume flow rates.

4.3.4 Volume flow rate correlations (I)

Both circulation flow rates v_C and exchange or interstage flow rates v_I (both $m^3\,s^{-1}$) were calculated by established literature correlations

$$v_C = N_C n D_i^3 \tag{4.18}$$

and

$$v_I = N_I n D_i^3, \tag{4.19}$$

where N_C and N_I are the circulation and interstage or exchange flow numbers, respectively (Vasconcelos et al., 1998). The flow numbers are $v_C = 1.5$ and $v_I = 0.6$ for standard $D_i = D_T/3$ Rushton turbines in the turbulent flow regime (Vasconcelos et al., 1998). Section 3.3.2 of publication I details how the numbers were calculated in other situations, such as with other impeller diameters and in the transition flow regime.

4.3.5 Compartment model simulations (III)

Numerical experiments were performed by simulating Monod-form substrate consumption, pulse addition of a tracer, and a pH-controlling alkaline pulse in four experimentally studied large-scale bioreactors from literature. Two stirred tank and two bubble column reactors were simulated, and their working volumes were on an industrially relevant scale, ranging from $8\,m^3$ up to $237\,m^3$. Table 4.4 lists the reactors and Figure 4.1 illustrates the used 3D compartment modeling methodology based closely on previously published hydrodynamic 2D compartment modeling and 2D and 3D networks-of-zones approaches (Delafosse et al., 2014; Hristov et al., 2001; Zahradník et al., 2001). Square or rectangular networks of 5 nested flow loops were utilized, yielding 10 radial columns per network. The two stirred tanks were equipped with radial impellers (Rushton turbines), and they were modeled with two stacked square networks per impeller. An additional single square network was added above the top impeller to model the stagnant top zone (Vrábel et al., 1999; Vrábel et al., 2000). The two bubble columns were modeled as single rectangular networks (Zahradník et al., 2001). The stacks of 2D axial-radial networks were multiplied to 12 tangential coordinates and joined by tangential circulation or exchange flows to obtain

Table 4.4 Reactors simulated with compartment models. Modified from publication III Table 1 under the Creative Commons BY 4.0 license.

Reactor	D_T m	V m^3	H/D_T -	α_G %	u_G $cm\,s^{-1}$	N -	Reference
Stirred tanks							
R4	2.09	23.8	3.33	5.90	0.923	10 800	(Vrábel et al., 1999)
R1	2.60	8.17	1.30	0	0	3600	(Langheinrich et al., 1998)
Bubble columns							
B13	1.60	40.2	12.5	23.3	25.0	7440	(Schügerl, 1993)
B6	3.70	237	5.95	17.0	6.50	3600	(Zahradník et al., 2001)

Symbols: D_T, tank diameter; V, working volume; H, working height; α_G, gas-holdup; u_G, superficial gas velocity at the middle of the reactor; N, number of compartments.

3D models (Delafosse et al., 2014; Hristov et al., 2001). The total number of compartments per reactor was 3600–10 800. The compartment model for reactor R4 was also used for previously unpublished results.

4.4 Numerical methods

4.4.1 Model evaluation and error analysis (I, II, IV)

The analytical models and approximations developed in publications I and II were evaluated against previously published experimental and numerical data using coefficients of determination (R^2 and Q^2), mean relative error, and coefficient of variation (COV). As a metric the conventional R^2 is based on absolute error, or the residuals between predicted and experimental value, whereas the supplementary coefficient of determination, Q^2, is based on logarithmic error. These metrics are detailed in Section 2.2 and Supplementary Section S3 of publication I.

Standard first-order propagation of error was used to assess the uncertainty in modeling due to the experimental variability of the parameters (publications I and II) and to estimate the error in quantities derived from experimental measurements (publication IV). Parameters were assumed to have zero covariance. The standard deviation (STD) σ_f of a function f of N parameters x_i is

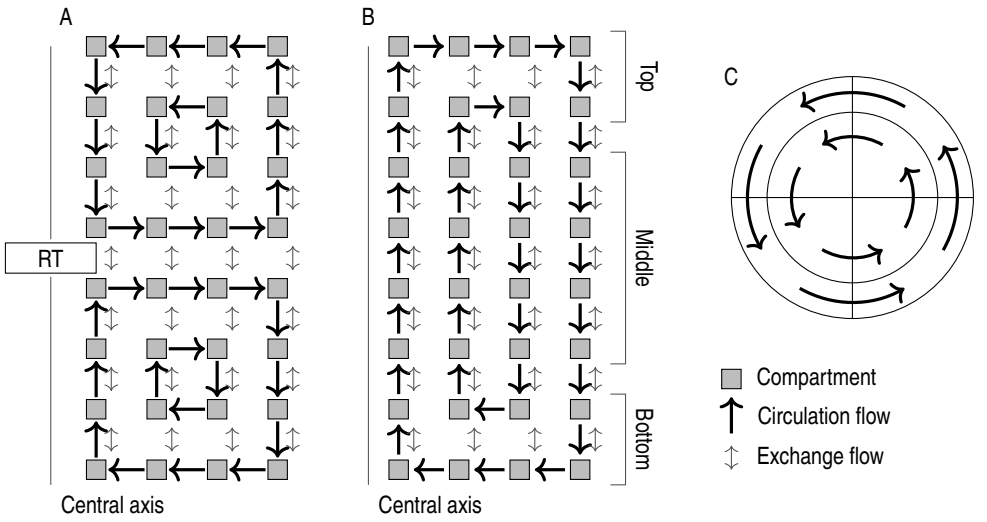

Figure 4.1 Compartment models. Modified from publication III Figure 1 under the Creative Commons BY 4.0 license. (A) Two square networks of nested loops (two in figure) composed the radial flow pattern induced by Rushton turbines in reactors R4 and R1. (B) The flow pattern in bubble columns was composed of a rectangular network of nested loops (two in figure). Axially adjacent compartments were connected by bidirectional exchange flows in both reactor types. (C) Tangentially adjacent compartments in stirred tanks were connected by unidirectional circulation flows. Bidirectional exchange flows were used instead of circulation flows in bubble columns.

approximately

$$\sigma_f = \sqrt{\sum_{i=1}^{N} \left(\partial f / \partial x_i\right)^2 \sigma_{x_i}^2}, \tag{4.20}$$

where σ_i is x_i's STD. The derivatives $\partial f / \partial x_i$ were calculated analytically for experimentally derived quantities, where the function f was simple, but numerically with a centered difference for model predictions, where the functions f were cumbersome for analytical differentiation. The axial dispersion coefficient d was found to have an error σ_d/d of 7–10 % depending on the reactor configuration (publication I).

4.4.2 Flux balance analysis (IV)

Two genome-scale models were used for flux balance analyses (FBAs): iAF1260 for *E. coli* (Feist et al., 2007) and iAbaylyiv4 for *A. baylyi* ADP1 (Durot et al., 2008). A previously described iterative procedure (Pacheco et al., 2019) was adopted for the co-culture FBAs. It was necessary to add a step that maximized the glucose importation reaction and to use the maximized value as an explicitly forced bound for the growth rate maximization step. As previously described, all gene-associated flux was minimized after growth rate maximization. In contrast to the original scheme, secreted metabolites were added to the medium for following iterations even if the microorganisms did not grow. Further details on the FBA methodology are given in Supplementary Section S1 of publication IV.

4.4.3 Initial value problems and systems of equations (III, IV)

Initial value problems were solved with the implicit backward-differentiation formula (BDF) method implemented in the scipy.integrate Python package. Steady-states were calculated with a custom integrator that used the backward Euler method and constant time steps solved with the stabilized biconjugate gradient algorithm implemented in the scipy.sparse.linalg Python package. The Jacobian matrices were calculated analytically for steady-state calculations and when using the BDF method in time integration. The steady-state calculations were initialized with ideal homogeneous reactor results. Previously unpublished results also used the same steady-state calculation methodology.

4.4.4 Software (I–IV)

Python programming language (http://www.python.org) was used for all computations, simulations, and analyses. The following Python packages were used (publications I–IV): cobrapy (Ebrahim et al., 2013), numpy (Harris et al., 2020), pandas (McKinney, 2010), scipy (Virtanen et al., 2020), and sympy (Meurer et al., 2017). WebPlotDigitizer (Rohatgi, 2020) was used to obtain literature data from original figures (publications I–III). GNU Image Manipulation Program 2.10.18 (http://www.gimp.org) was used in transforming previously published substrate contour lines to CDFs (publication II). The same software were used also for previously unpublished results.

5 SUMMARY OF RESULTS AND DISCUSSION

First, the development and validation of diffusion equation based modeling is summarized and discussed in Section 5.1. The models are then used to characterize large-scale bioreactors in general, and a previously unpublished example calculation is provided to demonstrate the use of the developed models (Section 5.2). The optimal placements of feed points suggested by diffusion equation are then modeled and simulated (Section 5.3). Finally, a co-culture system capable of reducing the effective heterogeneity is modeled and simulated, and the construction of such a co-culture system is presented (Section 5.4). The original publications (I–IV) and their supplementary materials contain more specific results and discussion. Sections 5.4.2 and 5.4.5 contain previously unpublished results.

5.1 Diffusion equation as a model

The development and validation of the model are briefly reviewed in Sections 5.1.1 and 5.1.2. Section 5.1.3 discusses assumptions, limitations, and possible improvements to the model.

5.1.1 Model development (I, II)

The first step in developing the diffusion equation models was to predict the axial dispersion coefficient, the main parameter. This was achieved by applying an analogy from basic heat transfer theory (publication I), the concept of resistances in series, to previously published 1D and 2D CMs (Vasconcelos et al., 1998; Vrábel et al., 2000). Figure 5.1 illustrates how the developed 1D dispersion coefficient model represents 2D axial-radial flow patterns by only exchange flows analogous to velocity fluctuations: The dispersion coefficient d ($\mathrm{m^2\,s^{-1}}$) is proportional to the working height H (m), but inversely proportional to the

vessel's cross-section A (m^2) and a total transfer resistance R ($\mathrm{s\,m}^{-3}$):

$$d = \frac{H}{AR}. \tag{5.1}$$

The total resistance R is the sum of impeller-wise circulation resistances R_C ($\mathrm{s\,m}^{-3}$) and interstage resistances R_I ($\mathrm{s\,m}^{-3}$) between impellers. The impeller-wise circulation resistances were calculated with impeller-wise working heights H_i (m) and impeller-wise circulation flows v_C ($\mathrm{m}^3\,\mathrm{s}^{-1}$) and length-scales L (m) in accordance with the finite-volume discretization of the 1D diffusion equation (Figure 2.3):

$$R_\mathrm{C} = \frac{H_\mathrm{i}}{v_\mathrm{C0}L_0 + v_\mathrm{CG}L_\mathrm{G}}. \tag{5.2}$$

The subscripts 0 and G denote mechanical and pneumatical flows and scales, respectively. Previous studies suggest that either $D_\mathrm{T}/3$ or $H_\mathrm{i}/3$ should be the length-scale (Vasconcelos et al., 1998; Vrábel et al., 2000). The harmonic mean of these two options was used as the length-scale:

$$L = \frac{2}{3}\frac{D_\mathrm{T}H_\mathrm{i}}{D_\mathrm{T} + H_\mathrm{i}}. \tag{5.3}$$

In the case of negligible pneumatic contribution $v_\mathrm{CG} = 0$ and equal mechanical circulation flows induced by each impeller, the total circulation resistance simplifies to

$$\sum R_\mathrm{C} = \frac{2}{3}\left(N_\mathrm{i} + \frac{H}{D_\mathrm{T}}\right)\frac{1}{v_\mathrm{C}}. \tag{5.4}$$

The whole working height was used in Equation 5.3 instead of an impeller-wise height for the pneumatic length-scale. The interstage resistances were calculated with mechanical and pneumatic interstage flows:

$$R_\mathrm{I} = \frac{1}{v_\mathrm{I0} + v_\mathrm{IG}}. \tag{5.5}$$

The calculation of the flow rates is based on previously published experimental correlations (Equations 4.18 and 4.19) as explained in Section 3.3.2 of publication I.

The majority of reactors equipped with N_i impellers were treated with N_i circulation and $N_\mathrm{i} - 1$ interstage resistances. In some configurations, the amount of circulation and interstage resistances could not conform to the presented

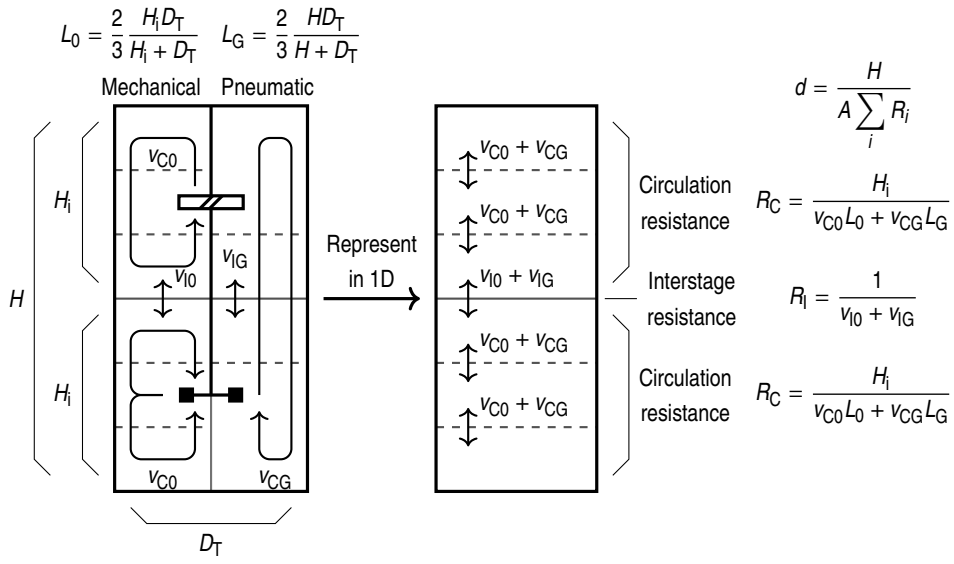

Figure 5.1 Resistances-in-series analogy. Modified from publication I Figure 1 under the Creative Commons BY 4.0 license. Symbols: d, axial dispersion coefficient ($m^2\,s^{-1}$); H, working height (m); A, cross-section (m^2); R, transfer resistance ($s\,m^{-3}$); v, volume flow ($m^3\,s^{-1}$); L, length-scale (m); H_i, impeller-wise working height (m); D_T, tank diameter (m).

standard due to impeller placement or high gas flow rate. In such cases the standard amounts were either increased or decreased as explained in Section 3.3.1 of publication I. These exceptions were a minority in the collected set of 832 mixing times.

Formulae for mixing time and other relevant variables were derived next (publication I). The formula for mixing time was found by first solving the dimensionless tracer concentration u as a function of time from Equation 4.10:

$$u = 1 + 2\sum_{k=1}^{\infty} \cos(k\pi x_0)\cos(k\pi x)\exp\left(-k^2\pi^2\frac{dt}{H^2}\right). \tag{5.6}$$

The mixing times are defined with u close to equilibrium, and at such times, the first time-dependent term in Equation 5.6 dominates the solution. The mixing time t_u could then be found using a first-order approximation:

$$t_u = \frac{H^2}{\pi^2 d}\ln\frac{2\cos(\pi x_0)\cos(\pi x)}{1-u}. \tag{5.7}$$

A STD based mixing time was obtained from the definition of variance:

$$\sigma^2(t) = \int_0^1 (1 - u(t))^2 \, \mathrm{d}x, \tag{5.8}$$

which yielded

$$t_\sigma = \frac{H^2}{2\pi^2 d} \ln \frac{2\cos^2(\pi x_0)}{\sigma^2} \tag{5.9}$$

after integration and simplification.

The profile of dimensionless substrate concentration in a fed-batch was integrated from Equation 4.11 (publication II):

$$u = \frac{M}{\sinh M} \cosh(M \min(x, x_0)) \cosh(M(1 - \max(x, x_0))) . \tag{5.10}$$

The variance of u (substrate concentration) was found by substituting u from Equation 5.10 into the definition of variance (Equation 5.8) and integrating:

$$\sigma^2 = M^2 \frac{x_0 \cosh^2(M(1 - x_0)) + (1 - x_0)\cosh^2(Mx_0)}{2\sinh^2 M} + M \frac{\cosh(M(1 - x_0))\cosh(Mx_0)}{2\sinh M} - 1. \tag{5.11}$$

The substrate's CDF was defined by solving for x in Equation 4.11 and recognizing that a randomly chosen point x obeys the uniform distribution (publication II):

$$F(u) = \frac{1}{M}\left(\operatorname{arcosh}\left(\frac{u}{u_{\min}}\right) + \operatorname{arcosh}\left(\frac{\max(u, u_{\mathrm{tres}})}{u_{\mathrm{tres}}}\right)\right), \tag{5.12}$$

where $u_{\min}$ is the minimum of dimensionless substrate concentration found at $x = 0$ if $x_0 \geq 0.5$ and at $x = 1$ if $x_0 < 0.5$. The other concentration value u_{tres} is found at the domain boundary ($x = 0$ or $x = 1$) closer to the feed point x_0. The probability density function (PDF) of the substrate was found by differentiating

the CDF with respect to u (publication II):

$$f(u) = \frac{1}{M} \frac{1}{\sqrt{u^2 - u_{\min}^2}} \qquad \text{when } u_{\min} < u < u_{\text{tres}} \tag{5.13}$$

$$f(u) = \frac{1}{M} \left(\frac{1}{\sqrt{u^2 - u_{\min}^2}} + \frac{1}{\sqrt{u^2 - u_{\text{tres}}^2}} \right) \qquad \text{when } u_{\text{tres}} < u \leq u_{\max}. \tag{5.14}$$

The maximum concentration $u_{\max}$ occurs at the feed point $x = x_0$.

Having defined the substrate's profile, variance, and distribution functions, dissolved oxygen was found from the local balance Equation 4.15 that utilizes the substrate profile (publication II):

$$O_{\text{L}}(x) = \max \left(0,\, h_O O_{\text{G}}(x) - \frac{\text{ODR} u(x)}{k_{\text{L}} a} \right). \tag{5.15}$$

Dissolved oxygen tension (DOT) is obtained from Equation 5.15 by dividing by the local gas-phase concentration with zero oxygen conversion, $h_O O_{\text{G}}(x)$. A temperature coefficient (K)

$$M_T = \frac{H^2 \Delta H_{\text{r}} \text{OUR}}{\rho C_p d} \tag{5.16}$$

allowed writing the temperature integrated from Equation 4.13 in a dimensionless form

$$\theta(x) = \frac{T(x) - \langle T \rangle}{M_T} \tag{5.17}$$

as (publication II)

$$\theta = \frac{1}{3} + \frac{x^2 + x_0^2}{2} - \max(x, x_0) + \frac{1}{M^2} - \frac{\cosh(Mx)\cosh(Mx_0)}{M \tanh M} + \frac{\sinh(M \max(x, x_0))\cosh(M \min(x, x_0))}{M}. \tag{5.18}$$

The axial profile of CO_2(g) was integrated from Equation 4.14 (publication II):

$$\frac{n_D(x)}{Q_D V_L} = \frac{1}{\sinh M}(\sinh(M\min(x,x_0))\cosh(M(1-x_0)) - \sinh(M(1-x))\cosh(Mx_0) + \sinh(M(1-\min(x,x_0)))\cosh(Mx_0)). \quad (5.19)$$

Assuming then that the total molar flow of gas remains constant throughout the reactor, the partial pressure and concentration of CO_2(g), p_{D_G} and D_G, can be obtained using the ideal gas law accounting for hydrostatic pressure. Solving for D_L in Equation 4.16 yields in turn

$$D_L(x) = h_D D_G(x) + \frac{Q_D u(x)}{k_L a}. \quad (5.20)$$

The axial distribution of CO_2(aq) implies an axial distribution of HCO_3^-(aq) as well due to the extremely rapid acid-base kinetics. A phosphoric acid buffer is often found in fermentations (Bylund et al., 1998; Larsson et al., 1996; Xu, Jahic, Blomsten, & Enfors, 1999), and combining the acid-base equilibria of CO_2(aq) and $H_2PO_4^-$(aq) into CO_2(aq)+HPO_4^{2-}(aq) $\longleftrightarrow$ HCO_3^-(aq)+$H_2PO_4^-$ allows estimating how the buffer and consequently pH locally adjust to the CO_2(aq) levels dictated by the gas phase. Supplementary Table S2 of publication II illustrates how the mean concentrations of $H_2PO_4^-$(aq), HPO_4^{-2}(aq), CO_2(aq), and HCO_3^-(aq) can be used to calculate the local equilibrium concentrations and pH at a given mean pH.

5.1.2 Validation (I, II)

The developed model was validated against literature data by predicting 832 mixing times and 17 tracer curves and by calculating 288 locally measured and reported substrate concentrations based on the mean of the concentrations (Figure 5.2). Previously published numerically simulated substrate concentrations were also used for validation purposes.

The mixing times and tracer data were predicted with 92.1 and 65.7 % coefficients of determinations (R^2), respectively, which are excellent numbers given the extent, comprehensiveness, and biotechnological relevance of the data (publication I). Greatest accuracy and precision were found for multi-impeller

reactors with typical standard geometries or close to it, where the specific power input is not the controlling factor (Bernauer et al., 2022; Jahoda & Machoň, 1994; Magelli et al., 2013; Vrábel et al., 2000) in the same way as with single-impellers (Nienow, 1997). The high prediction quality was lost when gas flow rates caused flooding, though. Using the parameters shown in Table 4.3 as indicated in publication II, the substrate concentrations calculated for the experimental reference data achieved $R^2 = 61.9\,\%$, which is also noteworthy considering that the model was not optimized to the data (publication II). The substrate profiles and CDFs calculated with the model matched the numerical reference data with good accuracy without parameter optimization (publication II).

5.1.3 Assumptions, limitations, applicability, and future improvements (I, II)

The main hydrodynamical assumption was to model all mixing as axial dispersion with a single dispersion coefficient, which is a continuous reformulation of successful and predictive 1D CMs (Vasconcelos et al., 1998). As illustrated in Figures 2.3 and 5.1, this approach compressed all spatial details of the flow field into a single overall dispersion coefficient. Despite good mixing time prediction performance with most multi-impeller configurations regardless of impeller types, single-impeller configurations and axial-only multi-impeller configurations with tight enough impeller spacing to cause merging of the impeller-wise flow patterns into a single circulation loop were poorly predicted (publication I). It is notable, that in the poorly predicted cases the model included no interstage resistances, which suggests that the circulation flow rates are not the most suitable basis for determining the circulation resistance within an impeller stage. Indeed, the established mixing time correlation (Equation 2.3) developed for single impellers is based on specific power input rather than circulation flow (Grenville & Nienow, 2003; Nienow, 1997). Redefining the circulation resistance to incorporate the single-impeller correlation might improve the model performance. Kolmogorov-scale micromixing effects (Dunlop & Ye, 1990) were not considered, but since mass transfer is a linear phenomenon, the incorporation of micromixing rate in the linearized substrate uptake rate would be mathematically simple.

Based on the typical rise velocity of bubbles, considered working heights, and the computed axial dispersion coefficient, some gas-phase dispersion would be

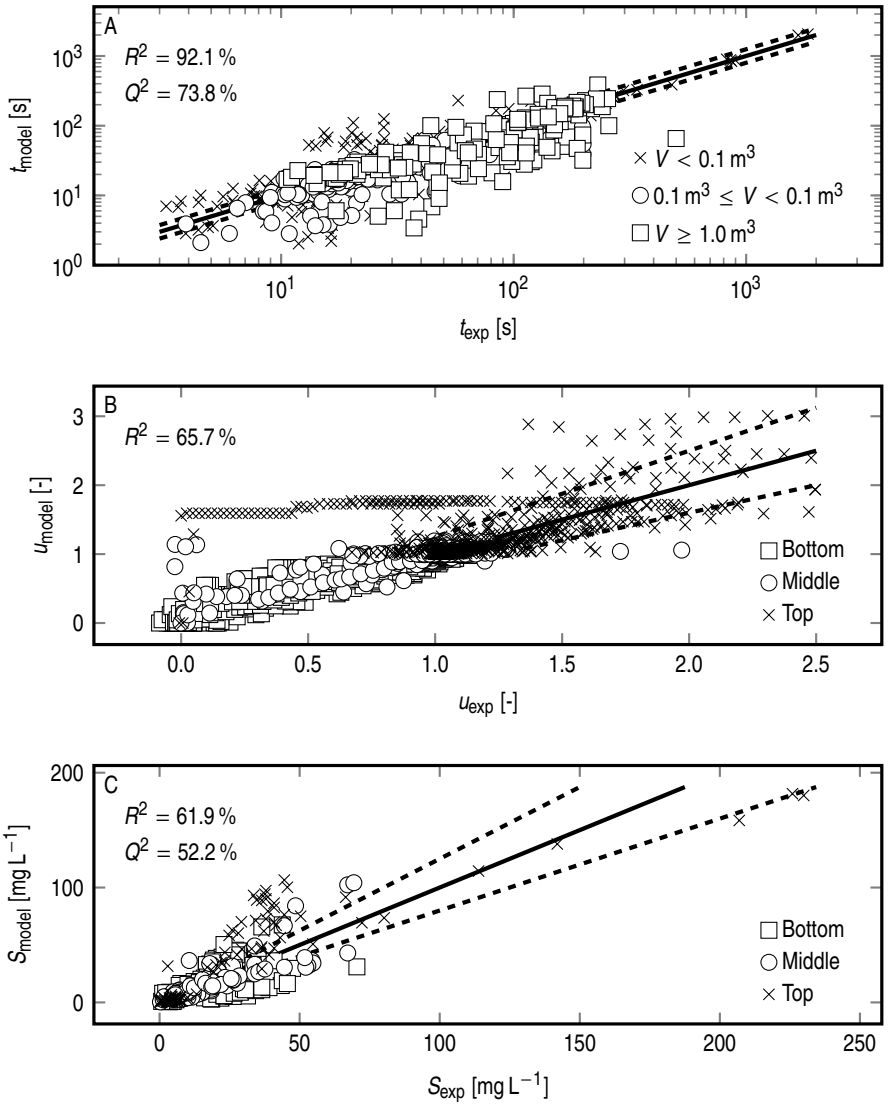

Figure 5.2 Validation of the analytical models. Solid lines indicate the ideal $y = x$ curve. Dashed lines indicate the 25 % multiplicative error limits ($y = 1.25x$ and $y = 0.80x$). (A) Mixing times grouped according to working volume scale (publication I). (B) Tracer signals grouped according to probe placement (publication I). The axis ranges were limited to $x = 2.5$ and $y = 3$ for clarity, leaving some of the top data invisible, but all data were included in the calculation of R^2. (C) Substrate concentrations measured at the top, middle, and bottom in four large-scale fermentation experiments (publication II).

expected. Thus, the typical axial dispersion model (plug flow with dispersion) would have been appropriate for O_2(g) and CO_2(g). However, the dispersion model also implies mixing of gas-phase. Plug flow was assumed for its simplicity and natural applicability to non-coalescing systems often found in bioprocessing contexts. Zero oxygen conversion was also assumed in the characterization and modeling, which was not unreasonable given the air and substrate flow rates that limited the theoretical maximum conversion. The developed DOT model does permit differing gas-phase compositions and even spatially heterogeneous oxygen transfer rate coefficients, but for simplicity and demonstration purposes they were kept homogeneous. A major simplification with DOT was to neglect the liquid-phase mixing of dissolved oxygen. The modeling of CO_2 implied saturation of the liquid phase such that all produced CO_2 entered the gas phase.

Depending on the purpose of modeling, estimating the axial profile of kinetic energy dissipation might be beneficial. This would allow incorporating spatially heterogeneous micromixing rates and oxygen transfer rate coefficients. It remains at the discretion of the modeler whether modeling to such detail is desirable in the context of an analytical 1D model mainly aimed at preliminary and general-level study. In this work the assumption of axially uniform gas holdup had no effect, but if required, the impact of hydrostatic pressure on gas holdup would be readily incorporated in the model as long as its influence on liquid-phase mixing can be ignored.

The main kinetic assumptions were to use a single rate expression to represent all the substrate uptake systems present in an organism, to linearize the net substrate uptake rate, and to derive profiles of quantities related to substrate consumption with zeroth-order kinetics weighted spatially by the substrate's profile. In the context of the steady-state diffusion equation, the profiles yielded by the linearized kinetics (Equation 4.2) and standard Monod kinetics were surprisingly similar (Supplementary Figure S1 of publication II). Furthermore, the linear kinetics are at least in some sense more realistic than Monod kinetics in heterogeneous conditions, where the microorganism may uptake the substrate at a rate exceeding the maximal rate parameter fitted at homogeneous conditions (Xu, Jahic, Blomsten, & Enfors, 1999). In accordance with the experimental findings, the linearization allows the cells exposed to higher-than-mean concentrations of substrate to assimilate at a higher rate than

the standard Monod kinetics would.

5.2 Characterization of large-scale bioreactors

The mixing times in high aspect ratio standard bioreactors are described in Section 5.2.1. Axial profiles of substrate, oxygen, carbon dioxide, temperature, and pH during fed-batch processes are treated in Section 5.2.2. Implications of the characterized axial profiles are discussed in Section 5.2.3. A previously unpublished application example of the developed model is provided in Section 5.2.4.

5.2.1 Mixing time (I)

Using the developed and validated resistances-in-series analogy to dispersion coefficient (Equation 5.1) and the mixing time Equation 5.7 (publication I), the mixing time as a function of stirrer rate or specific power input in standard geometry bioreactors could be simplified into readily usable forms. As discussed in publication I, the model, and by extension the characterization, is most applicable to multi-impeller configurations. Only turbulent regime is considered below, as large-scale reactors are expected to remain in the turbulent or higher transition regime even with viscous media. Effects of aeration are not considered in this characterization, but in general, low aeration rates tend to have only little influence on mixing times, and higher aeration rates either increase or decrease the mixing time depending on the relative strengths of mechanical and pneumatic factors (Vasconcelos et al., 1998, 1995).

Assuming then a standard geometry $H = N_\mathrm{i} D_\mathrm{T}$, standard impeller diameter $D_\mathrm{i} = D_\mathrm{T}/3$ yielding $N_\mathrm{C} = 1.5$ and $N_\mathrm{I} = 0.6$ circulation and interchange flow numbers for Rushton turbines (Vasconcelos et al., 1998, 1995), respectively, the widest possible spacing between feed x_0 and probe x, and the conventional $u = 95\,\%$ homogeneity threshold, the mixing time Equation 5.7 is simplified to

$$t_{95} \approx 2.64 N_\mathrm{i}(11N_\mathrm{i} - 5)/n. \tag{5.21}$$

Equation 5.21 can also be expressed in terms of volume V (m^3) and specific

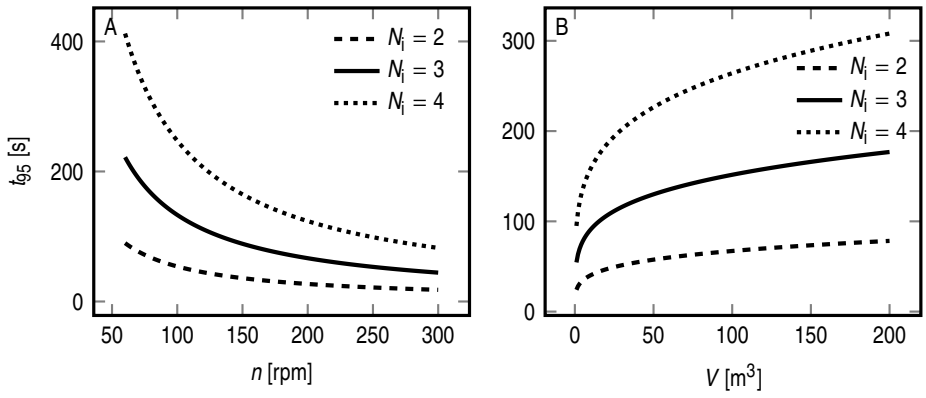

Figure 5.3 Characterization of longest possible 95 % mixing times in standard geometry bioreactors with 2–4 impellers as a function of stirrer rate (A) and volume (B). Panel B assumes 1 W kg^{-1} power input with an impeller-wise power number of 5.

power ϵ (W kg^{-1}):

$$t_{95} \approx 0.484 N_\mathrm{i}^{7/9} (11 N_\mathrm{i} - 5) \left(\frac{N_P V^{2/3}}{\epsilon} \right)^{1/3} . \tag{5.22}$$

The unaerated 95 % mixing time in standard geometry bioreactors is characterized in Figure 5.3 according to both Equations 5.21 and 5.22. With $N_P = 5$ typical to Rushton turbines, 1 W kg^{-1} specific power, and 2–4 impellers in standard geometry, the 95 % mixing time is 24–95 s in 1 m^3, 40–158 s in 10 m^3, and 67–264 s in 100 m^3, which highlights that the aspect ratio and the number of impellers have a vastly greater influence on mixing time than volume alone. In general, 2.5- and 4.6-fold mixing times are expected when increasing $N_\mathrm{i} = H/D_\mathrm{T}$ from two to three and four, respectively. It should be kept in mind, that most large-scale stirred tanks tend to be slightly shorter than standard geometry, approximately 75 % (Bernauer et al., 2022; Rosseburg et al., 2018; Vrábel et al., 1999; Vrábel et al., 2000; Xing et al., 2009).

The effect of non-ideal probe response and non-ideal tracer pulse on mixing times was also studied with the model (publication I). The main finding was that the product of stirrer rate and mixing time does not remain constant in the turbulent flow regime but increases as a function of the stirrer rate if the time-scale of probe response or duration of the tracer pulse are not sufficiently

smaller than the measured mixing time, at most a few percents of it. In literature, some studies have suggested that the dimensionless mixing time nt_{95} does not remain constant in the turbulent regime but starts to increase at very high Reynolds numbers. Based on the diffusion equation analysis, it is plausible that the observed increase has been due to probe and pulse effects at high Reynolds numbers corresponding to the shortest measured times (Section 4.2.1 of publication I). Probe dynamics could be at play also in the lower end of the Reynolds number spectrum, in the transition flow regime ($\mathrm{Re} < 10\,000$): Vasconcelos et al. (1996) mentioned that the transition-regime-corrected circulation flow rates (correction factor Equation 18 in publication I) decreased unphysically below the interstage flow rate at very low Reynolds numbers of 200 and below. In their configuration, the smallest turbulent eddies at $\mathrm{Re} \leq 200$ would have had a Kolmogorov-scale of approximately $(\nu/\epsilon)^{1/4} \approx 3\,\mathrm{mm}$, which is comparable to a conductivity probe's diameter. Thus, micromixing limitations around the probe may have been the reason for the unphysically corrected circulation flow rates.

5.2.2 Substrate, oxygen, temperature, carbon dioxide, and pH (II, III)

The distribution of dimensionless substrate concentration is characterized in Table 5.1 with $x_0 = 1$ and $M \in [1, 5.7]$. General top-fed axial profiles and CDFs of substrate are shown in Figure 5.4. To supplement the analytical characterization (publication II), results from a 3D CM simulation (publication III) are averaged radially and tangentially and included in Figure 5.4. The simulation was based on the reactor studied by Xu, Jahic, Blomsten, and Enfors (1999) large-scale fed-batch experiments (R4 in Table 4.4). With $M = 1$, the reactor is still quite homogeneous even though the time-scales of mixing and reaction are equal. However, with a time-scale of mixing four times the time-scale of reaction, or $M = 2$, the top feed increases the top concentration to approximately double the mean and decreases the bottom concentration almost down to half the mean. With $M = 4$ the top concentration is approximately four times the mean and the bottom concentrations less than a quarter of the mean. The averaged axial profile from a 3D CM simulation with standard Monod kinetics was in appreciable accordance with the simplified analytical results.

To give further context to the characterizations above, the substrate modulus

Table 5.1 Distribution of dimensionless substrate concentration.

Substrate modulus	1.00	1.41	2.00	2.83	4.00	5.66
Maximum	1.31	1.59	2.07	2.85	4.00	5.66
Upper quartile	1.10	1.18	1.30	1.42	1.48	1.38
Median	0.96	0.92	0.85	0.73	0.55	0.34
Lower quartile	0.88	0.78	0.62	0.42	0.23	0.09
Minimum	0.85	0.73	0.55	0.34	0.15	0.04
COV	0.14	0.25	0.44	0.69	1.01	1.35

Abbreviations: COV, coefficient of variation.

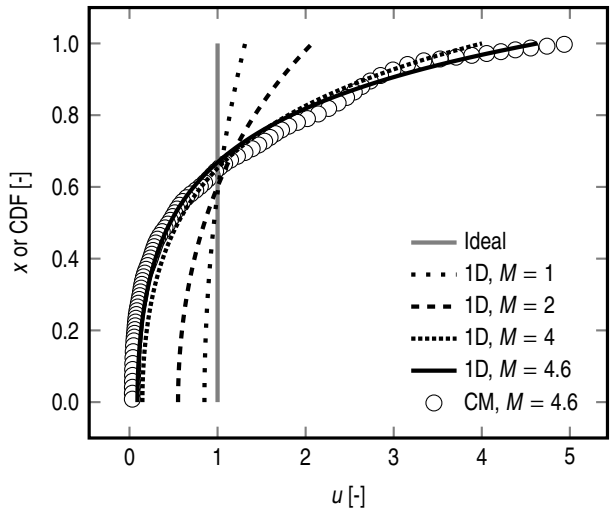

Figure 5.4 Dimensionless substrate concentration profile and CDF with a top feed. The vertical axis corresponds to both the axial coordinate and the substrate's CDF. Analytical 1D diffusion equation profiles were obtained from Equation 5.10 (publication II) and 3D CM profiles from a numerical simulation (publication III). Ideal homogeneous profile is shown for reference.

is interpreted in terms of the substrate feed rate Q_S, biomass concentration X, and maximal 95 % mixing time t_{95} with the probe and tracer pulse as far apart as possible (publication II). First, it is assumed that $\langle S \rangle = K_S = 0.05\,\mathrm{g\,L^{-1}}$, which would imply a half-maximal specific substrate uptake rate in the context of the Monod kinetics. Assuming then a $q_S = 1\,\mathrm{g\,g^{-1}\,h^{-1}}$ specific substrate uptake rate maximum, the modulus (Equation 4.12) can be approximated as

$$M \approx 0.0862 \sqrt{\frac{X}{\mathrm{g\,L^{-1}}} \frac{t_{95}}{\mathrm{s}}}. \tag{5.23}$$

An alternative evaluation is obtained by using the steady-state $r_S \approx Q_S$ approximation, which yields

$$M \approx 0.122 \sqrt{\frac{Q_S}{\mathrm{g\,L^{-1}\,h^{-1}}} \frac{t_{95}}{\mathrm{s}}} \tag{5.24}$$

as a function of substrate feed rate instead. Under a $t_{95} = 100\,\mathrm{s}$ mixing time, the substrate moduli of 1, 2, and 4 correspond to 1.35, 5.38, and $21.5\,\mathrm{g\,L^{-1}}$ biomass concentrations (Equation 5.23) or to 0.67, 2.69, and $10.7\,\mathrm{g\,L^{-1}\,h^{-1}}$ substrate feed rates (Equation 5.24).

The profiles of DOT, temperature, gaseous and dissolved carbon dioxide, and pH were developed based on the substrate's profile (publication II). General profiles are shown in Figure 5.5. A numerically simulated DOT profile obtained with Monod-kinetics is also shown (publication III). Just as the substrate concentration peaks at the feed point, the local DOT decreases due to a high local consumption rate (Figure 5.5A). An overall lower DOT and an exacerbated local DOT limitation near the feed point are observed with lower ratios of transfer to demand. The profile of temperature is considerably much smoother than the oxygen or substrate profiles (Figure 5.5B). The overall shape is defined by the feed point x_0 and the substrate modulus M, but the temperature coefficient M_T (Equation 5.16) defines the profile's magnitude. With a 100 s mixing time, a 1 °C temperature difference would require substrate and oxygen consumption rates of $16\,\mathrm{g\,L^{-1}\,h^{-1}}$. Similarly to temperature, the profile of CO_2 is quite smooth (Figure 5.5C). CO_2(g)'s response to substrate heterogeneity was found to depend on the feed point's location (publication II). With the feed above the middle, increasing heterogeneity decreased the volumetric mean of gaseous and dissolved CO_2, and vice versa, with the feed below the middle, increasing heterogeneity

increased the volumetric mean of CO_2. With a homogeneous liquid phase, the profile of CO_2 is linear under the assumptions of negligible axial dispersion and complete saturation. The profile of CO_2(aq) follows the gas-phase profile, but is in excess of the local gas-liquid equilibrium to balance the local production and transfer rates (publication II). As experiments show (Dahod, 1993), a higher stirrer rate and a correspondingly higher k_La would bring the concentration of CO_2(aq) closer to the local gas-liquid equilibrium (Equation 5.20). The deviation of pH from the mean depends on the heterogeneity of the CO_2(aq) distribution and the strength of the buffer (publication II). Figure 5.5D shows the axial distribution of pH under a linear CO_2(aq) profile corresponding to homogeneity of the substrate and rapid gas-liquid transfer.

5.2.3 Implications (II, III)

The heterogeneity in substrate concentration and dissolved oxygen concentration have been known or implied by experimental measurements and numerical simulations alike. The characterization (publications II and III) confirmed that oxygen limitations could easily occur at the feed point where substrate concentration may be excessive. In response, both aerobic overflow and anaerobic fermentation have been observed in large-scale fed-batches (Larsson et al., 1996; Xu, Jahic, Blomsten, & Enfors, 1999). Spending the majority of their time in low concentration zones, the microorganisms adapt their uptake rate and metabolism to concentrations lower than the volumetric mean (Figure 5.4). Once suddenly exposed to a high concentration closer to the feed point, the substrate uptake rate peaks, but also recovers relatively quickly (Sunya et al., 2012). In addition to the possible overflow or fermentative metabolism, responses to osmotic stress have been observed (Schweder et al., 1999).

Though not visible in Figure 5.5A, which does not include hydrostatic pressure, the feed's location has a large impact on oxygen transfer (publication II). If the feed is at the top, the benefit of hydrostatic pressure on oxygen solubility is eventually lost in an increasingly heterogeneous reactor, where the oxygen consumption induced by the substrate is concentrated at the feed point. Conversely, a bottom feed can concentrate the oxygen demand to the region with the greatest oxygen solubility and thus availability. Likewise, a top feed concentrates the CO_2 release into the top of the reactor, whereas a bottom feed

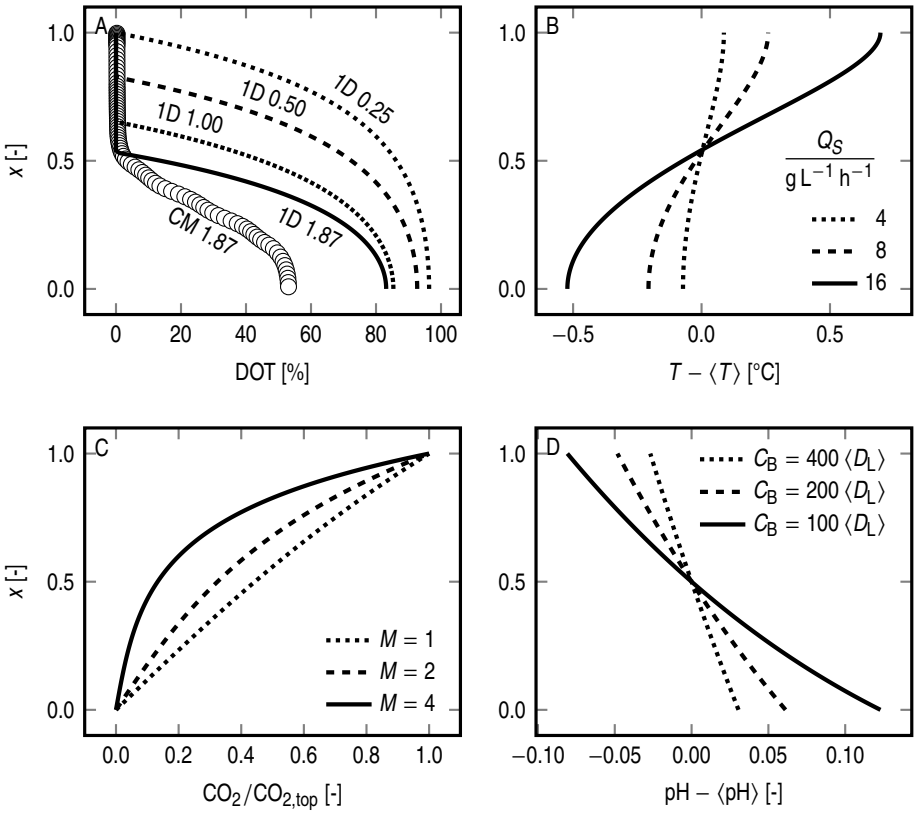

Figure 5.5 General profiles of oxygen, temperature, gaseous and dissolved carbon dioxide, and pH in a top-fed reactor. (A) Dissolved oxygen tension with $M = 4$. The curve labels refer to ratio of ODR to OTR. 1D refers to analytical 1D diffusion equation model (publication II). The CM curve has been radially and tangentially averaged from a 3D CM simulation (publication III). Hydrostatic pressure has been neglected. (B) Centered temperature with M calculated according to Equation 5.24 with $t_{95} = 100\,\mathrm{s}$ (publication II). M_T has been calculated with a $1\,\mathrm{g\,g^{-1}\,h^{-1}}$ consumption of oxygen per substrate without any oxygen limitations. (C) Dimensionless gas-phase carbon dioxide (publication II). Dissolved carbon dioxide deviates from the gas-liquid equilibrium according to local production rate and mass transfer rate constant (Equation 5.20). (D) Centered pH resulting from a linear profile of dissolved carbon dioxide with non-limiting gas-liquid transfer. Here, $\langle \mathrm{pH} \rangle$ is the pK_a of $H_2PO_4^-$. C_B is the summed concentration of $H_2PO_4^-$ and HPO_4^{2-}, and $\langle D_L \rangle$ is the mean concentration of dissolved carbon dioxide (publication II).

releases more CO_2 already at the bottom of the reactor, making the CO_2(g) profile approach its exit value earlier (publication II). Consequently, a bottom feed can result in more homogeneous profiles of CO_2(aq) and pH.

The characterization (publication II) suggested that a considerably nonuniform axial distribution of temperature is possible if the overall substrate and oxygen consumption rates are of the order of $10\,\mathrm{g\,L^{-1}\,h^{-1}}$ in a reactor with a 100 s 95 % mixing time. However, local temperature differences between the bulk liquid and the cooling surfaces could be a more likely issue in a viscous fermentation broth. Interestingly, a transient rise in temperature in response to a sudden glucose pulse in a chemostat culture of *E. coli* has been measured even though the measured difference was just a few hundredths of a Celsius degree (Sunya et al., 2012). This indicates that assimilation and oxidation of glucose is indeed capable of liberating a detectable amount of heat.

5.2.4 Application example (I, II, unpublished)

The practical use of the developed model (publications I and II) for a quick, preliminary investigation of a hypothetical fed-batch fermentation is demonstrated below with the following steps:

1. Estimate the axial dispersion coefficient
2. Estimate the substrate profile
3. Estimate the dissolved oxygen profile
4. Estimate the temperature profile
5. Estimate the carbon dioxide profiles
6. Estimate the pH profile.

The setup is based on a $100\,\mathrm{m^3}$ configuration ($N_\mathrm{i} = H/D_\mathrm{T} = 3$) studied with CFD by Nauha et al. (2018) and an experimental fed-batch study by Xu, Jahic, Blomsten, and Enfors (1999). Biomass concentrations of 4, 12, and $36\,\mathrm{g\,L^{-1}}$ applicable to the Xu, Jahic, Blomsten, and Enfors (1999) experiment are considered for an overall view of the expected gradients. The feed point was set to the unearated liquid height (Xu, Jahic, Blomsten, & Enfors, 1999). The example configuration and the used kinetic parameters are shown in Table 5.2.

Table 5.2 Reactor configuration and kinetic parameters used in the application example.

Parameter	Unit	Value	Source
Reactor configuration			
H_L	m	10.44	(Nauha et al., 2018)
D_T	m	3.48	(Nauha et al., 2018)
D_i	m	1.16	(Nauha et al., 2018)
N_i		3	(Nauha et al., 2018)
$x_0 H$	m	10.44	
Operating conditions			
n	rpm	110.7	(Nauha et al., 2018)
ϵ	$W\,kg^{-1}$	2	(Nauha et al., 2018)
u_G	$m\,s^{-1}$	0.05	(Nauha et al., 2018)
α_G	%	13.74	(Nauha et al., 2018)
$k_L a$	s^{-1}	0.148	(Nauha et al., 2018)
T	°C	35	(Xu, Jahic, Blomsten, & Enfors, 1999)
pH		7	(Xu, Jahic, Blomsten, & Enfors, 1999)
C_B	$mmol\,L^{-1}$	100	(Xu, Jahic, Blomsten, & Enfors, 1999)
Q_S	$g\,L^{-1}\,h^{-1}$	4	(Xu, Jahic, Blomsten, & Enfors, 1999)
p	bar	1.5	(Xu, Jahic, Blomsten, & Enfors, 1999)
Kinetics			
X	$g_X\,L^{-1}$	4, 12, and 36	(Xu, Jahic, Blomsten, & Enfors, 1999)
q_S	$g_S\,g_X^{-1}$	1.35	(Xu, Jahic, & Enfors, 1999)
K_S	$g_S\,L^{-1}$	0.05	(Xu, Jahic, & Enfors, 1999)
Y_{OS}	$g_O\,g_S^{-1}$	0.500, 0.625, and 1.000	(Bylund et al., 2000)
Others			
ΔH_r	$kJ\,kg_{O_2}^{-1}$	460	(Doran, 2013)
C_p	$J\,kg^{-1}$	4180	(Rumble, 2022)
ρ	$kg\,m^{-3}$	1000	
h_O	$mol_L\,mol_G^{-1}$	0.0275	(Sander, 2023)
h_D	$mol_L\,mol_G^{-1}$	0.660	(Sander, 2023)
pK_a		6.31	CO_2(aq) (Rumble, 2022)
		7.18	$H_2PO_4^-$(aq) (Rumble, 2022)

Symbols: H_L, liquid height; D_T, tank diameter; D_i, impeller diameter; N_i, amount of impellers; $x_0 H_L$, feed point; n, stirrer rate; ϵ, specific power; u_G, superficial gas velocity at half-height; α_G, gas holdup; $k_L a$, mass transfer rate constant; T, temperature; C_B, summed concentration of $H_2PO_4^-$ and HPO_4^{2-}; Q_S, substrate feed rate; p, head-space pressure; X, biomass concentration; q_S, maximal specific substrate uptake rate; K_S, substrate affinity constant; Y_{OS}, O_2 consumption per substrate; ΔH_r, reaction enthalpy of O_2 consumption; C_p, specific heat capacity of water; ρ, liquid density; h_O, Henry's constant for O_2; h_D, Henry's constant for CO_2;

5.2.4.1 Example: Determination of axial dispersion coefficient

1. Assemble reactor geometry and operating condition data: H_L, D_T, D_i, u_G, and n or ϵ and N_P. Collect also impeller clearances. Here, the bottom and impeller clearances were $D_\mathrm{T}/3$ and D_T, respectively.
2. If not otherwise available, estimate α_G *e.g.* by applying a suitable correlation or the simple estimation approach by Nauha et al. (2015). Here, the value calculated by Nauha et al. (2018) was used (Table 5.2).
3. Calculate H. Here, $H = (10.44\,\mathrm{m})/(1 - 0.1374) = 12.10\,\mathrm{m}$.
4. If a single-probe mixing time, usually t_{95}, is available, calculate d from Equation 5.7. If some other kind of mixing time is available, use an appropriate Equation from publication I to transform it to d.
5. If mixing times are not available, calculate d by the resistances-in-series analogy model. In this example, the loss of mechanical power and the contribution by pneumatic agitation are neglected.
   (a) Calculate N_I and N_C (Equations 15 and 17 of publication I). Here, $D_\mathrm{i} = D_\mathrm{T}/3$ results in $N_\mathrm{I} = 0.6$ and $N_\mathrm{C} = 1.5$, respectively (Vasconcelos et al., 1998, 1995). See Section 3.3.2 of publication I for transient regime correction, if applicable.
   (b) Calculate v_C (Equation 4.18) and v_I (Equation 4.19): In this case each impeller induces equal flow rates $v_\mathrm{C} = (1.5) \times (110.7\,\mathrm{rpm}) \times (1.16\,\mathrm{m})^3 = 4.32\,\mathrm{m^3\,s^{-1}}$ and $v_\mathrm{I} = (0.6) \times (110.7\,\mathrm{rpm}) \times (1.16\,\mathrm{m})^3 = 1.73\,\mathrm{m^3\,s^{-1}}$. The mean of adjacent impellers can be used for interstage flows when they are unequal.
   (c) Calculate R_I (Equation 5.5). Here, $R_\mathrm{I} = 1/v_\mathrm{I} = 0.579\,\mathrm{s\,m^{-3}}$, and thus $\sum R_\mathrm{I} = 1.16\,\mathrm{s\,m^{-3}}$. (Three impellers, no stagnant top zone, and no merging of impeller stages.)
   (d) Calculate R_C (Equation 5.2). This example conforms to the special case of equal circulation flows (pneumatic contribution was ignored), and thus Equation 5.4 applies for R_C: $\sum R_\mathrm{C} = (3/2) \times (3 + 12.1/3.48)/(4.32\,\mathrm{m^3\,s^{-1}}) = 2.25\,\mathrm{s\,m^{-3}}$. In general, impeller-wise R_C are calculated, which requires impeller-wise L calculated with H_i (Equation 5.3).
   (e) Calculate d (Equation 5.1) using total resistance $\sum R = 1.16\,\mathrm{s\,m^{-3}} + 2.25\,\mathrm{s\,m^{-3}} = 3.41\,\mathrm{s\,m^{-3}}$ and cross-section $A = \pi/4 \times (3.48\,\mathrm{m})^2 = 9.51\,\mathrm{m^2}$: $d = (10.44\,\mathrm{m})/((9.51\,\mathrm{m^2}) \times (3.41\,\mathrm{s\,m^{-3}})) = 0.374\,\mathrm{m^2\,s^{-1}}$.
   (f) Estimate longest 95 % mixing time (Equation 5.7): $t_{95} = (\ln(40)/\pi^2) \times (10.44\,\mathrm{m})^2/(0.374\,\mathrm{m^2\,s^{-1}})$.

5.2.4.2 Example: Estimation of substrate profile

1. Collect substrate feed rate and kinetic parameters: Q_S, q_S, X, K_S.
2. If not otherwise available, estimate $\langle S \rangle$ *e.g.* from a Michaelis-Menten or Monod-type approximation $Q_S \approx q_S X \langle S \rangle / (\langle S \rangle + K_S)$. Here, the approximation yielded 143, 16.4, and 4.48 $\mathrm{mg\,L^{-1}}$.
3. Calculate corresponding $\mathcal{M}$ (Equation 4.12): 1.75, 5.16, and 9.86.
4. Calculate $u = S/\langle S \rangle$ using Equation 5.10 (Figure 5.6A).

5.2.4.3 Example: Estimation of dissolved oxygen profile

1. If not otherwise available, estimate $k_\mathrm{L}a$ *e.g.* by applying a correlation or the simple estimation approach by Nauha et al. (2015). Here, the value provided by Nauha et al. (2018) was used (Table 5.2).
2. Estimate ODR (Equation 4.4). Here, Y_{OS} was assumed to rise linearly along with X from 0.5 $\mathrm{g\,g^{-1}}$ to 1.0 $\mathrm{g\,g^{-1}}$, and ODRs of 2.0, 2.5, and 4.0 $\mathrm{g\,L^{-1}\,h^{-1}}$ were calculated using Q_S.
3. Check oxygen input. Here, the aeration rate corresponds to 9 $\mathrm{g\,L^{-1}\,h^{-1}}$ of $\mathrm{O_2}$, and the gas-phase conversion is ignored.
4. Calculate zero-conversion-profile of $\mathrm{O_2(g)}$ from ideal gas equation. Hydrostatic pressure was taken into account here.
5. Calculate $\mathrm{O_2(aq)}$ using Equation 5.15 (Figure 5.6B).

5.2.4.4 Example: Estimation of temperature profile

1. Estimate realized oxygen uptake rate. Either integrate numerically $\mathrm{OUR} = \int_0^1 \min(k_\mathrm{L}a h_O O_\mathrm{G}(x),\ \mathrm{ODR}u(x))\mathrm{d}x$ or use the approximated efficiency factor Equation 18 of publication II. Here, oxygen uptake rates of 2.00, 2.36, and 2.28 $\mathrm{g\,L^{-1}\,h^{-1}}$ were obtained.
2. Calculate temperature profile using Equations 5.16 and 5.18 (Figure 5.6C).

5.2.4.5 Example: Estimation of carbon dioxide profiles

1. Estimate Q_D. Here, a respiratory quotient of 1 is assumed, which yields $Q_D = \mathrm{OUR} \times (44\,\mathrm{g\,mol^{-1}})/(32\,\mathrm{g\,mol^{-1}})$: 2.75, 3.25, and 3.14 $\mathrm{g\,L^{-1}\,h^{-1}}$.

2. Estimate molar flow (Equation 5.19) and molar fraction profile (divide molar flow by input molar flow of gas).

3. Calculate p_{D_G} from molar fraction and pressure profiles (Figure 5.6D). Hydrostatic pressure was taken into account here.

4. Calculate D_L (Equation 5.20). Here, the same $k_L a$ was used for CO_2 as for O_2 (Dahod, 1993), but it could be scaled by a factor of 0.89 (Royce & Thornhill, 1991). Use the ideal gas equation to transform D_L/h_D to partial pressure exerted by CO_2(aq) (Figure 5.6E).

5.2.4.6 Example: Estimation of pH profile

1. Determine the concentration of buffer components at the considered mean pH. Here, $H_2PO_4^-$ 60.2 mmol L^{-1} and HPO_4^{2-} 39.8 mmol L^{-1} at pH 7.

2. Determine concentration of HCO_3^- corresponding to mean CO_2(aq) (mean of D_L) at the considered mean pH. Here, means of CO_2(aq) 1.40, 0.964, and 0.701 mmol L^{-1}, and the means of HCO_3^- 6.85, 4.72, and 3.43 mmol L^{-1}.

3. Equilibrate both $CO_2(aq) \longleftrightarrow H^+ + HCO_3^-(aq)$ and $H_2PO_4^-(aq) \longleftrightarrow H^+ + HPO_4^{2-}(aq)$ locally such that CO_2(aq) obeys the profile Equation 5.20 in equilibrium (Supplementary Table S2 in publication II).

4. Calculate pH from either of the considered equilibria (Figure 5.6F).

5.3 Effect of feed point placements on heterogeneity

The impact of optimal feed point placement on reactor heterogeneity was studied both analytically with the 1D diffusion equations and numerically with 3D CMs. The derivation of optimal feed configurations and their effect on mixing time is described in Section 5.3.1. Large-scale reactors were already characterized with the conventional top feed in Section 5.2. Effects on substrate, DOT, and pH control are shown in Section 5.3.2. Finally, the results and their implications on the axial distributions of temperature, CO_2, and pH are discussed in Section 5.3.3.

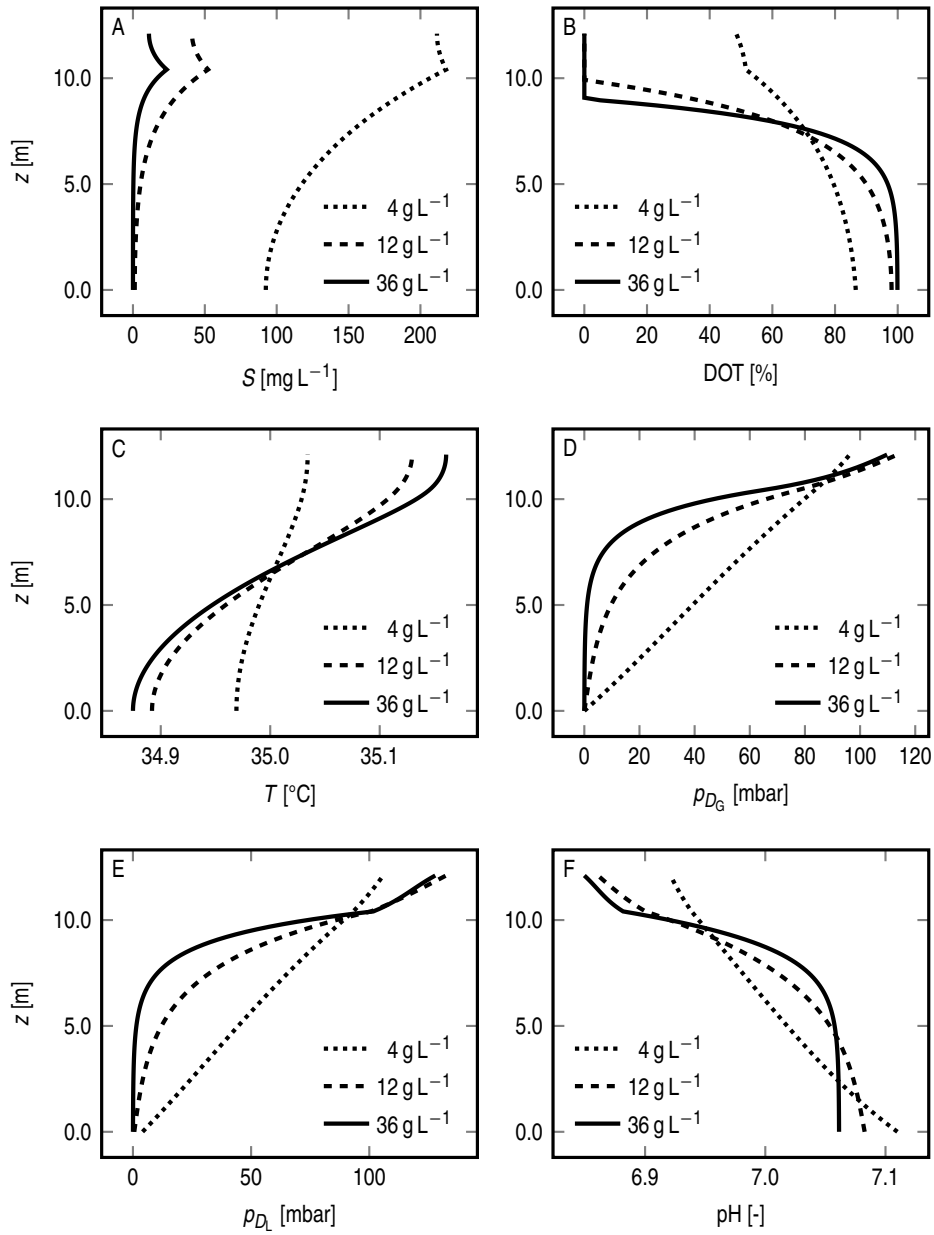

Figure 5.6 Example application of the developed model to a hypothetical 100 m^3 fed-batch fermentation (unpublished). The considered biomass concentrations were 4, 12, and 36 $g\,L^{-1}$. (A) Substrate concentration (Section 5.2.4.2). (B) Dissolved oxygen tension (Section 5.2.4.3). (C) Temperature (Section 5.2.4.4). (D) Partial pressure of CO_2(g) (Section 5.2.4.5). (E) Partial pressure exerted by CO_2(aq) (Section 5.2.4.5). (F) pH (Section 5.2.4.6).

5.3.1 Optimal feed points and mixing time (III)

The $\cos(k\pi x_0)$ term in the solution (Equation 5.6) of the transient 1D diffusion equation suggests that injecting the tracer in the middle $x_0 = 0.5$ eliminates all odd $k = 1,3,5,\ldots$ transient terms, making the second term $k = 2$ the limiting one. In effect, a four-fold (2^2) rate of approach to equilibrium is expected. The same is suggested also by symmetry: First it needs to be remembered that in this study all diffusion equations were solved with insulated, or zero-gradient boundaries, which imply symmetry. Then it is recognized that the 1D domain with a top-feed is halved by injecting to the middle, and that the two halves are symmetrical and analogous to the original top-fed situation but with half the original height. The mixing time Equations 5.7 and 5.9 imply a four-fold rate of mixing if the height is halved ($t_u \propto H^2$). Furthermore, using N symmetrically located feed points divide the working height by N, suggesting a total of $4N^2$-fold rate of mixing when comparing to the top feed. The optimal placement in the radial and tangential domains was studied similarly (publication III), and the identified optimal feed point configurations are exemplified in Figure 5.7.

Optimal multipoint feeds were simulated numerically in 3D CMs (publication III), and representative results are compiled in Table 5.3. Over 100 s STD based 95 % mixing times were simulated in each of the four industrial-scale reactors with a conventional top feed. In each reactor, the use of optimal multipoint feeds improved mixing substantially: compared to the common top feed configuration, over a doubled mixing rate was achieved in each reactor. Reactor R4 stirred with four Rushton turbines reached the diffusion equation's prediction of a 4- and 16-fold mixing rate relative to top feed upon employing 2 and 4 symmetrically placed axial feed locations ($A_1R_1T_1$ and $A_2R_2T_2$ in Table 5.3). The $H \approx 13D_T$ bubble column B13 also reached the prediction of a 4-fold mixing rate with a central feed placement ($A_1R_2T_2$).

The B6 bubble column and the R1 stirred tank did not achieve the mixing time reductions predicted by the diffusion equation with any of the studied feed configurations. The discrepancy in B6 was likely due to insufficient coverage of the column's large cross-section ($D_T = 3.7$ m) by the studied radial-tangential placements. Comparing the $A_1R_1T_1$ and $A_1R_2T_2$ configurations in B13 (Table 5.3) suggests that addition of radial or tangential feed coordinates might have

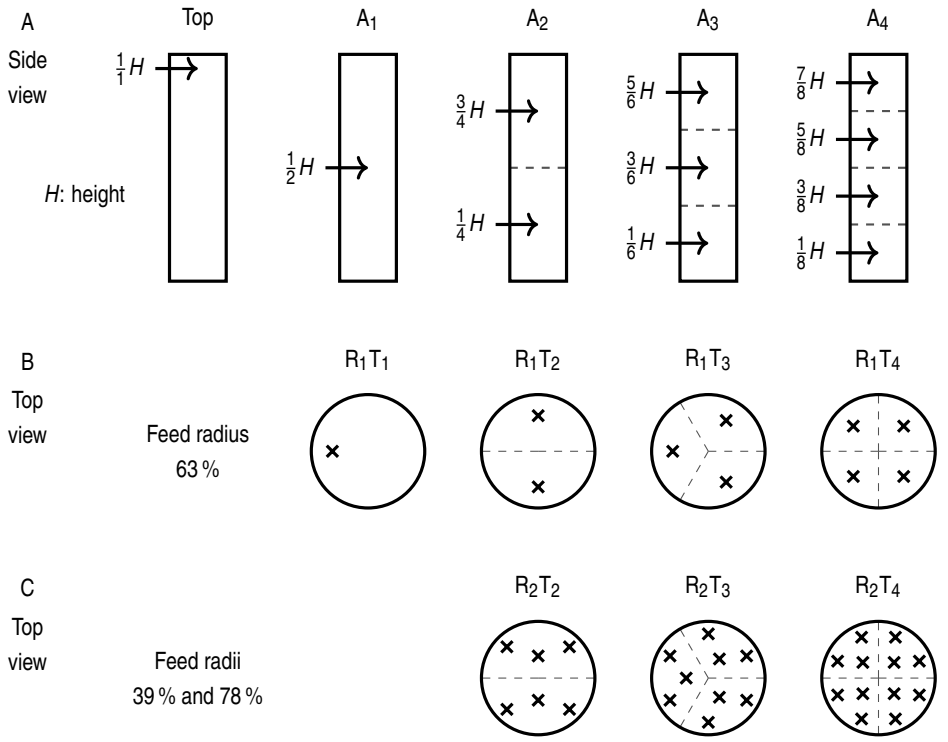

Figure 5.7 Optimal placement of multiple feed points. Modified from publication III Figure 3 under the Creative Commons BY 4.0 license.

Table 5.3 Simulated standard deviation based 95 % mixing times. Data reported in percentages relative to the respective top feed results shown below the reactor label. Ideal refers to 1D diffusion equation's prediction. Modified from publication III Table 3 under the Creative Commons BY 4.0 license.

Feed	R4 154 s	R1 141 s	B13 103 s	B6 135 s	Ideal
$A_1R_1T_1$	24	85	44	90	25
$A_1R_2T_2$	24	63	25	37	25
$A_2R_1T_1$	9	77	30	91	6
$A_2R_2T_2$	6	40	12	21	6
$A_4R_1T_1$	11	78	28	90	2
$A_4R_2T_2$	12	46	6	19	2

Notes: The feed arrangements $A_xR_yT_z$ contain x axial, y radial, and z tangential coordinates as in Figure 5.7. The reactors are described in Table 4.4.

yielded the predicted mixing rate improvements also in B6. Furthermore, bubble columns in general exhibit large circulation currents and uneven gas-liquid distributions that both deviate from the 1D diffusion model's assumptions. R1's configuration also violated the diffusion equation's assumptions: axial exchange is not the limiting form of mixing in a vessel equipped with a single impeller instead of multiple impellers. As such, deviation from model predictions could be expected.

Both stirred tank and bubble column mixing time correlations (Grenville & Nienow, 2003; Kawase & Moo-Young, 1989; Magelli et al., 2013) imply that the achieved reductions in mixing time, over 2- and 10-fold mixing rates, correspond to over 8- and 1000-fold increases in specific power input under the same volumes. The same correlations state that under constant specific power input the volumes would have been decreased by factors of over 20 and 31 600. Such increases in specific power input or reductions in working volume are infeasible, which highlights the potential of multipoint feeds. Though these results were preliminary in nature as they were simulated numerically and not experimented with real equipment, 2.9- to 6.6-fold mixing rates have been realized with placement of only two feed point in pneumatically agitated reactors (Fu et al., 2005).

5.3.2 Substrate, pH control, and oxygen (II, III)

As in the above mixing time analysis, symmetrically placed N axial feed locations divide the effective working height by N. This in turn divides the substrate modulus by the number of axial feed locations, all else being equal. Profiles of substrate and DOT were determined numerically in 3D CMs (publication III) and analytically by applying Equations 5.10 and 5.15 (publication II). The simulations corresponded to substrate moduli of 4.13–5.15. The two approaches were in perfect accordance over the substrate profile (Figure 5.8A). The simple zeroth-order kinetic approach to DOT estimation yielded zero profiles throughout contrary to the numerical DOT profiles ranging between 0.5–4 % (Figure 5.8B), as the used ODR-to-oxygen transfer rate (OTR) ratio was 1.87, indicating that the overall demand rate was almost twice the overall transfer rate. Efficient homogenization of both substrate and DOT profiles was achieved. Further modeling and simulations were also done to study the effects on pH-

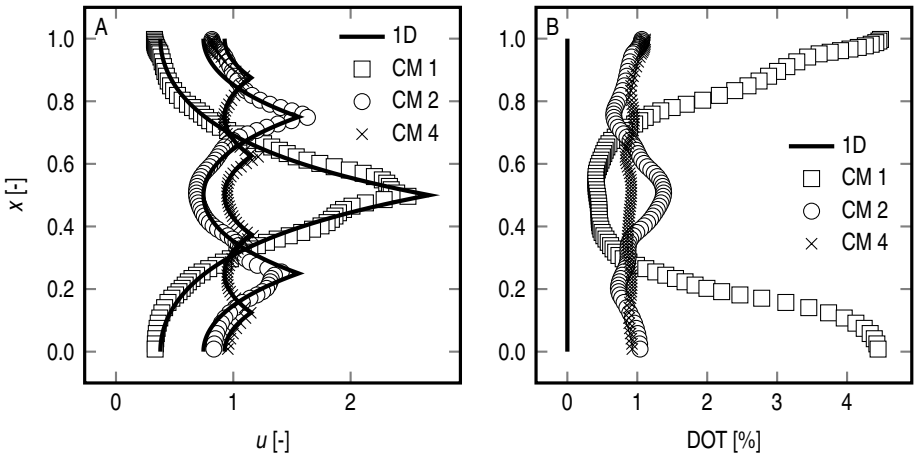

Figure 5.8 Effect of symmetrical feed configurations on profiles of substrate (A) and DOT (B). 1D refers to 1D diffusion equations (publication II). CM stands for 3D CM simulations with 1, 2, or 4 symmetrically placed feed points (publication III).

control, biomass yields, and biomass population heterogeneity (publication III). Altogether, the use of multiple symmetrically placed feed points recovered the ideal homogeneous reactor performance.

Substantial reductions in volumetric STD of substrate concentration were achieved in simulations (publication III) upon applying optimal feed locations: placing a single feed at the middle reduced the STD already to 40–69 % of the top feed, and two optimally placed feeds to 12–17 % (Table 5.4). The 1D diffusion equation's prediction of substrate's variance reduction (publication II) held up to and including two axial feed locations even in the R1 and B6 reactors, where the simulated mixing times were not decreased according to the prediction. According to the diffusion equation, four optimal points could have reduced the COV down to 1 % of the top-fed value, but 6–13 % were found in simulations instead. As with mixing times, eventually the diffusion equation was applied at such scales that its assumptions no longer held even in the R4 and B13 reactors, yielding discrepant results.

5.3.3 Effects on reactor performance (II, III)

In accordance with the analytical model (publication II), the optimal multipoint feeds homogenized the simulated reactors effectively (publication III): The

Table 5.4 Effect of symmetrical feed configurations on volumetric standard deviation of substrate concentration. Data reported in percentages relative to the respective top feed results shown below the reactor label. Ideal refers to 1D diffusion equation's prediction (publication II). Modified from publication III Table 3 under the Creative Commons BY 4.0 license.

Feed	R4 $41.6\,\mathrm{mg\,L^{-1}}$	R1 $121.0\,\mathrm{mg\,L^{-1}}$	B13 $57.1\,\mathrm{mg\,L^{-1}}$	B6 $116.9\,\mathrm{mg\,L^{-1}}$	Ideal
$A_1R_1T_1$	40	87	50	69	49
$A_2R_2T_2$	12	17	13	14	15
$A_4R_2T_2$	6	13	8	10	1

Notes: The feed arrangements $A_xR_yT_z$ contain *x* axial, *y* radial, and *z* tangential coordinates as in Figure 5.7. The reactors are described in Table 4.4.

volumetric STDs (Table 5.4) were initially higher than the volumetric means of 16.8–48.9 $\mathrm{mg\,L^{-1}}$ in the simulations, but eventually it was decreased well below the mean in each of the simulated reactors. Such decreases in volumetric variances imply an increase in biomass yield through decreases in the rate of maintenance metabolism (Maluta et al., 2020). Likewise, an optimally fed reactor is less liable to induce aerobic overflow or anaerobic fermentative metabolism, again increasing biomass yields. The simulations (publication III) and analysis alike (publication II) also suggested that the overall oxygen consumption could be increased. This is due to oxygen demand being more uniformly distributed across the whole volume, which avoids or at least mitigates transfer rate limitations. A uniform oxygen consumption profile also avoids axial temperature differences (publication II). Similarly, the pH gradients associated with pH control and the addition of concentrated acids or bases could be avoided by multipoint feeds (publication III). The CO_2 and pH analyses (publication II) implied that a homogeneous substrate concentration results in a linear profile of both gaseous and dissolved CO_2. Thus, the homogenization of CO_2(aq), and by extension pH, is limited when using multiple feed points for the substrate. A bottom feed releasing the CO_2 early on was found to perform better in this respect despite slower mixing.

Overall, a less stressful environment from the microorganism's perspective could be obtained. The population should furthermore perform more predictably in a reactor with a uniform substrate concentration (Morchain et al., 2014). It needs to be remembered, however, that the derived optima apply in the

ideal of homogeneous or isotropic dispersion without any distinct circulation loops. As such they serve as a generalized, well-performing starting point for the optimal placement in actual vessels where the circulation flow patterns and local differences in turbulence influence mixing.

5.4 Co-cultures

The concept of a co-culture based on interconnected carbon cross-feeding is presented first (Section 5.4.1). The homogenization of effective substrate profiles by the carbon cross-feeding scheme was studied using the 1D diffusion equation and 3D CM methodologies (Section 5.4.2). The control of the co-culture's strain ratio was then investigated (Section 5.4.3), and both the growth and stability of a knock-out co-culture of *A. baylyi* ADP1 and *E. coli* were experimentally confirmed (Section 5.4.4). Long-term genetic stability of the co-culture against destabilizing mutations during industrially relevant growth time-scales was studied (Section 5.4.5). Sections 5.4.2 and 5.4.5 present previously unpublished results.

5.4.1 Preliminary investigation of interconnected carbon cross-feeding (IV)

Figure 5.9 presents the concept of a co-culture of knock-out *A. baylyi* ADP1 and *E. coli*, where neither of the strains can grow on glucose in isolation, but only through interconnected carbon cross-feeding: In the proposed co-culture, a $\Delta gntT$ deletion mutant of *A. baylyi* ADP1 oxidizes glucose to gluconic acid as usual, but is unable to assimilate it. A $\Delta ptsI$ deletion mutant of *E. coli*, on the other hand, is unable to utilize glucose, but grows on the gluconic acid instead and excretes acetic acid. The cycle is completed as *A. baylyi* ADP1 $\Delta gntT$ utilizes the acetic acid.

The concept was then studied by conducting FBAs using genome-scale metabolic models of *A. baylyi* ADP1 and *E. coli*. Using the community FBA scheme modified from the one presented by Pacheco et al. (2019) as explained in Section 4.4.2, the FBAs predicted that a co-culture of knock-out *A. baylyi* ADP1 and *E. coli* could grow on glucose through oxidation of glucose to gluconate by *A. baylyi* ADP1, assimilation of gluconate and excretion of acetate by *E. coli*, and growth of *A. baylyi* ADP1 on acetate. The concept shown in Figure 5.9

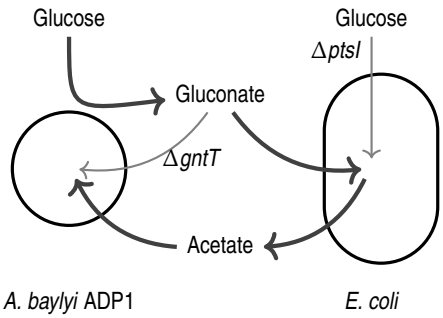

Figure 5.9 Interconnected carbon cross-feeding in a co-culture of knock-out *A. baylyi* ADP1 and *E. coli*. Modified with permission from publication IV Figure 1. Copyright 2019 American Chemical Society.

was thus preliminarily confirmed.

5.4.2 Homogenization of substrate profiles at large scale (unpublished)

The effect of interconnected carbon cross-feeding on the effective substrate profiles in heterogeneous large-scale reactors was modeled by applying the analytical 1D model developed in publications I and II. For simplicity, the conventional $x_0 = 1$ top feed was considered, and the analytical glucose profile (Equation 5.10) was used to weigh the volumetric source term of gluconate, which was consumed with similar linear kinetics as glucose (Equation 4.2). The substrate mass balance for gluconate concentration C ($\mathrm{g\,L^{-1}}$) under these conditions was

$$d\frac{\partial^2 C}{\partial z^2} + Q_C u = k_C C \tag{5.25}$$

where u refers to the dimensionless glucose profile (Equation 5.10), Q_C to the overall volumetric production and reaction rate of gluconate ($\mathrm{g\,L^{-1}\,h^{-1}}$), and $k_C = Q_C/\langle C\rangle$ to the linearized uptake rate constant of gluconate ($\mathrm{h^{-1}}$) obtained by dividing the volumetric source or reaction rate by the mean concentration $\langle C\rangle$ ($\mathrm{g\,L^{-1}}$). As a further simplification, gluconate was assumed to have the same substrate modulus as glucose, as both the volumetric reaction and feed rates and mean concentrations can be considered to be approximately the same

($Q_S \approx r_S \approx Q_C \approx r_C$ and $\langle S \rangle \approx \langle C \rangle$). A nondimensional balance

$$\frac{\partial^2 u_C}{\partial x^2} + M^2 u(x) = M^2 u_C \tag{5.26}$$

was then obtained, where $u_C = C/\langle C \rangle$ is the dimensionless concentration of gluconate. Integrating the gluconate mass balance Equation 5.26 resulted in a dimensionless concentration profile

$$u_C = \frac{M}{4\sinh^2 M}(\cosh(M(1-x))(2Mx + \sinh(2Mx)) + \cosh(Mx)(\sinh(M(1-2x)) + 2M(1-x)\cosh M + \sinh M)). \tag{5.27}$$

Due to the complexity of the derived gluconate profile, the profile of acetate was not estimated analytically.

The analytically estimated profiles of glucose (Equation 5.10) and gluconate (Equation 5.27) with $M = 2.9$ and $M = 4.6$ are shown in Figures 5.10A and 5.10B, respectively. The local deviation of the estimated gluconate profiles from the mean was approximately half the glucose profile's deviation, indicating that the gluconate profile was considerably less heterogeneous than the profile of glucose. The gluconate profile with $M = 4.6$ was less heterogeneous than the glucose profile with $M = 2.9$ despite having a 1.6-fold modulus corresponding to a 2.6-fold mixing time. It needs to be noted that these analyses assumed linearized kinetics with equal substrate moduli. The glucose profile was the Green's function's response to a glucose pulse at x_0, whereas the axial distribution of gluconate was the same function's response to the axial profile of glucose. As each integration smoothens the spatial profile, the obtained results were expected, and by extension, the axial profile of acetate should be even more homogeneous than the profile of gluconate.

To complement the analysis, the profiles of glucose, gluconate, and also acetate were estimated numerically with the 3D CM of R4 that was used in evaluating multipoint feeds in publication III (Figures 5.10C and 5.10D). For simplicity, the same $q_S = 1\,\mathrm{g\,g^{-1}\,h^{-1}}$ maximum specific uptake rate and $K_S = 0.025\,\mathrm{g\,L^{-1}}$ Monod-constant used in the feed point simulations (publication III) was used also for glucose-to-gluconate oxidation, gluconate-to-acetate conversion, and acetate consumption. The $1.09\,\mathrm{g\,g^{-1}}$ yield of gluconate on glucose was based on 1:1

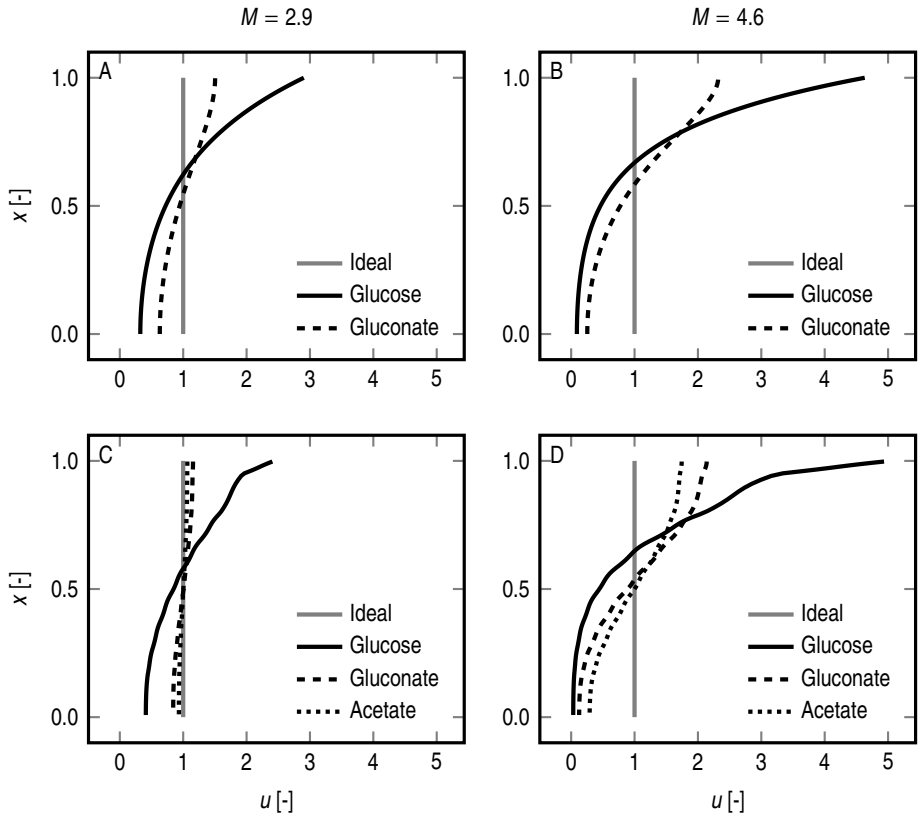

Figure 5.10 Homogenization of effective substrate profiles by the knock-out co-culture of *E. coli* and *A. baylyi* (unpublished). Two substrate or glucose moduli were used, $M = 2.9$ (A and C) and $M = 4.6$ (B and D). Profiles of glucose and gluconate were estimated analytically using Equations 5.10 and 5.27 (A and B) and numerically with 3D CM (C and D). Profiles of acetate were also simulated numerically (C and D). An ideal homogeneous profile is shown for reference. Each panel is given the same limits to emphasize the difference in heterogeneity.

Table 5.5 Homogenization of effective substrate profiles by the knock-out co-culture of *E. coli* and *A. baylyi* ADP1 in 3D CM simulations (unpublished).

Compound	M	Mean $\mathrm{mg\,L^{-1}}$	STD $\mathrm{mg\,L^{-1}}$	COV %
Glucose	2.89	136.5	74.5	59
Gluconate	2.89	19.6	2.1	11
Acetate	2.89	3.8	0.2	5
Glucose	4.63	39.4	46.1	135
Gluconate	4.63	8.5	5.8	73
Acetate	4.63	1.9	0.9	52

Symbols: M, substrate modulus. Abbreviations: STD, standard deviation; COV, coefficient of variation.

stoichiometry and molar masses, and a $0.15\,\mathrm{g\,g^{-1}}$ yield of acetate on gluconate was estimated from literature (Enjalbert et al., 2017). The means, STDs, and COVs of the three compounds are shown in Table 5.5. Two substrate moduli $M = H\sqrt{r_S/(\langle S\rangle\, d)} = H\sqrt{q_S X/((\langle S\rangle + K_S)d)}$ were used: $M = 4.6$ corresponded to $10\,\mathrm{g\,L^{-1}}$ biomass concentration of *A. baylyi* ADP1, that oxidizes glucose to gluconate, whereas $M = 2.9$ corresponded to $5\,\mathrm{g\,L^{-1}}$ concentration of *A. baylyi* ADP1. Based on Supplementary Section S2.3 of publication IV, a 1:2 ratio of *A. baylyi* ADP1 to *E. coli* biomass concentrations was used in the simulations (*E. coli*: $10\,\mathrm{g\,L^{-1}}$ at $M = 2.9$ and $20\,\mathrm{g\,L^{-1}}$ at $M = 4.6$). The COV of gluconate and acetate was considerably much less than the COV of glucose with both substrate moduli. As anticipated, the substrate concentrations experienced by the co-culture were homogeneous in comparison to the original glucose profiles. The osmotic stress caused by locally excessive glucose would remain, though.

5.4.3 Co-culture stability (IV)

The knock-out co-culture with interconnected carbon flow was then studied using a set of ordinary differential equations (ODEs) to confirm whether the cross-feeding stabilizes the growth of the two strains with respect to each other. The ratio of two strains in a co-culture was found to tend towards

$$\frac{X_1}{X_2} = \frac{\mathrm{d}X_1/\mathrm{d}t}{\mathrm{d}X_2/\mathrm{d}t}, \tag{5.28}$$

which was identified as the equilibrium strain ratio. The question was then whether this equilibrium ratio is stable *i.e.* time- and condition-independent. Simple unstructured Monod-form kinetic models of the two strains were developed, where the knock-out *A. baylyi* ADP1 converted glucose to gluconate and grew on acetate. Constant yields were assumed in each reaction. The simple ODE modeling led to

$$\frac{X_{\mathrm{Ab}}}{X_{\mathrm{Ec}}} = \frac{Y_{XA}Y_{NA}}{Y_{XN}} \tag{5.29}$$

as the target assuming only that the concentration of acetate remains constant. In Equation 5.29, Y_{XA} is the yield of *A. baylyi* ADP1 biomass on acetate ($\mathrm{g\,g^{-1}}$), Y_{NA} the yield of acetate on gluconate ($\mathrm{g\,g^{-1}}$), and Y_{XN} the yield of *E. coli* biomass on gluconate ($\mathrm{g\,g^{-1}}$). Numerical experiments confirmed that in the knock-out co-culture the concentration of acetate stabilized to a constant value after a brief accumulation phase (Supplementary Section S2.3 of publication IV).

According to Equation 5.29, the equilibrium ratio of the two strains is entirely defined by the yields of acetate on gluconate, *E. coli* biomass on gluconate, and *A. baylyi* ADP1 biomass on acetate. If the yield constants can be considered constant, the cross-feeding controls the population tightly towards a fixed ratio. Other co-culture combinations of *A. baylyi* ADP1 and *E. coli* strains representing competition, commensialism, and cooperator-cheater dynamics were studied similarly, but they were not found to be as stable as the obligately mutualistic knock-out co-culture (Supplementary Section S2.3 of publication IV). Unlike other co-culture pairs based on obligate mutualism (Mee et al., 2014; Shou et al., 2007; Wintermute & Silver, 2010), which in general have the same advantage of a stable equilibrium ratio, the developed cross-feeding scheme imposed no additional burden on the strains as no biosynthetically costly metabolites were exchanged.

5.4.4 Experiments (IV)

The FBAs and ODE modeling suggested that the knock-out co-culture both grows on glucose and has an inherently stable strain ratio. These predictions were confirmed experimentally. The four strains of *A. baylyi* ADP1 and four strains of *E. coli* were cultivated both in isolation and in all possible 16 pairs of

A. baylyi ADP1 and *E. coli* for 45–47 h in 200 µL volumes of a minimal medium at 30 °C. Glucose was provided as the only carbon source at a concentration of 50 mmol L^{-1}, and in co-cultures the inoculation ratio of the two strains was 1:1. Each strain or pair of strains was cultivated in triplicate. None of the knock-out strains grew in isolation, but each co-culture reached at least an OD of almost 1 (initial OD was approximately 0.1). Fluorescence intensities at the emission maxima of superfolder GFP and mScarlet also increased in accordance with the presence of the fluorescent protein expressing strains, which confirmed that both *A. baylyi* ADP1 and *E. coli* knock-out strains indeed grew in the co-cultures as predicted (Supplementary Figures S6 and S7 of publication IV).

The stability of the co-culture was tested by repeating the experiments with initial glucose concentrations of 50, 100, and 200 mmol L^{-1} using 1:1 inoculation ratio (six replicates) and with 50 mmol L^{-1} initial glucose concentration using inoculation ratios of 1, 2, 5, and 9 parts *E. coli* to 1 part *A. baylyi* ADP1 (three replicates). The OD and fluorescence intensities corresponding to *E. coli* (superfolder GFP) and *A. baylyi* ADP1 (mScarlet) in fluorescent knock-out co-cultures are shown in Figure 5.11. The increase in fluorescence intensities corresponding to the individual strains was quite stable in the knock-out co-culture regardless of the differing experimental conditions.

5.4.5 Long-term stability (unpublished)

In the co-culture used here, the Δ*ptsI* knock-out *E. coli* strain had still various glucose utilization possibilities (ABC transport system, proton symport, oxidation to gluconate and subsequent import) genetically intact (Carreón-Rodríguez et al., 2023). A mutation affecting the regulation of these genes could lead to a subpopulation capable of utilizing glucose, abolishing the engineered obligate mutualism. The likelihood of such an event was estimated by a mutation model (Rugbjerg et al., 2018). The model required two parameters (Equation 4.9): (1) production load, which is the reduction in the engineered strain's specific growth rate relative to the wild-type strain, and (2) escape rate, which denotes the rate at which the engineered microbes abolish the engineered pathway and revert to the original, unreduced growth rate. In this case, the production load could be termed knock-out load as well, and it was roughly estimated to be 50 % by the difference between the co-culture's and wild-type *E. coli*'s specific growth rates

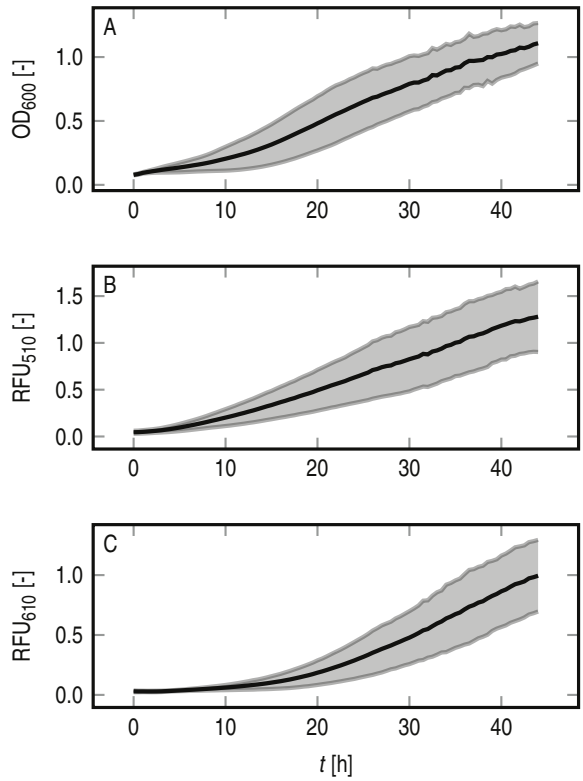

Figure 5.11 Growth (A) and fluorescent protein expression (B and C) of the co-culture of knock-out *A. baylyi* ADP1 and *E. coli*. Shaded areas represent combined sample standard deviations of the altogether 30 measurements comprising sextuplicate cultures with 50, 100, and 200 mmol L^{-1} initial glucose and 1:1 inoculation ratio and triplicate cultures with 50 mmol L^{-1} initial glucose and inoculation ratios of 1, 2, 5, and 9 parts *E. coli* to 1 part *A. baylyi* ADP1 (publication IV). Abbreviations: OD, optical density measured at 600 nm; RFU, relative fluorescence unit of the microwell plate reader measured at 510 and 610 nm.

at the beginning of batch cultures. Allowing for an initial lag phase, the time range 2.5–5.0 h was used for estimating the growth rates by fitting a standard exponential growth curve $X = X_0 \exp(\mu t)$ to the mean of 18 batch growth curves obtained at the three initial glucose concentrations with six replicates each.

Assuming then exponential growth of the co-culture (Equation 4.8) and that the knock-out *E. coli*'s escape occurred at a rate of $1 \cdot 10^{-5}$–$1 \cdot 10^{-8}$ per co-culture generation time (Rugbjerg et al., 2018), the half-life of the knock-out *E. coli* subpopulation would be 16–26 co-culture generations (Equation 4.9). The half-lives seem low given that Rugbjerg et al. (2018) estimated that industrially relevant cubic-meter-scale production volumes may require 60 generations or more. There is a notable difference, however: their scenario imposed the production load immediately since strain construction such that the clone bank already represents 25 generations or more, whereas the co-culturing scenario imposes the knock-out load on *E. coli* only once co-culturing with *A. baylyi* ADP1 with a glucose feed commences. Taking this into account, the 16–26 generations would be sufficient to transfer the co-culture in exponential growth from a milliliter scale preculture to tens of liters ($1\,\mathrm{mL} \times 2^{16}$) up to tens of cubic meters ($1\,\mathrm{mL} \times 2^{26}$). The half-life would be greater still and sufficient for industrially relevant cultivation times with a lower knock-out load.

It needs to be noted that these analyses assumed exponential growth throughout, which does not apply during the long constant-feed phases of fed-batch processes. Nevertheless, it can be concluded that in order to realize stable co-cultures in industrial scale by interconnected carbon cross-feeding or by any other means, the appearance rate of mutants capable of escaping the population control mechanism should be minimized. In the presented co-culture, the deletion of the remaining glucose uptake possibilities in *E. coli* ought to be sufficient. In general, decreasing the intrinsic mutation rate in the used strains by removing genomic insertion sequences should be beneficial in co-culture contexts (Rugbjerg et al., 2018; Suárez et al., 2017).

6 CONCLUSIONS

This study found axial diffusion equations suitable to model large-scale bioreactors. Using the resistances-in-series concept to compute axial dispersion coefficients *a priori*, mixing times could be predicted for an extensive body of over 800 previously published experimentally determined mixing times with high accuracy and precision. The model integrated differing mixing time quantification methods and experimental arrangements in reactor configurations with biotechnological applications. The model fitted previously published, experimentally and numerically determined spatial profiles of substrate concentration notably well without parameter optimization. Future work could extend the dispersion coefficient calculation method to pneumatically agitated bubble column and airlift reactors, providing also these reactor types with a simple analytical model.

Profiles of substrate, oxygen, temperature, pH, and carbon dioxide were characterized in a general way with a dimensionless number that is simple to compute or estimate for preliminary investigations. The derived profiles were in good accordance with available experimental and numerical data even without optimization. The profiles of substrate and oxygen are expected to be the most heterogeneous ones. Spatial profile of pH during addition of a concentrated acid or base is affected by the flow rate which ought to be kept minimal to avoid long-lasting gradients. The axial profile of temperature can be heterogeneous with a uniform cooling, but only if both the substrate feed and oxygen uptake rates are high enough. Local temperature differences between the bulk phase and heat transfer surfaces are more likely a problem. If the axial cooling profile were significantly nonuniform, a heterogeneous temperature profile could be found unless the cooling were concentrated in the feed point's vicinity. The profile of gaseous carbon dioxide is linear with a homogeneous substrate concentration and starts to deviate as heterogeneity increases. The local pH adjusts to the

profile of CO_2(aq), which is more homogeneous with a bottom feed. Similarly to CO_2(g), a linear profile of gaseous oxygen would be found with a homogeneous substrate profile if the overall O_2(g) conversion were significant. However, with a homogeneous substrate profile, the local differences in transfer rate coefficient would become more apparent in the profile of DOT.

In addition to characterizing the heterogeneity in large-scale reactors, the 1D diffusion equations suggested the means to its reduction. Generalized optimal feed point placements were found, and their effect on mixing and reaction was modeled analytically with steady-state 1D diffusion equations and simulated numerically in 3D CMs. Most of the relevant liquid-phase quantities were homogenized effectively by appropriate feed placements, which recovered biomass yields. Reactor control should be improved as well when the pH and oxygen probes represent the whole reactor. The actual implementation of multipoint feeds was not demonstrated, however. The most likely obstacles are in ensuring consistently equal volume flow rates in the feed points and in avoiding contamination. It remains to be shown whether the suggested feed arrangements are feasible.

A biological approach to substrate homogenization was also modeled. The concentration of a product is more homogeneous than the concentration of the actually fed substrate. For example, *A. baylyi* ADP1 oxidizes glucose to gluconic acid that is then assimilated. Upon deleting *A. baylyi* ADP1's gluconate importer and co-cultivating a glucose-knock-out *E. coli* that excretes acetate, a co-culture that experiences more homogeneous substrate concentrations could be built. According to the conducted modeling, the gluconate profile experienced by the knock-out *E. coli* would be approximately the same as the original glucose profile with half the substrate modulus, which corresponds to a four-fold rate of mixing. The profile of acetate encountered by the knock-out *A. baylyi* ADP1 would be even more homogeneous. Such a redistributed carbon flow with the potential for substrate homogenization was experimentally demonstrated by constructing and cultivating a stable co-culture of knock-out *E. coli* and *A. baylyi* ADP1. Long-term genetic stability might be an issue in the demonstrated co-culture, for *E. coli* had other glucose importer pathways still genetically intact even though they were not expressed. Greater stability would ensue if the remaining glucose uptake pathways were removed.

Economically viable operation requires efficient processes. High feed rates, biomass concentrations, and working volumes are likely required, which is associated with heterogeneity and decreased titer, yield, and productivity. The developed analytical model produces similar results as more involved numerical simulations, thus making the modeling of heterogeneous bioreactors and the evaluation of bioprocesses more accessible. The model allows a quick parametric study independent of reactor design using time-scale analyses: the time-scales of mixing and substrate uptake assign the substrate modulus, the oxygen demand and transfer rates control O_2(aq) levels, the time-scales of mixing and heat release affect the temperature differences, the time-scales of CO_2 release and transfer set the excess of CO_2(aq), and the ratio of mean CO_2(aq) concentration to the prevailing buffer governs the axial pH differences. The results of the quick calculation procedure could also be used as a starting point, or the initial value, for more involved simulations. More efficient homogenization of the large-scale reactors would be desirable, in addition to better understanding of their heterogeneity and its consequences. Two potential approaches to homogenization were demonstrated by modeling, and both of them were found efficient and capable of mitigating the substrate gradients experienced by the microorganisms. Multiple feed points are probably less complicated than co-cultures to implement at a large scale.

REFERENCES

Allman, A. R. (1999). Fermentors: Design, operation and applications. In E. M. T. El-Mansi & C. F. A. Bryce (Eds.), *Fermentation Microbiology and Biotechnology* (pp. 9–47). Taylor & Francis.

Alopaeus, V., Koskinen, J., & Keskinen, K. I. (1999). Simulation of the population balances for liquid–liquid systems in a nonideal stirred tank. Part 1 Description and qualitative validation of the model. *Chemical Engineering Science*, *54*(24), 5887–5899. https://doi.org/10.1016/S0009-2509(99)00170-0

Alopaeus, V., Moilanen, P., & Laakkonen, M. (2009). Analysis of stirred tanks with two-zone models. *AIChE Journal*, *55*(10), 2545–2552. https://doi.org/10.1002/aic.11850

Alves, S. S., Vasconcelos, J. M. T., & Barata, J. (1997). Alternative compartment models of mixing in tall tanks agitated by multi-Rushton turbines. *Chemical Engineering Research and Design*, *75*, 334–338. https://doi.org/10.1205/026387697523642

Anane, E., López, D. C., Neubauer, P., & Bournazou, M. N. C. (2017). Modelling overflow metabolism in *Escherichia coli* by acetate cycling. *Biochemical Engineering Journal*, *125*, 23–30. https://doi.org/10.1016/j.bej.2017.05.013

Atkinson, E., Tuza, Z., Perrino, G., Stan, G., & Ledesma-Amaro, R. (2022). Resource-aware whole-cell model of division of labour in a microbial consortium for complex-substrate degradation. *Microbial Cell Factories*, *21*, 115. https://doi.org/10.1186/s12934-022-01842-0

Baba, T., Ara, T., Hasegawa, M., Takai, Y., Okumura, Y., Baba, M., Datsenko, K. A., Tomita, M., Wanner, B. L., & Mori, H. (2006). Construction of *Escherichia coli* K-12 in-frame, single-gene knockout mutants: The Keio

collection. *Molecular Systems Biology*, *2*, 2006.0008. https://doi.org/10.1038/msb4100050

Baez, A., Flores, N., Bolívar, F., & Ramírez, O. T. (2009). Metabolic and transcriptional response of recombinant *Escherichia coli* to elevated dissolved carbon dioxide concentrations. *Biotechnology and Bioengineering*, *104*(1), 102–110. https://doi.org/10.1002/bit.22379

Baldyga, J., Bourne, J., & Yang, Y. (1993). Influence of feed pipe diameter on mesomixing in stirred tank reactors. *Chemical Engineering Science*, *48*(19), 3383–3390. https://doi.org/10.1016/0009-2509(93)80155-J

Bayer, T. S., Widmaier, D. M., Temme, K., Mirsky, E. A., Santi, D. V., & Voigt, C. A. (2009). Synthesis of methyl halides from biomass using engineered microbes. *Journal of the American Chemical Society*, *131*, 6508–6515. https://doi.org/10.1021/ja809461u

Bernauer, S., Eibl, P., Witz, C., Khinast, J., & Hardiman, T. (2022). Analyzing the effect of using axial impellers in large-scale bioreactors. *Biotechnology and Bioengineering*, *119*(9), 2494–2504. https://doi.org/10.1002/bit.28163

Bindels, D. S., Haarbosch, L., van Weeren, L., Postma, M., Wiese, K. E., Mastop, M., Aumonier, S., Gotthard, G., Royant, A., Hink, M. A., & Gadella Jr, T. W. J. (2017). mScarlet: A bright monomeric red fluorescent protein for cellular imaging. *Nature Methods*, *14*, 53–56. https://doi.org/10.1038/nmeth.4074

Brand, E., Junne, S., Anane, E., Cruz-Bournazou, M. N., & Neubauer, P. (2018). Importance of the cultivation history for the response of *Escherichia coli* to oscillations in scale-down experiments. *Bioprocess and Biosystems Engineering*, *41*(9), 1305–1313. https://doi.org/10.1007/s00449-018-1958-4

Bylund, F., Castan, A., Mikkola, R., Veide, A., & Larsson, G. (2000). Influence of scale-up on the quality of recombinant human growth hormone. *Biotechnology and Bioengineering*, *69*(2), 119–128. https://doi.org/10.1002/(SICI)1097-0290(20000720)69:2<119::AID-BIT1>3.0.CO;2-9

Bylund, F., Collet, E., Enfors, S., & Larsson, G. (1998). Substrate gradient formation in the large-scale bioreactor lowers cell yield and increases

by-product formation. *Bioprocess Engineering*, *18*, 171–180. https://doi.org/10.1007/s004490050427

Carreón-Rodríguez, O. E., Gosset, G., Escalante, A., & Bolívar, F. (2023). Glucose transport in *Escherichia coli*: From basics to transport engineering. *Microorganisms*, *11*(6), 1588. https://doi.org/10.3390/microorganisms11061588

Ceroni, F., Algar, R., Stan, G., & Ellis, T. (2015). Quantifying cellular capacity identifies gene expression designs with reduced burden. *Nature Methods*, *12*(5), 415–418. https://doi.org/10.1038/nmeth.3339

Cole, K. D., Beck, J. V., Haji-Sheikh, A., & Litkouhi, B. (2010). *Heat conduction using Green's functions* (2nd ed.). CRC Press. https://doi.org/10.1201/9781439895214

Cronin, D. G., Nienow, A. W., & Moody, G. W. (1994). An experimental study of mixing in a proto-fermenter agitated by dual Rushton turbines. *Food and Bioproducts Processing*, *72*, 35–40.

Dahod, S. K. (1993). Dissolved carbon dioxide measurement and its correlation with operating parameters in fermentation processes. *Biotechnology Progress*, *9*(6), 655–660. https://doi.org/10.1021/bp00024a014

de Berardinis, V., Vallenet, D., Castelli, V., Besnard, M., Pinet, A., Cruaud, C., Samair, S., Lechaplais, C., Gyapay, G., Richez, C., Durot, M., Kreimeyer, A., Fèvre, F. L., Schächter, V., Pezo, V., Döring, V., Scarpelli, C., Médigue, C., Cohen, G. N., ... Weissenbach, J. (2008). A complete collection of single-gene deletion mutants of *Acinetobacter baylyi* ADP1. *Molecular Systems Biology*, *4*, 174. https://doi.org/10.1038/msb.2008.10

Delafosse, A., Collignon, M., Calvo, S., Delvigne, F., Crine, M., Thonart, P., & Toye, D. (2014). CFD-based compartment model for description of mixing in bioreactors. *Chemical Engineering Science*, *106*, 76–85. https://doi.org/10.1016/j.ces.2013.11.033

Delvigne, F., Destain, J., & Thonart, P. (2005). Bioreactor hydrodynamic effect on *Escherichia coli* physiology: Experimental results and stochastic simulations. *Bioprocess and Biosystems Engineering*, *28*(2), 131–137. https://doi.org/10.1007/s00449-005-0018-z

Delvigne, F., Lejeune, A., Destain, J., & Thonart, P. (2006a). Modelling of the substrate heterogeneities experienced by a limited microbial popula-

tion in scale-down and in large-scale bioreactors. *Chemical Engineering Journal*, *120*(3), 157–167. https://doi.org/10.1016/j.cej.2006.03.034

Delvigne, F., Lejeune, A., Destain, J., & Thonart, P. (2006b). Stochastic models to study the impact of mixing on a fed-batch culture of saccharomyces cerevisiae. *Biotechnology progress*, *22*(1), 259–269. https://doi.org/10.1021/bp050255m

Doran, P. M. (2013). *Bioprocess engineering principles* (2nd ed.). Academic Press. https://doi.org/10.1016/C2009-0-22348-8

Dunlop, E. H., & Ye, S. J. (1990). Micromixing in fermentors: Metabolic changes in *Saccharomyces cerevisiae* and their relationship to fluid turbulence. *Biotechnology and Bioengineering*, *36*(8), 854–864. https://doi.org/10.1002/bit.260360816

Durot, M., Fèvre, F. L., de Berardinis, V., Kreimeyer, A., Vallenet, D., Combe, C., Smidtas, S., Salanoubat, M., Weissenbach, J., & Schachter, V. (2008). Iterative reconstruction of a global metabolic model of *Acinetobacter baylyi* ADP1 using high-throughput growth phenotype and gene essentiality data. *BMC Systems Biology*, *2*, 85. https://doi.org/10.1186/1752-0509-2-85

Ebrahim, A., Lerman, J. A., Palsson, B. O., & Hyduke, D. R. (2013). COBRApy: COnstraints-Based Reconstruction and Analysis for Python. *BMC Systems Biology*, *7*, 74. https://doi.org/10.1186/1752-0509-7-74

Eiteman, M. A., Lee, S. A., & Altman, E. (2008). A co-fermentation strategy to consume sugar mixtures effectively. *Journal of Biological Engineering*, *2*, 3. https://doi.org/10.1186/1754-1611-2-3

Enfors, S., Jahic, M., Rozkov, A., Xu, B., Hecker, M., Jürgen, B., Krüger, E., Schweder, T., Hamer, G., O'Beirne, D., Noisommit-Rizzi, N., Reuss, M., Boone, L., Hewitt, C., McFarlane, C., Nienow, A., Kovacs, T., Trägårdh, C., Fuchs, L., ... Manelius, Å. (2001). Physiological responses to mixing in large scale bioreactors. *Journal of Biotechnology*, *85*, 175–185. https://doi.org/10.1016/S0168-1656(00)00365-5

Enjalbert, B., Millard, P., Dinclaux, M., Portais, J., & Letisse, F. (2017). Acetate fluxes in *Escherichia coli* are determined by the thermodynamic control of the Pta-AckA pathway. *Scientific Reports*, *7*, 42135. https://doi.org/10.1038/srep42135

Feist, A. M., Henry, C. S., Reed, J. L., Krummenacker, M., Joyce, A. R., Karp, P. D., Broadbelt, L. J., Hatzimanikatis, V., & Palsson, B. Ø. (2007). A genome-scale metabolic reconstruction for *Escherichia coli* K-12 MG1655 that accounts for 1260 ORFs and thermodynamic information. *Molecular Systems Biology*, *3*, 121. https://doi.org/10.1038/msb4100155

Fitschen, J., Maly, M., Rosseburg, A., Wutz, J., Wucherpfennig, T., & Schlüter, M. (2019). Influence of spacing of multiple impellers on power input in an industrial-scale aerated stirred tank reactor. *Chemie Ingenieur Technik*, *91*(12), 1794–1801. https://doi.org/10.1002/cite.201900121

Fowler, J. D., & Dunlop, E. H. (1989). Effects of reactant heterogeneity and mixing on catabolite repression in cultures of *Saccharomyces cerevisiae*. *Biotechnology and Bioengineering*, *33*(8), 1039–1046. https://doi.org/10.1002/bit.260330813

Fu, C., Lu, S., & Wu, W. (2005). Optimal feeding for tower-type reactors. *AIChE Journal*, *51*, 713–724. https://doi.org/10.1002/aic.10346

George, S., Larsson, G., & Enfors, S. (1993). A scale-down two-compartment reactor with controlled substrate oscillations: Metabolic response of *Saccharomyces cerevisiae*. *Bioprocess Engineering*, *9*, 249–257. https://doi.org/10.1007/BF01061530

George, S., Larsson, G., Olsson, K., & Enfors, S. (1998). Comparison of the Baker's yeast process performance in laboratory and production scale. *Bioprocess Engineering*, *18*, 135–142. https://doi.org/10.1007/PL00008979

Grenville, R. K., & Nienow, A. W. (2003). Blending of miscible liquids. In E. L. Paul, V. A. Atiemo-Obeng, & S. M. Kresta (Eds.), *Handbook of industrial mixing* (pp. 507–542). John Wiley & Sons, Ltd. https://doi.org/10.1002/0471451452.ch9

Haldimann, A., & Wanner, B. L. (2001). Conditional-replication, integration, excision, and retrieval plasmid-host systems for gene structure-function studies of bacteria. *Journal of Bacteriology*, *183*(21), 6384–6393. https://doi.org/10.1128/JB.183.21.6384-6393.2001

Hansford, G. S., & Humphrey, A. E. (1966). The effect of equipment scale and degree of mixing on continuous fermentation yield at low dilution rates.

Biotechnology and Bioengineering, *8*(1), 85–96. https://doi.org/10.1002/bit.260080108

Haringa, C., Tang, W., Wang, G., Deshmukh, A. T., van Winden, W. A., Chu, J., van Gulik, W. M., Heijnen, J. J., Mudde, R. F., & Noorman, H. J. (2018). Computational fluid dynamics simulation of an industrial *P. chrysogenum* fermentation with a coupled 9-pool metabolic model: Towards rational scale-down and design optimization. *Chemical Engineering Science*, *175*, 12–24. https://doi.org/10.1016/j.ces.2017.09.020

Harris, C. R., Millman, K. J., van der Walt, S. J., Gommers, R., Virtanen, P., Cournapeau, D., Wieser, E., Taylor, J., Berg, S., Smith, N. J., Kern, R., Picus, M., Hoyer, S., van Kerkwijk, M. H., Brett, M., Haldane, A., Fernández del Río, J., Wiebe, M., Peterson, P., ... Oliphant, T. E. (2020). Array programming with NumPy. *Nature*, *585*, 357–362. https://doi.org/10.1038/s41586-020-2649-2

Hartmans, S., Smits, J. P., van der Werf, M. J., Volkering, F., & de Bont, J. A. M. (1989). Metabolism of styrene oxide and 2-phenylethanol in the styrene-degrading *Xanthobacter* strain 124X. *Applied and Environmental Microbiology*, *55*(11), 2850–2855. https://doi.org/10.1128/aem.55.11.2850-2855.1989

Hristov, H., Mann, R., Lossev, V., Vlaev, S. D., & Seichter, P. (2001). A 3-D analysis of gas-liquid mixing, mass transfer and bioreaction in a stirred bio-reactor. *Food and Bioproducts Processing*, *79*, 232–241. https://doi.org/10.1205/096030801753252306

Jahoda, M., & Machoň, V. (1994). Homogenization of liquids in tanks stirred by multiple impellers. *Chemical Engineering & Technology*, *17*(2), 95–101. https://doi.org/10.1002/ceat.270170205

Junne, S., Klingner, A., Kabisch, J., Schweder, T., & Neubauer, P. (2011). A two-compartment bioreactor system made of commercial parts for bioprocess scale-down studies: Impact of oscillations on *Bacillus subtilis* fed-batch cultivations. *Biotechnology Journal*, *6*(8), 1009–1017. https://doi.org/10.1002/biot.201100293

Kannisto, M., Aho, T., Karp, M., & Santala, V. (2014). Metabolic engineering of *Acinetobacter baylyi* ADP1 for improved growth on gluconate and

glucose. *Applied and Environmental Microbiology*, *80*(22), 7021–7027. https://doi.org/10.1128/AEM.01837-14

Kasat, G. R., & Pandit, A. B. (2004). Mixing time studies in multiple impeller agitated reactors. *The Canadian Journal of Chemical Engineering*, *82*, 892–904. https://doi.org/10.1002/cjce.5450820504

Käß, F., Junne, S., Neubauer, P., Wiechert, W., & Oldiges, M. (2014). Process inhomogeneity leads to rapid side product turnover in cultivation of *Corynebacterium glutamicum*. *Microbial Cell Factories*, *13*, 6. https://doi.org/10.1186/1475-2859-13-6

Kawase, Y., & Moo-Young, M. (1989). Mixing time in bioreactors. *Journal of Chemical Technology and Biotechnology*, *44*, 63–75. https://doi.org/10.1002/jctb.280440107

Kittler, S., Slouka, C., Pell, A., Lamplot, R., Besleaga, M., Ablasser, S., Herwig, C., Spadiut, O., & Kopp, J. (2021). Cascaded processing enables continuous upstream processing with *E. coli* BL21(DE3). *Scientific Reports*, *11*(1), 11477. https://doi.org/10.1038/s41598-021-90899-9

Laakkonen, M., Moilanen, P., Alopaeus, V., & Aittamaa, J. (2006). Dynamic modeling of local reaction conditions in an agitated aerobic fermenter. *AIChE Journal*, *52*(5), 1673–1689. https://doi.org/10.1002/aic.10782

Laakkonen, M., Moilanen, P., Alopaeus, V., & Aittamaa, J. (2007). Modelling local bubble size distributions in agitated vessels. *Chemical Engineering Science*, *62*(3), 721–740. https://doi.org/10.1016/j.ces.2006.10.006

Langheinrich, C., Nienow, A. W., Eddleston, T., Stevenson, N. C., Emery, A. N., Clayton, T. M., & Slater, N. K. H. (1998). Liquid homogenization studies in animal cell bioreactors of up to 8 m^3 in volume. *Food and Bioproducts Processing*, *76*, 107–116. https://doi.org/10.1205/096030898531873

Langheinrich, C., & Nienow, A. W. (1999). Control of pH in large-scale, free suspension animal cell bioreactors: Alkali addition and pH excursions. *Biotechnology and Bioengineering*, *66*(3), 171–179. https://doi.org/10.1002/(SICI)1097-0290(1999)66:3<171::AID-BIT5>3.0.CO;2-T

Larsson, G., Törnkvist, M., Ståhl-Wernersson, E., Trägårdh, C., Noorman, H., & Enfors, S. (1996). Substrate gradients in bioreactors: Origin and consequences. *Bioprocess Engineering*, *14*, 281–289. https://doi.org/10.1007/BF00369471

Luo, J., McIntyre, E. A., Bedore, S. R., Santala, V., Neidle, E. L., & Santala, S. (2022). Characterization of highly ferulate-tolerant *Acinetobacter baylyi* ADP1 isolates by a rapid reverse engineering method. *Applied and Environmental Microbiology*, *88*(2), e01780–21. https://doi.org/10.1128/AEM.01780-21

Machon, V., & Jahoda, M. (2000). Liquid homogenization in aerated multi-impeller stirred vessel. *Chemical Engineering and Technology*, *23*, 869–876. https://doi.org/10.1002/1521-4125(200010)23:10<869::AID-CEAT869>3.0.CO;2-B

Magelli, F., Montante, G., Pinelli, D., & Paglianti, A. (2013). Mixing time in high aspect ratio vessels stirred with multiple impellers. *Chemical Engineering Science*, *101*, 712–720. https://doi.org/10.1016/j.ces.2013.07.022

Maluta, F., Pigou, M., Montante, G., & Morchain, J. (2020). Modeling the effects of substrate fluctuations on the maintenance rate in bioreactors with a probabilistic approach. *Biochemical Engineering Journal*, *157*, 107536. https://doi.org/10.1016/j.bej.2020.107536

Mayr, B., Moser, A., Nagy, E., & Horvat, P. (1994). Scale-up on basis of structured mixing models: A new concept. *Biotechnology and Bioengineering*, *43*(3), 195–206. https://doi.org/10.1002/bit.260430303

McKinney, W. (2010). Data structures for statistical computing in Python. *Proceedings of the 9th Python in Science Conference*, 51–56. https://doi.org/10.25080/Majora-92bf1922-00a

Mee, M. T., Collins, J. J., Church, G. M., & Wang, H. H. (2014). Syntrophic exchange in synthetic microbial communities. *Proceedings of the National Academy of Sciences*, *111*(20), E2149–E2156. https://doi.org/10.1073/pnas.1405641111

Meurer, A., Smith, C. P., Paprocki, M., Čertík, O., Kirpichev, S. B., Rocklin, M., Kumar, A., Ivanov, S., Moore, J. K., Singh, S., Rathnayake, T., Vig, S., Granger, B. E., Muller, R. P., Bonazzi, F., Gupta, H., Vats, S., Johansson, F., Pedregosa, F., … Scopatz, A. (2017). SymPy: Symbolic computing in Python. *PeerJ Computer Science*, *3*, e103. https://doi.org/10.7717/peerj-cs.103

Moilanen, P., Laakkonen, M., Visuri, O., Alopaeus, V., & Aittamaa, J. (2008). Modelling mass transfer in an aerated 0.2m^3 vessel agitated by Rushton,

Phasejet and Combijet impellers. *Chemical Engineering Journal*, *142*(1), 95–108. https://doi.org/10.1016/j.cej.2008.01.033

Morchain, J., & Fonade, C. (2009). A structured model for the simulation of bioreactors under transient conditions. *AIChE Journal*, *55*(11), 2973–2984. https://doi.org/10.1002/aic.11906

Morchain, J., Gabelle, J., & Cockx, A. (2013). A coupling of biokinetic and population balance models to account for biologial heterogeneity in bioreactors. *AIChE Journal*, *59*(2), 369–379. https://doi.org/10.1002/aic.13820

Morchain, J., Gabelle, J., & Cockx, A. (2014). A coupled population balance model and CFD approach for the simulation of mixing issues in lab-scale and industrial bioreactors. *AIChE Journal*, *60*(1), 27–40. https://doi.org/10.1002/aic.14238

Morchain, J., Pigou, M., & Lebaz, N. (2017). A population balance model for bioreactor combining interdivision time distributions and micromixing concepts. *Biochemical Engineering Journal*, *126*, 135–145. https://doi.org/10.1016/j.bej.2016.09.005

Morchain, J., Quedeville, V., Fox, R. O., & Villedieu, P. (2021). The closure issue related to liquid–cell mass transfer and substrate uptake dynamics in biological systems. *Biotechnology and Bioengineering*, *118*(7), 2435–2447. https://doi.org/10.1002/bit.27752

Nadal-Rey, G., McClure, D. D., Kavanagh, J. M., Cornelissen, S., Fletcher, D. F., & Gernaey, K. V. (2021). Understanding gradients in industrial bioreactors. *Biotechnology Advances*, (107660), 107660. https://doi.org/10.1016/j.biotechadv.2020.107660

Nauha, E. K., & Alopaeus, V. (2015). Modeling outdoors algal cultivation with compartmental approach. *Chemical Engineering Journal*, *259*, 945–960. https://doi.org/10.1016/j.cej.2014.08.073

Nauha, E. K., Kálal, Z., Ali, J. M., & Alopaeus, V. (2018). Compartmental modeling of large stirred tank bioreactors with high gas volume fractions. *Chemical Engineering Journal*, *334*, 2319–2334. https://doi.org/10.1016/j.cej.2017.11.182

Nauha, E. K., Visuri, O., Vermasvuori, R., & Alopaeus, V. (2015). A new simple approach for the scale-up of aerated stirred tanks. *Chemical Engineering*

Research and Design, *95*, 150–161. https://doi.org/10.1016/j.cherd.2014.10.015

Neubauer, P., & Junne, S. (2016). Robuste industrielle Bioprozesse: Vom Laborzum Industriemaßstab und zurück. *BIOspektrum*, *22*, 204–207. https://doi.org/10.1007/s12268-016-0672-5

Ngu, V., Morchain, J., & Cockx, A. (2022). Spatio-temporal 1D gas-liquid model for biological methanation in lab scale and industrial bubble column. *Chemical Engineering Science*, *251*, 117478. https://doi.org/10.1016/j.ces.2022.117478

Nguyen, T. M., Telek, S., Zicler, A., Martinez, J. A., Zacchetti, B., Kopp, J., Slouka, C., Herwig, C., Grünberger, A., & Delvigne, F. (2021). Reducing phenotypic instabilities of a microbial population during continuous cultivation based on cell switching dynamics. *Biotechnology and Bioengineering*, *118*(10), 3847–3859. https://doi.org/10.1002/bit.27860

Nienow, A. W. (1997). On impeller circulation and mixing effectiveness in the turbulent flow regime. *Chemical Engineering Science*, *52*, 2557–2565. https://doi.org/10.1016/S0009-2509(97)00072-9

Nurwono, G., O'Keeffe, S., Liu, N., & Park, J. O. (2023). Sustainable metabolic engineering requires a perfect trifecta. *Current Opinion in Biotechnology*, *83*, 102983. https://doi.org/10.1016/j.copbio.2023.102983

Oldshue, J. Y. (1966). Fermentation mixing scale-up techniques. *Biotechnology and Bioengineering*, *8*(1), 3–24. https://doi.org/10.1002/bit.260080103

Oosterhuis, N. M. G., & Kossen, N. W. F. (1984). Dissolved oxygen concentration profiles in a production-scale bioreactor. *Biotechnology and Bioengineering*, *26*(5), 546–550. https://doi.org/10.1002/bit.260260522

Pacheco, A. R., Moel, M., & Segrè, D. (2019). Costless metabolic secretions as drivers of interspecies interactions in microbial ecosystems. *Nature Communications*, *10*, 103. https://doi.org/10.1038/s41467-018-07946-9

Pédelacq, J. D., Cabantous, S., Tran, T., Terwilliger, T. C., & Waldo, G. S. (2006). Engineering and characterization of a superfolder green fluorescent protein. *Nature Biotechnology*, *24*(1), 79–88. https://doi.org/10.1038/nbt1172

Pigou, M., & Morchain, J. (2015). Investigating the interactions between physical and biological heterogeneities in bioreactors using compartment,

population balance and metabolic models. *Chemical Engineering Science*, *126*, 267–282. https://doi.org/10.1016/j.ces.2014.11.035

Pinelli, D., & Magelli, F. (2000). Analysis of the fluid dynamic behavior of the liquid and gas phases in reactors stirred with multiple hydrofoil impellers. *Industrial & Engineering Chemistry Research*, *39*(9), 3202–3211. https://doi.org/10.1021/ie000216+

Ramos, I., Sharda, N., Villafana, R., Hill-Byrne, K., Cai, K., Pezzini, J., & Coffman, J. (2023). Fully integrated downstream process to enable next-generation manufacturing. *Biotechnology and Bioengineering*, *120*(7), 1869–1881. https://doi.org/10.1002/bit.28384

Rathore, A. S., Thakur, G., & Kateja, N. (2023). Continuous integrated manufacturing for biopharmaceuticals: A new paradigm or an empty promise? *Biotechnology and Bioengineering*, *120*(2), 333–351. https://doi.org/10.1002/bit.28235

Rohatgi, A. (2020). Webplotdigitizer: Version 4.4. https://automeris.io/WebPlotDigitizer

Rosseburg, A., Fitschen, J., Wutz, J., Wucherpfennig, T., & Schlüter, M. (2018). Hydrodynamic inhomogeneities in large scale stirred tanks – Influence on mixing time. *Chemical Engineering Science*, *188*, 208–220. https://doi.org/10.1016/j.ces.2018.05.008

Royce, P. N. C., & Thornhill, N. F. (1991). Estimation of dissolved carbon dioxide concentrations in aerobic fermentations. *AIChE Journal*, *37*(11), 1680–1686. https://doi.org/10.1002/aic.690371111

Rugbjerg, P., Myling-Petersen, N., Porse, A., Sarup-Lytzen, K., & Sommer, M. O. A. (2018). Diverse genetic error modes constrain large-scale bio-based production. *Nature Communications*, *9*, 787. https://doi.org/10.1038/s41467-018-03232-w

Rumble, J. R. (Ed.). (2022). *CRC Handbook of Chemistry and Physics* (103rd ed.). CRC Press/Taylor & Francis. Internet Version.

Sander, R. (2023). Compilation of Henry's law constants (version 5.0.0) for water as solvent. *Atmospheric Chemistry and Physics*, *23*(19), 10901–12440. https://doi.org/10.5194/acp-23-10901-2023

Santala, S., Efimova, E., Kivinen, V., Larjo, A., Aho, T., Karp, M., & Santala, V. (2011). Improved triacylglycerol production in *Acinetobacter baylyi*

ADP1 by metabolic engineering. *Microbial Cell Factories*, *10*, 36. https://doi.org/10.1186/1475-2859-10-36

Santala, S., Karp, M., & Santala, V. (2014). Rationally engineered synthetic coculture for improved biomass and product formation. *PLoS ONE*, *9*(12), e113786. https://doi.org/10.1371/journal.pone.0113786

Schügerl, K. (1993). Comparison of different bioreactor performances. *Bioprocess Engineering*, *9*, 215–223. https://doi.org/10.1007/BF00369405

Schweder, T., Krüger, E., Xu, B., Jürgen, B., Blomsten, G., Enfors, S.-O., & Hecker, M. (1999). Monitoring of genes that respond to process-related stress in large-scale bioprocesses. *Biotechnology and Bioengineering*, *65*(2), 151–159. https://doi.org/10.1002/(SICI)1097-0290(19991020)65:2<151::AID-BIT4>3.0.CO;2-V

Shewale, S. D., & Pandit, A. B. (2006). Studies in multiple impeller agitated gas-liquid contactors. *Chemical Engineering Science*, 489–504. https://doi.org/10.1016/j.ces.2005.04.078

Shou, W., Ram, S., & Vilar, J. M. (2007). Synthetic cooperation in engineered yeast populations. *Proceedings of the National Academy of Sciences*, *104*, 1877–1882. https://doi.org/10.1073/pnas.061057510

Spann, R., Glibstrup, J., Pellicer-Alborch, K., Junne, S., Neubauer, P., Roca, C., Kold, D., Lantz, A. E., Sin, G., Gernaey, K. V., & Krühne, U. (2019). CFD predicted pH gradients in lactic acid bacteria cultivations. *Biotechnology and Bioengineering*, *116*(4), 769–780. https://doi.org/10.1002/bit.26868

Straathof, A. J. J. (2014). Transformation of biomass into commodity chemicals using enzymes or cells. *Chemical Reviews*, *114*(3), 1871–1908. https://doi.org/10.1021/cr400309c

Straathof, A. J. J., Panke, S., & Schmid, A. (2002). The production of fine chemicals by biotransformations. *Current Opinion in Biotechnology*, *13*(6), 548–556. https://doi.org/10.1016/S0958-1669(02)00360-9

Suárez, G. A., Renda, B. A., Dasgupta, A., & Barrick, J. E. (2017). Reduced mutation rate and increased transformability of transposon-free *Acinetobacter baylyi* ADP1-ISx. *Applied and Environmental Microbiology*, *83*(17), e01025–17. https://doi.org/10.1128/AEM.01025-17

Sunya, S., Delvigne, F., Uribelarrea, J.-L., Molina-Jouve, C., & Gorret, N. (2012). Comparison of the transient responses of *Escherichia coli* to a glucose pulse of various intensities. *Applied microbiology and biotechnology*, *95*(4), 1021–1034. https://doi.org/10.1007/s00253-012-3938-y

Szenk, M., Dill, K. A., & de Graff, A. M. R. (2017). Why do fast-growing bacteria enter overflow metabolism? Testing the membrane real estate hypothesis. *Cell Systems*, *5*, 95–104. https://doi.org/10.1016/j.cels.2017.06.005

Tang, W., Deshmukh, A. T., Haringa, C., Wang, G., van Gulik, W., van Winden, W., Reuss, M., Heijnen, J. J., Xia, J., Chu, J., & Noorman, H. J. (2017). A 9-pool metabolic structured kinetic model describing days to seconds dynamics of growth and product formation by *Penicillium chrysogenum*. *Biotechnology and Bioengineering*, *114*, 1733–1743. https://doi.org/10.1002/bit.26294

Taylor, W. H., & Juni, E. (1961a). Pathways for biosynthesis of a bacterial capsular polysaccharide. I. Characterization of the organism and polysaccharide. *Journal of Bacteriology*, *81*, 688–693. https://doi.org/10.1128/jb.81.5.688-693.1961

Taylor, W. H., & Juni, E. (1961b). Pathways for biosynthesis of a bacterial capsular polysaccharide. II. Carbohydrate metabolism and terminal oxidation mechanisms of a capsule-producing coccus. *Journal of Bacteriology*, *81*, 694–703. https://doi.org/10.1128/jb.81.5.694-703.1961

Taylor, W. H., & Juni, E. (1961c). Pathways for biosynthesis of a bacterial capsular polysaccharide. III. Syntheses from radioactive substrates. *Journal of Bacteriology*, *236*(5), 1231–1234. https://doi.org/10.1016/S0021-9258(18)64154-7

Vaneechouette, M., Young, D. M., Ornston, L. N., de Baere, T., Nemec, A., van der Reijden, T., Carr, E., Thernberg, I., & Dijkshoorn, L. (2006). Naturally transformable *Acinetobacter* sp. strain ADP1 belongs to the newly described species *Acinetobacter baylyi*. *Applied and Environmental Microbiology*, *72*(1), 932–936. https://doi.org/10.1128/AEM.72.1.932âĂŞ936.2006

Vasconcelos, J. M. T., Alves, S. S., Nienow, A. W., & Bujalski, W. (1998). Scale-up of mixing in gassed multi-turbine agitated vessels. *The Canadian*

Journal of Chemical Engineering, *76*, 398–404. https://doi.org/10.1002/cjce.5450760308

Vasconcelos, J. M., Alves, S., & Barata, J. M. (1995). Mixing in gas-liquid contactors agitated by multiple turbines. *Chemical Engineering Science*, *50*(14), 2343–2354. https://doi.org/10.1016/0009-2509(95)00090-R

Vasconcelos, J. M., Barata, J. M., & Alves, S. (1996). Transitional mixing in multiple-turbine agitated tanks. *The Chemical Engineering Journal and the Biochemical Engineering Journal*, *63*(1), 53–58. https://doi.org/10.1016/0923-0467(95)03072-7

Versteeg, H. K., & Malalasekera, W. (2007). *An Introduction to Computational Fluid Dynamics: The finite volume method* (2nd ed.). Pearson Education Limited.

Virtanen, P., Gommers, R., Oliphant, T. E., Haberland, M., Reddy, T., Cournapeau, D., Burovski, E., Peterson, P., Weckesser, W., Bright, J., van der Walt, S. J., Brett, M., Wilson, J., Millman, K. J., Mayorov, N., Nelson, A. R. J., Jones, E., Kern, R., Larson, E., ... SciPy 1.0 Contributors. (2020). SciPy 1.0: Fundamental algorithms for scientific computing in Python. *Nature Methods*, *17*, 261–272. https://doi.org/10.1038/s41592-019-0686-2

Vrábel, P., van der Lans, R. G. J. M., Cui, Y. Q., & Luyben, K. C. A. M. (1999). Compartment model approach: Mixing in large scale aerated reactors with multiple impellers. *Chemical Engineering Research and Design*, *77*, 291–302. https://doi.org/10.1205/026387699526223

Vrábel, P., van der Lans, R. G. J. M., Luyben, K. C. A. M., Boon, L., & Nienow, A. W. (2000). Mixing in large-scale vessels stirred with multiple radial or radial and axial up-pumping impellers: Modelling and measurements. *Chemical Engineering Science*, *55*, 5881–5896. https://doi.org/10.1016/S0009-2509(00)00175-5

Vrábel, P., van der Lans, R. G. J. M., van der Schot, F. N., Luyben, K. C. A. M., Xu, B., & Enfors, S. (2001). CMA: Integration of fluid dynamics and microbial kinetics in modelling of large-scale fermentations. *Chemical Engineering Journal*, *84*, 463–474. https://doi.org/10.1016/S1385-8947(00)00271-0

Wintermute, E. H., & Silver, P. A. (2010). Emergent cooperation in microbial metabolism. *Molecular Systems Biology*, *6*, 407. https://doi.org/10.1038/msb.2010.66

Xia, T., Eiteman, M. A., & Altman, E. (2012). Simultaneous utilization of glucose, xylose and arabinose in the presence of acetate by a consortium of *Escherichia coli* strains. *Microbial Cell Factories*, *11*, 77. https://doi.org/10.1186/1475-2859-11-77

Xie, M., Xia, J., Zhou, Z., Chu, J., Zhuang, Y., & Zhang, S. (2014). Flow pattern, mixing, gas hold-up and mass transfer coefficient of triple-impeller configurations in stirred tank bioreactors. *Industrial & Engineering Chemistry Research*, *53*(14), 5941–5953. https://doi.org/10.1021/ie400831s

Xing, Z., Kenty, B. M., Li, Z. J., & Lee, S. S. (2009). Scale-up analysis for a CHO cell culture process in large-scale bioreactors. *Biotechnology and Bioengineering*, *103*(4), 733–746. https://doi.org/10.1002/bit.22287

Xu, B., Jahic, M., Blomsten, G., & Enfors, S. (1999). Glucose overflow metabolism and mixed-acid fermentation in aerobic large-scale fed-batch processes with *Escherichia coli*. *Applied Microbiology and Biotechnology*, *51*, 564–571. https://doi.org/10.1007/s002530051433

Xu, B., Jahic, M., & Enfors, S. (1999). Modeling of Overflow Metabolism in Batch and Fed-Batch Cultures of *Escherichia coli*. *Biotechnology Progress*, *15*, 81–90. https://doi.org/10.1021/bp9801087

Zahradník, J., Mann, R., Fialová, M., Vlaev, D., Vlaev, S. D., Lossev, V., & Seichter, P. (2001). A networks-of-zones analysis of mixing and mass transfer in three industrial bioreactors. *Chemical Engineering Science*, *56*, 485–492. https://doi.org/10.1016/S0009-2509(00)00252-9

Zhang, H., Pereira, B., Li, Z., & Stephanopoulos, G. (2015). Engineering *Escherichia coli* coculture systems for the production of biochemical products. *Proceedings of the National Academy of Sciences*, *112*(27), 8266–8271. https://doi.org/10.1073/pnas.1506781112

Zhou, K., Qiao, K., Edgar, S., & Stephanopoulos, G. (2015). Distributing a metabolic pathway among a microbial consortium enhances production of natural products. *Nature Biotechnology*, *33*(4), 377–383. https://doi.org/10.1038/nbt.3095

PUBLICATIONS

PUBLICATION
I

Modeling large-scale bioreactors with diffusion equations. Part I: Predicting axial dispersion coefficient and mixing times

Losoi, P., Konttinen, J., and Santala, V.

Biotecnology and Bionengineering. Manuscript accepted for publication.
https://doi.org/10.22541/au.168994090.09200674/v1

PUBLICATION II

Modeling large-scale bioreactors with diffusion equations. Part II: Characterizing substrate, oxygen, temperature, carbon dioxide, and pH profiles

Losoi, P., Konttinen, J., and Santala, V.

Biotecnology and Bionengineering. Manuscript accepted for publication.
https://doi.org/10.22541/au.168993582.23442290/v1

PUBLICATION III

Substantial gradient mitigation in simulated large-scale bioreactors by optimally placed multiple feed points

Losoi, P., Konttinen, J., and Santala, V.

Biotechnology and Bioengineering, *119*(12), 3549–3566
https://doi.org/10.1002/bit.28232

Received: 1 April 2022 | Revised: 29 July 2022 | Accepted: 11 September 2022

DOI: 10.1002/bit.28232

ARTICLE

BIOTECHNOLOGY BIOENGINEERING WILEY

Substantial gradient mitigation in simulated large-scale bioreactors by optimally placed multiple feed points

Pauli Losoi | **Jukka Konttinen** | **Ville Santala**

Faculty of Engineering and Natural Sciences, Tampere University, Tampere, Finland

Correspondence
Pauli Losoi, Faculty of Engineering and Natural Sciences, Tampere University, Hervanta Campus, Korkeakoulunkatu 8, Tampere 33720, Finland.
Email: pauli.losoi@tuni.fi

Funding information
Tampere University of Technology Graduate School; Academy of Finland

Abstract

The performance of large-scale stirred tank and bubble column bioreactors is often hindered by insufficient macromixing of feeds, leading to heterogeneities in pH, substrate, and oxygen, which complicates process scale-up. Appropriate feed placement or the use of multiple feed points could improve mixing. Here, theoretically optimal placement of feed points was derived using one-dimensional diffusion equations. The utility of optimal multipoint feeds was evaluated with mixing, pH control, and bioreaction simulations using three-dimensional compartment models of four industrially relevant bioreactors with working volumes ranging from 8 to 237 m^3. Dividing the vessel axially in equal-sized compartments and locating a feed point or multiple feed points symmetrically in each compartment reduced the mixing time substantially by more than a minute and mitigated gradients of pH, substrate, and oxygen. Performance of the large-scale bioreactors was consequently restored to ideal, homogeneous reactor performance: oxygen consumption and biomass yield were recovered and the phenotypical heterogeneity of the biomass population was diminished.

KEYWORDS
bioreactor, compartment model, feed point, industrial biotechnology, mixing time, scale-up

1 | INTRODUCTION

The transfer of a bioprocess from laboratory toward industrial scale would be relatively simple, if the large-scale reactors behaved exactly as the laboratory-scale reactors. However, the correspondence is far from perfect, which manifests itself as heterogeneity with respect to feed(s) (Bylund et al., 1998; Langheinrich & Nienow, 1999; Larsson et al., 1996; Xu et al., 1999) and insufficient oxygen transfer at the large scale (Oosterhuis & Kossen, 1984; Xu et al., 1999). For example, 10%–20% lower *Escherichia coli* biomass yields have been reported as a consequence in large-scale aerobic fed-batch processes (Bylund et al., 1998; Xu et al., 1999). Scale-up could be facilitated by improving the various modeling approaches to better estimate the large-scale behavior and the scale-up losses beforehand. As far as hydrodynamics are concerned, such predictive modeling is nowadays quite feasible with computational fluid dynamics (CFD) simulations of model fluids (water, air). However, the behavior of biomass is insufficiently known to be reliably predicted at a heterogeneous large scale. Another option would be to homogenize the large-scale reactor more efficiently to make it resemble the better-performing, more predictable small-scale reactors. This approach would have the advantage that both the bioreaction kinetics determined at the laboratory scale and the ideal homogeneous reactor model would retain their validity also at the larger scale.

Experiments suggest that feed point placement has a marked effect on mixing: feed at middle height mixes most rapidly and feed at the top most slowly (Alves et al., 1997; Cronin et al., 1994; Vrábel et al., 1999).

Correspondingly the substrate gradients are milder when the feed is brought to a bottom impeller instead of the stagnant top (Bylund et al., 1998; Larsson et al., 1996), a conventional choice. The use of multiple feed points has been suggested as well (Bylund et al., 1998; Cronin et al., 1994; Enfors et al., 2001; Larsson et al., 1996), and mixing indeed improves by appropriate placement of two feed points (Fu et al., 2005). The enhanced mixing has important consequences for bioreaction: yeast yields have been improved by placing the feed close to an impeller (Dunlop & Ye, 1990) or by using multiple feed points (Hansford & Humphrey, 1966). Numerical simulations have also shown similar improvements in both mixing and bioreaction upon relocating the feed from the top to vicinity of an impeller (Haringa et al., 2018; Morchain et al., 2014).

Upon considering multipoint feeds, the question is how they should be placed in a bioreactor for optimum performance. Literature suggests placement close to impellers or to otherwise well-mixed zones (Bylund et al., 1998; Cronin et al., 1994; Enfors et al., 2001; Larsson et al., 1996), but a general theoretically optimal placement is not defined. Earlier work on the subject relied on a brute-force search with case-specific compartment models (Fu et al., 2005), which suffers from exponential combinatorics as the number of feed points is increased. The aims of this work were to derive general and theoretically optimal feed point placements and to evaluate their relevance in mitigating the gradients found in large-scale bioreactors. The simple and general one-dimensional (1D) diffusion equation that has successfully described axial mixing in various high aspect ratio bioreactors (Kasat & Pandit, 2004; Kawase, 1989; Machon & Jahoda, 2000) was studied to deduce the optimal placements, and the effect of multiple optimally placed feed points on mixing and bioreaction was simulated in industrial-scale stirred tank and bubble column bioreactors with three-diemsnisonal (3D) compartment models.

2 | COMPUTATIONAL METHODS

2.1 | Reactor models

Four experimentally studied bioreactors were chosen from the literature for the numerical experiments. The reactors are listed in Table 1, and they cover industrially relevant stirred tanks and bubble columns with working volumes from 8 to 237 m^3 in different geometries and configurations with gas flow rates ranging from 0.085 to 0.98 vvm (vvm: volume flow rate of gas per volume of liquid per minute). Each reactor was simulated with a compartment model based on previously published modeling approaches. Figure 1 illustrates the used compartment models. Model details are given in Appendix A.

2.2 | Simulations

Three different situations were simulated in the large-scale bioreactors (Table 1) with the compartment models to evaluate the multiple feed point placements: (1) pulse addition of a tracer, (2) pulse of a pH-controlling alkaline agent, and (3) bioreaction with a Monod-type substrate consumption rate. The substrate concentration fields determined in case 3 were furthermore used to separately estimate the effects on dissolved oxygen concentration, substrate consumption, biomass yield, and adaptation of biomass-specific growth and substrate uptake rates. The model substrate was considered to be glucose. The bioreaction was simulated as a pseudosteady-state snap-shot (Hristov et al., 2001) of a fed-batch culture with the substrate consumption rate (g L^{-1} h^{-1})

$$r_S = q_S \frac{S}{S + K_S} X, \tag{1}$$

where q_S is the biomass-specific maximal substrate-consumption rate (g g^{-1} h^{-1}), S the substrate's concentration (g L^{-1}), K_S the affinity constant (g L^{-1}), and X the biomass concentration (10 g L^{-1}). The substrate feed rate was 4 g L^{-1} h^{-1} in the bioreaction simulations and it was modeled as a volumetric source in the compartment(s) closest to the feed coordinate(s). Table 2 lists the values for all kinetic parameters used in the simulations.

2.2.1 | Mixing time

Mixing times were simulated with various combinations of feed points by the pulse addition of a tracer. Tracer injection was always

TABLE 1 Modeled reactors

Reactor	T m	V m^3	H/T –	ϵ_G %	u_G cm s^{-1}	N_i –	D/T –	n rpm	References
Stirred tanks									
R4	2.09	23.8	3.33	5.90	0.923	4	1/3	115	Cui et al. (1996)
R1	2.00	8.17	1.30	0	0	1	2/9	60	Langheinrich et al. (1998)
Bubble columns									
B13	1.60	40.2	12.5	23.3	25.0				Schügerl (1993)
B6	3.70	237	5.95	17.0	6.50				Zahradník et al. (2001)

Note: Symbols: T, tank diameter; V, working volume; H, working height; ϵ_G, gas-holdup; u_G, superficial gas velocity at reactor's half-height; N_i, number of impellers; D, impeller diameter; n, stirrer speed.

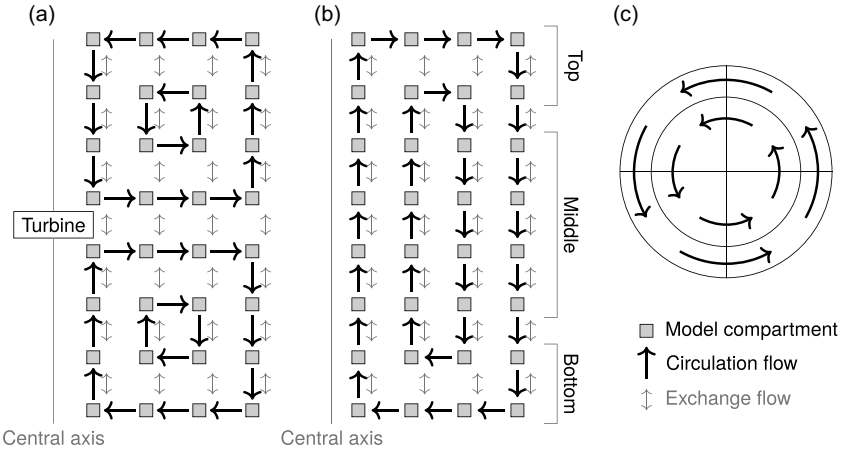

FIGURE 1 Compartment models. (a) Two square networks of nested loops (two in figure) composed the radial flow pattern induced by Rushton turbines in reactors R4 and R1. (b) The flow pattern in bubble columns was composed of a rectangular network of nested loops (two in figure). Axially adjacent compartments were connected by exchange flows in both reactor types. Conceptually the bubble column was composed of top, middle, and bottom parts such that the middle part contained only vertical circulation flows. (c) Tangentially adjacent compartments in stirred tanks were unidirectionally connected by circulation flows. In bubble columns, exchange flows were used instead of circulation flows.

initialized at the compartment(s) closest to the feed coordinate(s). To circumvent the effects of probe placement on mixing time (Cui et al., 1996), the simulated mixing times were defined in a global sense by monitoring the standard deviation of the dimensionless tracer concentration ($u = C/(V^{-1}\int_V C\,\mathrm{d}V)$) in the whole modeled volume V:

$$\sigma(t) = \sqrt{\int_V (1 - u(t))^2\,\mathrm{d}V}. \tag{2}$$

A 95% mixing time t_{95} is commonly determined in point-probe experiments (e.g., Cui et al., 1996; Vrábel et al., 1999), and here the threshold for simulated mixing time was similarly set to $\sigma(t_{95}) = 5\%$ despite the inherent differences in local and volume-based mixing time quantification. Unless explicitly stated otherwise, the presented (Equation 2) volume-based definition of mixing time is used.

A complementary measure of macromixing performance was obtained by calculating an inhomogeneity number (Mayr et al., 1992).

$$N_I = \sigma(t_{95}/2), \tag{3}$$

which is the median of the monotonously decreasing standard deviation in the mixing time interval $t \in [0, t_{95}]$. It is possible that two feed arrangements have practically identical mixing times t_{95}, but in such a scenario, the lower inhomogeneity number N_I implies more homogeneous reactor contents during the time interval and thus better mixing performance. Compared to the definition used by Mayr et al. (1992), standard deviation was used here instead of mean absolute deviation, the time interval's end was set to the mixing time threshold, and the median of deviation was calculated instead of the mean. Unlike the mean, the median is robust to the inevitable differences in initial conditions ($t = 0$), which are due to unequal feed compartment sizes within and across the modeled reactors.

2.2.2 | pH-control

The effect of feed points on pH-control (situation 2) was simulated with a 100 mmol L^{-1} carbonate buffer solution ($pK_a = 6.35$) initially at a pH of 4.8. A pulse of carbonate was then added to raise the overall pH to 6, and the evolution of pH was monitored for 10 s. The local pHs were calculated from the local carbonate concentrations $[CO_3^{2-}]$ as

$$pH = pK_a + \log_{10}\frac{[CO_3^{2-}]}{[HCO_3]}. \tag{4}$$

Owing to the pH's nonlinear definition, its volumetric mean was time-dependent even though the carbonate concentration's mean was not.

2.2.3 | Dissolved oxygen

The consumption of oxygen along with substrate was modeled only in R4 (experimentally determined oxygen transfer data not available for others) by setting the dissolved oxygen consumption rate (mg L^{-1} h^{-1}) to

$$r_O = Y_{OS}\frac{O}{O + K_O} r_S, \tag{5}$$

where Y_{OS} is the oxygen mass required for the aerobic consumption of a substrate (glucose) mass (g g^{-1}), O the dissolved oxygen concentration (mg L^{-1}), and K_O the affinity constant for oxygen (mg L^{-1}). Equation (5) implies that the aerobically respired proportion of substrate is $O/(O + K_O)$ of the total consumption. Oxygen was provided by oxygen transfer at a volumetric rate (mg L^{-1} h^{-1}) of

$$k_L a(O_e - O), \quad (6)$$

where the oxygen transfer coefficient was $k_L a$ = 180 h^{-1} as measured in the R4 reactor (Xu et al., 1999) at the same operating conditions as simulated here (115 rpm stirrer speed, 35°C temperature, 1.5 bar head-space pressure). To focus solely on the effect of feed point placement, oxygen was not modeled in the gas phase, but a homogeneous oxygen solubility O_e (mg L^{-1}) was assumed throughout the reactor (equal partial pressure of oxygen in the whole volume). The effect of hydrostatic and head-space pressures on the overall oxygen solubility was taken into account, however, and the spatially homogeneous equilibrium concentration of oxygen (O_e) was taken at the partial pressure of oxygen (21% of air) at the reactor's middle height (water density 994 kg m^{-3}). At the 35°C temperature, the dimensionless Henry's constant (concentration in liquid/concentration in gas) for oxygen was 0.0266 (Sander, 2015).

2.2.4 | Time-scale of substrate consumption

The local time-scales τ_S (s^{-1}) of substrate consumption were calculated by linearizing the substrate uptake rate (Equation 1) with respect to the substrate concentration ($r_S = S/\tau_S$) and taking the inverse of the first-order rate-pseudoconstant $1/\tau_S$:

$$\tau_S = \frac{S + K_S}{q_S X}. \quad (7)$$

TABLE 2 Kinetic parameters

Parameter	Value	Unit	Source
X	10	$g_X\ L^{-1}$	10; Morchain et al. (2014)
q_S	1	$g_S\ g_X^{-1}\ h^{-1}$	1.25; Xu et al. (1999)
			0.6356; Anane et al. (2017)
q_d	0.025	$g_X\ g_X^{-1}\ h^{-1}$	0.04; Xu et al. (1999)
			0.0129; Anane et al. (2017)
K_S	0.025	$g_S\ L^{-1}$	0.05; Xu et al. (1999)
			0.0370; Anane et al. (2017)
K_O	0.1	$mg_O\ L^{-1}$	0.1; Morchain et al. (2013)
Y_{XS}	0.5	$g_X\ g_S^{-1}$	0.51; Xu et al. (1999)
			0.49; Xu et al. (1999)
Y_{OS}	1.067	$g_O\ g_S^{-1}$	Stoichiometry
T_X	2.5	h	$1.25/(Y_{XS}q_S)$; Morchain and Fonade (2009); Morchain et al. (2013)
T_S	0.025	h	$0.01T_X$; Morchain et al. (2014)
$\Delta\mu$	0.05	$g_X\ g_X^{-1}\ h^{-1}$	$Y_{XS}q_S/10$
Δq	0.10	$g_S\ g_X^{-1}\ h^{-1}$	$q_S/10$
$k_L a$	180	h^{-1}	180; Xu et al. (1999)
O_e	12.69	$mg_O\ L^{-1}$	Estimated

Note: Symbols: X, biomass concentration; q_S, biomass-specific maximal substrate uptake rate; q_d, biomass-specific decay rate; K_S, substrate affinity constant; K_O, oxygen affinity constant; Y_{XS}, maximal biomass yield on substrate; Y_{OS}, oxygen demand of substrate; T_X, adaptation time-scale of growth; T_S, adaptation time-scale of substrate uptake; $\Delta\mu$, discretization of specific growth rate; Δq, discretization of specific substrate uptake rate; $k_L a$, oxygen transfer coefficient; O_e, oxygen solubility.

2.2.5 | Biomass yield

An instantaneous nonconstant biomass yield y_{XS} ($g\ g^{-1}$) was calculated by assuming a maximal yield Y_{XS} of biomass on the substrate and a first-order decay of biomass at a specific rate (h^{-1}) of q_d (similar to Anane et al., 2017; Xu et al., 1999):

$$y_{XS} = \frac{Y_{XS} r_S - q_d X}{r_S} = Y_{XS} - \frac{q_d}{q_S}\left(1 + \frac{K_S}{S}\right). \quad (8)$$

2.2.6 | Adaptation of biomass-specific rates

A population balance was used to simulate the adaptation of biomass-specific growth and substrate uptake rates similarly to Morchain et al. (2013, 2014). In short, the 10 g L^{-1} total biomass was conceptually divided into 10 classes, each with their own specific growth rate (h^{-1}) $\mu_i = Y_{XS}q_S(2i - 1)/20$, where $i \in 1, 2, ..., 10$. Each of the classes then represented the amount of biomass growing at the specific growth rate characteristic to the class. For example, if each of the 10 classes contained 1 g L^{-1} biomass, 10% of the whole population would grow at a rate of 0.025 h^{-1}, 10% at 0.075 h^{-1}, and so on, and the population's averaged specific growth rate would be 0.25 h^{-1}. The transfer rate ($g\ L^{-1}\ h^{-1}$) of biomass from class i was (Morchain et al., 2013, 2014)

$$\frac{X_i}{\Delta\mu}\left(\frac{1}{T_X} + \mu_i\right)\left\{Y_{XS}q_S\frac{S}{S + K_S} - \mu_i\right\}, \quad (9)$$

where X_i is the biomass concentration in class i ($g\ L^{-1}$), $\Delta\mu$ the difference in specific growth rate between adjacent classes (h^{-1}), T_X the time-scale of growth rate adaptation (h^{-1}) as defined by Morchain and Fonade (2009) and Morchain et al. (2013), and μ_i the specific growth rate of class i (h^{-1}). The term $Y_{XS}q_S S/(S + K_S)$ represents the equilibrium growth rate (h^{-1}) defined by the local environment (Morchain et al., 2013, 2014). With a positive adaptation rate (Equation 9), the class i's biomass was transferred to the class above (i + 1) and with a negative rate to the class below (i − 1). In total, the population tries to adapt toward the equilibrium growth rate (all of the biomass at the two classes closest to equilibrium), but the heterogeneity of local substrate concentrations results in a distribution of growth rates (Morchain et al., 2013, 2014).

The distribution of specific substrate uptake rate ($g\ g^{-1}\ h^{-1}$) was modeled similarly to the specific growth rate (Equation 9) but with classes $q_i = q_S(2i - 1)/20$ ($i \in 1, 2, ..., 10$), class discretization Δq ($g\ g^{-1}\ h^{-1}$), time constant T_S (h^{-1}) as defined by Morchain et al. (2014), and equilibrium term $q_S S/(S + K_S)$ ($g\ g^{-1}\ h^{-1}$). Further details of the population balance methodology can be found in the works of Morchain et al. (2013, 2014).

2.3 | Software

`Python3.8.5` language (www.python.org) and the packages `scipy1.5.2` (Virtanen et al., 2020), `numpy1.19.2` (Harris et al., 2020), and `pandas1.1.3` (McKinney, 2010; The Pandas Development Team, 2020) were used for all calculations and simulations. Mixing times reported in the literature were recovered from the published figures with WebPlotDigitizer (Rohatgi, 2020).

2.4 | Numerical methods

The initial value problems (mixing time and pH) were solved with the BDF-method (backward differentiation formula) of the `scipy.integrate` module. The fed-batch steady-states (bioreaction) were solved by integration with the backward Euler method using constant time steps until the steady state was reached. The step vectors were solved from analytically calculated Jacobians with the stabilized biconjugate gradient algorithm (`bicgstab` in `scipy.sparse.linalg`). Ideal homogeneous reactor results were used as initial guesses for the large-scale fed-batch simulations.

3 | THEORETICAL ASPECTS

3.1 | 1D diffusion equations

Feed point placement was analyzed separately in the axial, radial, and tangential dimensions by using 1D diffusion equations:

$$\frac{\partial u}{\partial t} = d\frac{\partial^2 u}{\partial z^2}, \tag{10}$$

$$\frac{\partial u}{\partial t} = d\left(\frac{1}{r}\frac{\partial u}{\partial r} + \frac{\partial^2 u}{\partial r^2}\right), \tag{11}$$

$$\frac{\partial u}{\partial t} = d\frac{1}{r^2}\frac{\partial^2 u}{\partial \phi^2}, \tag{12}$$

respectively, as models of macromixing. In Equations (10–12), u is the injected substance's dimensionless concentration normalized by the injected quantity to yield a spatial mean of 1, t time (s), d turbulent diffusivity ($m^2\ s^{-1}$) assumed to cover all forms of transport, z axial coordinate (m), r radial coordinate (m), and ϕ tangential coordinate. The domains were $[0, H]$ for axial, $[0, R]$ for radial, and $[0, \Phi]$ for tangential, where H is the height (m), R the radius (m), and Φ the cylindrical sector ($0 < \Phi \leq 2\pi$) of the modeled volume. Each of the three domains was insulated (zero-gradient, symmetry) with no mass transfer across the boundaries. The axial and radial dimensions were solved with a point-addition of feed at z_0 or r_0 as the initial condition. In general, the tangential dimension should be solved with a periodic boundary, but setting the feed pulse to the domain's middle and using the symmetry boundary conditions is equivalent and in the context of this work more convenient. Therefore, the tangential dimension was solved with closed boundaries and the feed pulse at $\phi_0 = \Phi/2$. Only $\Phi = 2\pi$ (whole cylinder) and integer fractions thereof are valid tangential domains owing to the symmetry boundaries.

The diffusion equations are analogous to transient heat conduction in insulated domains, and their solutions can be found, for example, in heat transfer textbooks (e.g., Cole & Beck, 2010). In each of the three dimensions, the time-dependent concentration relative to equilibrium after a pulse addition of feed is a series, whose time-dependent terms decay exponentially:

$$u_x = 1 + \sum_{m=1}^{\infty} A_{xm}\exp(-k_{xm}t). \tag{13}$$

The pre-exponential terms A_{xm} are

$$A_{zm} = 2\cos\left(m\pi\frac{z_0}{H}\right)\cos\left(m\pi\frac{z}{H}\right), \tag{14}$$

$$A_{rm} = \frac{J_0(\beta_m r_0/R)J_0(\beta_m r/R)}{(J_0(\beta_m))^2}, \tag{15}$$

$$A_{\phi m} = 2\cos(m\pi)\cos\left(2m\pi\frac{\phi}{\Phi}\right), \tag{16}$$

in the axial, radial, and tangential dimensions, respectively. J_0 in Equation (15) is the zeroth-order Bessel function of the first kind and β_m is the mth root of the first-order Bessel function of the first kind. The respective axial, radial, and tangential first-order rate constants k_{xm} are

$$k_{zm} = m^2\pi^2\frac{d}{H^2}, \tag{17}$$

$$k_{rm} = \beta_m^2\frac{d}{R^2}, \tag{18}$$

$$k_{\phi m} = 4m^2\pi^2\frac{d}{\Phi^2 r^2}. \tag{19}$$

It is worth noting that the 1D tangential solution depends also on the radial coordinate through Equation (19). In general, the radial and tangential domains are interconnected, but they were studied separately here.

3.2 | Axial placement of a single feed point

Given that the macromixing limitations in typical high aspect ratio bioreactors exist predominantly in the axial direction (Cronin et al., 1994; Vasconcelos et al., 1995), the optimal placement of a single feed point was first studied by analyzing the axial diffusion equation. The first term in the series (Equation 10) dominates the solution's long-term behavior and thus the mixing time through $t_{95} \sim 1/k_{z1}$ (Kawase, 1989), as the rest of the terms decay exponentially faster (m^2 in rate constants, Equation 17). The factor $\cos(m\pi z_0/H)$ in the pre-exponentials (Equation 14) suggests that placing the feed at the middle ($z_0/H = 0.5$) would remove the solution's first, rate-limiting term as the relation $\cos(0.5m\pi) = 0$ holds with all odd m. The solution's next limiting term would then be the second term ($m = 2$)

associated with a four-fold rate constant $k_{z2} = 2^2 k_{z1}$. According to the model, placing the feed at the center $z_0 = 0.5H$ instead of the top $z_0 = H$ (or bottom $z_0 = 0$) improves macromixing substantially by reducing the mixing time to a quarter of the original.

Figure 2 shows how the feed point's position along a reactor's working height affects macromixing according to the 1D axial diffusion equation. Three cases were considered with experimental data available for comparison: (1) The effect of feed location on global mixing time defined in Section 2.2.1 (Cronin et al., 1994). (2) The effect of measurement position on locally measured mixing time while injecting the tracer at the top (Vrábel et al., 1999). Local measurement and injection positions are interchangeable (z and z_0 in Equation 14). (3) The effect of injection position in both turbulent and transition (impeller Reynolds number $Re_i = 250$) regimes while measuring the mixing time at the bottom (Alves et al., 1997). The cited experiments covered in total 28 injection or measurement positions in working volumes ranging from 59 L to over 20 m^3 stirred with two to four impellers. The experiments suggested that the center ($z_0 = 0.5H$) is superior to the top or bottom. The rest of the injection positions resulted in a funnel-like distribution of mixing times around the optimal center. A similar axial distribution was predicted by the diffusion equation as well. Owing to its simple and spatially homogeneous nature, the model was incapable of predicting the asymmetry that was present in some of the experimental data, which was due to the stagnant flow close to the liquid surface (Cronin et al., 1994). The good agreement found between the predictions and literature data suggests that the simple diffusion equations could be used to predict the effect of feed placement.

3.3 | Axial placement of multiple feed points

Motivated by both the marked potential of correct feed placement in reducing the mixing time and the predictive power of the axial diffusion equation, the axial placement of multiple feed points was analyzed next. As the first-order rate constants of the axial equation are inversely proportional to the reactor's working height squared, H^2, any reduction in height would greatly increase the mixing rate (i.e., decrease the mixing time) if the turbulent diffusivity d remained constant ($k_{zm} \sim d/H^2$, Equation 17). Likewise, increasing the diffusivity would improve the rate in a given geometry. However, decreasing the actual working height is impractical and a greater diffusivity would require a higher power input (Kawase, 1989). How could this square relationship then be exploited without changing the reactor's geometry or the stirrer's power? The symmetry or zero-gradient boundaries of the model equation (Section 3.1) imply that placing N feed points symmetrically across the whole height at axial positions of

$$\frac{z_i}{H} = \frac{2i - 1}{2N} \quad i = 1, 2, \ldots, N, \tag{20}$$

divides the working height into N equally sized compartments having a height of H/N each. As the height is replaced by H/N in Equation

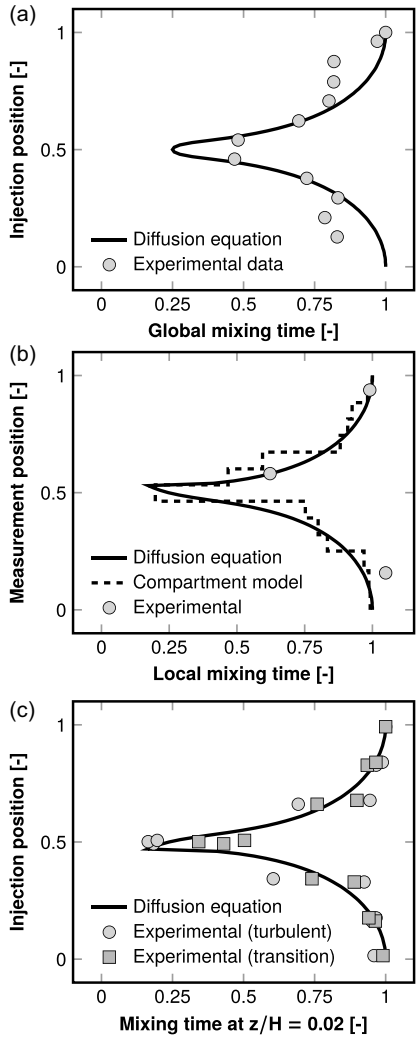

FIGURE 2 Effect of single feed point placement on mixing times. Both the experimental and modeled mixing time profiles have been normalized by the respective values found at the top (vertical axis 1) and the axial positions by the working height. Diffusion equation refers in each panel to the one-dimensional axial diffusion equation defined in Equations (10), (13), (14), and (17). (a) The tracer injection point was varied and the global mixing time (Section 2.2.1) was measured. The 12 decolorization experiment data points are from a 600 L stirred tank with two impellers (Cronin et al., 1994). (b) The tracer injection point was kept at 94% of working height and the local mixing time was determined across the height. The three experimental data points are from an over 20 m^3 aerated tank stirred with four impellers (Vrábel et al., 1999) and the compartment model predictions are from the same study. (c) The measurement point was kept at 2% of working height and the local mixing time was measured as a function of the tracer injection position. The 13 experimental data points are from a 60 L stirred tank with three impellers both in turbulent and transition (impeller Reynolds number $Re_i = 250$) flow regimes (Alves et al., 1997).

(17), the limiting rate constant increases in proportion to N^2: two symmetrically placed feed points multiply the mixing rate by 4 and three points by 9. Compared with a single feed at the top, four ideally placed feed points multiply the rate in theory by 64 (4×4^2). Figure 3a illustrates the optimal axial placement of feed points (Equation 20). Interestingly, a similar symmetry is often used in the placement of multiple impellers.

3.4 | Radial-tangential placement

In bubble columns and lower aspect ratio single-impeller stirred tanks, the radial and tangential dimensions may also limit the overall rate of mixing. As with the axial dimension, the respective 1D diffusion equations reveal optimal feed placement in the radial-tangential plane. Both the use of (1) only one or (2) two or more radial coordinates need to be considered.

For case 1 (single radial coordinate), the optimal radial-tangential placement is found analogously to the single- and multipoint axial placements: The first ($m = 1$) radial term is eliminated by finding the radial feed point that satisfies the condition

$$J_0\left(\beta_1 \frac{r_0}{R}\right) = 0, \tag{21}$$

which yields $r_0/R \approx 0.628$ (see Equation 15). The new limiting radial term ($m = 2$) is then associated with a $(\beta_2/\beta_1)^2 \approx 3.35$ fold rate. Placement of multiple feed points in the tangential dimension behaves in the same way as in the axial dimension: placing N feed points symmetrically across the whole tangential domain divides the effective domain size by N and multiplies the limiting rate constant by N^2. As conclusion, the feed points should be placed symmetrically at approximately 63% radius around the whole reactor. Figure 3b illustrates the optimal radial-tangential placement of feed points with one radial coordinate.

Considering two or more radial coordinates (case 2), the radial pre-exponentials (Equation 15) have the useful property that the Nth pre-exponential has exactly N roots at the interval $r_0 \in [0, R]$. The Nth radial term remains zero when the N radial feed coordinates r_i satisfy the condition

$$J_0\left(\beta_N \frac{r_i}{R}\right) = 0, \quad i = 1, 2, ..., N, \tag{22}$$

which yields optimal feed coordinates r_i at

$$\frac{r_i}{R} = \frac{\alpha_i}{\beta_N}, \tag{23}$$

where α_i is the ith root of J_0. The remaining limiting lower-order terms ($m < N$) are then eliminated by assigning the radial feed points

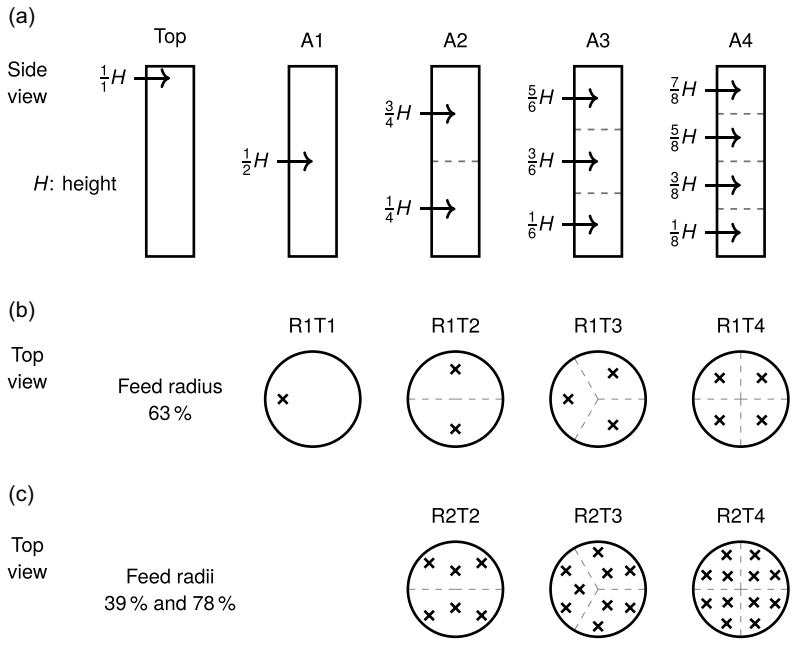

FIGURE 3 Optimal placement of multiple feed points. (a) Axial domain should be divided (dashed lines) into equal subdomains with a centrally placed feed point in each. The arrows represent the feed positions relative to the liquid height. (b) Given one radial coordinate the feed points should be placed symmetrically across the perimeter of 63% radius. (c) With two radial coordinates, the inner 39% radius receives one symmetrically placed feed point per subdivision and the outer 78% radius two symmetrically placed feed points per subdivision. A feed arrangement AxRyTz is composed of the radial-tangential pattern RyTz at every axial position of Ax.

r_i appropriate weights w_i, which are found from the linear system of equations

$$\begin{bmatrix} J_0(\beta_1 r_1/R) & J_0(\beta_1 r_2/R) & \cdots & J_0(\beta_1 r_N/R) \\ J_0(\beta_2 r_1/R) & J_0(\beta_2 r_2/R) & \cdots & J_0(\beta_2 r_N/R) \\ \vdots & \vdots & \ddots & \vdots \\ J_0(\beta_{N-1} r_1/R) & J_0(\beta_{N-1} r_2/R) & \cdots & J_0(\beta_{N-1} r_N/R) \\ 1 & 1 & 1 & 1 \end{bmatrix} \begin{bmatrix} w_1 \\ w_2 \\ \vdots \\ w_N \end{bmatrix} = \begin{bmatrix} 0 \\ 0 \\ \vdots \\ 1 \end{bmatrix}. \tag{24}$$

With two feed points, the optimal feed coordinates are 34.4% and 78.7% of radius weighted in proportions of approximately 1 : 2.31. The weighting can be implemented by using multiple tangential coordinates with equal flow rates on a given radial coordinate or by setting nonuniform feed flow rates in proportion to the weights. However, to retain equal tangential rate constants in the different radial positions, the outer radial coordinates require more feed points than the inner ones to keep equal perimeters Φr in Equation (19). Equal rate constants are preserved if the number of feed points at the different radii is proportional to the radii themselves. For example, a radius of 2 units would require twice the number of tangential feed points used at a radius of 1 unit. Satisfying the optimum criteria for both the radial and tangential dimensions simultaneously is difficult, but a reasonable compromise can be obtained by rounding the radial coordinates close to the actual optima such that integer ratios are obtained. As conclusion, the feed points ought to be placed at concentric circles around the reactor. The circle radii are to have integer ratios and the number of symmetrically placed feed points in the circles are to follow the same integer ratios. Figure 3c illustrates a near-optimal radial-tangential placement with two radial coordinates 39% and 78% of radius, which have been rounded from the optimal 34.3% and 78.7%.

4 | RESULTS

The large-scale bioreactor simulations were carried out with a single top feed for reference and with nine optimal (Sections 3.2–3.4) feed arrangements AxRyTz, where *x*, *y*, and *z* refer to the number of axial, radial, and tangential coordinates, respectively. 1, 2, or 4 axial coordinates (A1, A2, and A4, respectively) with a single feed point (R1T1), two feed points (R1T2), or six feed points (R2T2) each were used in the optimal feed arrangements, which are illustrated in Figure 3.

4.1 | Mixing

The mixing times and inhomogeneity numbers resulting from all tracer simulations are compiled in Table 3. As an illustration of the improvements attained by optimal feeds, Figure 4 shows both the time evolution of the tracer concentration's standard deviation and the inhomogeneity numbers (median standard deviation in the mixing time interval) in reactor B13 with representative feed arrangements. The time-evolution of standard deviation was similar also in the other reactors (Supporting Information: Figure S1). With the typical single feed at the top the simulated mixing times were over 100 s in each of the four reactors. The mixing times were reduced to less than half of the original in reactors R4 and B13 when the single feed point was placed at the middle height (feed arrangement A1R1T1). In R4, the central placement resulted in a four-fold mixing rate (mixing time a quarter of the original) as predicted in Section 3.2, but the B13's slightly over two-fold rate did not reach the prediction. In reactors R1 and B6, the mixing rates relative to the top feed were modest at 1.2- and 1.1-fold, respectively. However, the central placement reduced the inhomogeneity numbers at least to 85% and at best to 57% relative to the top feed in reactors R1, B13, and B6 with the under four-fold mixing rates.

Upon employing multiple feed points at the middle height (A1R2T2), mixing in the high aspect ratio bubble column B13 reached the predicted four-fold rate relative to the top feed. Similarly to B13, the lower aspect-ratio bubble column B6 was mixed with an almost three-fold rate. The mixing rate in reactor R1 increased to 1.6-fold relative to the top feed. The feed arrangement A1R2T2 reduced the inhomogeneity numbers to 47% and 53% in reactors R1 and B6, respectively, where the predicted four-fold rate was not met.

Incrementing axial feed coordinates (feed arrangements A2RyTz and A4RyTz) diminished the mixing times further in each reactor. The absolute improvements were considerable: considering the top feed as a starting point, the mixing time was reduced by more than a minute in each reactor. The multi-impeller stirred tank R4 achieved even the 16-fold mixing rate predicted in Section 3.3 with two axial coordinates (A2R2T2), but in the other reactors, the relative improvements did not meet the prediction. Surprisingly four axial coordinates (A4RyTz) resulted in longer mixing times than two (A2RyTz) in R4. A substantial 16-fold mixing rate relative to the top feed was attained also in B13 with the feed arrangement A4R2T2. The inhomogeneity numbers were reduced further in each reactor when multiple axial coordinates were utilized. With the A4RyTz feed arrangements, the inhomogeneity numbers were diminished even down to 34%, 45%, 26%, and 49% in reactors R4, R1, B13, and B6, respectively.

4.2 | Concentration gradients

All pH-control and bioreaction simulation results with 10 g L^{-1} biomass concentration are compiled in Table B1. Similarly to the mixing time simulations, the addition of feed points resulted in more homogeneous behavior of the reactors. The volumetric standard deviation of each simulated variable or quantity was reduced, and the volumetric means approached the value found in an ideal homogeneous reactor. With multiple feed points, the reactors R4 and B13 approximated the ideal homogeneous reactor more closely than the reactors R1 and B6.

Considerable gradients in pH and substrate and dissolved oxygen concentrations were found in each reactor when the feed was at the

TABLE 3 Mixing times and inhomogeneity numbers in reactors R4, R1, B13, and B6 with top feed and optimal multipoint feeds

	R4		R1		B13		B6	
Feed	t_{95}/s	N_I	t_{95}/s	N_I	t_{95}/s	N_I	t_{95}/s	N_I
Top	154	0.263	141	0.404	103	0.297	135	0.387
A1R1T1	36.4	0.268	120	0.343	45.2	0.169	122	0.307
A1R1T2	36.5	0.267	97.3	0.206	45.1	0.150	58.0	0.344
A1R2T2	36.5	0.272	88.5	0.188	26.0	0.380	49.4	0.207
A2R1T1	13.6	0.219	109	0.289	31.4	0.188	123	0.309
A2R1T2	12.9	0.127	77.5	0.196	28.8	0.087	52.9	0.301
A2R2T2	9.01	0.250	55.8	0.172	12.8	0.259	28.5	0.208
A4R1T1	16.9	0.145	110	0.294	29.2	0.205	122	0.307
A4R1T2	16.6	0.090	77.8	0.183	23.9	0.077	52.5	0.295
A4R2T2	17.8	0.103	64.5	0.182	6.36	0.225	26.2	0.188

Note: The feed arrangements AxRyTz contain *x* axial, *y* radial, and *z* tangential coordinates (Figure 3). Symbols: t_{95}, mixing time; N_I, inhomogeneity number.

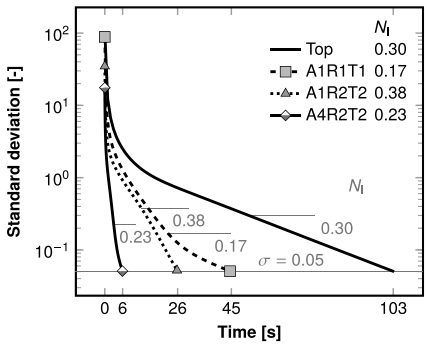

FIGURE 4 Standard deviation of dimensionless tracer concentration in reactor B13 after tracer pulse with top feed and various optimal multipoint feeds. The feed arrangements AxRyTz contain *x* axial, *y* radial, and *z* tangential coordinates (Figure 3). The 5% line is the threshold for mixing time. The horizontal lines represent the inhomogeneity numbers N_I (median standard deviations in the mixing time interval). Note the logarithmic scaling of the vertical axis.

top. The pH and concentration of substrate was always the highest close to the top feed point and lowest at the bottom of the reactor. In contrast, the concentration of dissolved oxygen was lowest in the top feed zone and highest away from it. Multiple feed points displayed the same patterns: pH and substrate concentration remained the highest and dissolved oxygen concentration the lowest in the vicinity of the feed points. However, both the highs and lows in pH and concentrations were brought closer to the mean when multiple feed points were in use. Figure 5 illustrates this by showing the substrate and oxygen gradients and how they were mitigated by the addition of feed points in reactor R4. The substrate gradients were of similar nature in the other reactors as well (Supporting Information: Figures S2–S4), and the pH gradients 10 s after the carbonate pulse (Supporting Information: Figure S5) were similar to the substrate gradients. In each reactor, the magnitude of the gradients seemed to correlate with the mixing times and standard deviations shown in Tables 3 and B1, respectively. In reactors R4 and B13, there were virtually no gradients of substrate, oxygen, and pH left with the multipoint feed arrangements A2R2T2 and A4R2T2. In reactors R1 and B6, the gradients were not entirely removed by the multipoint feeds, but their magnitude was reduced.

Figure 6 shows the volume distribution of pH in the reactor R1 10 s after pH correction pulse, and the distributions were similar in the other reactors (Supporting Information: Figure S6). The volume distributions of substrate and dissolved oxygen concentration were similar (Figure 7) to the pH distributions: the top feed resulted in broad distributions centered relatively far away from the ideals, and multiple feed points narrowed the distributions and centered them closer to the ideals. The spread (broadness) of the volume distributions is quantified by the volumetric standard deviations shown in Table B1. Likewise, the deviation of volumetric means from the ideal reactor values in Table B1 represents how far from the ideal the distributions were centered.

The bioreaction simulations were carried out also with a higher, X = 50 g L^{-1}, biomass concentration, and the results are compiled in Supporting Information: Table S1. Overall the gradients were steeper in each case than with the lower 10 g L^{-1} biomass concentration, and similarly, the use of multiple optimally placed feed points mitigated the gradients substantially (Supporting Information: Figure S7). Interestingly, the substrate gradients were so severe in each reactor with the top feed that the overall biomass yield was negative, which indicates that the simulated 50 g L^{-1} biomass was higher than what would actually have been achievable with the given biomass yield definition (Equation 8). In reactors R4 and B13, the feed arrangement A4T2T2 recovered a positive biomass yield and thus the feasibility of the 50 g L^{-1} biomass concentration (Supporting Information: Table S1).

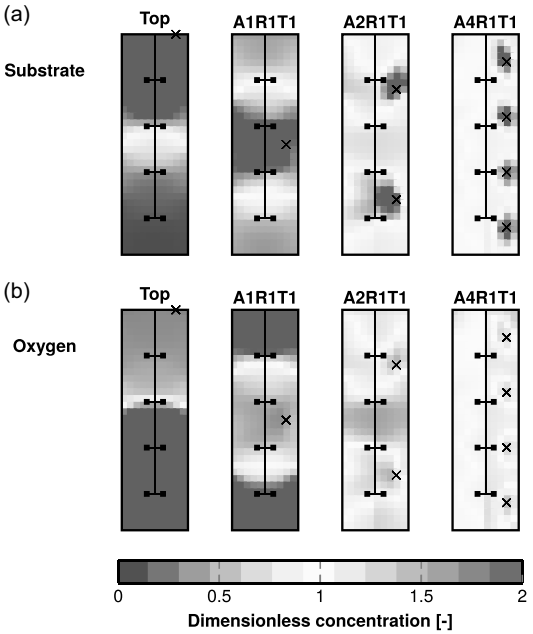

FIGURE 5 Simulated concentration of substrate (a) and dissolved oxygen (b) in reactor R4 with 10 g L^{-1} biomass concentration and a 4 g L^{-1} h^{-1} substrate feed rate at the top or through an optimal multipoint feed. The concentrations have been normalized by respective concentrations (substrate 16.7 mg L^{-1}, oxygen 0.113 mg L^{-1}) calculated in an ideal homogeneous reactor at the same conditions. Note the color scale limits (values above twice the ideal reactor value are shown as 2). The feed arrangements AxR1T1 contain x axially distributed feed points (Figure 3).

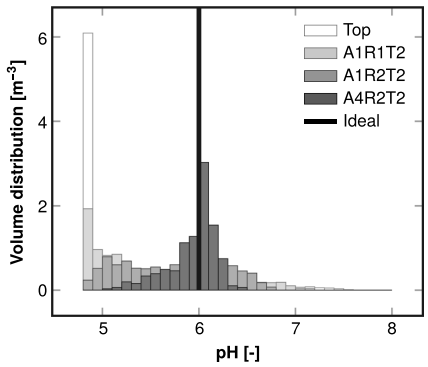

FIGURE 6 Distribution of pH in reactor R1 10 s after pH-correcting pulse of carbonate in a 100 mmol L^{-1} carbonate buffer solution initially at a pH of 4.8. Responses to top and optimal multipoint pulses are shown. Ideal homogeneous reactor behavior is shown for reference (whole volume has pH 6). The feed arrangements AxRyTz contain *x* axial, *y* radial, and *z* tangential coordinates (Figure 3).

4.3 | Adaptation of biomass

Figure 8 shows representative distributions of biomass-specific growth and substrate uptake rates simulated in reactor B13 with a 10 g L^{-1} biomass concentration. The results were similar in the other reactors as well (Supporting Information: Figures S8–S10). The top feed produced broad specific growth and uptake rate distributions (biomass distributed to several classes), but the use of multiple feed points narrowed them toward the ideal (biomass in two classes). The specific growth rate's distribution was spatially homogeneous even with the top feed with only minimal volumetric standard deviation in the biomass classes. In contrast, the uptake rate's distribution was spatially heterogeneous even when multiple feed points were used. However, the standard deviations relative to the respective means were decreased by the use of multiple feed points. The spread of the distributions correlated with the standard deviations shown in Table B1. With the higher X = 50 g L^{-1} biomass concentration, the trends were the same but the distributions were centered to classes with lower specific rates (Supporting Information: Figure S11). It should be remembered that the equilibrium growth rates used in determining the growth rate distributions were calculated with a constant biomass yield (no biomass decay).

5 | DISCUSSION

5.1 | Mixing

Notable improvements in bioreactor mixing were realized in the simulations with the feed arrangements derived in Section 3. Both R4 and B13 achieved mixing times of 10 s (Table 3), which are common in laboratory-scale reactors (Delafosse et al., 2014). In each reactor, the mixing rates were more than doubled (mixing time half of the original) relative to the common top feed setting. These reductions in mixing time can be given context by considering alternative ways to achieve them. Single- and multi-impeller stirred tank and bubble column mixing time correlations state that the mixing time is related to specific power input by $t_{95} \propto (P/(\rho V))^{-1/3}$ (Kawase, 1989; Magelli et al., 2013). A doubled mixing rate would require an 8-fold specific power, and the over 10-fold improvements simulated in R4 and B13 would demand infeasible, over 1000-fold power inputs. Another way to highlight the effect of feed point number and placement is to consider how much smaller a volume would have the same mixing time with the same specific power without feed optimization. The same correlations imply that under constant specific power, the mixing time is related to reactor diameter by $t_{95} \propto T^{2/3}$ and thus to volume by $t_{95} \propto V^{2/9}$. The more than doubled mixing rates achieved in each reactor would then demand an over 20-fold reduction in volume, and the 10-fold mixing rates observed in R4 and B13 correspond to mixing $10^{-9/2} \approx 1/31600$-fold volumes. As far as the macromixing time is concerned, the optimal feed arrangements figuratively scaled the simulated large-scale reactors down to a laboratory scale. Furthermore, the inhomogeneity numbers were

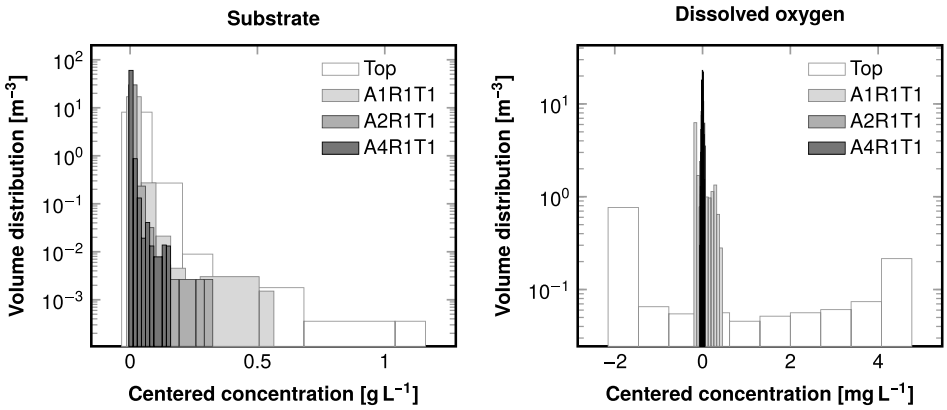

FIGURE 7 Distribution of substrate (left) and dissolved oxygen (right) in reactor R4 with 10 g L^{-1} biomass concentration and a 4 g L^{-1} h^{-1} substrate feed rate at the top or through an optimal multipoint feed. The substrate distributions were similar in the other reactors as well (not shown, for visual comparison, see Figures 5 and Supporting Information: Figures S2–S4). The concentrations have been centered by respective mean concentrations such that the mean of each shown distribution is 0. The feed arrangements AxRyTz contain *x* axial, *y* radial, and *z* tangential coordinates (see Figure 3). Note the logarithmic scaling of the vertical axis.

FIGURE 8 Simulated distribution of biomass-specific growth (a) and substrate uptake (b) rates in reactor B13 with 10 g L^{-1} biomass concentration and a 4 g L^{-1} h^{-1} substrate feed at the top or through an optimal multipoint feed. The two highest classes with only negligible biomass are not shown. The error bars represent volumetric standard deviations. The feed arrangements AxRyTz contain *x* axial, *y* radial, and *z* tangential coordinates (Figure 3). The ideal homogeneous reactor results are shown for reference.

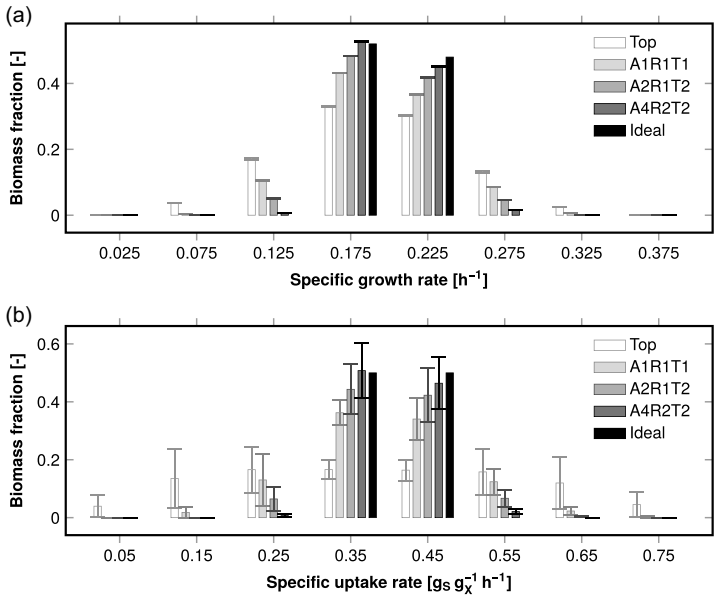

overall reduced in each reactor as the number of feed points was increased, which implies a lesser degree of heterogeneity in the reactor during the mixing time interval even when the mixing times were not considerably shortened by the addition of feed points.

It is necessary to remember, though, that the simulated mixing time improvements may have been greater than what could be obtained in practice, but experiments in pneumatically agitated reactors have confirmed that 2.9- to 6.6-fold mixing rates are feasible by appropriate placement of only two feed points (Fu et al., 2005). For comparison, the feed arrangements A1R1T2 and A2R1T1 with two feed points achieved 2.2- and 3.2-fold rates, respectively, in the bubble column B13. Another point of concern might be that the simulations were based on models that have been validated with water as the working fluid instead of viscous and potentially non-Newtonian fermentation broths. In general, the flow conditions in a bioreactor may enter the transition regime between laminar and turbulent flow owing to the broth's viscosity. However, as was shown in Figure 2c, the axial placement of a single feed point affects mixing

in a viscous model fluid in transition regime (Re_i = 250) in almost the same way as in water in turbulent regime (Alves et al., 1997). The experimentally observed trend of axial placement was similar to the diffusion model's prediction in both cases. Similarly, a 1D compartment model structure (discretization of a 1D diffusion equation) can describe multi-impeller bioreactor mixing even in the transition regime with Re_i down to 400 (Vasconcelos et al., 1996). Considering also that the main resistance to mixing in multi-impeller bioreactors occurs at the boundaries between impeller regions (Cronin et al., 1994; Vasconcelos et al., 1995), where the exchange flow begins to diminish markedly as Re_i decreases below 10,000 (Vasconcelos et al., 1996), the use of multiple axial feed coordinates can be expected to be highly beneficial also in the transition regime relevant to many fermentations as the main axial flow barriers are circumvented. Given that mixing in real fermentation broths is relatively little studied and quantified, some uncertainty with respect to actual fermentations persists when using models validated with model fluids. This same concern would have applied equally for hydrodynamically more sophisticated, CFD-based simulations as well.

Some of the feed arrangements performed as predicted in Section 3, but others fell short of the ambitious expectations. The bubble column B13's initial deviation from A1R1T1 (single point at the middle height) prediction was understandable since the axial diffusion model (Equation 10) assumed homogeneity in the radial and tangential dimensions, and bubble columns with substantial gas flow are generally rather heterogeneous radially (Degaleesan et al., 1997). With multiple feed points at the middle height (A1R2T2), the assumed radial-tangential homogeneity was re-established sufficiently and B13 was mixed with the expected four-fold rate. The B6 bubble column did not quite achieve the four-fold rate, though, which was likely due to the column's large diameter (3.7 m) and cross-section's insufficient coverage by the studied radial-tangential placements. Adding further radial or tangential feed coordinates might have resulted in the expected four-fold rate. In the bubble columns (B13 and B6), a large circulation current spanned the whole vessel contributing to deviations from the 1D diffusion models. Furthermore, the feed placement derivation could not account for the uneven distribution of liquid and gas within the bubble columns. It seems, therefore, that two or more radial and tangential coordinates should be used in both bubble columns and stirred tanks with high gas flow rates leading to impeller flooding and bubble column resembling flow fields (Alves & Vasconcelos, 1995; Machon & Jahoda, 2000). The R1's discrepancy between prediction and simulation is readily explained by the reactor's configuration: in a single-impeller vessel with a low aspect ratio, the overall mixing is not limited in the same way by axial exchange between impeller regions like in high aspect ratio multi-impeller vessels. Consequently, the simple diffusion equation cannot be as predictive for the single-impeller vessel than for multi-impeller ones. Reactor R4 attained the predicted 4- and 16-fold rates with one and two axial feed coordinates, respectively, but fell short of the expectations thereafter. The axial diffusion equation with a single, global diffusivity parameter is most applicable at modeling a reactor as a whole. Therefore, as the number of axial feed points is increased, the equation is applied at smaller spatial scales where its suitability in modeling the reactor is eventually lost as it cannot include the effects of local advective flows or local differences in turbulence. Despite the fact that the ambitious predictions regarding the number of axial feed coordinates ($t_{95} \sim N^{-2}$) were not entirely met, the presented results imply that large-scale bioreactors could be homogenized effectively by employing the proposed multipoint feeds.

5.2 | Reactor performance

Performing a Taylor-expansion and spatial-averaging on the concave Monod-type substrate uptake expression leads to (Pulkkinen & Metzler, 2015)

$$\left\langle \frac{S}{S + K_S} \right\rangle = \frac{\langle S \rangle}{\langle S \rangle + K_S} - \frac{K_S \sigma_S^2}{(\langle S \rangle + K_S)^3} \tag{25}$$

where the spatial averaging is denoted by angle brackets $\langle\rangle$ and the substrate concentration's volumetric standard deviation by σ_S. Equation (25) shows that heterogeneity ($\sigma_S > 0$) in substrate concentration leads to a decrease in the overall substrate consumption rate, all else being equal. Therefore, more efficient mixing has the potential to increase the rate of Monod-type reactions. As the overall substrate consumption was 4 g L^{-1} h^{-1} (equal to feed rate) by definition in these fed-batch snap-shot simulations, Equation (25) implies that an increase in substrate concentration's standard deviation caused by the competition between reaction and mixing necessitates a corresponding increase in the reaction's driving force, the substrate's mean concentration. This trend is apparent in Table B1 and Supporting Information: Table S1: lower substrate concentration means were associated with lower standard deviations, and the same can be observed in the simultaneous decrease of both the mean and standard deviation of the substrate uptake's timescale. Similarly, higher mean dissolved oxygen concentration with top feeding was due to suboptimal capability to consume oxygen. Figure 5B and Supporting Information: Figure S8 reveal that with unoptimal top feeding, the concentration of oxygen was high only where substrate was limiting. Vice versa, oxygen concentrations were low where the substrate was abundant, that is, close to the feed. Volumetric means of substrate concentration, substrate consumption time-scale, and dissolved oxygen concentration were brought close to ideal homogeneous reactor values, which translates to the removal of the reaction mixing competition and restoration of ideal reactor performance in large reactors. Furthermore, the oxygen consumption capacity was improved by the more effective homogenization. With a higher 50 g L^{-1} biomass concentration, the substrate and oxygen consumptions' time-scales were lower and correspondingly, the competition between reaction, oxygen transfer, and mixing was more severe (Supporting Information: Table S1 and Figure S7). However, the volumetric means were still brought close to ideal by the proposed multipoint feeds even though a higher degree of heterogeneity remained (Supporting Information: Table S1). It needs

to be remembered, though, that the simulation method addressed only oxygen heterogeneity caused by the bioreaction. Other heterogeneity-contributing factors, that is, local differences in gas holdup, gas-phase concentrations, mass transfer coefficient, and hydrostatic pressure, were deliberately omitted to isolate the effect of substrate feeding. The simulations showed that the reaction's contribution to oxygen heterogeneity was removed by appropriate feeding.

Yield improvements with baker's yeast have been reported when feed points were added (Hansford & Humphrey, 1966) to a stirred tank reactor and when a single feed point was placed close to an impeller (Dunlop & Ye, 1990). In the $X = 10\ g\ L^{-1}$ simulations reported here, the ideal homogeneous reactor biomass yield was restored by the addition of feed points. In the $X = 50\ g\ L^{-1}$ simulations, the yields did not reach the ideal reactor values, but they were improved considerably nevertheless in each case. In reactors R4 and B13, a positive biomass yield was re-established (Supporting Information: Table S1) by the A4R2T2 feed arrangement, which indicated that the appropriate addition of feed points could increase the upper limit of biomass concentration that is achievable in a given reactor. Unlike in the referenced experiments, in the simulations presented here, the yield improvements were entirely due to macromixing improvements as micromixing was not modeled. However, more efficient macromixing should also enhance micromixing. Local mass-transfer preceding the substrate uptake by the cells is proportional to the difference between the bulk concentration and the local concentrations within the smallest turbulent eddies (Dunlop & Ye, 1990). Analogously to the pH distribution shown in Figure 6, insufficient mixing associated with the conventional top feed leads to substrate depletion in a large fraction of the total volume as is visualized in Figures 5A and Supporting Information: Figure S7. Regions with low bulk concentration are bound to suffer micromixing limitations as the driving force of mass-transfer, the concentration difference, is already exhausted. Restoring a homogeneous macroscale concentration field can then be expected to maintain the necessary, reaction-driving concentration difference between the bulk and the local. In stirred tanks, the micromixing time-scales can be further optimized by bringing the feed points closer to the impellers (Dunlop & Ye, 1990).

5.3 | Physiological consequences

One of the most often mentioned problems in bioreactor scale-up is the acetate production with *E. coli* (Eiteman & Altman, 2006; Enfors et al., 2001; Xu et al., 1999) due to anaerobic mixed acid fermentation, aerobic overflow metabolism, or both (Xu et al., 1999). The mechanisms behind both of these are related: too high a substrate concentration and uptake rate can exceed either the local oxygen availability or the cell's oxidative capacity. Accumulation of formate, a product of anaerobic metabolism, revealed the presence of anoxic regions in experiments conducted in the R4 reactor (Xu et al., 1999). Similarly, the simulated high substrate concentrations close to the top feed created locally high demands of oxygen, which resulted in oxygen depletion in the R4's upper part (Figures 5 and Supporting Information: Figure S7). Though not simulated here, the high substrate concentrations found close to the top feed could lead also to aerobic overflow (Szenk et al., 2017). Similar side-formation of ethanol is known with *Saccharomyces cerevisiae*. As could be anticipated, the simulations suggested two benefits in multipoint feeding: (1) High substrate concentrations were avoided, which should aid in preventing aerobic overflow. (2) Oxygen depletion was avoided, which ought to prevent anaerobic metabolism. Appropriate feeding may then aid in accomplishing one of the goals of fed-batch operations: avoidance of high substrate concentrations, which result in side-product formation and oxygen limitations.

Extremes of substrate, dissolved oxygen, dissolved carbon dioxide concentration, pH (Amanullah et al., 2001; Langheinrich & Nienow, 1999), and temperature, along other factors may stress the host organism and influence product formation. Microbial stress responses are activated when the cells are exposed to overly high concentration of substrate in the feed zone (Enfors et al., 2001; Schweder et al., 1999). In the pH control simulations, a small but nontrivial portion of the reactor's volume remained at a relatively high pH even 10 s after the pulse. Experimentally in the 8 m^3 R1 reactor, the addition of carbonate resulted in 0.6 unit pH excursions above the targeted value (Langheinrich & Nienow, 1999), which resembles what was simulated here. However, the experiments cannot be directly compared to the simulations owing to the different initial pH and buffer concentrations. Based on the simulation results, multipoint feeding should reduce the stress responses caused by poor mixing.

Cultivation history influences the culture's response to an excess of substrate or the presence of alternative substrates such as organic acid side-products (Brand et al., 2018; Enjalbert, 2015). Unlike chemical catalysts, cells monitor their surroundings and adjust themselves continuously. In a heterogeneous large-scale bioreactor, this leads to unnecessary back-and-forth switching of gene expression as the cells are constantly being exposed to different environments (Enfors et al., 2001; Schweder et al., 1999). Another consequence is that the population does not necessarily have the time to adapt to the changing conditions, which results in heterogeneity in the reactor's biological phase, the population of cells. Similarly to earlier simulations with the population balance methodology, both the growth and substrate uptake rate distributions were broad in a heterogeneous reactor (Morchain et al., 2014). Figures 8 and Supporting Information: Figures S8–S11 show how the efficient homogenization of the liquid phase also yielded a more homogeneously-responding population. It should be noted that the simulations presented here were conducted with a substrate concentration field that was not influenced by the population balance (one-way coupling as used by Pigou & Morchain, 2015). Including the effects of the population's substrate uptake rate adaptation on the substrate concentration field would have been more correct (Morchain et al., 2014), but due to the relatively low adaptation time-scale of the uptake rate this was not strictly necessary.

5.4 | Bioreactor control

Usually, the pH and dissolved oxygen tension within a bioreactor are measured by single or at most a few probes. With the typical top feed both of these quantities are expected to be quite heterogeneous in a large-scale reactor, which also has experimental evidence (Langheinrich & Nienow, 1999; Oosterhuis & Kossen, 1984). In such a situation, the sensors are no longer representative of the reactor as a whole. Indeed, in a large-scale aerobic *E. coli* fermentation experiment conducted in reactor R4, the two oxygen probes showed no oxygen limitations even though the measured formate accumulation implied that approximately 11% of the reactor should have been anoxic (Xu et al., 1999). The X = 10 g L^{-1} simulations (Table B1) with a top feed showed a relative standard deviation of 119% in dissolved oxygen concentration, whereas the multipoint feed A4R2T2 reduced the relative standard deviation even down to 8%. It is easy to observe in Figures 5B and Supporting Information: Figure S8B that a single oxygen tension probe cannot represent the whole reactor with the top and A1R1T1 feeds, whereas with the multipoint feeds, the whole reactor could be represented by a single probe quite reliably. Likewise a point-measurement of pH in a heterogeneous reactor might lead to faulty pH-control, where the control is activated or deactivated too soon or too late as the pH probe represents only its immediate vicinity (Langheinrich & Nienow, 1999). Table B1 shows that 10 s after the correcting pulse with the top feeding, the mean pH was over 0.5 pH units below the target in each reactor even though the carbonate pulse was exactly the amount required to achieve the desired pH of 6. Such a situation could lead to overapplication of pH correctives unless the delay caused by mixing is properly accounted for by the control algorithm or by multiple probes (Langheinrich & Nienow, 1999). With multipoint feeds A2R2T2 and A4R2T2, the mean pH after 10 s was within 0.06 pH units of target even in the slowly mixing R1 reactor. Such a situation is less prone to overdosage of correctives. Appropriate multipoint feeds should then result in more precise and efficient reactor control as the sensors would represent the actual conditions within the reactor more reliably across the whole working volume.

5.5 | Implementation

The diffusion model, these simulations as well as intuition suggest that distributing the feed evenly throughout the whole volume should lead to most efficient mixing. This is in accordance with the suggestions of placing an inlet at each impeller or to multiple well-mixed zones (Cronin et al., 1994; Enfors et al., 2001; Fowler & Dunlop, 1989; Larsson et al., 1996). Extending the diffusion equation-derived feed placements shown in Figure 3 would eventually lead to a homogeneous and full coverage of the entire working volume. A simple way to achieve a thorough distribution of feed into the whole volume might be based on, for example, perforated rods or a perforated coil analogous to heat transfer equipment. Simulations and experiments should establish, whether such a feed arrangement would be feasible in bioreactors. Figure 2 showed that the placement of a single feed point is rather sensitive, but distributing the feed as evenly throughout the volume as possible ought to overcome this sensitivity.

Two concerns, biological contamination and engineering complications, are easily raised upon considering multipoint feeds. Depending on the nature of the product, contamination may result in the failure of up to 17% of fermentations (Morandi & Valeri, 1988). Processes involving slowly growing host organisms are particularly susceptible. The extra internals required by a multipoint feed would hamper mixing and mass and heat transfer to some extent, but the severeness of this would probably be comparable to that of heat transfer internals. Hydraulic losses within the feed pipes are likely to be manageable, as in fermentations, the feed flow rates are quite small relative to working volume. Ensuring approximately equal volume flow rates through multiple feed points may be complex, but a thorough coverage of the working volume with the feed points would probably be less sensitive to differences in flow rates.

6 | CONCLUSIONS

Optimal placement of multiple feed points was derived from 1D diffusion equations. The effect on both mixing and bioreaction in industrially relevant stirred tank and bubble column bioreactors was then evaluated with compartment model simulations. Placing multiple feed points at the middle height of equal-height axial subdivisions improved mixing and reaction substantially: Simulated mixing times were reduced from the scale of minutes to the scale of 10 s, which mitigated substrate gradients and restored ideal homogeneous reactor performance. The heterogeneity in pH and concentration of dissolved oxygen was reduced as well. The implications regarding bioreactor scale-up are considerable. The use of appropriately placed feed points could homogenize large-scale reactors effectively and consequently (1) alleviate one of the most cited scale-up problems, the heterogeneity of substrate, oxygen, and pH, (2) reduce side-product formation, (3) maintain optimal biomass and product yields, and (4) improve reactor control. Another benefit is that even the simple homogeneous ideal reactor model remains applicable when the large scale resembles the small.

ACKNOWLEDGMENTS

This work was financially supported by Tampere University of Technology Graduate School and Academy of Finland (grant no. 310188).

CONFLICT OF INTEREST

The authors declare no conflict of interest.

DATA AVAILABILITY STATEMENT

The data that support the findings of this study are available from the corresponding author upon reasonable request.

ORCID

Pauli Losoi http://orcid.org/0000-0002-1319-6503

REFERENCES

Alves, S. S., & Vasconcelos, J. M. T. (1995). Mixing in gas-liquid contactors agitated by multiple turbines in the flooding regime. *Chemical Engineering Science*, *50*(14), 2355–2357. https://doi.org/10.1016/0009-2509(95)00091-I

Alves, S. S., Vasconcelos, J. M. T., & Barata, J. (1997). Alternative compartment models of mixing in tall tanks agitated by multi-Rushton turbines. *Chemical Engineering Research and Design*, *75*(3), 334–338. https://doi.org/10.1205/026387697523642

Amanullah, A., McFarlane, C. M., Emery, A. N., & Nienow, A. W. (2001). Scale-down model to simulate spatial pH variations in large-scale bioreactors. *Biotechnology and Bioengineering*, *73*(5), 390–399. https://doi.org/10.1002/bit.1072

Anane, E., López, D. C., Neubauer, P., & Bournazou, M. N. C. (2017). Modelling overflow metabolism in *Escherichia coli* by acetate cycling. *Biochemical Engineering Journal*, *125*, 23–30. https://doi.org/10.1016/j.bej.2017.05.013

Brand, E., Junne, S., Anane, E., Cruz-Bournazou, M. N., & Neubauer, P. (2018). Importance of the cultivation history for the response of *Escherichia coli* to oscillations in scale-down experiments. *Bioprocess and Biosystems Engineering*, *41*(9), 1305–1313. https://doi.org/10.1007/s00449-018-1958-4

Bylund, F., Collet, E., Enfors, S., & Larsson, G. (1998). Substrate gradient formation in the large-scale bioreactor lowers cell yield and increases by-product formation. *Bioprocess Engineering*, *18*, 171–180. https://doi.org/10.1007/s004490050427

Cole, K. D., Beck, J. V., Haji-Sheikh, A., & Litkouhi, B. (2010). *Heat conduction using Green's functions* (2 ed.). CRC Press. https://doi.org/10.1201/9781439895214

Cronin, D. G., Nienow, A. W., & Moody, G. W. (1994). An experimental study of mixing in a proto-fermenter agitated by dual Rushton turbines. *Food and Bioproducts Processing*, *72*, 35–40.

Cui, Y. Q., van der Lans, R. G. J. M., Noorman, H. J., & Luyben, K. C. A. M. (1996). Compartment mixing model for stirred reactors with multiple impellers. *Chemical Engineering Research and Design*, *74*, 261–271.

Degaleesan, S., Dudukovic, M. P., Toseland, B. A., & Bhatt, B. L. (1997). A two-compartment convective-diffusion model for slurry bubble column reactors. *Industrial & Engineering Chemistry Research*, *36*(11), 4670–4680. https://doi.org/10.1021/ie970200s

Delafosse, A., Collignon, M., Calvo, S., Delvigne, F., Crine, M., Thonart, P., & Toye, D. (2014). CFD-based compartment model for description of mixing in bioreactors. *Chemical Engineering Science*, *106*, 76–85. https://doi.org/10.1016/j.ces.2013.11.033

Dudukovic, M. P. (2000). Opaque multiphase reactors: Experimentation, modeling and troubleshooting. *Oil & Gas Science and Technology*, *55*(2), 135–158. https://doi.org/10.2516/ogst:2000008

Dunlop, E. H., & Ye, S. J. (1990). Micromixing in fermentors: Metabolic changes in *Saccharomyces cerevisiae* and their relationship to fluid turbulence. *Biotechnology and Bioengineering*, *36*(8), 854–864. https://doi.org/10.1002/bit.260360816

Eiteman, M. A., & Altman, E. (2006). Overcoming acetate in *Escherichia coli* recombinant protein fermentations. *Trends in Biotechnology*, *24*(11), 530–536. https://doi.org/10.1016/j.tibtech.2006.09.001

Enfors, S., Jahic, M., Rozkov, A., Xu, B., Hecker, M., Jürgen, B., Krüger, E., Schweder, T., Hamer, G., O'Beirne, D., Noisommit-Rizzi, N., Reuss, M., Boone, L., Hewitt, C., McFarlane, C., Nienow, A., Kovacs, T., TrägÅdh, C., Fuchs, L., … Manelius, Å. (2001). Physiological responses to mixing in large scale bioreactors. *Journal of Biotechnology*, *85*(2), 175–185. https://doi.org/10.1016/S0168-1656(00)00365-5

Enjalbert, B., Cocaign-Bousquet, M., Portais, J., & Letisse, F. (2015). Acetate exposure determines the diauxic behavior of *Escherichia coli* during the glucose-acetate transition. *Journal of Bacteriology*, *197*(19), 3173–3181. https://doi.org/10.1128/JB.00128-15

Fowler, J. D., & Dunlop, E. H. (1989). Effects of reactant heterogeneity and mixing on catabolite repression in cultures of *Saccharomyces cerevisiae*. *Biotechnology and Bioengineering*, *33*(8), 1039–1046. https://doi.org/10.1002/bit.260330813

Fu, C., Lu, S., & Wu, W. (2005). Optimal feeding for tower-type reactors. *AIChE Journal*, *51*(3), 713–724. https://doi.org/10.1002/aic.10346

Hansford, G. S., & Humphrey, A. E. (1966). The effect of equipment scale and degree of mixing on continuous fermentation yield at low dilution rates. *Biotechnology and Bioengineering*, *8*(1), 85–96. https://doi.org/10.1002/bit.260080108

Haringa, C., Tang, W., Wang, G., Deshmukh, A. T., van Winden, W. A., Chu, J., van Gulik, W. M., Heijnen, J. J., Mudde, R. F., & Noorman, H. J. (2018). Computational fluid dynamics simulation of an industrial P. chrysogenum fermentation with a coupled 9-pool metabolic model: Towards rational scale-down and design optimization. *Chemical Engineering Science*, *175*8, 12–24. https://doi.org/10.1016/j.ces.2017.09.020

Harris, C. R., Millman, K. J., van der Walt, S. J., Gommers, R., Virtanen, P., Cournapeau, D., Wieser, E., Taylor, J., Berg, S., Smith, N. J., Kern, R., Picus, M., Hoyer, S., van Kerkwijk, M. H., Brett, M., Haldane, A., FernándezdelRío, J., Wiebe, M., … Oliphant, T. E. (2020). Array programming with NumPy. *Nature*, *585*, 357–362. https://doi.org/10.1038/s41586-020-2649-2

Hristov, H., Mann, R., Lossev, V., Vlaev, S. D., & Seichter, P. (2001). A 3-D analysis of gas-liquid mixing, mass transfer and bioreaction in a stirred bio-reactor. *Food and Bioproducts Processing*, *79*(4), 232–241. https://doi.org/10.1205/096030801753252306

Jaworski, Z., Nienow, A. W., & Dyster, K. N. (1996). An LDA study of the turbulent flow field in a baffled vessel agitated by an axial, down-pumping hydrofoil impeller. *The Canadian Journal of Chemical Engineering*, *74*1, 3–15. https://doi.org/10.1002/cjce.5450740103

Kasat, G. R., & Pandit, A. B. (2004). Mixing time studies in multiple impeller agitated reactors. *The Canadian Journal of Chemical Engineering*, *82*(5), 892–904. https://doi.org/10.1002/cjce.5450820504

Kawase, Y., & Moo-Young, M. (1989). Mixing time in bioreactors. *Journal of Chemical Technology and Biotechnology*, *44*, 63–75. https://doi.org/10.1002/jctb.280440107

Langheinrich, C., & Nienow, A. W. (1999). Control of pH in large-scale, free suspension animal cell bioreactors: Alkali addition and pH excursions. *Biotechnology and Bioengineering*, *66*(3), 171–179. https://doi.org/10.1002/(SICI)1097-0290(1999)66:3<171::AID-BIT5>3.0.CO;2-T

Langheinrich, C., Nienow, A. W., Eddleston, T., Stevenson, N. C., Emery, A. N., Clayton, T. M., & Slater, N. K. H. (1998). Liquid homogenization studies in animal cell bioreactors of up to 8 m^3 in volume. *Food and Bioproducts Processing*, *76*(2), 107–116. https://doi.org/10.1205/096030898531873

Larsson, G., Törnkvist, M., StÅhl-Wernersson, E., TrägÅdh, C., Noorman, H., & Enfors, S. (1996). Substrate gradients in bioreactors: Origin and consequences. *Bioprocess Engineering*, *146*, 281–289. https://doi.org/10.1007/BF00369471

Machon, V., & Jahoda, M. (2000). Liquid homogenization in aerated multi-impeller stirred vessel. *Chemical Engineering and Technology*, *23*(10), 869–876. https://doi.org/10.1002/1521-4125(200010)23:10<869::AID-CEAT869>3.0.CO;2-B

Magelli, F., Montante, G., Pinelli, D., & Paglianti, A. (2013). Mixing time in high aspect ratio vessels stirred with multiple impellers. *Chemical Engineering Science*, *101*, 712–720. https://doi.org/10.1016/j.ces.2013.07.022

Mayr, B., Horvat, P., & Moser, A. (1992). Engineering approach to mixing quantification in bioreactors. *Bioprocess Engineering*, *8*, 137–143. https://doi.org/10.1007/BF01254229

McKinney, W. (2010). Data structures for statistical computing in Python. *Proceedings of the 9th Python in Science Conference*, *445*, 51–56. https://doi.org/10.25080/Majora-92bf1922-00a

Morandi, M., & Valeri, A. (1988). Industrial scale production of β-interferon, *Bioprocesses Including Animal Cell Culture* (pp. 57–72). Springer Berlin Heidelberg.

Morchain, J., & Fonade, C. (2009). A structured model for the simulation of bioreactors under transient conditions. *AIChE Journal*, *55*(11), 2973–2984. https://doi.org/10.1002/aic.11906

Morchain, J., Gabelle, J., & Cockx, A. (2013). A coupling of biokinetic and population balance models to account for biologial heterogeneity in bioreactors. *AIChE Journal*, *59*(2), 369–379. https://doi.org/10.1002/aic.13820

Morchain, J., Gabelle, J., & Cockx, A. (2014). A coupled population balance model and cfd approach for the simulation of mixing issues in lab-scale and industrial bioreactors. *AIChE Journal*, *60*(1), 27–40. https://doi.org/10.1002/aic.14238

Nauha, E. K., Kálal, Z., Ali, J. M., & Alopaeus, V. (2018). Compartmental modeling of large stirred tank bioreactors with high gas volume fractions. *Chemical Engineering Journal*, *334*, 2319–2334. https://doi.org/10.1016/j.cej.2017.11.182

Nauha, E. K., Visuri, O., Vermasvuori, R., & Alopaeus, V. (2015). A new simple approach for the scale-up of aerated stirred tanks. *Chemical Engineering Research and Design*, *95*, 150–161. https://doi.org/10.1016/j.cherd.2014.10.015

Oosterhuis, N. M. G., & Kossen, N. W. F. (1984). Dissolved oxygen concentration profiles in a production-scale bioreactor. *Biotechnology and Bioengineering*, *26*(5), 546–550. https://doi.org/10.1002/bit.260260522

Pigou, M., & Morchain, J. (2015). Investigating the interactions between physical and biological heterogeneities in bioreactors using compartment, population balance and metabolic models. *Chemical Engineering Science*, *126*, 267–282. https://doi.org/10.1016/j.ces.2014.11.035

Pulkkinen, O., & Metzler, R. (2015). Variance-corrected Michaelis-Menten equation predicts transient rates of single-enzyme reactions and response times in bacterial gene-regulation. *Scientific Reports*, *5*, 17820. https://doi.org/10.1038/srep17820

Rohatgi, A. (2020). Webplotdigitizer: Version 4.4. Accessed March, 2022. https://automeris.io/WebPlotDigitizer

Sander, R. (2015). Compilation of Henry's law constants (version 4.0) for water as solvent. *Atmospheric Chemistry and Physics*, *15*, 4399–4981. https://doi.org/10.5194/acp-15-4399-2015

Schügerl, K. (1993). Comparison of different bioreactor performances. *Bioprocess Engineering*, *9*, 215–223. https://doi.org/10.1007/BF00369405

Schweder, T., Krüger, E., Xu, B., Jürgen, B., Blomsten, G., Enfors, S.-O., & Hecker, M. (1999). Monitoring of genes that respond to process-related stress in large-scale bioprocesses. *Biotechnology and Bioengineering*, *65*(2), 151–159. https://doi.org/10.1002/(SICI)1097-0290(19991020)65:2<151::AID-BIT4>3.0.CO;2-V

Szenk, M., Dill, K. A., & de Graff, A. M. R. (2017). Why do fast-growing bacteria enter overflow metabolism? Testing the membrane real estate hypothesis. *Cell Systems*, *5*(2), 95–104. https://doi.org/10.1016/j.cels.2017.06.005

The Pandas Development Team. (2020). Pandas (Version 1.1.3). Zenodo. https://doi.org/10.5281/zenodo.4067057

Vasconcelos, J. M., Alves, S., & Barata, J. M. (1995). Mixing in gas-liquid contactors agitated by multiple turbines. *Chemical Engineering Science*, *50*(14), 2343–2354. https://doi.org/10.1016/0009-2509(95)00090-R

Vasconcelos, J. M., Barata, J. M., & Alves, S. (1996). Transitional mixing in multiple-turbine agitated tanks. *The Chemical Engineering Journal and the Biochemical Engineering Journal*, *63*(1), 53–58. https://doi.org/10.1016/0923-0467(95)03072-7

Versteeg, H. K., & Malalasekera, W. (2007). *An introduction to computational fluid dynamics* (2 ed.). Pearson Education Limited.

Virtanen, P., Gommers, R., Oliphant, T. E., Haberland, M., Reddy, T., Cournapeau, D., Burovski, E., Peterson, P., Weckesser, W., Bright, J., van der Walt, S. J., Brett, M., Wilson, J., Millman, K. J., Mayorov, N., Nelson, A. R. J., Jones, E., Kern, R., Larson, E., … SciPy 1.0 Contributors. (2020). SciPy 1.0: Fundamental algorithms for scientific computing in python. *Nature Methods*, *17*3, 261–272. https://doi.org/10.1038/s41592-019-0686-2

Vrábel, P., van der Lans, R. G. J. M., Cui, Y. Q., & Luyben, K. C. A. M. (1999). Compartment model approach: Mixing in large scale aerated reactors with multiple impellers. *Chemical Engineering Research and Design*, *77*(4), 291–302. https://doi.org/10.1205/026387699526223

Vrábel, P., van der Lans, R. G. J. M., Luyben, K. C. A. M., Boon, L., & Nienow, A. W. (2000). Mixing in large-scale vessels stirred with multiple radial or radial and axial up-pumping impellers: Modelling and measurements. *Chemical Engineering Science*, *55*(23), 5881–5896. https://doi.org/10.1016/S0009-2509(00)00175-5

Vrábel, P., van der Lans, R. G. J. M., van der Schot, F. N., Luyben, K. C. A. M., Xu, B., & Enfors, S. (2001). CMA: Integration of fluid dynamics and microbial kinetics in modelling of large-scale fermentations. *Chemical Engineering Journal*, *84*, 463–474. https://doi.org/10.1016/S1385-8947(00)00271-0

Xu, B., Jahic, M., Blomsten, G., & Enfors, S. (1999). Glucose overflow metabolism and mixed-acid fermentation in aerobic large-scale fed-batch processes with *Escherichia coli*. *Applied Microbiology and Biotechnology*, *51*, 564–571. https://doi.org/10.1007/s002530051433

Xu, B., Jahic, M., & Enfors, S. (1999). Modeling of overflow metabolism in batch and fed-batch cultures of *Escherichia coli*. *Biotechnology Progress*, *15*, 81–90.

Zahradník, J., Mann, R., Fialová, M., Vlaev, D., Vlaev, S. D., Lossev, V., & Seichter, P. (2001). A networks-of-zones analysis of mixing and mass transfer in three industrial bioreactors. *Chemical Engineering Science*, *56*(2), 485–492. https://doi.org/10.1016/S0009-2509(00)00252-9

SUPPORTING INFORMATION

Additional supporting information can be found online in the Supporting Information section at the end of this article.

How to cite this article: Losoi, P., Konttinen, J., & Santala, V. (2022). Substantial gradient mitigation in simulated large-scale bioreactors by optimally placed multiple feed points. *Biotechnology and Bioengineering*, 1–18. https://doi.org/10.1002/bit.28232

APPENDIX A: COMPARTMENT MODELING

The stirred reactors R1 and R4 with one and four Rushton turbines, respectively, were modeled by combining axisymmetric two-dimensional (2D) compartment modeling approaches (Cui et al., 1996; Vrábel et al., 1999, 2000) with 2D/3D networks-of-zones models (Delafosse et al., 2014; Hristov et al., 2001; Zahradník et al., 2001). The radial flow pattern of each impeller was composed of two stacked square networks of nested flow loops (Delafosse et al., 2014; Hristov et al., 2001; Zahradník et al., 2001). Furthermore, one square network of nested loops was used at the top of the reactor to model the stagnant surface. The stagnant top was assumed to reach a quarter from the surface toward the top impeller, which is similar to previous works (Vrábel et al., 1999, 2000) and matches experimental

observations (Cronin et al., 1994; Jaworski et al., 1996) as well. In the multi-impeller reactor R4, the square networks reached from the impeller plane midway toward the next impeller. The compartments within a square network of nested loops were of equal volume (Cui et al., 1996; Hristov et al., 2001; Vrábel et al., 1999, 2000; Zahradník et al., 2001). The effect of turbulence was modeled by connecting adjacent rows of compartments by axial exchange flows of equal magnitude (Cui et al., 1996; Vrábel et al., 1999, 2000). The tangential dimension was incorporated by multiplying the described 2D pattern tangentially. A tangential circulation flow then connected the 2D axial-radial patterns unidirectionally and formed closed loops around the reactor to model the swirling induced by the impellers (Delafosse et al., 2014; Hristov et al., 2001). Liquid volumes in the aerated R4's compartments were reduced by the global gas-holdup.

Both R1's and R4's impeller-wise total circulation flows were estimated to be $Q_C = 1.5nD^3$ ($m^3\ s^{-1}$), similarly to Cui et al. (1996); Vrábel et al. (1999, 2000), where n is the stirrer speed (s^{-1}) and D the impeller diameter (m). The 80% averaging factor used by Cui et al. (1996) and Vrábel et al. (1999, 2000) was not used here, as the model's structure incorporated also the shorter flow paths compensated for by the averaging in the cited studies. Each impeller's total circulation flow rate was then divided equally between the nested flow loops (Delafosse et al., 2014; Hristov et al., 2001; Zahradník et al., 2001). The total tangential circulation flow in an impeller region was assumed to be equal to the impeller's radial flow pattern's circulation flow (Delafosse et al., 2014; Hristov et al., 2001), and it was also divided equally between the nested tangential loops. It has been suggested that circulation in the stagnant surface should be slower than in the top impeller region (Vrábel et al., 1999, 2000). Therefore, the stagnant top loop's circulation flow rate was assumed to be one eight of the top impeller's circulation flow, which resulted in a doubled circulation time relative to the top impeller. The exchange flows $Q_E = N_E nD^3$ ($m^3\ s^{-1}$) were kept equal throughout the reactors, and the exchange flow numbers were fitted to $N_E = 0.539$ in R4 and $N_E = 0.274$ in R1 by matching the model outputs to yield the reported locally measured mixing times of 165 s in R4 (Vrábel et al., 1999, 2001; Xu et al., 1999) and 124 s in R1 (Langheinrich et al., 1998). The fitted exchange flows were divided equally across the compartments on each of the reactors' cross-section planes. It should be noted that the exchange flow numbers depend on the used compartment model structure (Alves et al., 1997; Cui et al., 1996; Vrábel et al., 1999).

Given that the gas-induced flow rates are similar to the exhange flows in a stirred tank (Vrábel et al., 1999, 2000), they were not modeled separately here. In effect, the exchange flow number covered both exchange and gas-induced flows. Such an approach is appropriate when the impellers are not flooded (Vrábel et al., 2000) and the gas flow is not heterogeneous, as is the case here: $u_G = 0.923\ cm^3\ s^{-1}$ in R4 is well below the $3\ cm^3\ s^{-1}$ transition threshold suggested for general use by Nauha et al. (2015). Under flooding conditions, the compartment model structure would require a change toward a bubble column compartment structure (described below) for the lowest, flooded impeller (Alves & Vasconcelos, 1995; Machon & Jahoda, 2000; Nauha et al., 2018).

The bubble columns B6 and B13 were modeled similarly to the stirred tanks, but with single rectangular networks of nested flow loops (Zahradník et al., 2001). The bubble columns were conceptually divided into bottom, middle, and top parts (Figure 1). The bottom and top parts had heights equal to the tank diameter (Degaleesan et al., 1997), and the rest of the column was considered the middle part. The compartment volumes were kept equal within the bottom, middle, and top parts of the reactor. The overall circulation flow rates Q_C were estimated by using a correlation for the average liquid upflow velocities (Degaleesan et al., 1997)

$$\frac{u_L}{\text{cm s}^{-1}} = 2.2\left(\frac{u_G}{\text{cm s}^{-1}}\frac{T}{\text{cm}}\right)^{0.4}. \tag{A1}$$

The velocity was multiplied by half the reactor's cross-section as, in general, approximately one half of the cross-section flows up and the other half down (Degaleesan et al., 1997). In Equation (A1), u_G is the superficial gas velocity and T the reactor's diameter. The circulation flow rates were then divided across the nested loops with a quadratic profile matching an experimentally determined radial profile of liquid velocity in the reactor's middle part (Degaleesan et al., 1997). Exchange flow rates Q_E were determined by finite-volume discretization (Versteeg & Malalasekera, 2007) of eddy diffusivities estimated from literature data. The gas-holdups and eddy diffusivities were radially homogeneous in the uppermost row of the top part and downmost row of the bottom part, but both of these properties were smoothed in the axial direction linearly toward the radially heterogeneous profiles of the middle part. For comparison, Degaleesan et al. (1997) modeled the top and bottom parts as single homogeneous compartments. Axial mean eddy diffusivity d_z was approximated with (Degaleesan et al., 1997)

$$\frac{d_z}{\text{cm}^2\ \text{s}^{-1}} = 106.6\left(\frac{u_G}{\text{cm s}^{-1}}\frac{T}{\text{cm}}\right)^{0.3} - 2325\left(\frac{\text{cm}}{T}\right)^{0.8}, \tag{A2}$$

and radial with (Degaleesan et al., 1997)

$$\frac{d_r}{\text{cm}^2\ \text{s}^{-1}} = 13.0\left(\frac{u_G}{\text{cm s}^{-1}}\frac{T}{\text{cm}}\right)^{0.3} - 350\left(\frac{\text{cm}}{T}\right)^{0.8}. \tag{A3}$$

The radial profiles of axial and radial eddy diffusivities were modeled with linear and quadratic polynomial forms, respectively, approximating the measured distributions reported by Degaleesan et al. (1997). As tangential eddy diffusivity was not measured by Degaleesan et al. (1997), it was taken to be a quarter of the axial mean value, which is close to measurements reported by Dudukovic (2000). The tangential eddy diffusivity's radial profile was assumed to be the same as the radial eddy diffusivity's. The B6's overall gas-holdup ($\epsilon_G = 17\%$) was reported by Zahradník et al. (2001) and the B13's mean gas-holdup ($\epsilon_G = 23\%$) was estimated with the correlation (Degaleesan et al., 1997)

$$\epsilon_G = 0.07\left(\frac{u_G}{\text{cm s}^{-1}}\right)^{0.474-0.00626\frac{T}{\text{cm}}}. \tag{A4}$$

The radial profiles of gas-holdup were modeled according to the quadratic profile observed experimentally by Degaleesan et al. (1997). Axially the gas-holdups were corrected by hydrostatic pressure (water density 997 kg m^{-3}) such that the reactor's overall

gas-holdups were not changed. Ideal gas behavior and 101,325 Pa head-space pressure were assumed in the corrections. Liquid volumes in the compartments were reduced by the local gas-holdups.

Five nested loops (10 columns radially) per network and 12 tangential coordinates were used for each reactor. Both stirred tanks were modeled with two stacked square networks (altogether 20 compartments axially) per impeller and a single square network for the stagnant surface above the top impeller. The bubble columns were modeled with single rectangular networks with 62 and 30 rows in the B13 and B6 reactors, respectively. In total, the reactors were modeled with 3600–10,800 compartments.

In terms of computation requirements, the compartment models yield much smaller systems (3600–10,800 computational cells) to be solved than CFD (100,000 cells, even 1,000,000 cells). Compared to a CFD-based approach (Delafosse et al., 2014) where the compartment models are derived from a CFD-determined flow field, the simple hydrodynamics approach (Cui et al., 1996; Degaleesan et al., 1997; Vrábel et al., 1999, 2000) enabled a flexible and quick programmatic construction of the compartment models. It should be noted that axial impellers could be modeled by the hydrodynamics approach as well (Vrábel et al., 2000).

APPENDIX B: pH-CONTROL AND BIOREACTION SIMULATION RESULTS

Table B1

TABLE B1 Simulation results in an ideal homogeneous reactor and in reactors R4, R1, B13, and B6 with top feed and selected optimal multipoint feeds in the form "mean ± standard deviation."

	Top/ideal	A1R1T1	A2R2T2	A4R2T2
pH	6			
R4	5.55 ± 0.68	5.92 ± 0.27	6.00 ± 0.02	6.00 ± 0.00
R1	5.18 ± 0.64	5.25 ± 0.66	5.90 ± 0.32	5.94 ± 0.25
B13	5.44 ± 0.71	5.86 ± 0.40	6.00 ± 0.05	6.00 ± 0.04
B6	5.12 ± 0.62	5.42 ± 0.66	5.96 ± 0.18	5.98 ± 0.12
S/mg L^{-1}	16.7			
R4	34.0 ± 41.6	20.3 ± 16.8	17.1 ± 4.8	16.8 ± 2.3
R1	48.9 ± 121.0	38.3 ± 104.8	20.9 ± 21.0	19.6 ± 15.5
B13	33.4 ± 57.1	22.0 ± 28.8	17.6 ± 7.5	17.0 ± 4.4
B6	46.3 ± 116.9	35.7 ± 80.1	19.4 ± 16.9	18.5 ± 11.9
τ_S/s	15			
R4	21.2 ± 15.0	16.3 ± 6.0	15.2 ± 1.7	15.0 ± 0.8
R1	26.6 ± 43.5	22.8 ± 37.7	16.5 ± 7.5	16.0 ± 5.6
B13	21.0 ± 20.5	16.9 ± 10.4	15.3 ± 2.7	15.1 ± 1.6
B6	25.7 ± 42.1	21.8 ± 28.8	16.0 ± 6.1	15.7 ± 4.3
O/mg L^{-1}	0.113			
R4	2.18 ± 2.60	0.233 ± 0.186	0.120 ± 0.028	0.114 ± 0.009
$Y_{OS}^{-1}r_O$/g L^{-1} h^{-1}	2.12			
R4	1.77 ± 0.79	2.10 ± 0.14	2.12 ± 0.06	2.12 ± 0.07
y_{XS}/%	43.8			
R4	33.2 ± 18.5	42.8 ± 2.7	43.6 ± 0.8	43.7 ± 0.4
R1	32.7 ± 22.2	38.4 ± 11.4	42.7 ± 3.5	42.9 ± 2.9
B13	37.2 ± 12.1	42.7 ± 3.1	43.5 ± 1.2	43.7 ± 0.7
B6	34.3 ± 19.9	35.4 ± 19.3	43.3 ± 1.6	43.4 ± 1.5

Note: Symbols: O, dissolved oxygen concentration; $Y_{OS}^{-1}r_O$, aerobic substrate consumption rate; S, substrate concentration; τ_S, substrate consumption time-scale; y_{XS}, biomass yield.

Supporting information for
Substantial gradient mitigation in simulated large-scale bioreactors by optimally placed multiple feed points

Pauli Losoi * Jukka Konttinen Ville Santala

Faculty of Engineering and Natural Sciences, Tampere University, Hervanta campus, Korkeakoulunkatu 8, Tampere, 33720, Finland

* Corresponding author, pauli.losoi@tuni.fi

Table S1: Bioreaction simulation results in an ideal homogeneous reactor and in reactors R4, R1, B13, and B6 with top feed and selected optimal multi-point feeds in the form "mean ± standard deviation" with $X = 50\,\mathrm{g\,L^{-1}}$ biomass concentration. Other kinetic parameters are exactly the same as in Table 2 of main text.

	Top/ideal	A1R1T1	A2R2T2	A4R2T2
S / $\mathrm{mg\,L^{-1}}$	2.17			
R4	4.14 ± 15.65	3.28 ± 10.66	2.44 ± 3.36	2.28 ± 1.99
R1	13.1 ± 94.8	12.5 ± 92.9	4.18 ± 15.48	3.51 ± 10.39
B13	7.19 ± 40.90	4.65 ± 22.37	2.71 ± 5.39	2.42 ± 3.29
B6	13.9 ± 97.1	9.22 ± 64.97	3.72 ± 12.85	3.12 ± 8.86
τ_S / s	1.82			
R4	2.10 ± 1.13	2.04 ± 0.77	1.98 ± 0.24	1.96 ± 0.14
R1	2.74 ± 6.82	2.70 ± 6.69	2.10 ± 1.11	2.05 ± 0.75
B13	2.32 ± 2.94	2.13 ± 1.61	2.00 ± 0.39	1.97 ± 0.24
B6	2.80 ± 6.99	2.46 ± 4.68	2.07 ± 0.93	2.02 ± 0.60
O / $\mathrm{mg\,L^{-1}}$	0.113			
R4	7.00 ± 4.70	3.35 ± 2.68	0.658 ± 0.544	0.180 ± 0.101
$Y_{OS}^{-1} r_O$ / $\mathrm{g\,L^{-1}\,h^{-1}}$	2.12			
R4	0.961 ± 1.461	1.58 ± 1.67	2.03 ± 0.98	2.11 ± 0.54
y_{XS} / %	18.7			
R4	−357 000 ± 797 000	−473 ± 754	−14.9 ± 50.0	11.6 ± 15.3
R1	−1 770 000 ± 8 080 000	−779 000 ± 304 000	−526 ± 1380	−405 ± 1250
B13	−345 000 ± 919 000	−1600 ± 4290	−66.1 ± 126.3	0.163 ± 29.684
B6	−426 000 ± 1 897 000	−164 000 ± 814 000	−191 ± 395	−51.0 ± 98.2

Symbols: O, dissolved oxygen concentration; $Y_{OS}^{-1} r_O$, aerobic substrate consumption rate; S, substrate concentration; τ_S, substrate consumption time-scale; y_{XS}, biomass yield.

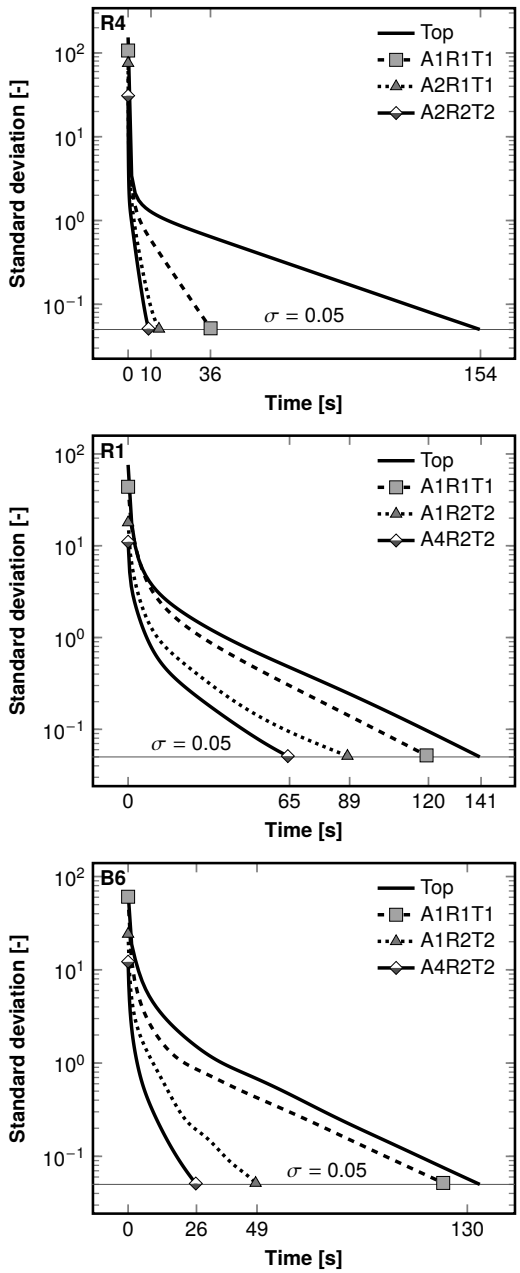

Figure S1: Standard deviation of dimensionless tracer concentration in reactors R4 (top), R1 (middle), and B6 (bottom) after tracer pulse with top feed and various optimal multi-point feeds. The feed arrangements AxRyTz contain x axial, y radial, and z tangential coordinates (see Figure 3 in main text). The 5 % line is the threshold for mixing time. Note the logarithmic scaling of the vertical axis.

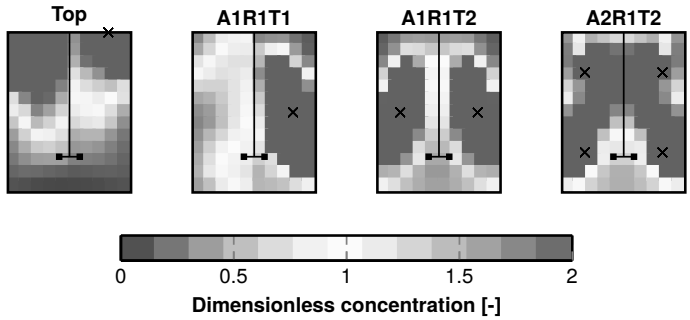

Figure S2: Simulated concentration of substrate in reactor R1 with $10\,\mathrm{g\,L^{-1}}$ biomass concentration and a $4\,\mathrm{g\,L^{-1}\,h^{-1}}$ substrate feed rate at the top or through an optimal multi-point feed. The concentrations have been normalized by the respective substrate concentration $16.7\,\mathrm{mg\,L^{-1}}$ calculated in an ideal homogeneous reactor at the same conditions. The feed arrangements AxRyTz contain x axial, y radial, and z tangential coordinates (see Figure 3 in main text).

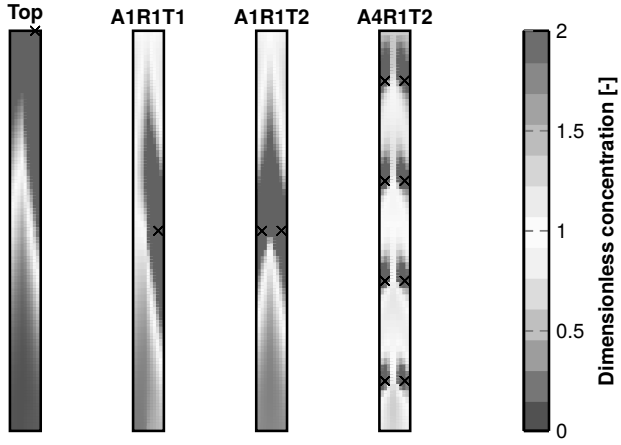

Figure S3: Simulated concentration of substrate in reactor B13 with $10\,\mathrm{g\,L^{-1}}$ biomass concentration and a $4\,\mathrm{g\,L^{-1}\,h^{-1}}$ substrate feed rate at the top or through an optimal multi-point feed. The concentrations have been normalized by the respective substrate concentration $16.7\,\mathrm{mg\,L^{-1}}$ calculated in an ideal homogeneous reactor at the same conditions. The feed arrangements AxRyTz contain x axial, y radial, and z tangential coordinates (see Figure 3 in main text).

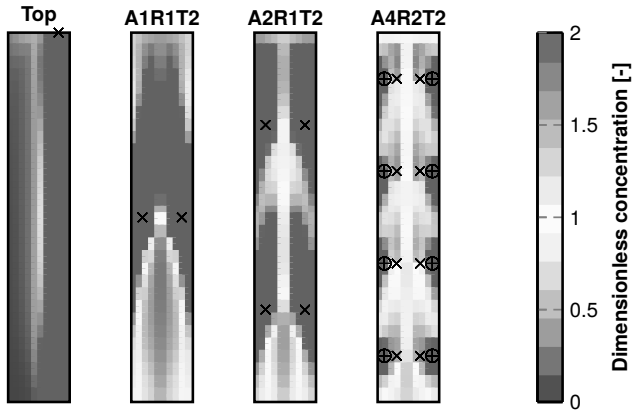

Figure S4: Simulated concentration of substrate in reactor B6 with $10\,\mathrm{g\,L^{-1}}$ biomass concentration and a $4\,\mathrm{g\,L^{-1}\,h^{-1}}$ substrate feed rate at the top or through an optimal multi-point feed. The concentrations have been normalized by the respective substrate concentration $16.7\,\mathrm{mg\,L^{-1}}$ calculated in an ideal homogeneous reactor at the same conditions. The feed arrangements AxRyTz contain x axial, y radial, and z tangential coordinates (see Figure 3 in main text).

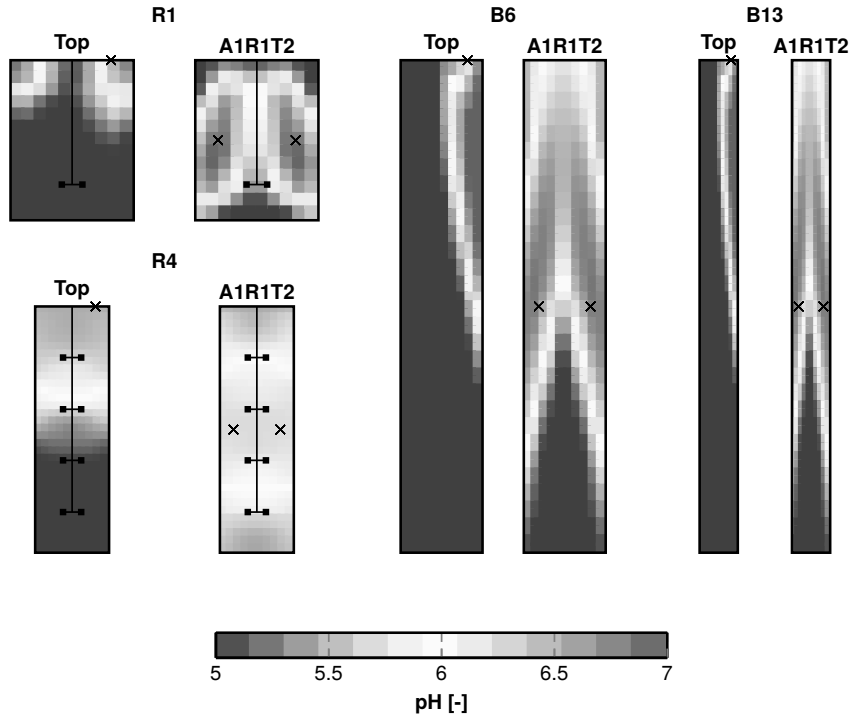

Figure S5: Simulated pH in reactors R1 (upper left), R4 (lower left), B6 (center), and B13 (right) 10 s after pH-correcting pulse of carbonate in a $100\,\mathrm{mmol\,L^{-1}}$ carbonate buffer solution initially at a pH of 4.8. Responses to top and A1R1T2 pulse are shown. The A1R1T2 feed arrangement contains two feed points tangentially opposite to each other at middle height and 63 % radius (see Figure 3 in main text).

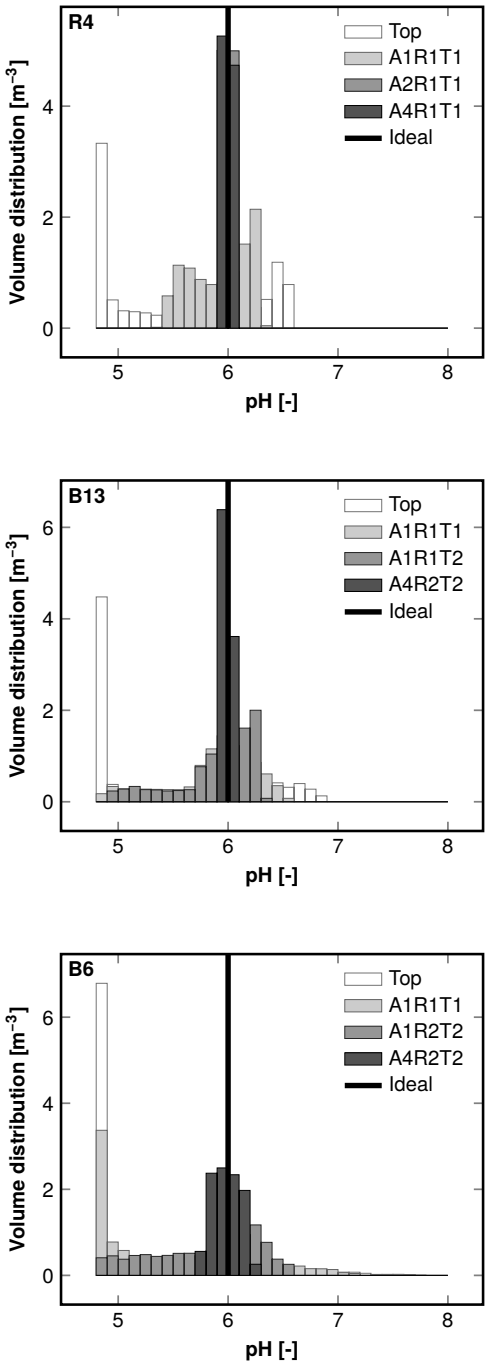

Figure S6: Distribution of pH in reactors R4 (top), B13 (middle), and B6 (bottom) 10 s after pH-correcting pulse of carbonate in a 100 mmol L^{-1} carbonate buffer solution initially at a pH of 4.8. Responses to top and optimal multi-point pulses are shown. Ideal homogeneous reactor behaviour is shown for reference (whole volume has pH 6). The feed arrangements AxRyTz contain x axial, y radial, and z tangential coordinates (see Figure 3 in main text).

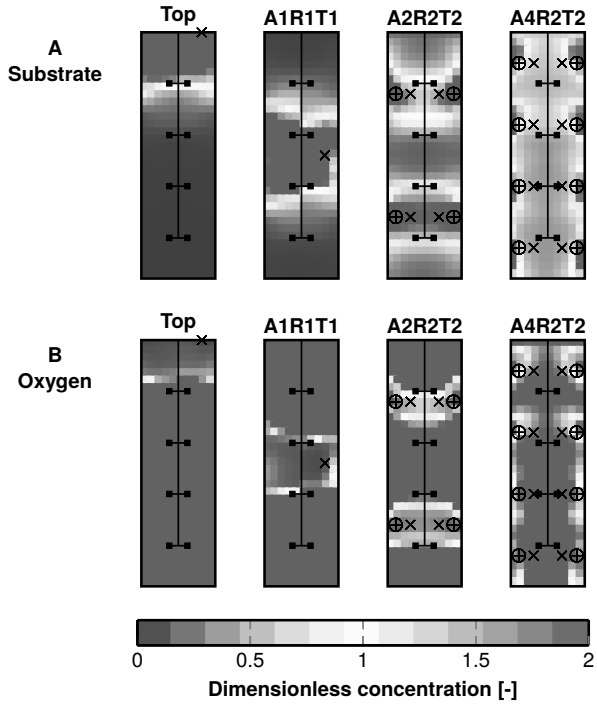

Figure S7: Simulated concentration of substrate and dissolved oxygen in reactor R4 with $50\,\mathrm{g\,L^{-1}}$ biomass concentration and a $4\,\mathrm{g\,L^{-1}\,h^{-1}}$ substrate feed rate at the top or through an optimal multi-point feed. The concentrations have been normalized by respective concentrations (substrate $2.17\,\mathrm{mg\,L^{-1}}$, oxygen $0.113\,\mathrm{mg\,L^{-1}}$) calculated in an ideal homogeneous reactor at the same conditions. Note the color scale limits (values above twice the ideal reactor value are shown as 2). The feed arrangements AxRyTz contain x axial, y radial, and z tangential coordinates (see Figure 3 in main text). The substrate gradients were similar in the other reactors (R1, B13, and B6) as well (not shown).

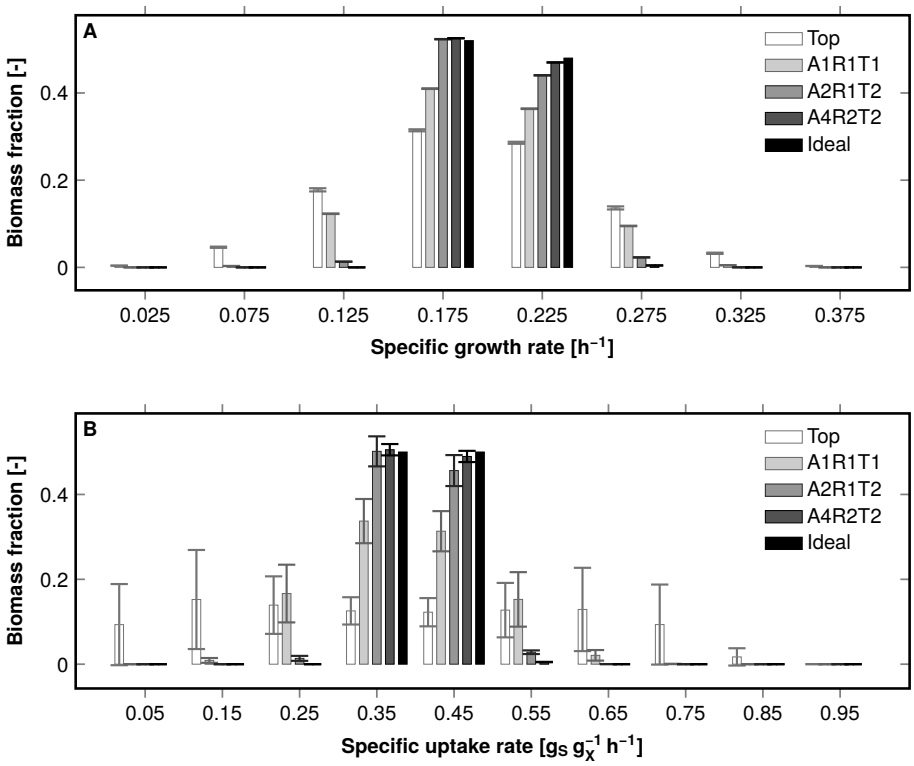

Figure S8: Simulated distribution of biomass-specific growth (A) and substrate uptake (B) rates in reactor R4 with 10 g L^{-1} biomass concentration and a 4 g L^{-1} h^{-1} substrate feed at the top or through an optimal multi-point feed. In panel A the two highest classes with only negligible biomass are not shown. The error bars represent volumetric standard deviations. The feed arrangements AxRyTz contain x axial, y radial, and z tangential coordinates (see Figure 3 in main text). The ideal homogeneous reactor results are shown for reference.

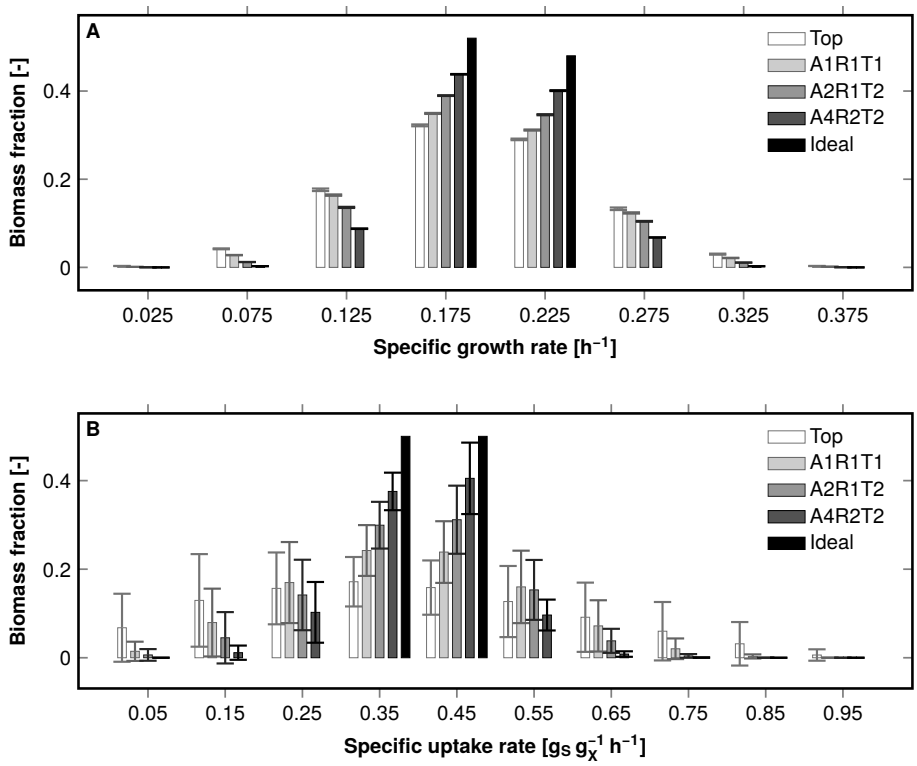

Figure S9: Simulated distribution of biomass-specific growth (A) and substrate uptake (B) rates in reactor R1 with 10 g L^{-1} biomass concentration and a 4 g L^{-1} h^{-1} substrate feed at the top or through an optimal multi-point feed. In panel A the two highest classes with only negligible biomass are not shown. The error bars represent volumetric standard deviations. The feed arrangements AxRyTz contain x axial, y radial, and z tangential coordinates (see Figure 3 in main text). The ideal homogeneous reactor results are shown for reference.

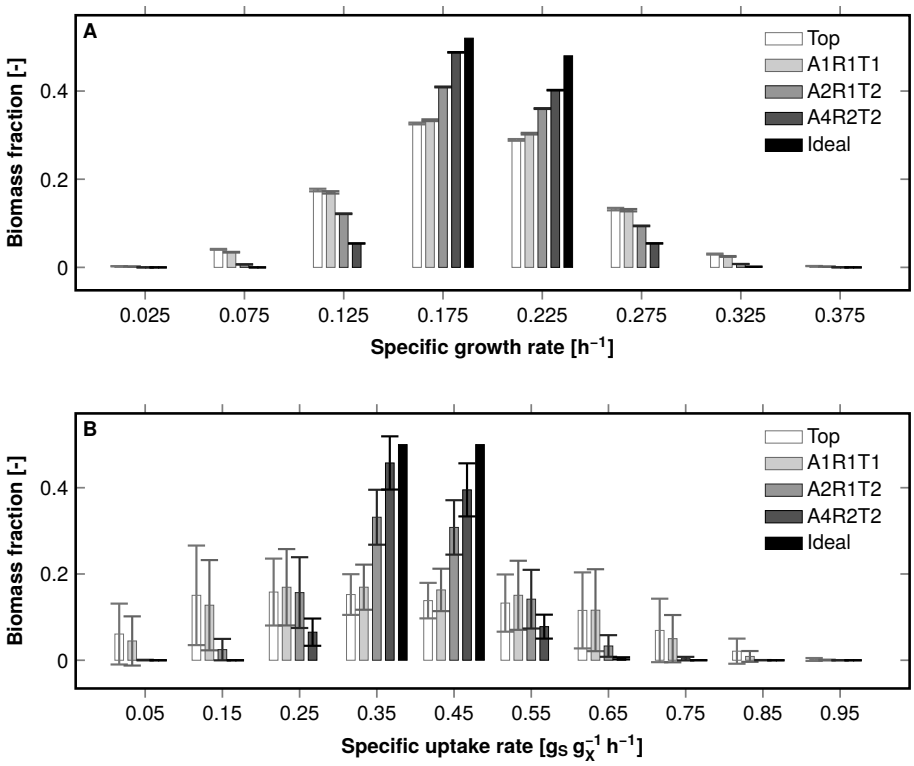

Figure S10: Simulated distribution of biomass-specific growth (A) and substrate uptake (B) rates in reactor B6 with 10 g L^{-1} biomass concentration and a 4 g L^{-1} h^{-1} substrate feed at the top or through an optimal multi-point feed. In panel A the two highest classes with only negligible biomass are not shown. The error bars represent volumetric standard deviations. The feed arrangements AxRyTz contain x axial, y radial, and z tangential coordinates (see Figure 3 in main text). The ideal homogeneous reactor results are shown for reference.

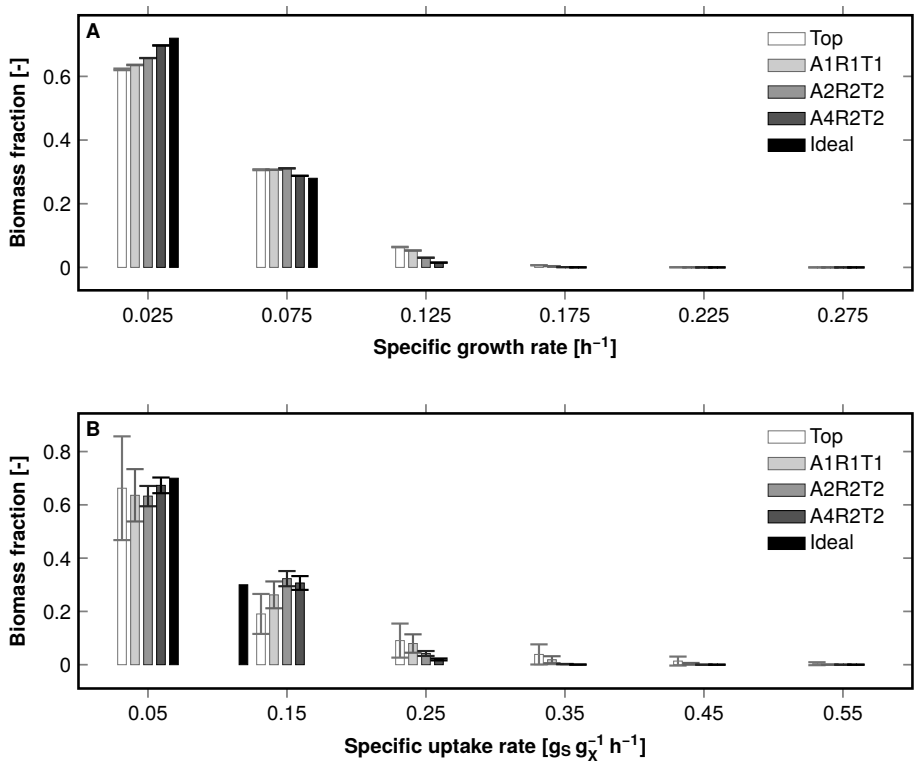

Figure S11: Simulated distribution of biomass-specific growth (A) and substrate uptake (B) rates in reactor B13 with 50 g L^{-1} biomass concentration and a 4 g L^{-1} h^{-1} substrate feed at the top or through an optimal multi-point feed. The four highest classes with only negligible biomass are not shown. The error bars represent volumetric standard deviations. The feed arrangements AxRyTz contain x axial, y radial, and z tangential coordinates (see Figure 3 in main text). The ideal homogeneous reactor results are shown for reference. The results were similar in the other reactors (R4, R1, and B6) as well (not shown).

PUBLICATION
IV

Enhanced population control in a synthetic bacterial consortium by interconnected carbon cross-feeding

Losoi, P. S., Santala, V. P., and Santala, S. M.

ACS Synthetic Biology, *8*(12), 2642–2650
https://doi.org/10.1021/acssynbio.9b00316

ACS SyntheticBiology
Cite This: ACS Synth. Biol. 2019, 8, 2642−2650
Letter
pubs.acs.org/synthbio

Enhanced Population Control in a Synthetic Bacterial Consortium by Interconnected Carbon Cross-Feeding

Pauli S. Losoi,* Ville P. Santala, and Suvi M. Santala

Faculty of Engineering and Natural Sciences, Tampere University, Hervanta campus, Korkeakoulunkatu 8, Tampere, 33720, Finland

Supporting Information

ABSTRACT: Engineered microbial consortia can provide several advantages over monocultures in terms of utilization of mixed substrates, resistance to perturbations, and division of labor in complex tasks. However, maintaining stability, reproducibility, and control over population levels in variable conditions can be challenging in multispecies cultures. In our study, we modeled and constructed a synthetic symbiotic consortium with a genetically encoded carbon cross-feeding system. The system is based on strains of *Escherichia coli* and *Acinetobacter baylyi* ADP1, both engineered to be incapable of growing on glucose on their own. In a culture supplemented with glucose as the sole carbon source, growth of the two strains is afforded by the exchange of gluconate and acetate, resulting in inherent control over carbon availability and population balance. We investigated the system robustness in terms of stability and population control under different inoculation ratios, substrate concentrations, and cultivation scales, both experimentally and by modeling. To illustrate how the system might facilitate division of genetic circuits among synthetic microbial consortia, a green fluorescent protein sensitive to pH and a slowly maturing red fluorescent protein were expressed in the consortium as measures of a circuit's susceptibility to external and internal variability, respectively. The symbiotic consortium maintained stable and linear growth and circuit performance regardless of the initial substrate concentration or inoculation ratio. The developed cross-feeding system provides simple and reliable means for population control without expression of non-native elements or external inducer addition, being potentially exploitable in consortia applications involving precisely defined cell tasks or division of labor.

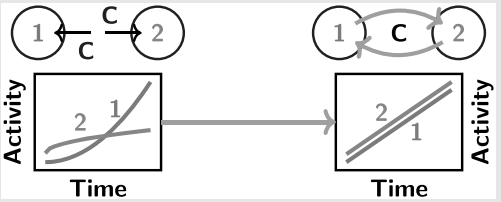

KEYWORDS: *synthetic consortium, cross-feeding, population control, consortium modeling*

Synthetic biology enables the production of new-to-nature products with rationally designed multistep pathways. Along with the increased complexity of the pathways and products, new challenges related to the functionality, stability, and overburden of the cells have emerged. Sophisticated production platforms may require timed regulation and specialized synthesis patterns executed by multilayer circuit designs.[1] For all happening in one cell, the circuits are often prone to destabilization and loss of functionality, especially in up-scaled processes.[2,3] Synthetic microbial consortia serve as an increasingly attractive platform for bioproduction due to their ability to address some of the challenges that are difficult to overcome with single-strain cultures. Benefits of consortia include for example broader metabolic diversity,[4] more efficient substrate utilization,[5−7] tolerance to perturbations and metabolic imbalances,[8] and possibility to distribute multitask operations between different cells to alleviate metabolic burden.[9] A number of applications ranging from bioremediation to drug production exploiting either natural or synthetic consortia have been recently reported.[10] For example, genetically encoded task distribution between two microbial species has been employed in the production of diterpene chemotherapeutics, oxygenated taxanes.[11] Neither of the strains was capable of producing oxygenated taxanes on its own, demonstrating the great potential of cocultures in the synthesis of complex products involving multiple reaction steps.

Despite the several advantages of coculture systems, challenges related to population control and complex (and potentially counterproductive) interactions between the different strains exist. In addition, optimizing the growth conditions for all subpopulations is more complicated than for single-strain cultures. Genetic circuits exploiting for example cell-to-cell signaling can be applied to establish spatiotemporal control over the functions of different cells.[12−14] However, it is desirable to engineer the cells for symbiotic relationship in order to improve stability and to control population ratios, competition for nutrients, and disadvantageous interactions.[15] One approach is to provide separate carbon sources for consortium members,[5,16] sometimes allowing one strain to grow only on side-products of another strain.[11,17] Examples of genetically encoded nutrient cross-feeding based on amino acid or essential metabolite exchange have also been reported.[18−20]

Modeling and predicting consortium behavior and performance is also more complicated than for monocultures.

Received: July 29, 2019
Published: November 21, 2019

DOI: 10.1021/acssynbio.9b00316
ACS Synth. Biol. 2019, 8, 2642−2650

Unstructured kinetic models are relatively straightforward to assemble and apply with cooperativity coefficients,[19,20] but a mechanistic formulation[4,18,21] demands prior knowledge of the consortium at hand. Genome-scale models have more predictive potential, but their correct application in community flux balance analysis (FBA) methods requires careful consideration of both the solution procedure and the variables and quantities involved. Many multistrain FBAs do not decouple the community members from each other, but allow for direct exchange between strains during an optimization step,[19,22] which may result in extensive and nonrealistic cross-feeding as some community members waste resources to support the rest of the community.[23] To avoid such "altruism" without employing nonlinear objective functions,[24] the strains need to be optimized separately, in a decoupled manner.[25] However, this complicates accounting for community structure without resorting to dynamic FBAs.

For a multistep production pathway, balanced production of intermediates as well as having a sufficiently long and stable production window is important.[26] When a pathway is split between several hosts,[11,16] sustaining the balance becomes even more crucial, but also more challenging. Thus, appropriate intermediate transfer rates and strict control over the growth of subpopulations are required. Some cocultures of two strains have involved a mixture of mutualistic and synergistic population dynamics, in which only one of the strains is unconditionally dependent on the interactions, whereas the other at most benefits from coexistence.[4,11,17] In this type of one-way mutualism, the control over subpopulations is somewhat loose, and may not necessarily endure in longer cultivations or with varying substrate concentrations. On the other hand, mutually obligate cross-feeding of amino acids[20] or other essential metabolites[18,19] carries a cost to the contributing strains and may be unbalanced in terms of quantity and quality. It also may interfere with the (over)-expression of the production pathway enzymes and enable the existence of noncontributing subpopulations.[27]

Given the potential constraints of essential metabolite exchange as a basis for population control, our aim in this study was to model and construct a synthetic consortium with interconnected carbon cross-feeding that sets no additional burden on the strains. The system is based solely on the cooperative utilization of a single carbon source, glucose. We employed as hosts *Escherichia coli* K-12 and the soil bacterium *Acinetobacter baylyi* ADP1, which has been previously used both in synthetic microbial consortia for removal of inhibitory compounds[17,28,29] and in production of industrially relevant compounds from various substrates.[30−32] In order to implement the cross-feeding between *E. coli* and *A. baylyi* ADP1, engineered strains incapable of glucose utilization alone were used. In minimal salts medium supplemented with glucose, *A. baylyi* ADP1 oxidizes glucose to gluconate,[33−35] which is then transported into the cells, but the Δ*gntT* mutant (high-affinity gluconate permease gene deleted) cannot import the gluconate.[36] *E. coli* Δ*ptsI* (PTS enzyme I gene deleted) in turn cannot utilize glucose,[37] but can grow on gluconate made available by *A. baylyi* ADP1 Δ*gntT*. While utilizing gluconate, *E. coli* Δ*ptsI* produces acetate[38] which serves as the carbon source for *A. baylyi* ADP1 Δ*gntT*.[28] Thus, the availability of carbon source is dependent on both strains as illustrated in Figure 1, resulting in inherent growth control. We used FBA to predict the carbon flow and unstructured kinetic modeling to investigate consortium behavior and robustness in terms of stability and population control. A generalized model of an obligately mutualistic pair, such as a pair of auxotrophs,[18−20] was also derived in order to compare the interconnected carbon cross-feeding with other two-way cross-feeding systems. To confirm the stability predicted by modeling, we performed experiments under different inoculation ratios, substrate concentrations, and cultivation scales. As a demonstration of how the population control provided by the interconnected carbon cross-feeding system might apply to division of labor among a synthetic microbial consortium, the superfolder green fluorescent protein sfGFP[39] and the monomeric red fluorescent protein mScarlet[40] were used as a surrogate of a genetic circuit distributed in the consortium. The sfGFP's pH-sensitivity[41] and the mScarlet's long maturation time[42] corresponded then to the circuit's susceptibility to external conditions and internal variability,[2] respectively.

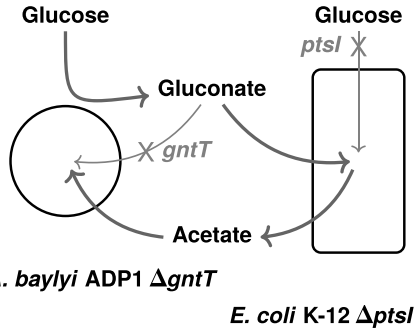

Figure 1. Carbon flow in the synthetic consortium of engineered *Escherichia coli* (Ec) and *Acinetobacter baylyi* ADP1 (Ab) based on cooperative utilization of glucose. Ab oxidizes glucose to gluconate,[33−35] but the Δ*gntT* (high-affinity gluconate permease) mutant is incapable of importing gluconate.[36] The EcΔ*ptsI* (PTS enzyme I) mutant cannot utilize glucose[37] but is capable of growing on the gluconate made available by AbΔ*gntT*. Upon growth on gluconate EcΔ*ptsI* produces acetate,[38] which in turn serves as a carbon source for AbΔ*gntT*.[28]

■ RESULTS AND DISCUSSION

To combine the strengths of both FBA and kinetic modeling, FBAs on genome-scale models[43,44] were used to predict the growth-enabling carbon cross-feeding between the glucose-negative strains, *A. baylyi* ADP1 (Ab) Δ*gntT* and *E. coli* (Ec) Δ*ptsI*, and kinetic models were used to assess the population control. Adopting the decoupled iterative scheme[25] with a slight modification, FBAs predicted that growth of a consortium of AbΔ*gntT* and EcΔ*ptsI* is enabled by conversion of glucose to gluconate by AbΔ*gntT*, growth on gluconate by EcΔ*ptsI*, and growth of AbΔ*gntT* on acetate excreted by EcΔ*ptsI* (Figure 1). The results were sensitive to oxygen availability (Supporting Information, section S1), as metabolite excretion is dependent on allowed oxygen input in FBAs.[25]

Having established that carbon cross-feeding should allow growth of the knockout strains in the coculture, the AbΔ*gntT*:EcΔ*ptsI* consortium was modeled with kinetic equations to analytically confirm whether the cross-feeding (Figure 1) results in inherent growth control as hypothetized. Considering a consortium of two strains with biomass concentrations X_1 and X_2 (mass/volume), respectively, its

DOI: 10.1021/acssynbio.9b00316
ACS Synth. Biol. 2019, 8, 2642−2650

population control can be assessed by studying the time derivative of the strain ratio X_1/X_2. Provided that the biomass concentration of strain 2 is either increasing or decreasing ($dX_2/dt \neq 0$), the change in the strain ratio with respect to time can be written as (section S2)

$$\frac{d(X_1/X_2)}{dt} = \frac{1}{X_2}\frac{dX_2}{dt}\left(\frac{dX_1/dt}{dX_2/dt} - \frac{X_1}{X_2}\right) \quad (1)$$

This formulation resembles mass or heat transfer toward an equilibrium state, in which $X_2^{-1}\,dX_2/dt$ represents the time-scale (1/time), and the difference in parentheses represents the driving force of transfer. At equilibrium the strain ratio is constant and both sides of eq 1 equal zero, which allows identifying

$$\frac{X_1}{X_2} = \frac{dX_1/dt}{dX_2/dt} \quad (2)$$

as the equilibrium ratio to which the consortium is ultimately adapting. Investigating whether this equilibrium ratio exists (eq 2 can be satisfied) and if it does, whether it is constant or variable, allows predicting whether the relative population levels are volatile or stable, respectively. Defining the equilibrium ratio also enables analytical comparison of consortia that have different population dynamics.

Considering then an unstructured kinetic model of the AbΔ*gntT*:EcΔ*ptsI* consortium in batch culture with growth according to the Monod equation, conversion of glucose to gluconate by AbΔ*gntT*, consumption of gluconate and excretion of acetate by EcΔ*ptsI*, and consumption of acetate by AbΔ*gntT*, the equilibrium ratio of AbΔ*gntT* to EcΔ*ptsI* simplifies to (sections S2.1 and S2.2)

$$\frac{X_{Ab}}{X_{Ec}} = \frac{Y_{AX}Y_{NA}}{Y_{NX}} \quad (3)$$

given that the concentration of acetate (A) is constant ($dA/dt = 0$). In eq 3, Y_{AX} is the yield of Ab biomass on acetate, Y_{NX} is the yield of Ec biomass on gluconate, and Y_{NA} is the yield of acetate on gluconate (mass/mass). Numerical integrations of the ordinary differential equation (ODE) system consisting of concentrations of AbΔ*gntT* and EcΔ*ptsI* biomasses, glucose, gluconate, and acetate resulted invariably in acetate reaching a steady state of constant concentration after an initial accumulation period (Supporting Information, Figure S2), which supported the assumption of constant acetate concentration used in deriving eq 3. Equation 3 then effectively states that the equilibrium ratio of AbΔ*gntT* to EcΔ*ptsI* is determined solely by how much acetate is produced from gluconate by EcΔ*ptsI* (Y_{NA}) and how much biomass can be formed from acetate by AbΔ*gntT* (Y_{AX}) and from gluconate by EcΔ*ptsI* (Y_{NX}). Consequently the equilibrium ratio should even be adjustable, for example by genetically engineering *E. coli* to excrete more acetate.[11] Considering the yield coefficients as constants, eq 3 furthermore implies tight population control toward an unchanging, stable strain ratio. For comparison, an equivalent result was obtained with a generalized model of an obligately mutualistic pair (section S2.4), such as a pair of auxotrophs.[18−20] Tight population control seems therefore to be a general property of mutually obligate cross-feeding. The conducted modeling also allowed the stable equilibrium ratio of mutually obligate cross-feeding to emerge as a result, in contrast to models that utilize cooperativity coefficients and implicitly assume a stable equilibrium ratio (section S2.5).

In order to assess whether a stable equilibrium strain ratio is unique to obligate mutualism, similar expressions of equilibrium ratios were also derived for three other consortia of *A. baylyi* ADP1 and *E. coli* by pairing both the wild-type and knockout strains (section S2.2). The resulting consortia Ab:Ec, AbΔ*gntT*:Ec, and Ab:EcΔ*ptsI* corresponded to competition, commensialism, and cooperator−cheater dynamics, respectively. After solving the associated ODE systems numerically, it was concluded that none of these consortia without the two-way coupling had a stable equilibrium ratio in the same sense as AbΔ*gntT*:EcΔ*ptsI*. The equilibrium ratios of these three consortia either existed only under too restrictive conditions or were susceptible to acetate fluctuations, as $dA/dt \approx 0$ did not apply (sections S2.2 and S2.3). As the equilibrium ratios were not stable but nonexistent or changing over time, the other consortia were under looser control. These simple kinetic analyses highlighted how the interconnected carbon cross-feeding system present in AbΔ*gntT*:EcΔ*ptsI* enhances population control by defining a stable equilibrium ratio of strains. As a consequence, a distributed expression of circuits or pathways can be expected to be more balanced in AbΔ*gntT*:EcΔ*ptsI*. Other mutualistic pairs[18−20] have the same advantage in general, but often with the cost of sharing essential metabolites, which imposes additional burden on the strains.

Having identified the interconnected carbon cross-feeding as a promising system, the consortia were studied experimentally to confirm the predictions presented above. *A. baylyi* ADP1 and *E. coli* were genetically engineered to express mScarlet and sfGFP, respectively, under a constitutive promoter, and the genes were integrated into genomes to avoid unpredictable plasmid copy number effects[45] and to more accurately represent the performance of each strain in the consortium. A gene cassette[46] carrying sfGFP under the constitutive promoter BBa_J23100 and a gentamicin resistance gene was introduced to wild-type Ec and knockout EcΔ*ptsI* genomes by ϕ80 phage integrase,[47] yielding the fluorescent strains designated as Eg and Ekg, respectively. For Ab and AbΔ*gntT*, sfGFP was replaced by mScarlet, and a gene cassette[48] containing appropriate flanking regions and a chloramphenicol resistance gene was utilized to facilitate genomic integration to the neutral[48] locus ACIAD3381 (*poxB*, pyruvate dehydrogenase) by natural transformation. The resulting fluorescent Ab and AbΔ*gntT* strains were designated as Ar and Akr. Table 1 summarizes the strains constructed and utilized in this work.

The eight strains were then cultivated for 45−47 h in small scale (200 μL) at 30 °C in a minimal medium with 50 mM glucose as the sole carbon source. All strains were cultured as three biological replicates in isolation and in all 16 possible Ab:Ec-pairs. Akin to previous studies involving obligately cross-feeding consortia,[18−20] none of the knockout strains could grow in isolation, but each consortium, and remarkably also the double knockout ones, accumulated a considerable optical density at 600 nm (OD_{600}) (Figure S6). However, all consortia with two knockout strains (Ak or Akr with Ek or Ekg) also grew slower than the other consortia with one or no knockout strains.[19] This can be attributed to both EcΔ*ptsI* and AbΔ*gntT* growing only on substrates derived from glucose, namely gluconate and acetate, respectively, which inevitably were less available (0 mM at time t = 0 h) than glucose initially at time t = 0 h (50 mM). Fluorescence intensities

DOI: 10.1021/acssynbio.9b00316
ACS Synth. Biol. 2019, 8, 2642−2650

Table 1. Constructed and Utilized Strains[a]

	description	source
Ab	*A. baylyi* ADP1	DSM 24193
Ak	Ab Δ*gntT*::Kan(R)	36
Ar	Ab Δ*poxB*::mScarlet	this work
Akr	Ak Δ*poxB*::mScarlet	this work
Ec	*E. coli* BW25113	CGSC 7636
Ek	Ec Δ*ptsI*::Kan(R)	CGSC 9918[37]
Eg	Ec *attϕ*80::sfGFP	this work
Ekg	Ek *attϕ*80::sfGFP	this work

[a]The kanamycin resistant Kan(R) glucose knock-out strains are designated with k, sfGFP-carrying strains with g, and mScarlet-carrying strains with r. The mScarlet and sfGFP cassettes carried also resistance genes for chloramphenicol and gentamicin, respectively. DSM stands for Deutsche Sammlung von Mikroorganismen und Zellkulturen and CGSC for Yale University Coli Genetic Stock Center.

corresponding to emission maxima of sfGFP and mScarlet also grew considerably, but only if a strain with the corresponding fluorescent protein gene was present in the culture (Figure S7). The steady rise of not only OD_{600}, but also of both sfGFP and mScarlet fluorescences when applicable therefore indicated that both knockout strains grew in the Ab*ΔgntT*:Ec*ΔptsI* consortia as FBAs predicted.

An additional 18 h cultivation of Akr:Ekg at the same conditions in a 0.5 L aerated bioreactor resulted likewise in growth of both OD_{600} and fluorescences (section S6), demonstrating scalability of the carbon cross-feeding. High-performance liquid chromatograph analyses of the cultivation further supported the carbon flow (Figure 1) indicated by FBAs. Traces of gluconate were detected, and in accordance with the numerical integrations of the kinetic model of Ab*ΔgntT*:Ec*ΔptsI*, no acetate accumulated (sections S2.3 and S6). The cross-feeding not only enabled growth of the knockout strains, but also kept the overall carbon flow in balance. On the other hand, the slowness of growth afforded by the two-way cross-feeding is disadvantageous from a bioprocessing perspective, as it could lead to prohibitively low overall productivities if the system were to be applied in production of bulk chemicals.[49] Identifying the limiting intermediate, likely acetate in this case (section S6), and increasing its rate of production[11] could elevate the overall growth rate. Another challenge is that the present implementation is based on pure glucose as the carbon source. This could complicate the system's application at large scale, as cost considerations make heterogeneous feed mixtures preferable in industry.[50]

As the unstructured kinetic model predicted interconnected carbon cross-feeding to result in a stable equilibrium ratio (eq 3), the stability of Ab*ΔgntT*:Ec*ΔptsI* was tested experimentally with respect to time and initial substrate concentration by monitoring fluorescence of the mScarlet:sfGFP model circuit embedded in Akr:Ekg. The small-scale experiments were repeated under initial glucose concentrations of 50 mM, 100 mM, 200 mM, and the OD_{600} and fluorescences measured from Akr:Ekg and Ar:Eg (Ab*ΔgntT*:Ec*ΔptsI* and Ab:Ec with mScarlet and sfGFP) are shown in Figure 2. The knockout

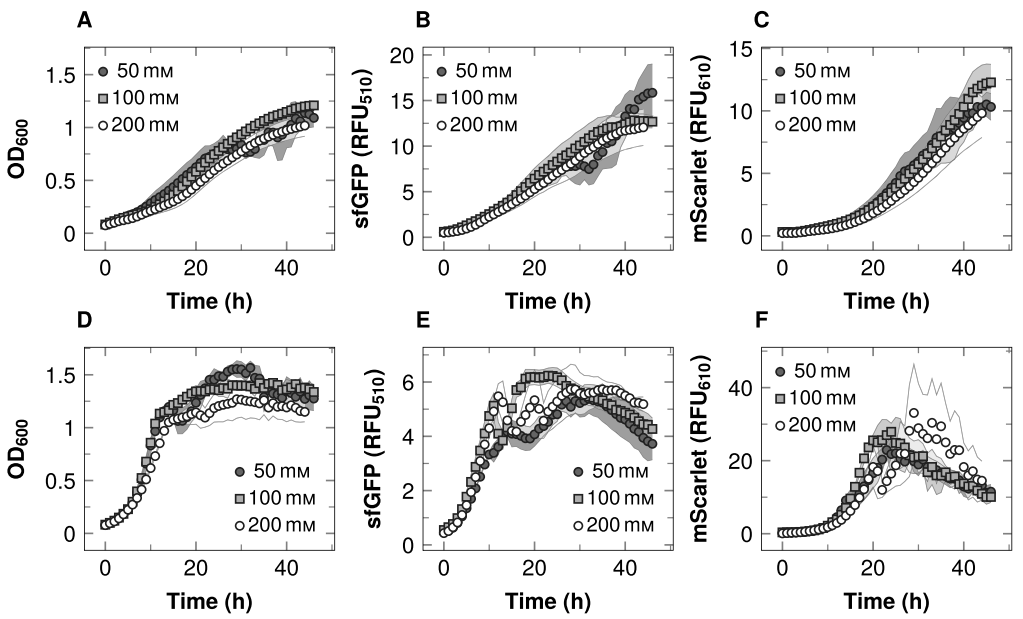

Figure 2. Effect of initial glucose concentration on Akr:Ekg (A, B, C) and Ar:Eg (D, E, F) consortia in a defined medium at 30 °C. Optical density at 600 nm (A, D) and fluorescence intensities corresponding to sfGFP at 510 nm (B, E) and to mScarlet at 610 nm (C, F) were measured. Fluorescence intensities are reported in the relative fluorescence units (RFUs) of the plate reader divided by 1000. Each line stands for an initial glucose concentration, and the data are shown as means of six biological replicates. Shaded areas represent sample standard deviations. At some points the error bands are smaller than the markers. For clarity, the data are presented hourly.

DOI: 10.1021/acssynbio.9b00316
ACS Synth. Biol. 2019, 8, 2642−2650

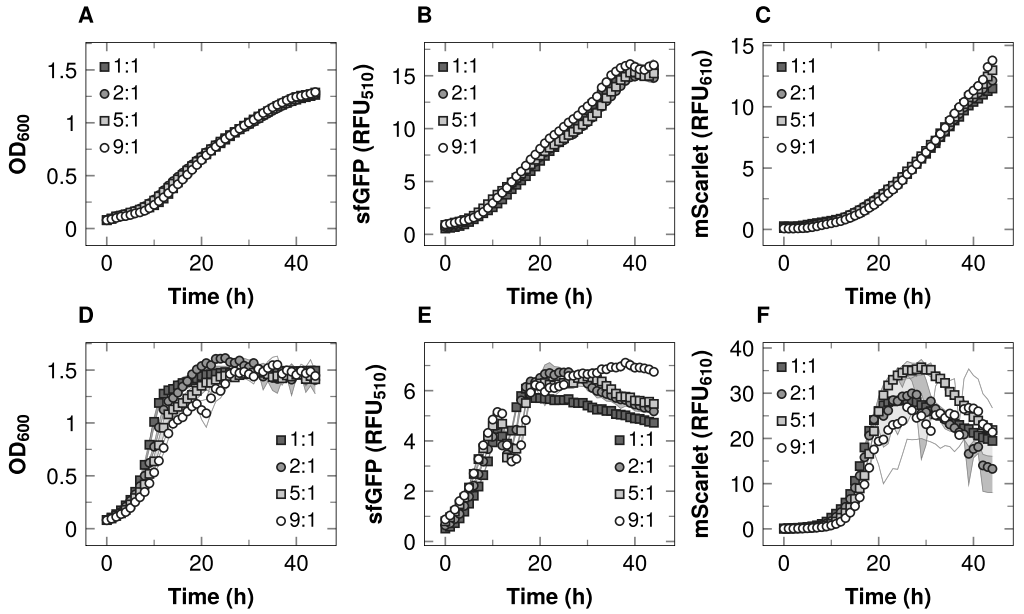

Figure 3. Effect of inoculation ratios on Akr:Ekg (A, B, C) and Ar:Eg (D, E, F) consortia cultivated in a defined medium with 100 mM glucose at 30 °C. Optical density at 600 nm (A, D) and fluorescence intensities corresponding to sfGFP at 510 nm (B, E) and to mScarlet at 610 nm (C, F) were measured. Each line represents an initial Ec to Ab ratio in terms of OD_{600}. RFUs stand for the plate reader's relative fluorescence units divided by 1000. The data are presented as means of three biological replicates with shaded areas representing sample standard deviations. The error bands for Akr:Ekg are smaller than the markers. The data are shown hourly for clarity.

strains Akr and Ekg were cultured also in isolation at the same time as negative controls (Figure S8), and no growth was observed. The initial glucose concentration of 25 mM was also tested, but these cultivations were exhausted too quickly to be compared with the others. The initial glucose concentration had no discernible effect on growth or fluorescence of either Akr:Ekg or Ar:Eg. Regardless of initial concentration of glucose, Ar:Eg followed a typical batch growth pattern of lag, exponential, and stationary phases, whereas Akr:Ekg grew in a much more steady and linear fashion. The same trends applied also to sfGFP and mScarlet fluorescences. In accordance with the analytically predicted stable equilibrium ratio, Akr:Ekg maintained the balance between mScarlet and sfGFP; averaged over the three initial glucose concentrations, the ratio of mScarlet to sfGFP varied by a factor of 3.3 ± 1.3 (max/min) in Akr:Ekg, whereas in Ar:Eg the factor was over 5-fold larger (18.4 ± 7.4) as mScarlet reached maximum activity several hours after sfGFP. The uncertainty derives from mScarlet and sfGFP sample standard deviations propagating error to mScarlet-sfGFP and max-min ratios and to averaging max/min over the three experiments containing six biological replicates each. In terms of balanced expression required by multilayer circuits and multistep production pathways,[11−14,16,26] Akr:Ekg was superior to the wild-type Ar:Eg consortium.

It was then tested whether the presented carbon flow in Ab*ΔgntT*:Ec*ΔptsI* would stabilize growth and distributed expression by exerting control also over initial strain ratio as could be expected based on the kinetic model. The Akr:Ekg consortium and Ar:Eg for reference were cultivated with initial Ec to Ab ratios of 1:1, 2:1, 5:1, and 9:1 in terms of OD_{600} using 100 mM glucose as the carbon source at otherwise same conditions. The courses of these cultivations are shown in Figure 3, and to further emphasize the difference between Akr:Ekg and Ar:Eg, the ratio of mScarlet to sfGFP is depicted in Figure 4. As before, the knockout strains Akr and Ekg were cultured also in isolation as negative controls (Figure S8), and no growth was observed. Agreeing with the analytically predicted stable equilibrium ratio, the variation in inoculum composition caused practically no variation at all in Akr:Ekg performance: OD_{600} and both fluorescences rose as almost linear functions of time with nearly identical slopes. With higher proportions of Ab in inoculum the ratio of mScarlet to sfGFP fluorescence was proportionally higher at first, but Akr:Ekg stabilized the ratio remarkably well to similar low-sloped linear functions of time. Ar:Eg, however, displayed imbalances in mScarlet and sfGFP activities similarly to the earlier experiments with varying initial substrate concentrations. Additionally, a sharp decline in sfGFP activity was observed at 15 h with higher initial Ec proportions. This was likely caused by Ec acidifying the culture,[17] which in turn would have reduced sfGFP fluorescence:[41] pH declined clearly in larger-scale cultivations of Ar:Eg (with equal proportions of Ab and Ec initially) and Ec in isolation (Figure S9). In contrast to Ar:Eg, the long and stable production window demonstrated by Akr:Ekg for up to 40 h underlined how the interconnected cross-feeding system stabilized the distributed circuit also against external factors (modeled by sfGFP's pH sensitivity) and internal variability (represented by mScarlet's long maturation time).

DOI: 10.1021/acssynbio.9b00316
ACS Synth. Biol. 2019, 8, 2642−2650

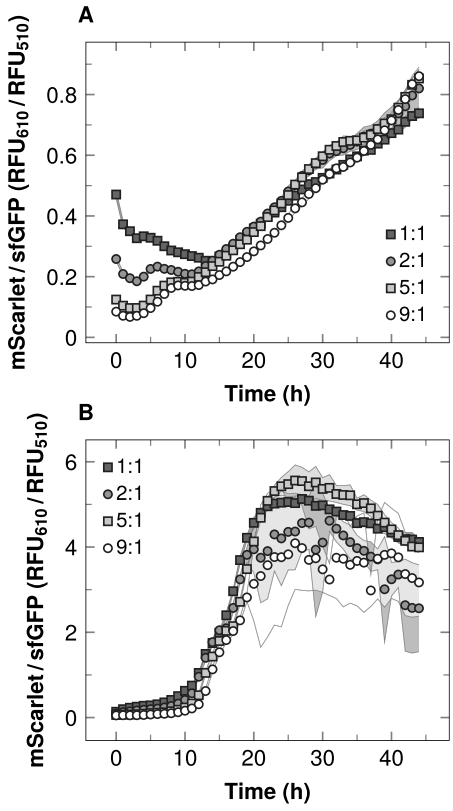

Figure 4. Effect of consortium inoculation ratios on the balance between mScarlet and sfGFP in Akr:Ekg (A) and Ar:Eg (B) consortia. Cultivations were performed with Ec to Ab inoculation ratios of 1:1, 2:1, 5:1, and 9:1 in terms of OD_{600} at 30 °C in a defined medium with 100 mM glucose. RFUs at 510 nm and 610 nm are the relative fluorescence units of the microwell plate reader divided by 1000. Three biological replicates were cultivated, and the presented data are ratios of mScarlet means to sfGFP means. Shaded areas correspond to sample standard deviations. For Akr:Ekg the error bands are mostly smaller than the markers. The data are presented hourly for clarity.

Unlike the cross-feeding system presented in this work, where neither of the strains grows directly on the provided substrate, many cross-feeding concepts have involved a one-way coupling of carbon flow, where one of the strains grows on the supplied substrate and the other one grows on products of the initially growing strain.[4,11,17,29] The equilibrium ratio afforded by such one-way carbon flow also has a stable term analogous to eq 3 (section S2.2), and published performances of such consortia also point at stable functioning. However, as growth and metabolism of one strain is not constrained by the other, the equilibrium ratio is susceptible to a transient term as well (section S2.2). Consequently stability is not as universally guaranteed as in mutually obligate cross-feeding, which in general results in a stable equilibrium ratio (section S2.4). Previous implementations of mutually obligate cross-feeding have been based on exchange of biosynthetically costly metabolites[18−20] required and utilized by all consortium members simultaneously. Exchange of essential metabolites carries an additional cost to the contributing strains, which might give rise to noncontributing, cheating subpopulations.[27] Release of essential metabolites may also be delayed until near cell death.[18] Altogether such metabolites are not as readily exchanged as gluconate and acetate, which are costless[25] side-products not utilized by the contributing Ab and Ec strains themselves[19] in AbΔ*gntT*:EcΔ*ptsI*.

The presented carbon cross-feeding system has therefore several advantages compared to other forms of population control: it does not require expression of non-native genes as it is based entirely on native host metabolism, it imposes predictable and robust equilibrium strain ratios, it does not demand the strains to donate essential metabolites required by themselves, and it provides easily modelable and optimizable, almost linear growth and expression patterns. The system was functional even across cultivation scales, and it should be applicable in balancing distributed expression of circuits[9] or pathways[6,11,16] without separate feeds[5,16] or adjustment of inoculation ratios.[7,16] The cross-feeding system should also be less susceptible to fluctuating conditions[2] and deleterious mutations[3] than systems based on external inducers[2,6,26] or complex genetic circuitry,[1,2,9,12−14] as it is implemented by only two simple gene deletions. Conversely, the developed system is host-specific and not necessarily directly transferable to other species, but introducing non-native genes in implementing the cross-feeding might enable its generalization. On the basis of the presented theoretical analyses and experimental results, it is concluded that interconnected carbon cross-feeding provides simple yet reliable population control, and consequently an attractive platform for balanced and robust expression of distributed genetic circuits[9,13] or production pathways.[11,16] An application of AbΔ*gntT*:EcΔ*ptsI* could for example combine production of lipid molecules[29,30] or breakdown of aromatic compounds[31,32] by Ab with an upgrade by a heterologous downstream module in Ec.

■ METHODS

Strain Construction. The wild-type strains designated as Ab and Ec were *A. baylyi* ADP1 (DSM 24193) and *E. coli* K-12 BW25113 (CGSC 7636), respectively. The knockout strain AbΔ*gntT* (ACIAD0544 high-affinity gluconate permease gene deleted)[36] was a kind gift from Véronique de Berardinis (Genoscope, France) and EcΔ*ptsI* (PTS enzyme I gene deleted)[37] was obtained from Yale University Coli Genetic Stock Center (CGSC 9918). In both knockout strains the deleted gene is replaced by a kanamycin resistance gene. All the fluorescent strains Ar, Akr, Eg, and Ekg constructed in this work had a genomically integrated fluorescent protein expression cassette along with a chloramphenicol (Ab) or gentamicin (Ec) resistance gene for selection.

Genomic integrations of the sfGFP expression cassette into Ec and EcΔ*ptsI* were performed with conditional-replication, integration, and modular (CRIM) plasmids as described previously.[47] The CRIM plasmids Burden Monitor phi80 version (Addgene plasmid no. 66074) and pAH123 (Addgene plasmid no. 66077) were kind gifts from Tom Ellis.[46] Supporting Information section S4 contains additional details.

The mScarlet cassette was similar to the sfGFP cassette[46] in design (section S3), and it was ordered from GenScript (New Jersey, USA). For integration into *A. baylyi* ADP1 genome, the mScarlet cassette was inserted within a gene cassette[48] overwriting the neutral ACIAD3381-locus (*poxB*, pyruvate

DOI: 10.1021/acssynbio.9b00316
ACS Synth. Biol. 2019, 8, 2642−2650

dehydrogenase). The cassette was integrated into Ab and AbΔ*gntT* by natural transformation in the solid phase by pipetting 300 ng of the transforming DNA directly on single colonies on LA plates (15 g/L agar, 10 g/L tryptone, 5 g/L yeast extract, 1 g/L NaCl, and 10 g/L glucose). The plates were incubated overnight at room temperature, and the colonies were replated on other LA plates with 25 mg/L chloramphenicol for selection.

Small-Scale Cultivations. Small-scale cultivations were performed with 200 μL culture volumes on 96-well plates in a mineral salts medium[51] (section S5) with 50 mM, 100 mM, and 200 mM glucose as the carbon source. The plates were incubated in a Spark multimode microplate reader (Tecan, Switzerland) with temperature control set to 30 °C. Optical density at 600 nm, and fluorescence intensities with excitation−emission filter-pairs of 485−510 nm (sfGFP) and 580−610 nm (mScarlet) were recorded every 30 min. Gain was set to a fixed value of 50 for the fluoresence measurements. Plates were shaken in between measurements. Precultivations were performed in the same medium with 10 mM Na-acetate, 10 mM Na-gluconate, and 10 mM glucose as the carbon sources at 30 °C with 300 rpm shaking. The targeted initial OD_{600} for the microwell plates was 0.1.

Numerical Work. Data analyses and ODE integrations were performed using the Python programming language (http://www.python.org) along with scipy,[52] numpy,[53] and pandas[54] packages. The cobrapy package[55] was utilized for FBAs. Sample standard deviations s_f of functions f with variables x_i were calculated including error propagation with zero covariance: $s_f = \left(\sum_{i=1}^{k} (\partial f/\partial x_i)^2 s_{x_i}^2\right)^{1/2}$.

FBAs were conducted according to a previously described iterative scheme,[25] but with an additional step prepended to each iteration: first the glucose importing exchange reaction was maximized, and the maximized value was set as a fixed bound for the subsequent growth rate maximizing optimization step. After growth reaction maximization, an additional minimization of the sum of all gene-associated flux was carried out as described,[25] but given also the constraint of maximized glucose import. Contrary to the previously presented method,[25] secreted metabolites were incorporated into computational medium in subsequent iteration regardless of growth status. The utilized genome-scale models of *A. baylyi* ADP1 and *E. coli* were iAbaylyiv4[44] and iAF1260,[43] respectively. Computational medium was made to resemble the defined medium used in experiments. Section S1 contains additional details.

■ ASSOCIATED CONTENT

Supporting Information

The Supporting Information is available free of charge at https://pubs.acs.org/doi/10.1021/acssynbio.9b00316.

Additional results, discussion, and methods for flux balance analyses, kinetic modeling, strain and plasmid construction, and experiments (PDF)

■ AUTHOR INFORMATION

Corresponding Author

*E-mail: pauli.losoi@tuni.fi.

ORCID

Pauli S. Losoi: 0000-0002-1319-6503

Author Contributions

P.S.L., V.P.S., and S.M.S. designed the study. P.S.L. performed modeling, strain construction, and larger-scale experiments. V.P.S. and S.M.S. performed small-scale experiments and supervised the study.

Notes

The authors declare no competing financial interest.

■ ACKNOWLEDGMENTS

Funding was provided by Academy of Finland (Grant Nos. 310135 and 310188) and Tampere University of Technology Graduate School (P.S.L.). The authors thank Tapio Lehtinen for his comments on the manuscript.

■ REFERENCES

(1) Gupta, A., Brockman Reizman, I. M., Reisch, C. R., and Prather, K. L. J. (2017) Dynamic regulation of metabolic flux in engineered bacteria using a pathway-independent quorum-sensing circuit. *Nat. Biotechnol. 35*, 273−279.

(2) Moser, F., Broers, N. J., Hartmans, S., Tamsir, A., Kerkman, R., Roubos, J. A., Bovenberg, R., and Voigt, C. A. (2012) Genetic Circuit Performance Under Conditions Relevant for Industrial Bioreactors. *ACS Synth. Biol. 1*, 555−564.

(3) Rugbjerg, P., Myling-Petersen, N., Porse, A., Sarup-Lytzen, K., and Sommer, M. O. A. (2018) Diverse genetic error modes constrain large-scale bio-based production. *Nat. Commun. 9*, 787.

(4) Minty, J. J., Singer, M. E., Scholz, S. A., Bae, C., Ahn, J., Foster, C. E., Liao, J. C., and Lin, X. N. (2013) Design and characterization of synthetic fungal-bacterial consortia for direct production of isobutanol from cellulosic biomass. *Proc. Natl. Acad. Sci. U. S. A. 110*, 14592−14597.

(5) Xia, T., Eiteman, M. A., and Altman, E. (2012) Simultaneous utilization of glucose, xylose and arabinose in the presence of acetate by a consortium of *Escherichia coli* strains. *Microb. Cell Fact. 11*, 77.

(6) Shin, H., McClendon, S., Vo, T., and Chen, R. R. (2010) *Escherichia coli* Binary Culture Engineered for Direct Fermentation of Hemicellulose to a Biofuel. *Appl. Environ. Microbiol. 76*, 8150−8159.

(7) Tsai, S., Goyal, G., and Chen, W. (2010) Surface Display of a Functional Minicellulosome by Intracellular Complementation Using a Synthetic Yeast Consortium and Its Application to Cellulose Hydrolysis and Ethanol Production. *Appl. Environ. Microbiol. 76*, 7514−7520.

(8) Shade, A., Peter, H., Allison, S. D., Baho, D. L., Berga, M., Bürgmann, H., Huber, D. H., Langenheder, S., Lennon, J. T., Martiny, J. B., Matulich, K. L., Schmidt, T. M., and Handelsman, J. (2012) Fundamentals of microbial community resistance and resilience. *Front. Microbiol. 3*, 417.

(9) Regot, S., Macia, J., Conde, N., Furukawa, K., Kjellén, J., Peeters, T., Hohmann, S., de Nadal, E., Posas, F., and Solé, R. (2011) Distributed biological computation with multicellular engineered networks. *Nature 469*, 207−211.

(10) Roell, G. W., Zha, J., Carr, R. R., Koffas, M. A., Fong, S. S., and Tang, Y. J. (2019) Engineering microbial consortia by division of labor. *Microb. Cell Fact. 18*, 35.

(11) Zhou, K., Qiao, K., Edgar, S., and Stephanopoulos, G. (2015) Distributing a metabolic pathway among a microbial consortium enhances production of natural products. *Nat. Biotechnol. 33*, 377−383.

(12) Basu, S., Gerchman, Y., Collins, C. H., Arnold, F. H., and Weiss, R. (2005) A synthetic multicellular system for programmed pattern formation. *Nature 434*, 1130−1134.

(13) Tamsir, A., Tabor, J. J., and Voigt, C. A. (2011) Robust multicellular computing using genetically encoded NOR gates and chemical 'wires'. *Nature 469*, 212−215.

(14) Chen, Y., Kim, J. K., Hirning, A. J., Josić, K., and Bennett, M. R. (2015) Emergent genetic oscillations in a synthetic microbial consortium. *Science 349*, 986−989.

(15) Johns, N. I., Blazejewski, T., Gomes, A. L. C., and Wang, H. H. (2016) Principles for designing synthetic microbial communities. *Curr. Opin. Microbiol. 31*, 146−153.
(16) Zhang, H., Pereira, B., Li, Z., and Stephanopoulos, G. (2015) Engineering *Escherichia coli* coculture systems for the production of biochemical products. *Proc. Natl. Acad. Sci. U. S. A. 112*, 8266−8271.
(17) Santala, S., Karp, M., and Santala, V. (2014) Rationally Engineered Synthetic Coculture for Improved Biomass and Product Formation. *PLoS One 9*, e113786.
(18) Shou, W., Ram, S., and Vilar, J. M. G. (2007) Synthetic cooperation in engineered yeast populations. *Proc. Natl. Acad. Sci. U. S. A. 104*, 1877−1882.
(19) Wintermute, E. H., and Silver, P. A. (2010) Emergent cooperation in microbial metabolism. *Mol. Syst. Biol. 6*, 407.
(20) Mee, M. T., Collins, J. J., Church, G. M., and Wang, H. H. (2014) Syntrophic exchange in synthetic microbial communities. *Proc. Natl. Acad. Sci. U. S. A. 111*, E2149−E2156.
(21) Schmidt, J. K., Riedele, C., Regestein, L., Rausenberger, J., and Reichl, U. (2011) A Novel Concept Combining Experimental and Mathematical Analysis for the Identification of Unknown Interspecies Effects in a Mixed Culture. *Biotechnol. Bioeng. 108*, 1900−1911.
(22) Khandelwal, R. A., Olivier, B. G., Röling, W. F. M., Teusink, B., and Bruggeman, F. J. (2013) Community Flux Balance Analysis for Microbial Consortia at Balanced Growth. *PLoS One 8*, e64567.
(23) Koch, S., Benndorf, D., Fronk, K., Reichl, U., and Klamt, S. (2016) Predicting compositions of microbial communities from stoichiometric models with applications for the biogas process. *Biotechnol. Biofuels 9*, 17.
(24) Zomorrodi, A. R., and Maranas, C. D. (2012) OptCom: A Multi-Level Optimization Framework for the Metabolic Modeling and Analysis of Microbial Communities. *PLoS Comput. Biol. 8*, e1002363.
(25) Pacheco, A. R., Moel, M., and Segrè, D. (2019) Costless metabolic secretions as drivers of interspecies interactions in microbial ecosystems. *Nat. Commun. 10*, 103.
(26) Santos, C. N. S., Koffas, M., and Stephanopoulos, G. (2011) Optimization of a heterologous pathway for the production of flavonoids from glucose. *Metab. Eng. 13*, 392−400.
(27) Gore, J., Youk, H., and van Oudenaarden, A. (2009) Snowdrift game dynamics and facultative cheating in yeast. *Nature 459*, 253−256.
(28) Kannisto, M. S., Mangayil, R. K., Shrivastava-Bhattacharya, A., Pletschke, B. I., Karp, M. T., and Santala, V. P. (2015) Metabolic engineering of *Acinetobacter baylyi* ADP1 for removal of *Clostridium butyricum* growth inhibitors produced from lignocellulosic hydrolysates. *Biotechnol. Biofuels 8*, 198.
(29) Salmela, M., Lehtinen, T., Efimova, E., Santala, S., and Mangayil, R. (2018) Metabolic pairing of aerobic and anaerobic production in a one-pot batch cultivation. *Biotechnol. Biofuels 11*, 187.
(30) Santala, S., Efimova, E., and Santala, V. (2018) Dynamic decouplig of biomass and wax ester biosynthesis in *Acinetobacter baylyi* by an autonomously regulated switch. *Metab. Eng. Commun. 7*, e00078.
(31) Luo, J., Lehtinen, T., Efimova, E., Santala, V., and Santala, S. (2019) Synthetic metabolic pathway for the production of 1-alkenes from lignin-derived molecules. *Microb. Cell Fact. 18*, 48.
(32) Salmela, M., Lehtinen, T., Efimova, E., Santala, S., and Santala, V. (2019) Alkane and wax ester production from lignin-related aromatic compounds. *Biotechnol. Bioeng. 116*, 1934−1945.
(33) Taylor, W. H., and Juni, E. (1961) Pathways for Biosynthesis of a Bacterial Capsular Polysaccharide. I. Characterization of the Organism and Polysaccharide. *J. Bacteriol. 81*, 688−693.
(34) Taylor, W. H., and Juni, E. (1961) Pathways for Biosynthesis of a Bacterial Capsular Polysaccharide. II. Carbohydrate Metabolism and Terminal Oxidation Mechanisms of a Capsule-Producing Coccus. *J. Bacteriol. 81*, 694−703.
(35) Vaneechouette, M., Young, D. M., Ornston, L. N., de Baere, T., Nemec, A., van der Reijden, T., Carr, E., Thernberg, I., and Dijkshoorn, L. (2006) Naturally Transformable *Acinetobacter* sp. Strain ADP1 Belongs to the Newly Described Species *Acinetobacter baylyi*. *Appl. Environ. Microbiol. 72*, 932−936.
(36) de Berardinis, V., et al. (2008) A complete collection of single-gene deletion mutants of *Acinetobacter baylyi* ADP1. *Mol. Syst. Biol. 4*, 174.
(37) Baba, T., Ara, T., Hasegawa, M., Takai, Y., Okumura, Y., Baba, M., Datsenko, K. A., Tomita, M., Wanner, B. L., and Mori, H. (2006) Construction of *Escherichia coli* K-12 in-frame, single-gene knockout mutants: the Keio collection. *Mol. Syst. Biol. 2*, 2006.0008.
(38) Enjalbert, B., Millard, P., Dinclaux, M., Portais, J., and Letisse, F. (2017) Acetate fluxes in *Escherichia coli* are determined by the thermodynamic control of the Pta-AckA pathway. *Sci. Rep. 7*, 42135.
(39) Pédelacq, J., Cabantous, S., Tran, T., Terwilliger, T. C., and Waldo, G. S. (2006) Engineering and characterization of a superfolder green fluorescent protein. *Nat. Biotechnol. 24*, 79−88.
(40) Bindels, D. S., Haarbosch, L., van Weeren, L., Postma, M., Wiese, K. E., Mastop, M., Aumonier, S., Gotthard, G., Royant, A., Hink, M. A., and Gadella, T. W. J., Jr (2017) mScarlet: a bright monomeric red fluorescent protein for cellular imaging. *Nat. Methods 14*, 53−56.
(41) Roberts, T. M., Rudolf, F., Meyer, A., Pellaux, R., Whitehead, E., Panke, S., and Held, M. (2016) Identification and Characterization of a pH-stable GFP. *Sci. Rep. 6*, 28166.
(42) Balleza, E., Kim, J. M., and Cluzel, P. (2018) Systematic characterization of maturation time of fluorescent proteins in living cells. *Nat. Methods 15*, 47−51.
(43) Feist, A. M., Henry, C. S., Reed, J. L., Krummenacker, M., Joyce, A. R., Karp, P. D., Broadbelt, L. J., Hatzimanikatis, V., and Palsson, B. O. (2007) A genome-scale metabolic reconstruction for *Escherichia coli* K-12 MG1655 that accounts for 1260 ORFs and thermodynamic information. *Mol. Syst. Biol. 3*, 121.
(44) Durot, M., Le Fèvre, F., de Berardinis, V., Kreimeyer, A., Vallenet, D., Combe, C., Smidtas, S., Salanoubat, M., Weissenbach, J., and Schachter, V. (2008) Iterative reconstruction of a global metabolic model of *Acinetobacter baylyi* ADP1 using high-throughput growth phenotype and gene essentiality data. *BMC Syst. Biol. 2*, 85.
(45) Wong Ng, J., Chatenay, D., Robert, J., and Poirier, M. G. (2010) Plasmid copy number noise in monoclonal populations of bacteria. *Phys. Rev. E 81*, 011909.
(46) Ceroni, F., Algar, R., Stan, G., and Ellis, T. (2015) Quantifying cellular capacity identifies gene expression designs with reduced burden. *Nat. Methods 12*, 415−418.
(47) Haldimann, A., and Wanner, B. L. (2001) Conditional-Replication, Integration, Excision, and Retrieval Plasmid-Host Systems for Gene Structure-Function Studies of Bacteria. *J. Bacteriol. 183*, 6384−6393.
(48) Santala, S., Efimova, E., Kivinen, V., Larjo, A., Aho, T., Karp, M., and Santala, V. (2011) Improved Triacylglycerol Production in *Acinetobacter baylyi* ADP1 by Metabolic Engineering. *Microb. Cell Fact. 10*, 36.
(49) van Dien, S. (2013) From the first drop to the first truckload: commercialization of microbial processes for renewable chemicals. *Curr. Opin. Biotechnol. 24*, 1061−1068.
(50) Lemoine, A., Limberg, M. H., Kästner, S., Oldiges, M., Neubauer, P., and Junne, S. (2016) Performance loss of *Corynebacterium glutamicum* cultivations under scale-down conditions using complex media. *Eng. Life Sci. 16*, 620−632.
(51) Hartmans, S., Smits, J. P., van der Werf, M. J., Volkering, F., and de Bont, J. A. M. (1989) Metabolism of Styrene Oxide and 2-Phenylethanol in the Styrene-Degrading *Xanthobacter* Strain 124X. *Appl. Environ. Microbiol. 55*, 2850−2855.
(52) Jones, E., Oliphant, T., and Peterson, P., et al. (2001) *SciPy: Open source scientific tools for Python*, The SciPy Community, http://www.scipy.org/.
(53) van der Walt, S., Colbert, S. C., and Varoquaux, G. (2011) The NumPy Array: A Structure for Efficient Numerical Computation. *Comput. Sci. Eng. 13*, 22−30.

DOI: 10.1021/acssynbio.9b00316
ACS Synth. Biol. 2019, 8, 2642−2650

(54) McKinney, W. (2010) Data Structures for Statistical Computing in Python. *Proceedings of the 9th Python in Science Conference*, 51−56.
(55) Ebrahim, A., Lerman, J. A., Palsson, B. O., and Hyduke, D. R. (2013) COBRApy: COnstraints-Based Reconstruction and Analysis for Python. *BMC Syst. Biol.* 7, 74.

DOI: 10.1021/acssynbio.9b00316
ACS Synth. Biol. 2019, 8, 2642−2650

Supplementary Text for Enhanced Population Control in a Synthetic Bacterial Consortium by Interconnected Carbon Cross-Feeding

Pauli S. Losoi Ville P. Santala Suvi M. Santala

Contents

List of Figures

List of Tables

S1 Flux Balance Analyses

This section describes how the carbon flow of the double knock-out AbΔ*gntT*:EcΔ*ptsI* consortium was predicted using flux balance analyses (FBAs) with an iterative scheme [1]. Table S1 shows the iteration progress and the appearance of gluconate and acetate. In the double knock-out AbΔ*gntT*:EcΔ*ptsI* consortium, neither *Acinetobacter baylyi* ADP1 Δ*gntT* (AbΔ*gntT*) nor *Escherichia coli* Δ*ptsI* (EcΔ*ptsI*) was capable of growing in the first iteration. Ak converted glucose to gluconate, however. Given the gluconate made available by *A. baylyi* ADP1, *E. coli* was capable of growing and produced acetate as a consequence (when oxygen input was less than or equal to 12.5 mmol g_{DW}^{-1} h^{-1}). Growth of *A. baylyi* ADP1 is then observed in the third step, as acetate has been made available by *E. coli*. As for the wild-type Ab:Ec consortium, both *A. baylyi* ADP1 and *E. coli* grew independetly.

Despite all its merits, the growth rate maximization commonly employed in FBAs has a drawback: it implicitly assumes a perfectly adapted population, which in the case of *E. coli* resulted in no acetate production given a sufficient oxygen input. Not all of acetate produced by *E. coli* can be explained by fermentative metabolism alone under glucose

Table S1: Growth statuses and secreted metabolites in the iterative [1] FBAs. Growth of a strain in a particular iteration step (rows) with a given oxygen input (columns) is indicated by boldface font of the listed metabolites. For example, Ak (*A. baylyi* ADP1 Δ*gntT*) grew in Ak:Ek at third iteration with oxygen inputs of 10 mmol g_{DW}^{-1} h^{-1} and 12.5 mmol g_{DW}^{-1} h^{-1} but not with 15 mmol g_{DW}^{-1} h^{-1}, whereas Ek (*E. coli* Δ*ptsI*) grew with all oxygen inputs. Both wild-type strains Ab (*A. baylyi* ADP1) and Ec (*E. coli*) grew in Ab:Ec during all iterations as neither was dependent of the other. Formate was not utilized by any of the consortium members even though it was secreted in the FBA simulations. Abbreviations: Glcn gluconate, Ace acetate, For formate.

Iteration	Strain	10 $mmol_{O_2}$ g_{DW}^{-1} h^{-1}	12.5 $mmol_{O_2}$ g_{DW}^{-1} h^{-1}	15 $mmol_{O_2}$ g_{DW}^{-1} h^{-1}
Ak:Ek				
1	Ak	Glcn	Glcn	Glcn
	Ek			
2	Ak	Glcn	Glcn	Glcn
	Ek	**H_2O, CO_2, Ace, H^+**	**H_2O, CO_2, Ace**	**H_2O, CO_2**
3	Ak	**H_2O, CO_2, Glcn, For**	**H_2O, CO_2, Glcn, For**	Glcn
	Ek	**H_2O, CO_2, Ace, H^+**	**H_2O, CO_2, Ace**	**H_2O, CO_2**
4	Ak	**H_2O, CO_2, Glcn, For**	**H_2O, CO_2, Glcn, For**	
	Ek	**H_2O, CO_2, Ace, H^+**	**H_2O, CO_2, Ace**	
Ab:Ec				
1	Ab	**H_2O, CO_2, Glcn, For**	**H_2O, CO_2, Glcn, For**	**H_2O, CO_2, Glcn, For**
	Ec	**H_2O, CO_2, Ace, H^+**	**H_2O, CO_2, Ace, H^+**	**H_2O, CO_2, H^+**
2	Ab	**H_2O, CO_2, Glcn, For**	**H_2O, CO_2, Glcn, For**	**H_2O, CO_2, Glcn, For**
	Ec	**H_2O, CO_2, Ace, H^+**	**H_2O, CO_2, Ace, H^+**	**H_2O, CO_2, H^+**

excess [2–4], and to compensate for this defect the FBAs were conducted at different oxygen availabilities.

The analyses were performed using the Python (`www.python.org`) programming language and the `cobrapy` library [5]. The libraries `numpy` [6] and `pandas` [7] were used both in preparation and analysis. The utilized genome-scale models of *A. baylyi* ADP1 and *E. coli* were `iAbaylyiv4` [8] and `iAF1260` [9], respectively. Growth associated maintenance (GAM) was set to 59.81 $mmol_{ATP}$ g_{DW}^{-1} h^{-1} (default of `iAF1260`) and non-growth associated maintenance (NGAM) to zero in both models. Setting NGAM to zero was necessary to keep the optimizations feasible when the knock-out strains were incapable of growing. The computational medium allowed for 8 mmol g_{DW}^{-1} h^{-1} glucose, oxygen as indicated above, and unlimited Ca^{2+}, Cl^-, Co^{2-}, Fe^{2+}, K^+, Mg^{2+}, Mn^{2+},

MoO_4^{2-}, NH_4^+, HPO_4^-, Na^+, SO_4^{2-}, Zn^{2+}, H^+, and H_2O, mimicking the medium used in both small- and larger-scale experiments (Table S6).

To correctly model for the effect of *ptsI* knock-out in *E. coli*, the reactions `GLCt2pp` (gluose-proton symport), `GLCabcpp` (glucose-ABC-transport system), and `GLCDpp` (glucose dehydrogenase) were permanently knocked out in iAF1260. Gluconate transport reaction from extracellular environment directly to cytoplasm (`TRANS-RXN-GLUCONATE`) was disabled in the `iAbaylyiv4` model and replaced by transport from extracellular space to periplasm in order to correctly model for *gntT* knock-out in *A. baylyi* ADP1. If these reactions were not removed, EcΔ*ptsI* (Ek) could have imported glucose through its other transport systems, and AbΔ*gntT* (Ak) could have imported gluconate through the passive transport of gluconate from extracellular environment to cytosol, rendering the knock-outs effectless.

The FBAs with an iterative scheme [1] were conducted with an additional step prepended to each iteration. Glucose importing exchange reactions (`EXF-GLC(E)` in `iAbaylyiv4` and `EX_glc_e_` in `iAF1260`) were maximized for first, prior to the actual growth rate maximization and subsequent gene-associated flux minimization. This was necessary to enable conversion of glucose to gluconate by AbΔ*gntT*. As AbΔ*gntT* was unable to grow on its own on glucose as the sole carbon source, the optimization procedure would not have resulted in glucose oxidation either. The maximized glucose import was then set as a fixed bound for the growth rate maximization and gene-associated flux minimization. As both knock-out strains AbΔ*gntT* and EcΔ*ptsI* were incapable of growing initially, it was necessary to incorporate the secreted metabolites into the computational medium regardless of the growth statuses, contrary to the original iterative FBA method [1]. The linking between `iAbaylyiv4` and `iAF160` extracellular metabolites was done manually.

S2 Unstructured Kinetic Models

In this section the unstructured kinetic models referred to in the main text are derived. First, before the actual models are derived, the generalized conditions for a stable coculture are identified. Considering then a two-strain culture with biomass concentrations X_1 and X_2 (mass volume^{-1}), the biomass ratio of strain 1 to strain 2, X_1/X_2 (mass mass^{-1}), differentiated with respect to time t is

$$\frac{\mathrm{d}\left(X_1/X_2\right)}{\mathrm{d}t} = \frac{1}{X_2}\frac{\mathrm{d}X_1}{\mathrm{d}t} - \frac{X_1}{X_2^2}\frac{\mathrm{d}X_2}{\mathrm{d}t} \tag{S1}$$

In general, setting eq S1 to equal zero allows deducing *under which conditions* the strain ratio would be constant ($\mathrm{d}\left(X_1/X_2\right)/\mathrm{d}t = 0$) [10]. Whenever the biomass concentration

of strain 2 is either growing or decaying ($\mathrm{d}X_2/\mathrm{d}t \neq 0$), eq S1 is equivalent with

$$\frac{\mathrm{d}\left(X_1/X_2\right)}{\mathrm{d}t} = \frac{1}{X_2}\frac{\mathrm{d}X_2}{\mathrm{d}t}\left(\frac{\mathrm{d}X_1/\mathrm{d}t}{\mathrm{d}X_2/\mathrm{d}t} - \frac{X_1}{X_2}\right) \tag{S2}$$

and consequently $\mathrm{d}\left(X_1/X_2\right)/\mathrm{d}t$ equals zero (constant strain ratio) when

$$\frac{X_1}{X_2} = \frac{\mathrm{d}X_1/\mathrm{d}t}{\mathrm{d}X_2/\mathrm{d}t} \tag{S3}$$

Given eq S3 and that $\mathrm{d}\left(X_1/X_2\right)/\mathrm{d}t$ is proportional to the opposite of X_1/X_2 (eq S2), the term $\left(\mathrm{d}X_1/\mathrm{d}t\right)\left(\mathrm{d}X_2/\mathrm{d}t\right)^{-1}$ is defined as the *target ratio* the consortium is adapting to generally. Furthermore, $\left(\mathrm{d}X_1/\mathrm{d}t\right)\left(\mathrm{d}X_2/\mathrm{d}t\right)^{-1}$ is specifically identified as the *equilibrium ratio* when eq S3 holds (equivalent with $\mathrm{d}\left(X_1/X_2\right)/\mathrm{d}t = 0$). The distinction is made, for the target ratio can be defined whenever $\mathrm{d}X_2/\mathrm{d}t \neq 0$ holds, whereas the equilibrium ratio may have additional restrictions for existence (examples will be seen in Section S2.2).

Conventionally the rate of biomass growth is defined as the product of a specific (net) growth rate μ (time^{-1}) and the biomass concentration

$$\frac{\mathrm{d}X_i}{\mathrm{d}t} = \mu_i X_i \tag{S4}$$

which makes eq S3 equivalent with

$$\mu_1 = \mu_2 \tag{S5}$$

As also intuition suggests, eq S5 states that the strain ratio remains constant (is the equilibrium ratio) only when the specific net growth rates are equal. If a strain ratio X_1/X_2 is identified by studying eq S5 in the context of an unstructured kinetic model, the ratio is then the equilibrium ratio (eqs S5 and S3 are equivalent). Conversely, if an equilibrium ratio cannot be identified, conditions necessary for the equilibrium ratio to exist are found instead.

Given the context of this study, the task is then to define the equilibrium ratios for the consortia under consideration. However, models for the strains need to derived first (Section S2.1) in order to identify the equilibrium ratios (Section S2.2). The involved ordinary differential equation (ODE) systems are then numerically solved to investigate whether any of the involved assumptions significantly influenced the results (Section S2.3). To facilitate comparison between the interconnected carbon cross-feeding and other two-way cross-feeding systems, such as those present in auxotroph pairs [11–13], a generalized model of an obligately mutualistic pair is also derived and discussed in Section S2.4. Finally, Section S2.5 compares the presented modeling framework with models involving cooperativity coefficients [12, 13].

S2.1 Models of *A. baylyi* ADP1 and *E. coli*

For both *A. baylyi* ADP1 and *E. coli*, the specific growth rate μ_i (time^{-1}) on a substrate i (mass volume^{-1}) was modeled as

$$\mu_i = \mu_i^* \frac{i}{K_i + i} \tag{S6}$$

where μ_i^* is the maximal specific growth rate (time^{-1}) and K_i is an affinity constant (mass volume^{-1}). To make the subsequent equations more readable, the shorthand notation $i^* = i/(K_i + i)$ is used, which results in

$$\mu_i = \mu_i^* i^* \tag{S7}$$

The growth rates of *A. baylyi* ADP1 (a) and *E. coli* (e) are modeled as sums of growth rates on different substrates. *A. baylyi* ADP1 can oxidize glucose (G) to gluconate (N) [14–16] and utilize acetate (A) and gluconate [16], whereas *E. coli* utilizes glucose and gluconate. Additionally, *E. coli* is assumed to produce acetate [4] linearly upon utilization of glucose and gluconate. *E. coli* could utilize acetate simultaneously with glucose or gluconate, but net accumulation of acetate has been found to occur only at elevated acetate concentrations of approximately 10 mM or more [4]. Consequently, *E. coli* is considered only as a net producer of acetate in this analysis. Furthermore, a dilution factor D (time^{-1}) and glucose feed f_G (mass volume^{-1} time^{-1}) are considered in order to not limit the analysis only to pure batch cultivations. In batch cultures both $D = 0$ and $f_\mathrm{G} = 0$ apply, whereas in fed-batches and continuous operations $D > 0$ and $f_\mathrm{G} > 0$ are found instead.

Denoting then *A. baylyi* ADP1 concentration (mass volume^{-1}) as X_a, and *E. coli* concentration (mass volume^{-1}) as X_e, the biomass concentration time derivatives are

$$\frac{\mathrm{d}X_\mathrm{a}}{\mathrm{d}t} = \left(\mu_\mathrm{Aa}^* A^* + \mu_\mathrm{Na}^* N^* - D\right) X_\mathrm{a} \tag{S8}$$

$$\frac{\mathrm{d}X_\mathrm{e}}{\mathrm{d}t} = \left(\mu_\mathrm{Ge}^* G^* + \mu_\mathrm{Ne}^* N^* - D\right) X_\mathrm{e} \tag{S9}$$

which allows identifying the specific net growth rates of *A. baylyi* ADP1 and *E. coli*, μ_a and μ_e, respectively, as

$$\mu_a = \mu_\mathrm{Aa}^* A^* + \mu_\mathrm{Na}^* N^* - D \tag{S10}$$

$$\mu_e = \mu_\mathrm{Ge}^* G^* + \mu_\mathrm{Ne}^* N^* - D \tag{S11}$$

Setting these specific net growth rates equal (as in eq S5) cancels the dilution rates and allows defining the equilibrium ratio from

$$\mu_\mathrm{Aa}^* A^* + \mu_\mathrm{Na}^* N^* = \mu_\mathrm{Ge}^* G^* + \mu_\mathrm{Ne}^* N^* \tag{S12}$$

In order to then find a consortium's equilibrium ratio of *A. baylyi* ADP1 to *E. coli*, $X_a/X_e = (dX_a/dt)\,(dX_e/dt)^{-1}$, the terms G^*, N^*, and A^* are required. To identify these, mass balances for glucose, gluconate, and acetate as well as the reactions catalyzed by *A. baylyi* and *E. coli* along with their rates have to be defined first. *A. baylyi* ADP1 can catalyze the following reactions:

$$\mathrm{G} \xrightarrow{\mathrm{R_1}} \mathrm{Y_{GN}\,N}$$

$$\mathrm{N} \xrightarrow{\mathrm{R_3}} \mathrm{Y_{Na}\,X_a}$$

$$\mathrm{A} \xrightarrow{\mathrm{R_5}} \mathrm{Y_{Aa}\,X_a}$$

which correspond to glucose oxidation to gluconate (R_1), growth on gluconate (R_3), and growth on acetate (R_5). The yield coefficients Y_{sp} denote the mass of p produced per a mass of s consumed. The fact that *A. baylyi* ADP1 gains energy from oxidation of glucose to gluconate [17, 18] is implicitly accounted for by the Y_{Na} and Y_{Aa} yield coefficients. *E. coli*, on the other hand, can catalyze the reactions

$$\mathrm{G} \xrightarrow{\mathrm{R_2}} \mathrm{Y_{Ge}\,X_e + Y_{GA}\,A}$$

$$\mathrm{N} \xrightarrow{\mathrm{R_4}} \mathrm{Y_{Ne}\,X_e + Y_{NA}\,A}$$

which stand for growth on glucose (R_2) and gluconate (R_4) along with linear acetate excretion.

The reaction rates R ($\mathrm{mass_s\,volume^{-1}\,time^{-1}}$) for the five reactions are then written based on the reaction substrates $s \in (G, N, A)$:

$$R_1 = q^*_{\mathrm{Ga}} X_{\mathrm{a}} G^* \tag{S13}$$

$$R_2 = \mu^*_{\mathrm{Ge}} X_{\mathrm{e}} Y^{-1}_{\mathrm{Ge}} G^* \tag{S14}$$

$$R_3 = \mu^*_{\mathrm{Na}} X_{\mathrm{a}} Y^{-1}_{\mathrm{Na}} N^* \tag{S15}$$

$$R_4 = \mu^*_{\mathrm{Ne}} X_{\mathrm{e}} Y^{-1}_{\mathrm{Ne}} N^* \tag{S16}$$

$$R_5 = \mu^*_{\mathrm{Aa}} X_{\mathrm{a}} Y^{-1}_{\mathrm{Aa}} A^* \tag{S17}$$

where μ^*_{ij} is the maximal specific growth rate ($\mathrm{time^{-1}}$) of strain j on substrate i, and q^*_{ij} is the maximal specific reaction rate ($\mathrm{mass_i\,mass_j^{-1}\,time^{-1}}$) of i catalyzed by j. Figure S1 illustrates the five-reaction unstructured kinetic model of an *A. baylyi* ADP1:*E. coli* consortium, and Table S2 shows how the five reactions are used in modeling the four consortia with and without gene deletions.

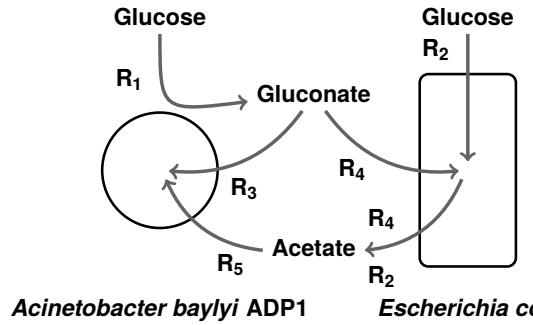

Figure S1: Reactions R_i in an unstructured kinetic model of an *A. baylyi* ADP1:*E. coli* consortium. Table S2 shows how the reactions are used in modeling the four consortia with and without genetic knock-outs.

Considering glucose feed f_G, dilution factor D, and the defined reactions rates, mass balances for glucose, gluconate, and acetate are written as

$$\frac{dG}{dt} = f_G - R_1 - R_2 - DG \tag{S18}$$

$$\frac{dN}{dt} = Y_{GN}R_1 - R_3 - R_4 - DN \tag{S19}$$

$$\frac{dA}{dt} = Y_{GA}R_2 + Y_{NA}R_4 - R_5 - DA \tag{S20}$$

In batch cultures both the glucose feed f_G and the dilution factor D equal zero.

Given the reaction rate eqs S13, S14, S15, S16, and S17, and the mass balance eqs S18, S19, and S20, the terms G^*, N^*, and A^* are solved to be

$$G^* = \frac{f_G - (dG/dt) - DG}{q^*_{Ga}X_a + \mu^*_{Ge}X_eY^{-1}_{Ge}} \tag{S21}$$

$$N^* = \frac{Y_{GN}q^*_{Ga}X_aG^* - (dN/dt) - DN}{\mu^*_{Na}X_aY^{-1}_{Na} + \mu^*_{Ne}X_eY^{-1}_{Ne}} \tag{S22}$$

$$A^* = \frac{Y_{GA}\mu^*_{Ge}X_eY^{-1}_{Ge}G^* + Y_{NA}\mu^*_{Ne}X_eY^{-1}_{Ne}N^* - (dA/dt) - DA}{\mu^*_{Aa}X_aY^{-1}_{Aa}} \tag{S23}$$

S2.2 Optimal consortium compositions

With the terms G^*, N^*, and A^* (eqs S21, S22, and S23) at hand, the *A. baylyi* ADP1 and *E. coli* specific net growth rates (eqs S10 and S11) can be defined to identify the

Table S2: Reactions used in modeling the four *A. baylyi* ADP1:*E. coli* consortia, AbΔ*gntT*:EcΔ*ptsI*, AbΔ*gntT*:Ec, Ab:EcΔ*ptsI*, and Ab:Ec. A reaction's presence in a particular consortium is marked with + or 0, and - is used to designate a reaction's absence. 0 is used to show which reactions have been omitted in Section S2.2 in order to simplify equations. However, both + and 0 reactions were used in solving the initial value problems (Section S2.3).

Reaction	AbΔ*gntT*:EcΔ*ptsI*	AbΔ*gntT*:Ec	Ab:EcΔ*ptsI*	Ab:Ec
1	+	0	+	+
2	-	+	-	+
3	-	-	+	+
4	+	0	+	0
5	+	+	0	0

equilibrium ratio, $X_a/X_e = (dX_a/dt)\,(dX_e/dt)^{-1}$, in the four consortia involving *A. baylyi* ADP1 and *E. coli*, namely AbΔ*gntT*:EcΔ*ptsI*, AbΔ*gntT*:Ec, Ab:EcΔ*ptsI*, and Ab:Ec. To facilitate derivation, the following shorthand notation is used for glucose, gluconate, and acetate: $i' = (di/dt) + Di$.

AbΔ*gntT*:EcΔ*ptsI* In AbΔ*gntT*:EcΔ*ptsI*, the reactions R_1, R_4, and R_5 are active, corresponding to glucose oxidation by *A. baylyi* ADP1 to gluconate, growth on gluconate and simultaneous excretion of acetate by *E. coli*, and growth on acetate by *A. baylyi* ADP1. Given these reactions and the equations defined above in Section S2.1, the equilibrium ratio is found from $\mu^*_{Aa}A^* = \mu^*_{Ne}N^*$ (eq S12) to be

$$\frac{X_a}{X_e} = \frac{Y_{Aa}Y_{Na}}{Y_{Ne}} - \frac{Y_{Aa}A'}{Y_{Ne}\,(Y_{GN}\,(f_G - G') - N')} \tag{S24}$$

The first term on the right-hand side is stable (no time-dependent terms), whereas the second is transient (contains time-dependent terms). Equation S24 then implies that whatever disturbances the consortium might face (transient term), the equilibrium ratio will return afterwards to the stable term defined by the yield coefficients.

Assuming only that acetate reaches a steady state of constant concentration, $dA/dt \approx 0$, and that the dilution rate is neglicible (equals zero in batch, only small in fed-batch), $D \approx 0$, cancels the transient term entirely and simplifies eq S24 to

$$\frac{X_a}{X_e} = \frac{Y_{Aa}Y_{NA}}{Y_{Ne}} \tag{S25}$$

Considering the yield coefficients are constants, eqs S24 and S25 state that there is a uniquely defined, constant equilibrium ratio of *A. baylyi* ADP1 to *E. coli* the

consortium adapts to even after potential perturbations. Therefore, the double knock-out AbΔ*gntT*:EcΔ*ptsI* consortium is expected to be stable due to population control provided by the interconnected carbon cross-feeding.

The equilibrium ratio (eq S25) provided by the cross-feeding could also be adjusted by genetic engineering, as it is essentially a function of only three yield coefficients, Y_{Aa}, Y_{NA}, and Y_{Ne}. Of these three parameters, the yield of acetate on gluconate by *E. coli* Δ*ptsI* (Y_{NA}) is probably the most amenable to engineering: the yield could be increased for example by knocking out *atpFH* required in oxidative phosphorylation [19]. Likewise metabolic engineering could be used to either increase or decrease the biomass yields.

AbΔ*gntT*:Ec As for AbΔ*gntT*:Ec, *A. baylyi* ADP1 oxidizes glucose to gluconate and *E. coli* grows on glucose and gluconate and excretes acetate while doing so. *A. baylyi* ADP1 grows on the acetate secreted by *E. coli*, but as it cannot import gluconate, the reaction R_3 is set to zero. In deriving the equilibrium strain ratio expression, reactions R_1 and R_4 (glucose oxidation by *A. baylyi* ADP1, gluconate utilization by *E. coli*) are also set to zero in order to simplify the analysis. Given the simplifications, AbΔ*gntT*:Ec becomes a commensialistic consortium, in which AbΔ*gntT* benefits from Ec without having an influence on Ec. The equilibrium ratio of *A. baylyi* ADP1 in AbΔ*gntT*:Ec is then found from $\mu^*_{\mathrm{Aa}} A^* = \mu^*_{\mathrm{Ge}} G^*$ (eq S12):

$$\frac{X_{\mathrm{a}}}{X_{\mathrm{e}}} = \frac{Y_{\mathrm{Aa}} Y_{\mathrm{Na}}}{Y_{\mathrm{Ge}}} - \frac{Y_{\mathrm{Aa}} A'}{Y_{\mathrm{Ge}} \left(f_{\mathrm{G}} - G'\right)} \tag{S26}$$

As before, the equilibrium ratio is composed of both a stable and a transient term.

Assuming again that both $\mathrm{d}A/\mathrm{d}t \approx 0$ and $D \approx 0$ apply, eq S26 simplifies to the stable term only:

$$\frac{X_{\mathrm{a}}}{X_{\mathrm{e}}} = \frac{Y_{\mathrm{Aa}} Y_{\mathrm{GA}}}{Y_{\mathrm{Ge}}} \tag{S27}$$

Like with AbΔ*gntT*:EcΔ*ptsI*, the equilibrium ratio simplified to a function of yield coefficients only, suggesting stability. However, numerical integrations (Section S2.3) of the ODE system indicated that the assumption of constant acetate concentration, $\mathrm{d}A/\mathrm{d}t \approx 0$, does not hold as well as in AbΔ*gntT*:EcΔ*ptsI*. Considering that growth and acetate production of *E. coli* is entirely independent of *A. baylyi* ADP1, it is logical to expect that *E. coli* is capable of accumulating acetate beyond *A. baylyi* ADP1's needs, collapsing the simple eq S27 back to the more complex eq S26 with the transient term as $\mathrm{d}A/\mathrm{d}t \approx 0$ does not apply. Additionally, the expressions and consequently dynamics would be more complex if glucose oxidation to gluconate by *A. baylyi* ADP1 (R_1) and gluconate utilization by *E. coli* (R_4) were considered.

Ab:EcΔ*ptsI* The Ab:EcΔ*ptsI* consortium was modeled with the reactions R_1, R_3, and R_4, which corresponded to glucose oxidation to gluconate by *A. baylyi* ADP1 and growth

on gluconate by both *A. baylyi* ADP1 and *E. coli*. However, to simplify derivation of the equilibrium strain ratio, the yield from gluconate to acetate by *E. coli* is set to equal zero. Likewise, acetate utilization by *A. baylyi* ADP1 was set to zero as none was produced by *E. coli*. With these simplifications, Ab:EcΔ*ptsI* has cooperator-cheater dynamics, in which EcΔ*ptsI* benefits from and also has a negative effect on Ab as they both grow on gluconate. Taking these into account, the equilibrium ratio of *A. baylyi* ADP1 in Ab:EcΔ*ptsI* is attained when $\mu^*_{\mathrm{Na}} N^* = \mu^*_{\mathrm{Ne}} N^*$ (eq S12), which leads to the identity

$$\mu^*_{\mathrm{Na}} = \mu^*_{\mathrm{Ne}} \tag{S28}$$

Equation S28 implies that the AbΔ*gntT*:EcΔ*ptsI* consortium has an equilibrium ratio only if the specific growth rates on gluconate are equal, $\mu^*_{\mathrm{Na}} = \mu^*_{\mathrm{Ne}}$ ($\mathrm{d}\left(X_\mathrm{a}/X_\mathrm{e}\right)/\mathrm{d}t = 0$), which hardly can hold.

Now in contrast to both AbΔ*gntT*:EcΔ*ptsI* and AbΔ*gntT*:Ec, no equilibrium ratio could be defined as such. It follows then, that the strain ratio is not as predictable and controllable in Ab:EcΔ*ptsI* as in AbΔ*gntT*:EcΔ*ptsI* or AbΔ*gntT*:Ec. Again, the expressions would be more complex if acetate excretion by *E. coli* and utilization by *A. baylyi* ADP1 were taken into account.

Ab:Ec The wild-type Ab:Ec consortium includes all reactions from R_1 to R_5. However, to simplify derivation of the optimal strain proportions, the reactions R_4 and R_5 corresponding to gluconate utilization by *E. coli* and acetate utilization by *A. baylyi* ADP1 are omitted. The consortium involves direct competition between Ab and Ec, as they both utilize ultimately glucose. The equilibrium ratio of *A. baylyi* ADP1 to *E. coli* is then found from $\mu^*_{\mathrm{Na}} N^* = \mu^*_{\mathrm{Ge}} G^*$ (eq S12) after simplification:

$$\frac{X_\mathrm{a}}{X_\mathrm{e}} = \frac{\mu^*_{\mathrm{Ge}}}{Y_{\mathrm{Ne}}} \frac{Y_{\mathrm{Na}} N'}{\left(\frac{Y_{\mathrm{Na}} Y_{\mathrm{GN}} q^*_{\mathrm{Ga}}}{\mu^*_{\mathrm{Ge}}} - 1\right)\left(f_\mathrm{G} - G'\right) - Y_{\mathrm{Na}} N' q^*_{\mathrm{Ga}}} \tag{S29}$$

The equilibrium ratio contains no stable terms, but only a transient term. In effect, the equilibrium ratio is proportional only to time-dependent terms and is therefore susceptible to perturbations.

If gluconate concentration were constant ($\mathrm{d}N/\mathrm{d}t \approx 0$) and dilution neglicible ($D \approx 0$), then the term N' would equal zero and the identity $\mu^*_{\mathrm{Na}} N^* = \mu^*_{\mathrm{Ge}} G^*$ would lead to

$$Y_{\mathrm{Na}} Y_{\mathrm{GN}} q^*_{\mathrm{Ga}} = \mu^*_{\mathrm{Ge}} \tag{S30}$$

instead. Analogously to Ab:EcΔ*ptsI*, the equilibrium ratio would exist ($\mathrm{d}\left(X_\mathrm{a}/X_\mathrm{T}\right)/\mathrm{d}t = 0$) only if $Y_{\mathrm{Na}} Y_{\mathrm{GN}} q^*_{\mathrm{Ga}} = \mu^*_{\mathrm{Ge}}$ held, which seems unlikely. As with AbΔ*gntT*:Ec and Ab:EcΔ*ptsI* alike, the expressions would be more complex if all the relevant reactions were fully taken into account. Consequently the Ab:Ec consortium itself cannot be expected to be as stable as AbΔ*gntT*:EcΔ*ptsI* under any conditions.

Conclusion Based on these simple kinetic analyses, it is concluded that the interconnected carbon cross-feeding present in AbΔ*gntT*:EcΔ*ptsI* best guarantees that a consortium has a stable equilibrium ratio to which the strain ratio adapts. Furthermore, the equilibrium ratio provided by the interconnected cross-feeding seems adjustable, for example by genetic engineering affecting the relevant yields (from gluconate to acetate, and gluconate and acetate to biomasses in this case). As the other consortia corresponding to commensialism, cooperator-cheater, and competition dynamics either had equilibrium ratios susceptible to external perturbations or required too restrictive conditions for existence, the AbΔ*gntT*:EcΔ*ptsI* consortium with interconnected carbon cross-feeding was considered the most promising for further study.

S2.3 Initial value problem solutions

The behaviour of the derived *A. baylyi* ADP1:*E. coli* consortium models was inspected numerically in both batch and fed-batch modes. The batch simulations had the same initial glucose concentrations and inoculations ratios as the conducted small-scale experiments. Because of the large number of parameters present in the models, the experimental results could not be directly compared to the numerical results presented here. All simulations were performed in Python using the `scipy` library's [20] `solve_ivp` function with the default `RK45` method. The libraries `numpy` [6] and `pandas` [7] were also used in preparation and analysis.

Taking the five reactions as shown in Table S2 (both + and 0), and the relevant mass balances in eqs S8, S9, S18, S19, and S20, the four ODE systems corresponding to the four *A. baylyi* ADP1:*E. coli* consortia were solved in both batch and fed-batch mode with varying initial substrate concentrations, feed parameters, and inoculation ratios as described in Table S3. The fed-batches of volume $V = 1\,\mathrm{L}$ had always an initial glucose concentration of $0.1\,\mathrm{g\,L^{-1}}$ and a feed with

1. Glucose concentration $S_0 = 520\,\mathrm{g\,L^{-1}}$
2. Initial flow-rate $F_0 = 0.001\,\mathrm{L\,h^{-1}}$
3. Maximal flow-rate $F_{\max} = 0.01\,\mathrm{L\,h^{-1}}$
4. Time t dependency of flow-rate $F = \min\left(F_0 e^{\beta t}, F_{\max}\right)$ characterized by an exponential coefficient β ($\mathrm{time^{-1}}$), which was varied between fed-batches.

In fed-batches the dilution factor D was then $D = F/V$ and glucose feed $f_{\mathrm{G}} = S_0 F/V$. In batch simulations the culture volume played no role. The yield coefficients Y_{sp} ($\mathrm{mass_p\,mass_s^{-1}}$) and maximal specific rates μ^*_{ij} ($\mathrm{time^{-1}}$) used in the kinetic models are shown in Table S4. All affinity constants K_i were taken to be $0.05\,\mathrm{g\,L^{-1}}$ as in [23], and *A. baylyi* ADP1's maximal specific glucose oxidation rate q^*_{Ga} was assumed to be $2.0\,\mathrm{g_G\,g_a^{-1}\,h^{-1}}$.

The obtained solutions to the initial value problems are summarized in Figures S2 and S3 for batch and fed-batch modes, respectively. It was shown in Section S2.2, that

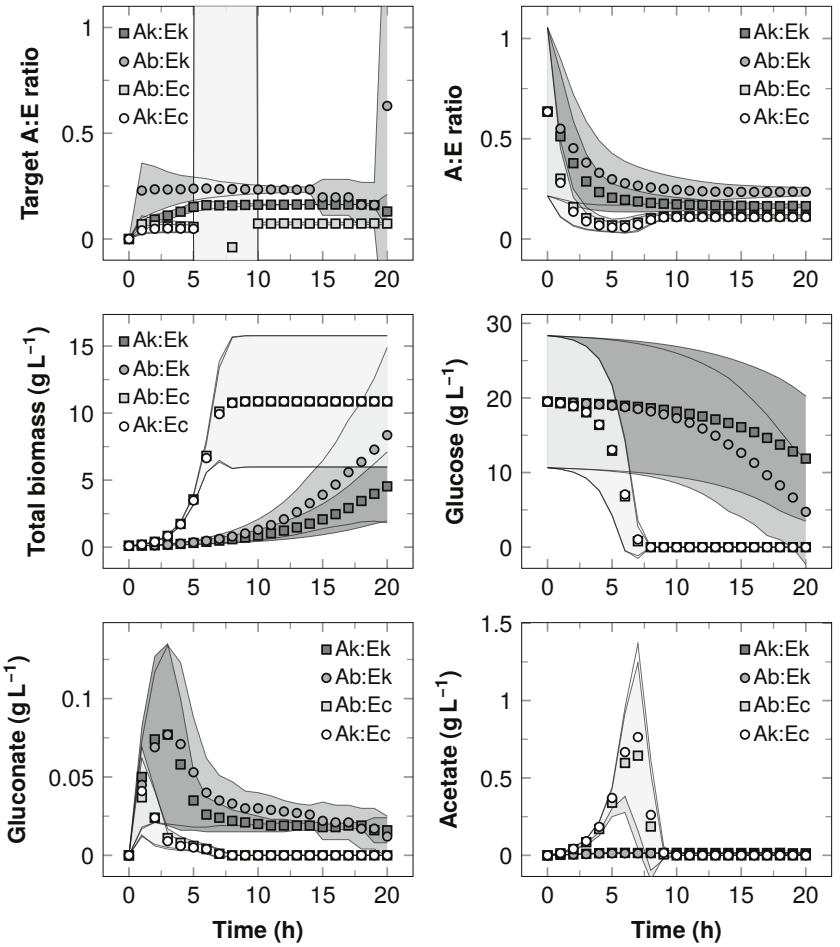

Figure S2: Initial value problem solutions in batch mode. Ab stands for *A. baylyi* ADP1, Ak for AbΔ*gntT*, Ec for *E. coli*, and Ek for EcΔ*ptsI*. The reported data are means of the six simulations with different initial conditions (Table S3). The variability between simulations is shown as error bands corresponding to sample standard deviations. Both Ab:Ec and Ak:Ec displayed very high variability in target A:E ratio between 5 h and 10 h due to acetate fluctuations. The legend in glucose panel was omitted for clarity.

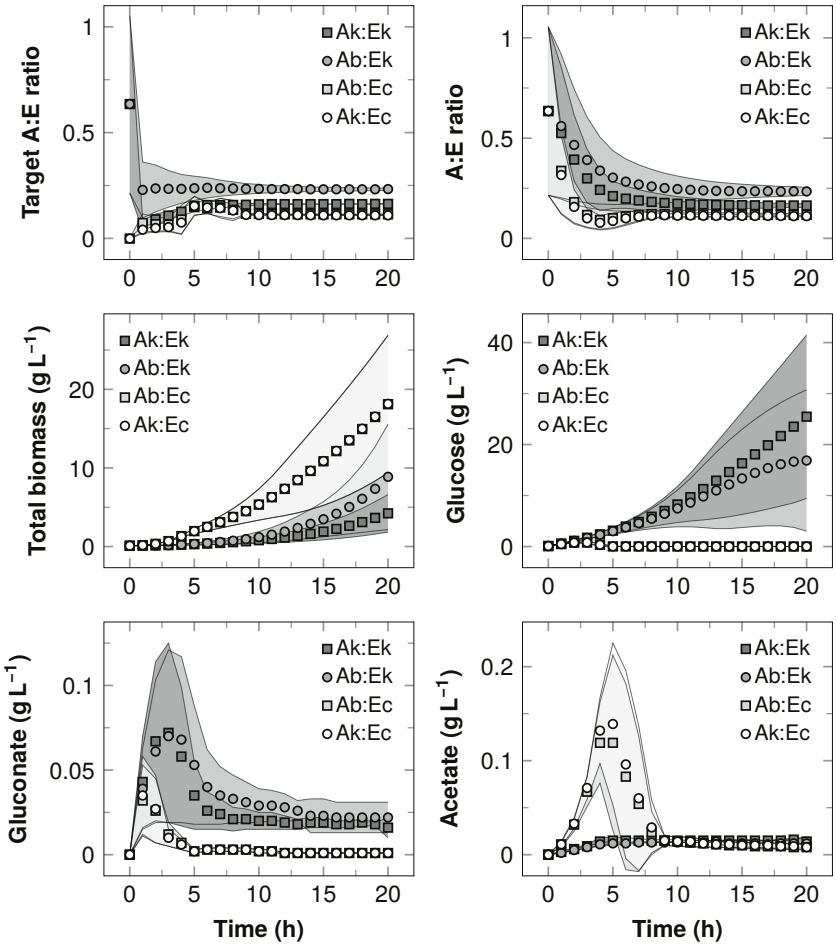

Figure S3: Initial value problem solutions in fed-batch mode. Ab stands for *A. baylyi* ADP1, Ak for AbΔ*gntT*, Ec for *E. coli*, and Ek for EcΔ*ptsI*. The reported data are means of the six simulations with different initial conditions (Table S3). The variability between simulations is shown as error bands corresponding to sample standard deviations.

Table S3: Initial value problem parameters. X_a and X_e stand for initial biomass concentrations of *A. baylyi* ADP1 and *E. coli*, respectively. G is the initial glucose concentration. β is the exponential coefficient of the feed flow-rate F in fed-batches. Zero exponential $\beta = 0$ corresponds to constant feed rate.

Batch	X_a / g L^{-1}	X_e / g L^{-1}	G / g L^{-1}
1	0.050	0.050	9.00
2	0.050	0.050	18.00
3	0.050	0.050	36.00
4	0.033	0.067	18.00
5	0.017	0.083	18.00
6	0.010	0.090	18.00
Fed-batch	X_a / g L^{-1}	X_e / g L^{-1}	β / h^{-1}
1	0.050	0.050	0.00
2	0.050	0.050	0.10
3	0.050	0.050	0.20
4	0.033	0.067	0.10
5	0.017	0.083	0.10
6	0.010	0.090	0.10

both AbΔ*gntT*:EcΔ*ptsI* and AbΔ*gntT*:Ec have unique and constant equilibrium strain ratios given that acetate concentration A is constant and dilution D is neglicible. Figures S2 and S3 demonstrate that the *target* ratio, and by extension also *equilibrium* ratio, of *A. baylyi* ADP1 to *E. coli*, $(\mathrm{d}X_a/\mathrm{d}t)\,(\mathrm{d}X_e/\mathrm{d}t)^{-1}$ in AbΔ*gntT*:EcΔ*ptsI* remained stable in both batches and fed-batches with only small deviations caused by the barely visible initial acetate build-ups. Target ratios were plotted instead of equilibrium ratios (defined in Section S2) to facilitate comparison between consortia (some equilibrium ratios could not be defined, Section S2.2). In AbΔ*gntT*:Ec, however, acetate accumulated ($\mathrm{d}A/\mathrm{d}t \neq 0$) markedly both in batches and fed-batches as growth and acetate secretion by *E. coli* was not in any way limited by *A. baylyi* ADP1. As a consequence, the target ratio (and by extension equilibrium ratio) of *A. baylyi* ADP1 did not remain constant, but displayed an oscillation. The actual *A. baylyi* ADP1 to *E. coli* ratio (X_a/X_e) also varied less in AbΔ*gntT*:EcΔ*ptsI* than in AbΔ*gntT*:Ec.

As for Ab:EcΔ*ptsI* and Ab:Ec, it was shown that the equilibrium strain ratio either existed only under restrictive conditions or contained only transient terms (eqs S28, S29, and S30), and consequently neither performed as steadily as AbΔ*gntT*:EcΔ*ptsI*; Ab:Ec was in general similar to AbΔ*gntT*:Ec with an oscillation in both target and actual *A. baylyi* ADP1 to *E. coli* ratios, and ratios varied more in Ab:EcΔ*ptsI* than in AbΔ*gntT*:EcΔ*ptsI*.

Table S4: Yield coefficients Y_{sp} (mass of p produced per mass of s consumed) and maximal specific growth rates μ^*_{sx} (rate of x growing on s) used in solving the initial value problems. *A. baylyi* ADP1 biomass yield on gluconate (Y_{Na}) was estimated by considering that an engineered *A. baylyi* ADP1 expressing PykF (pyruvate kinase from *E. coli*), which was found to have similar biomass yield as the wild-type [21], accumulated $0.30\,\mathrm{g\,L^{-1}}$ biomass given 10 mM glucose in a minimal medium [22]. The biomass yield on glucose was then translated to gluconate by considering the ratio of their molar masses. Due to lack of more precise information, *E. coli* biomass yield on gluconate (Y_{Ne}) was assumed to be similar to yield on glucose (Y_{Ge}) [23], but divided by the ratio of gluconate's molar mass to glucose's molar mass. The same was applied to *E. coli*'s maximal specific growth rate on gluconate (μ^*_{Ne}).

Yields Y_{sp}	$\mathrm{g_p\,g_s^{-1}}$	Source
Y_{Na}	0.32	[21, 22]
Y_{Aa}	0.50	[22]
Y_{Ge}	0.50	[23]
Y_{Ne}	0.46	[23], molar masses
Y_{GN}	1.09	Molar masses
Y_{GA}	0.10	[4]
Y_{NA}	0.15	[4]
Maximal specific growth rates μ^*_{sx}	$\mathrm{h^{-1}}$	Source
μ^*_{Aa}	0.69	[22]
μ^*_{Na}	0.18	[21]
μ^*_{Ge}	0.66	[23]
μ^*_{Ne}	0.61	[23], molar masses

S2.4 Generalized mutualistic pair

A general model of an obligately mutualistic pair (for example of auxotrophs [11–13]) is derived in this section to enable analytical comparison of such pairs with the presented interconnected carbon cross-feeding scheme. The generalized model considers two strains, 1 and 2, and three compounds, A, B, and C. Both strains grow on carbon source C. Additionally, strain 1 requires compound B produced by strain 2, which in turn requires compound A produced by strain 1. The generalized mutualistic pair is illustrated in Figure S4.

Using the same notation conventions as in Sections S2.1 and S2.2, specific net growth rate of strain 1 is modeled by

$$\mu_1 = \mu^*_{\mathrm{C1}} C^* B^* - D \tag{S31}$$

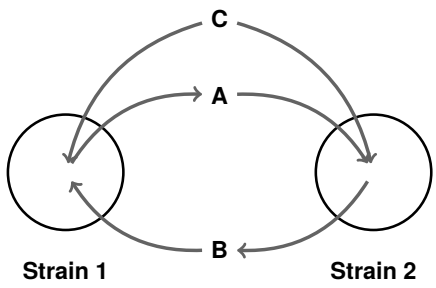

Figure S4: Generalized obligately mutualistic pair. Both strains 1 and 2 grow on carbon source C. However, strain 1 also requires compound B produced only by strain 2. Strain 2 in turn requires compound A produced only by strain 1.

and of strain 2 by

$$\mu_2 = \mu^*_{C2} C^* A^* - D \tag{S32}$$

Denoting the specific net production rate of compound A by strain 1 as q^*_A ($\mathrm{g\,g^{-1}\,h^{-1}}$) and the mass of A consumed per mass of strain 2 formed as Y_A ($\mathrm{g\,g^{-1}}$), the mass balance for compound A is

$$\frac{\mathrm{d}A}{\mathrm{d}t} = q^*_A X_1 - Y_A \mu^*_{C2} C^* A^* X_2 - DA \tag{S33}$$

which leads to

$$A^* = \frac{q^*_A X_1 - A'}{Y_A \mu^*_{C2} C^* X_2} \tag{S34}$$

The mass balance for B is similar to A, but strains 1 and 2 are interchanged. The equilibrium ratio $X_1/X_2 = (\mathrm{d}X_1/\mathrm{d}t)\,(\mathrm{d}X_2/\mathrm{d}t)^{-1}$ is then by definition found from $\mu^*_{C1} C^* B^* - D = \mu^*_{C2} C^* A^* - D$ (eq S5), which simplifies to

$$\frac{X_1}{X_2} = \frac{A'}{2q^*_A X_2} + \sqrt{\left(\frac{A'}{2q^*_A X_2}\right)^2 + \frac{Y_A q^*_B}{Y_B q^*_A} - \frac{Y_A B'}{Y_B q^*_A X_2}} \tag{S35}$$

As such the expression for equilibrium ratio seems rather complex, but like with AbΔ*gntT*:EcΔ*ptsI*, it is a sum of stable and transient terms. Assumptions of constant concentrations of A and B and neglicible dilution simplifies eq S35 to the stable term

$$\frac{X_1}{X_2} = \sqrt{\frac{Y_A q^*_B}{Y_B q^*_A}} \tag{S36}$$

The overall different appearance of eqs S35 and S36 from the corresponding equations of AbΔ*gntT*:EcΔ*ptsI* can be explained by the fact that this model of a generalized mutualistic

pair did not connect compounds A and B with one another (to not lose generality). In the interconnected carbon cross-feeding, glucose, gluconate, and acetate were all part of the same carbon flow.

As could be expected by intuition, an obligately mutualistic pair in general has the same desirable feature as interconnected carbon cross-feeding, a stable equilibrium ratio. However, the cross-feeding presented in this study sets no additional burden on the participating strains unlike mutualism based on auxotrophies. Instead, the glucose to gluconate oxidation is beneficial to *A. baylyi* ADP1 Δ*gntT* [17, 18] even though it cannot use the gluconate itself, and acetate is an inevitable but wanted side-product of *E. coli* Δ*ptsI* metabolism in this context. Auxotrophic mutualism in turn necessitates the strains to share biosynthetically costly metabolites required also by themselves, which is an additional burden with no immediate benefit on the contributing strain (the benefit is realized only later, it is decoupled). Such a decoupling of the giving from the benefit of giving could lead to cheater subpopulations emerging, which could destabilize the mutualism in the long run. Another potential issue with auxotrophies is that some necessary metabolites might become commonly available only near cell death [11].

S2.5 Models with cooperativity coefficients

This section briefly reviews and discusses coculture ODE models involving cooperativity coefficients [12, 13] in the light of the modeling framework used in this study. In short, the cooperativity coefficient C is used to model coculture dynamics with biomass time derivatives [12] (shown here only for strain 1, strain 2 is similar)

$$\frac{\mathrm{d}X_1}{\mathrm{d}t} = C_2 \frac{X_2}{X_1 + X_2} \tag{S37}$$

or [13]

$$\frac{\mathrm{d}X_1}{\mathrm{d}t} = C_2 X_2 \frac{X_1}{X_1 + b} \tag{S38}$$

with a buffer term b for low-cell-density growth. A logistic carrying capacity is usually also used [12, 13], but it was omitted here for brevity as it cancels out in determining the equilibrium ratio. Modeling biomass growth as in eq S37 and setting $\mu_1 = \mu_2$ leads immediately to

$$\frac{X_1}{X_2} = \sqrt{\frac{C_2}{C_1}} \tag{S39}$$

as the equilibrium ratio $X_1/X_2 = (\mathrm{d}X_1/\mathrm{d}t)\,(\mathrm{d}X_2/\mathrm{d}t)^{-1}$, which means that the model structure present in eq S37 inherently assumes the consortium to adapt towards a fixed equilibrium strain ratio. Using the cooperativity model in eq S38 with $\mu_1 = \mu_2$ leads in turn to a more complex expression for equilibrium ratio, which resembles the generalized

mutualistic pair (eq S35):

$$\frac{X_1}{X_2} = -\frac{b}{2X_2} + \sqrt{\left(\frac{b}{2X_2}\right)^2 + \frac{C_2 b}{C_1 X_2} + \frac{C_2}{C_1}} \tag{S40}$$

Letting the buffer term become neglicible, $b/X_2 \approx 0$, simplifies eq S40 to eq S39. Furthermore, the cooperativity coefficients C could be given a physical interpretation based on the generalized mutualism model in Section S2.4 (eq S36).

Based on the analyses it is apparent that using such a model structure as in eqs S37 and S38 implicitly assumes mutualistic dynamics. In the context of the cited studies utilizing these model structures to quantify cooperation levels [12, 13], the inherent assumption agrees with the consortium dynamics (mutualism). However, the implication should be considered prior to application in other contexts. For example, in this study the inherent assumption would not have been appropriate. In contrast to *assuming* a stable equilibrium ratio to be present in mutualism, the analyses presented in this study allowed it to emerge as a *result* for the generalized mutualistic pair (Section S2.4) as well as interconnected carbon cross-feeding (Section S2.2).

S3 mScarlet Gene Cassette Construction

This section describes how the mScarlet expression cassette was constructed using the insert ordered from GenScript, USA, and a gene cassette [24] overwriting the neutral ACIAD3381-locus (*poxB*, pyruvate dehydrogenase). The mScarlet insert consisted of

1. MunI (MfeI) recognition site
2. BBa_J23100 promoter present also in the sfGFP cassette [25]
3. Synthetic ribosome binding site (RBS) present also in the sfGFP cassette [25], but shortened 3 bp from 3'-end to accommodate the NdeI recognition site
4. NdeI recognition site which supplied the start codon
5. 6His-tag [26]
6. Gly-Ser-Gly-linker between 6His-tag and mScarlet
7. mScarlet sequence based on the amino acid sequence [27] codon optimized for *E. coli* by GenScript, start codon excluded
8. Two stop codons
9. XhoI recognition site.

The insert is illustrated in Figure S5 and its sequences are shown in Table S5. The pUC57 plasmid provided by GenScript with the mScarlet insert was first amplified by growing its initial *E. coli* host in lysogeny broth (LB). Using MunI and XhoI restriction enzymes

Table S5: Sequences of the mScarlet construct inserted into a gene cassette [24] overwriting the neutral ACIAD0544 locus (*poxB*, pyruvate dehydrogenase). The shown mScarlet sequence is based on the amino acid sequence published in the original work [27]. The actual coding sequence was codon optimized for *E. coli* by GenScript.

Part	Sequence (5′ → 3′)	bp	Source
Upstream			
MunI	CAATTG	6	
Promoter	TTGACGGCTAGCTCAGTCCTAGGTACAGTGCTAGC	35	[25]
RBS	TACTAGAGAAATCAAATTAAGGAGGTAAG	29	[25]
NdeI (1 to 3)	CAT	3	
Coding sequence			
NdeI (4 to 6)	ATG	3	
His-tag	CATCATCATCATCATCAC	18	
GSG-linker	GGTTCTGGT	9	
mScarlet	GTGAGCAAGGGCGAGGCAGTGATCAAGGAGTTCATGCGGTTC AAGGTGCACATGGAGGGCTCCATGAACGGCCACGAGTTCGAG ATCGAGGGCGAGGGCGAGGGCCGCCCCTACGAGGGCACCCAG ACCGCCAAGCTGAAGGTGACCAAGGGTGGCCCCCTGCCCTTC TCCTGGGACATCCTGTCCCCTCAGTTCATGTACGGCTCCAGG GCCTTCACCAAGCACCCCGCCGACATCCCCGACTACTATAAG CAGTCCTTCCCCGAGGGCTTCAAGTGGGAGCGCGTGATGAAC TTCGAGGACGGCGGCGCCGTGACCGTGACCCAGGACACCTCC CTGGAGGACGGCACCCTGATCTACAAGGTGAAGCTCCGCGGC ACCAACTTCCCTCCTGACGGCCCCGTAATGCAGAAGAAGACA ATGGGCTGGGAAGCGTCCACCGAGCGGTTGTACCCCGAGGAC GGCGTGCTGAAGGGCGACATTAAGATGGCCCTGCGCCTGAAG GACGGCGGCCGCTACCTGGCGGACTTCAAGACCACCTACAAG GCCAAGAAGCCCGTGCAGATGCCCGGCGCCTACAACGTCGAC CGCAAGTTGGACATCACCTCCCACAACGAGGACTACACCGTG GTGGAACAGTACGAACGCTCCGAGGGCCGCCACTCCACCGGC GGCATGGACGAGCTGTACAAG	693	[27]
Stop	TAA	3	
Downstream			
Stop	TAA	3	
XhoI	CTCGAG	6	
Total		808	

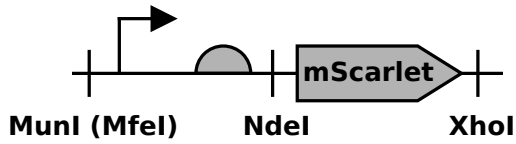

Figure S5: The mScarlet construct inserted into a gene cassette [24, see Figure 2] overwriting the neutral ACIAD0544 locus (*poxB*, pyruvate dehydrogenase). The promoter BBa_J23100 and ribosome binding site were from [25]. See Table S5 for the sequences. Figure prepared with DNAplotlib [28].

(Fermentas, Lithuania), both the pUC57 mScarlet and the ADP1 gene cassette [24] were digested. The mScarlet insert was then ligated into the plasmid backbone using T4 DNA Ligase in T4 DNA Ligase Buffer (Thermo Scientific, USA).

The ligated plasmid product with the mScarlet insert was transformed by electroporation into *E. coli* XL1 (Stratagen, USA) for amplification and extraction. Cells were made electrocompetent, and the transformation was conducted using a MicroPulser electroporator (Bio-Rad, USA) with the Eco-1 program. The electroporated cell suspension was plated on a LA plate (15 g L^{-1} agar, 10 g L^{-1} tryptone, 5 g L^{-1} yeast extract, 1 g L^{-1} NaCl, and 10 g L^{-1} glucose) with 25 mg L^{-1} chloramphenicol. The colonies of transformed *E. coli* XL1 that grew on the plate were bright red even to naked eye. A bright red colony was selected for amplification, and the mScarlet-carrying gene cassette plasmid was extracted using GeneJET Plasmid MiniPrep Kit (Thermo Scientific). Integration of the resulting mScarlet gene cassette into *A. baylyi* ADP1 has been described in the main text.

S4 sfGFP Integrations

This section briefly describes how the sfGFP-carrying Burden Monitor expression cassette [25] was integrated into both *E. coli* and *E. coli* Δ*ptsI* using the conditional-replication, integration, and modular plasmids as described in the original publication [29]. Prior to all transformations cells were cultured in LB medium at 37 °C with 300 RPM shaking and made electrocompetent, and all transformations were conducted using a MicroPulser electroporator (Bio-Rad) with the Eco-1 program. *E. coli* was first transformed with the Int (integrase) expressing helper plasmid pAH123. The pAH123 helper plasmid carried also an ampicillin resistance gene. After transformation, *E. coli* was resistant to ampicillin as expected and grew on the selective LA plates containing 100 mg L^{-1} ampicillin.

The pAH123 carrying *E. coli* strains were then further transformed with pBM (Burden Monitor phi80 version plasmid), yielding gentamicin-resistant strains. Immediately after

Table S6: Composition of the defined medium used in experiments and precultivations. The medium is based on a mineral salt medium [30]. A carbon source was always added to medium prior to use as described in main text.

Component	mg L^{-1}	Component	mg L^{-1}
K_2HPO_4	3880	$ZnSO_4 \cdot 7\,H_2O$	2
NaH_2PO_4	1630	$CaCl_2 \cdot 2\,H_2O$	1
$(NH_4)_2SO_4$	2000	$MnCl_2 \cdot 2\,H_2O$	1
$MgCl_2 \cdot 6\,H_2O$	100	$CoCl_2 \cdot 6\,H_2O$	0.4
EDTA	10	$CuSO_4 \cdot 5\,H_2O$	0.2
$FeSO_4 \cdot 7\,H_2O$	5	$Na_2MoO_4 \cdot 2\,H_2O$	0.2

electroporation the cells were incubated in LB medium at 37 °C for 1 h and furthermore at 42 °C for 30 min. The higher temperatures drove Int synthesis and inhibited helper plasmid replication [29]. The electroporated cell suspensions were then transferred to LA plates with 15 mg L^{-1} gentamicin, and visibly green colonies were formed within few days of incubation at 37 °C. Curing of the helper plasmid pAH123 was confirmed by transferring colonies of the pBM-transformed strains to ampicillin containing LA plates. No growth was observed on the ampicillin plates.

S5 Microwell Cultivations

Prior to experiments, all strains were stored at −80 °C in 10 $\%_v$ glycerol and plated on LA plates supplemented with antibiotics whenever applicable (25 mg L^{-1} chloramphenicol for mScarlet strains, 15 mg L^{-1} gentamicin for sfGFP strains, and 30 mg L^{-1} kanamycin for non-fluorescent knock-out strains). Precultivations and actual cultivation experiments were performed in the mineral salt medium described in Table S6. No antibiotics were used in precultivations and experiments.

Figures S6 and S7 show the optical densities at 600 nm (OD_{600}) and fluorescence intensities corresponding to sfGFP and mScarlet emission maxima in the initial small-scale experiments, which were used to verify the growth of the double knock-out *A. baylyi* ADP1 Δ*gntT*:*E. coli* Δ*ptsI* consortium. All consortia accumulated OD_{600} indicating growth, and the fluorescence intensities were considerable only when respective fluorescent protein genes were present in the culture. As expected, none of the knock-out strains Ak (*A. baylyi* Δ*gntT*), Akr (Ak with mScarlet), Ek (*E. coli* Δ*ptsI*), and Ekg (Ek with sfGFP) grew in isolation (`A-----`, `Af----`, `---E--`, and `---Ef-`, respectively, in Figure S6). The lack of growth of the control (knock-out) strains therefore indicated that the growth of *A. baylyi* Δ*gntT*:*E. coli* Δ*ptsI* consortia was enabled by cross-feeding rather than

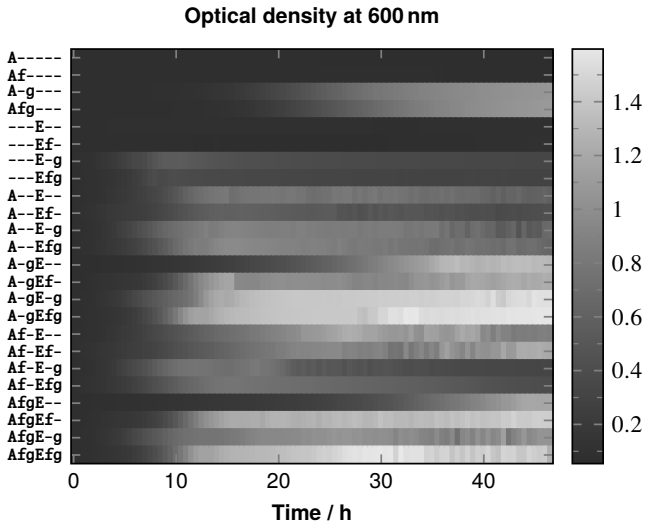

Figure S6: Optical density at 600 nm in the initial small-scale experiments. A denotes *A. baylyi* ADP1 and E *E. coli*. Fluorescent protein gene is denoted with f and the ability to utilize glucose with g. In effect, the wild-type *A. baylyi* ADP1 is denoted with A-g, and the mScarlet-carrying knock-out strain with Af-. Each horizontal lane corresponds to mean of three biological replicates cultivated in defined medium (Table S6) with 50 mM glucose at 30 °C.

growth-restoring mutations. Methods related to these experiments are given in the main text.

In all subsequent small-scale cultivations presented in the main text, the fluorescent knock-out strains Akr and Ekg were cultured in isolation as negative controls at the same time on the same microwell plates to ensure that the growth of the Akr:Ekg consortium was genuinely due to cross-feeding. These negative controls are shown in Figure S8. No growth of the negative controls was ever observed in the experiments, making it safe to assume that no growth-restoring mutations occurred.

S6 Bioreactor Cultivations

S6.1 Results

To further support the proposed carbon flow and to demonstrate the scalability of the carbon cross-feeding system, a bioreactor cultivation of Akr:Ekr (AbΔ*gntT*:EcΔ*ptsI* with

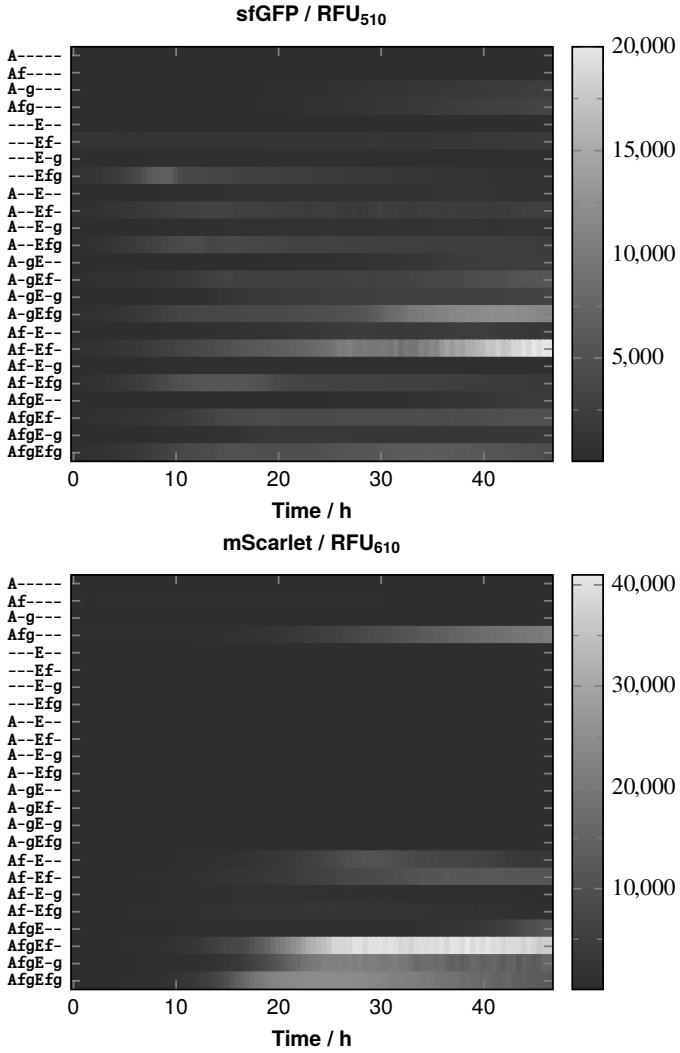

Figure S7: Fluorescence intensities at 510 nm and 610 nm in the initial small-scale experiments. A denotes *A. baylyi* ADP1 and E *E. coli*. Fluorescent protein gene is denoted with f and the ability to utilize glucose with g. For example the mScarlet-carrying knock-out *A. baylyi* ADP1 strain is denoted Af-. RFUs stand for the relative fluoresence units of the microwell plate reader. Each horizontal lane represents the mean of three biological replicates grown in defined medium (Table S6) with 50 mM glucose at 30 °C.

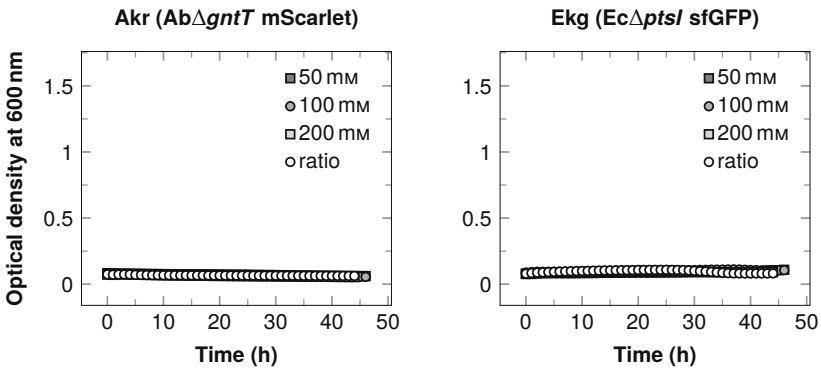

Figure S8: Optical density at 600 nm of the negative controls, Akr and Ekg, in the small-scale experiments. The concentrations (mM) refer to glucose concentration experiments depicted in main text Figure 2, and ratio refers to the inoculation ratio experiment depicted in main text Figure 3 (all ratio experiments were performed at the same time on the same plate). The vertical axis limits match Figures 2 and 3 of main text. The data are shown as means of three biological replicates, and the sample standard deviations are too small to be seen.

mScarlet and sfGFP, respectively) was carried out with approximately hourly sampling. Figure S9 shows the measured optical densities, pHs and concentrations of glucose and acetate. For reference, cultivations with Eg as well as Akr:Eg and Ar:Eg were also carried out.

Akr:Ekg was capable of growing in the bioreactor, demonstrating the scalability of the proposed carbon cross-feeding. However, like in the small-scale cultivations, its growth rate was much lower than those of the other cultures. Akr:Ekg cultivation received an almost 5 mM residual acetate concentration from precultivations, which was consumed rapidly within the first 4 h, and the residual gluconate from precultivation was below 1 mM. After this initial stage of growth, Akr:Ekg ceased to grow for approximately 6 h. Given that (i) *A. baylyi* strains oxidize glucose to gluconate [14–16] and (ii) the wild-type *E. coli* accumulated acetate readily when cultured alone and is known to produce acetate also from gluconate [4], it seems fair enough to assume that growth was restored at 10 h due to acetate formed by Ekg. Comparing to the ODE framework and the numerical solutions obtained (Section S2), it seems likely that Akr:Ekg used most of the first 10 h on adapting its *A. baylyi* ADP1 to *E. coli* -ratio towards the optimum. Regardless of low growth rate, glucose was consumed by Akr:Ekg during the whole cultivation time. As the used *E. coli* strain Ekg was unable to grow on glucose in small-scale experiments (Figure S8), the drop in glucose concentration was due to glucose oxidation to gluconate by *A. baylyi* ADP1 Δ*gntT* [14–16]. The steady descent of pH along with the steady

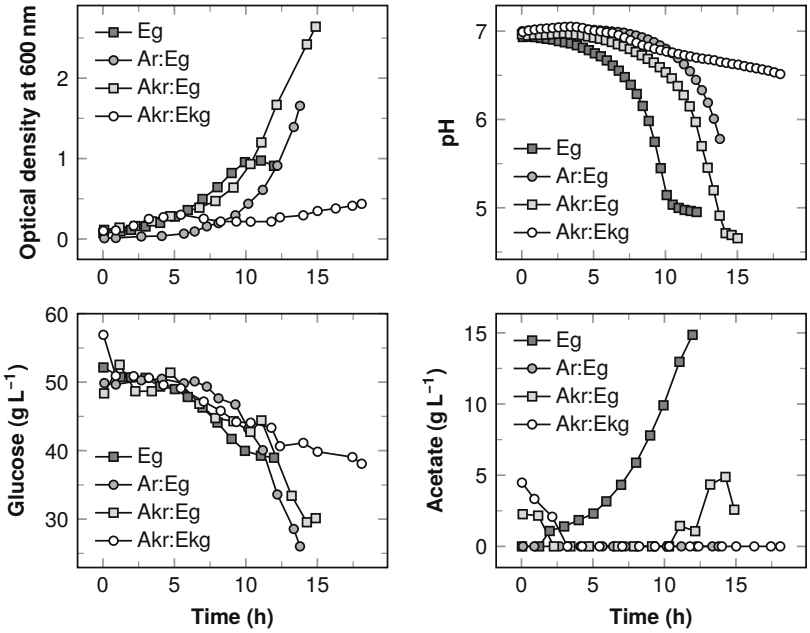

Figure S9: Additional cultivations of the consortia and wild-type *E. coli* in a bioreactor. Ar stands for *A. baylyi* ADP1 with mScarlet, Akr for ArΔ*gntT*, Eg for *E. coli* with sfGFP, and Ekg for EgΔ*ptsI*. Samples were drawn at approximately 1 h intervals. Neither biological nor technical replicates were made of these supplementary experiments. OD_{600} was measured with a spectrophotometer, glucose and acetate concentration were measured with a high-performance liquid chromatograph, and pH was continuously monitored by the reactor's control tower.

drop of glucose concentration also supports gluconate production. Traces of gluconate were detected during the cultivation, and the concentration was approximately 1–2 mM by the end of the cultivation. This indicates that *E. coli* Δ*ptsI* consumed gluconate continuously and simultaneously to its production by *A. baylyi* ADP1 Δ*gntT*. Altogether, these additional observations were consistent with the smaller-scale experiments, the ODE framework, and the proposed carbon flow (glucose to gluconate by *A. baylyi* ADP1 Δ*gntT*, gluconate utilized and acetate excreted by *E. coli* Δ*ptsI*, and acetate utilized by *A. baylyi* ADP1 Δ*gntT*).

As for Eg and Akr:Eg, acetate accumulated towards the end of the cultivations, like in [31]. Eg accumulated acetate much earlier, which demonstrates the efficiency of acetate removal by Akr. Therefore it seems likely that acetate was the limiting factor in Akr:Ekg.

Analogous to [19], increasing acetate excretion by *E. coli* might increase growth of the Akr:Ekg consortium. On the other hand, this also provided experimental support for not assuming a constant acetate concentration in *A. baylyi* ADP1 Δ*gntT*:*E. coli* consortia. Section S2 along with these findings indicate, that the two-way coupled *A. baylyi* ADP1 Δ*gntT*:*E. coli* Δ*ptsI* consortium should be more stable than the others. As a final note it is observed that culture acidity rose the quickest in Eg, but also markedly in Akr:Eg and Ar:Eg, which provides an explanation for steep descents of sfGFP fluorescence in some of the small-scale cultivations presented in main text (Figures 2 and 3).

S6.2 Precultivations

Precultivations for the reactor experiments were carried out in two stages. The first stage was started 24–36 h prior to reactor start-up as a 5 mL tube culture inoculated from LA-plates. In the second stage 4 mL of the tube-culture was used to inoculate 50 mL cultures in flasks 12–18 h prior to reactor inoculation. Both precultivation stages were incubated with 250 RPM or 300 RPM shaking at temperature of either 37 °C (*E. coli*) or 30 °C (*A. baylyi* ADP1). Precultures were performed with the same defined medium (Table S6) as the actual experiments. The wild-type *A. baylyi* ADP1 and *E. coli* strains were precultivated with 10 g L^{-1} glucose. The knock-out *A. baylyi* ADP1 Δ*gntT* was precultivated with 2.5 g L^{-1} glucose and 75 mM acetate, and *E. coli* Δ*ptsI* was precultivated with 50 mM gluconate. Glucose was used along with acetate in precultivating *A. baylyi* ADP1 Δ*gntT*, because its oxidation to gluconate is beneficial even when the gluconate is not utilized [17, 18].

S6.3 Bioreactor configuration and operation

The reactor was a 1 L UniVessel Glass Culture Vessel (Sartorius, Germany) connected to a Biostat B plus control tower (Sartorius) monitoring temperature and pH. The reactor's impeller was a six-blade Rushton turbine with a diameter of 4.5 cm. A stirring rate of 350 RPM was used in all cultivations.

The targeted working volume was 0.55 L, but some variation occurred because of reactor sterilization in autoclave. Inoculum volumes of 50 mL were used such that the initial optical density would be at most 0.1. Equal amounts of strains in terms of optical density were used in inoculating consortia. The input rate of filtered air was set to 0.55 L min^{-1} (gas at 20 °C temperature and 1.2 bar absolute pressure), approximating a volume-specific flow-rate of 1 VVM. Temperature was maintained at 30 °C.

S6.4 Sample analyses

The reactor cultivations were sampled approximately hourly. 2 mL samples were drawn and divided to 1 mL aliquots. Right after sampling, optical densities at 600 nm and

700 nm were measured from one aliquot with a Ultrospec 500 pro spectrophotometer (Amersham Biosciences, UK). Optical densities were measured at 700 nm as well, because mScarlet has absorption maximum at 569 nm and it could therefore bias the OD_{600} measurements [32]. However, the bias at 600 nm remained neglicible.

The cells were removed from the other 1 mL aliquot by centrifugation, and concentrations of glucose and acetate were quantified from supernatants (stored at −20 °C and thawed) with a high-performance liquid chromatograph (HPLC). A LC-20 AD Prominence liquid chromatograph, SIL-20 AC Prominence auto sampler, and RID-10 A refractive index detector (Shimadzu, Japan) were used with a 30 cm Rezex RHM-Monosaccharide H^+ (8 %) column (Phenomenex, USA). The column was operated with 40 °C temperature and 0.6 mL min^{-1} flow. Filtered (0.2 µm) 5 mM H_2SO_4 was used as the mobile phase. For confirmation of gluconate accumulation, the supernatants were further analyzed with an Agilent (California, Unites States) 1100 series HPLC composed of G1322A degasser, G1311A pump, G1315A diode array detector (DAD), G1313A autosampler, G1316A thermostatted column compartment, and a 30 cm Rezex RHM-Monosaccharide H^+ (8 %) column (Phenomenex). The HPLC was again operated with 40 °C column temperature and 0.6 mL min^{-1} flow, but with filtered (0.2 µm) H_2O as the mobile phase. DAD Signals were recored at 195 nm and 210 nm. Glucose was visible at 195 nm, but not at 210 nm. However, gluconate was detectable at both wavelengths, and the concentrations were estimated from peak heights at 210 nm.

Supplementary References

1. Pacheco, A. R., Moel, M., and Segrè, D. (2019). Costless metabolic secretions as drivers of interspecies interactions in microbial ecosystems. *Nat. Commun. 10*, 103.

2. Xu, B., Jahic, M., Blomsten, G., and Enfors, S. (1999). Glucose overflow metabolism and mixed-acid fermentation in aerobic large-scale fed-batch processes with *Escherichia coli*. *Appl. Microbiol. Biotechnol. 51*, 564–571.

3. Pigou, M., and Morchain, J. (2015). Investigating the interactions between physical and biological heterogeneities in bioreactors using compartment, population balance and metabolic models. *Chem. Eng. Sci. 126*, 267–282.

4. Enjalbert, B., Millard, P., Dinclaux, M., Portais, J., and Letisse, F. (2017). Acetate fluxes in *Escherichia coli* are determined by the thermodynamic control of the Pta-AckA pathway. *Sci. Rep. 7*, 42135.

5. Ebrahim, A., Lerman, J. A., Palsson, B. O., and Hyduke, D. R. (2013). COBRApy: COnstraints-Based Reconstruction and Analysis for Python. *BMC Syst. Biol. 7*, 74.

6. van der Walt, S., Colbert, S. C., and Varoquaux, G. (2011). The NumPy Array: A Structure for Efficient Numerical Computation. *Comput. Sci. Eng. 13*, 22–30.

7. McKinney, W. In *Proceedings of the 9th Python in Science Conference*, ed. by van der Walt, S., and Millman, J., 2010, pp 51–56.

8. Durot, M., Fèvre, F. L., de Berardinis, V., Kreimeyer, A., Vallenet, D., Combe, C., Smidtas, S., Salanoubat, M., Weissenbach, J., and Schachter, V. (2008). Iterative reconstruction of a global metabolic model of *Acinetobacter baylyi* ADP1 using high-throughput growth phenotype and gene essentiality data. *BMC Syst. Biol. 2*, 85.

9. Feist, A. M., Henry, C. S., Reed, J. L., Krummenacker, M., Joyce, A. R., Karp, P. D., Broadbelt, L. J., Hatzimanikatis, V., and Palsson, B. O. (2007). A genome-scale metabolic reconstruction for *Escherichia coli* K-12 MG1655 that accounts for 1260 ORFs and thermodynamic information. *Mol. Syst. Biol. 3*, 121.

10. Minty, J. J., Singer, M. E., Scholz, S. A., Bae, C., Ahn, J., Foster, C. E., Liao, J. C., and Lin, X. N. (2013). Design and characterization of synthetic fungal-bacterial consortia for direct production of isobutanol from cellulosic biomass. *Proc. Natl. Acad. Sci. U.S.A. 110*, 14592–14597.

11. Shou, W., Ram, S., and Vilar, J. M. G. (2007). Synthetic cooperation in engineered yeast populations. *Proc. Natl. Acad. Sci. U.S.A. 104*, 1877–1882.

12. Wintermute, E. H., and Silver, P. A. (2010). Emergent cooperation in microbial metabolism. *Mol. Syst. Biol. 6*, 407.

13. Mee, M. T., Collins, J. J., Church, G. M., and Wang, H. H. (2014). Syntrophic exchange in synthetic microbial communities. *Proc. Natl. Acad. Sci. U.S.A. 111*, E2149–E2156.

14. Taylor, W. H., and Juni, E. (1961). Pathways for Biosynthesis of a Bacterial Capsular Polysaccharide. I. Characterization of the Organism and Polysaccharide. *J. Bacteriol. 81*, 688–693.

15. Taylor, W. H., and Juni, E. (1961). Pathways for Biosynthesis of a Bacterial Capsular Polysaccharide. II. Carbohydrate Metabolism and Terminal Oxidation Mechanisms of a Capsule-Producing Coccus. *J. Bacteriol. 81*, 694–703.

16. Vaneechouette, M., Young, D. M., Ornston, L. N., de Baere, T., Nemec, A., van der Reijden, T., Carr, E., Thernberg, I., and Dijkshoorn, L. (2006). Naturally Transformable *Acinetobacter* sp. Strain ADP1 Belongs to the Newly Described Species *Acinetobacter baylyi*. *Appl. Environ. Microbiol. 72*, 932–936.

17. Müller, R. H., and Babel, W. (1986). Glucose as an energy donor in acetate growing *Acinetobacter calcoaceticus*. *Arch. Microbiol. 144*, 62–66.

18. van Schie, B. J., Pronk, J. T., Hellingwerf, K. J., van Dijken, J. P., and Kuenen, J. G. (1987). Glucose-dehydrogenase-mediated Solute Transport and ATP Synthesis in *Acinetobacter calcoaceticus*. *J. Gen. Microbiol. 133*, 3427–3435.

19. Zhou, K., Qiao, K., Edgar, S., and Stephanopoulos, G. (2015). Distributing a metabolic pathway among a microbial consortium enhances production of natural products. *Nat. Biotechnol. 33*, 377–383.

20. Jones, E., Oliphant, T., Peterson, P., et al. (2001). SciPy: Open source scientific tools for Python., `http://www.scipy.org/`.

21. Kannisto, M., Aho, T., Karp, M., and Santala, V. (2014). Metabolic Engineering of *Acinetobacter baylyi* ADP1 for Improved Growth on Gluconate and Glucose. *Appl. Environ. Microbiol. 80*, 7021–7027.

22. Kannisto, M., Efimova, E., Karp, M., and Santala, V. (2017). Growth and wax ester production of an *Acinetobacter baylyi* ADP1 mutant deficient in exopolysaccharide capsule synthesis. *J. Ind. Microbiol. Biotechnol. 44*, 99–105.

23. Xu, B., Jahic, M., and Enfors, S. (1999). Modeling of Overflow Metabolism in Batch and Fed-Batch Cultures of *Escherichia coli*. *Biotechnol. Prog. 15*, 81–90.

24. Santala, S., Efimova, E., Kivinen, V., Larjo, A., Aho, T., Karp, M., and Santala, V. (2011). Improved Triacylglycerol Production in *Acinetobacter baylyi* ADP1 by Metabolic Engineering. *Microb. Cell Fact. 10*, 36.

25. Ceroni, F., Algar, R., Stan, G., and Ellis, T. (2015). Quantifying cellular capacity identifies gene expression designs with reduced burden. *Nat. Methods 12*, 415–418.

26. Hochuli, E., Bannwarth, W., Döbeli, H., Gentz, R., and Stüber, D. (1988). Genetic Approach to Facilitate Purification of Recombinant Protein with a Novel Metal Chelate Adsorbent. *Nat. Biotechnol. 6*, 1321–1323.

27. Bindels, D. S., Haarbosch, L., van Weeren, L., Postma, M., Wiese, K. E., Mastop, M., Aumonier, S., Gotthard, G., Royant, A., Hink, M. A., and Gadella Jr, T. W. J. (2017). mScarlet: a bright monomeric red fluorescent protein for cellular imaging. *Nat. Methods 14*, 53–56.

28. Der, B. S., Glassey, E., Bartley, B. A., Enghuus, C., Goodman, D. B., Gordon, D. B., Voigt, C. A., and Gorochowski, T. E. (2017). DNAplotlib: Programmable Visualization of Genetic Designs and Associated Data. *ACS Synth. Biol. 7*, 1115–1119.

29. Haldimann, A., and Wanner, B. L. (2001). Conditional-Replication, Integration, Excision, and Retrieval Plasmid-Host Systems for Gene Structure-Function Studies of Bacteria. *J. Bacteriol. 183*, 6384–6393.

30. Hartmans, S., Smits, J. P., van der Werf, M. J., Volkering, F., and de Bont, J. A. M. (1989). Metabolism of Styrene Oxide and 2-Phenylethanol in the Styrene-Degrading *Xanthobacter* Strain 124X. *Appl. Environ. Microbiol. 55*, 2850–2855.

31. Santala, S., Karp, M., and Santala, V. (2014). Rationally Engineered Synthetic Coculture for Improved Biomass and Product Formation. *PLoS One 9*, e113786.

32. Hecht, A., Endy, D., Salit, M., and Munson, M. S. (2016). When Wavelengths Collide: Bias in Cell Abundance Measurements Due to Expressed Fluorescent Proteins. *ACS Synth. Biol. 5*, 1024–1027.